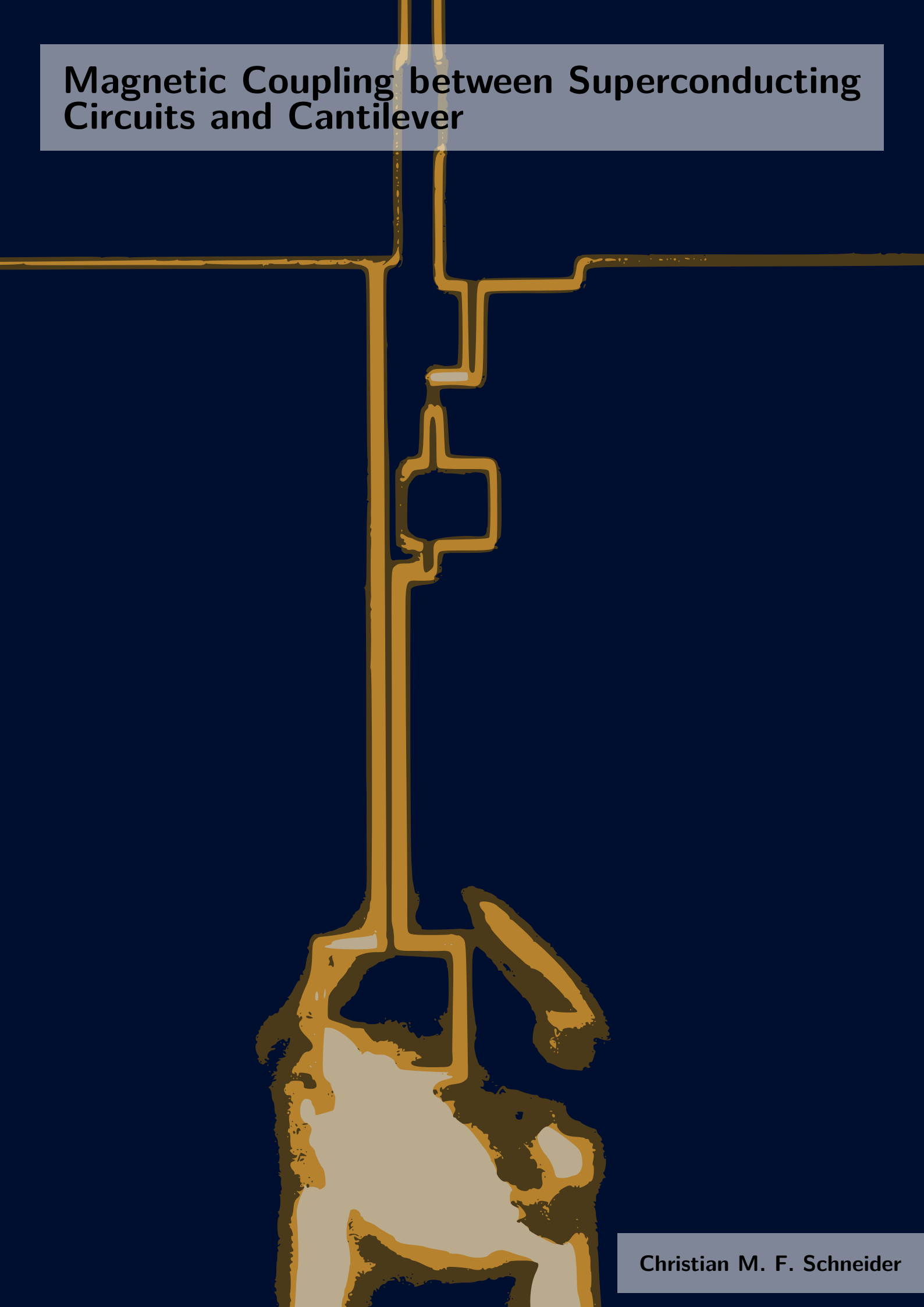


Magnetic Coupling between Superconducting Circuits and Cantilever



Christian M. F. Schneider



Magnetic Coupling between Superconducting Circuits and a Cantilever

DISSERTATION

by

Christian Markus Florian Schneider

submitted to the Faculty of Mathematics, Computer Science, and Physics of the University of Innsbruck in partial fulfillment of the requirements for the degree of Doctor of Philosophy (PhD)

Innsbruck, May 2021

Carried out at the Institute of Experimental Physics under the supervision of

UNIV.-PROF. DR. GERHARD KIRCHMAIR

with the co-supervisors

UNIV.-PROF. DR. RUDOLF GRIMM

UNIV.-PROF. DR. ORIOL ROMERO-ISART

UNIV.-PROF. DR. MARKUS ASPELMEYER

Abstract

This dissertation describes the development of magnetic coupling between a superconducting circuit and a mechanical oscillator. Based on a theoretical proposal [1] and pioneering work [2–4], the setup discussed in this thesis comprises a cantilever magnetically coupled to a superconducting interference device (SQUID) circuit. This setup has the potential to enter the strong single-photon coupling regime, where the coherent coupling rate between the mechanical system and the superconducting circuit is bigger than the loss rates of both, allowing to engineer macroscopic mechanical quantum states. To achieve the strong coupling, the cantilever is equipped with either a permanent magnet, or a superconductor located in magnetic (gradient) fields. This thesis describes the theoretical framework, implementation, characterizations and optimizations of this setup in a direct current circuit and in a microwave resonator circuit. While still not reaching the limit of strong-single-photon coupling, this work paves the way towards further optimized setups.

Kurzfassung

Diese Dissertation beschreibt die Realisierung einer magnetischen Kopplung zwischen einem supraleitenden Schaltkreis und einem mechanischen Oszillator. Basierend auf einem theoretischen Entwurf [1] und Pionierarbeiten [2–4], umfasst der in dieser Arbeit behandelte Aufbau einen Cantilever, der magnetisch mit einer supraleitenden Interferenzschaltung (SQUID) gekoppelt ist. Dieser Aufbau hat das Potenzial, in den Bereich der starken Ein-Photon-Kopplung vorzudringen. Hier ist die kohärente Kopplungsrate zwischen dem mechanischen System und dem supraleitendem Schaltkreis größer als die Verlustraten der beiden Systeme, was die Erzeugung makroskopischer mechanischer Quantenzustände ermöglicht. Um die starke Kopplung zu erreichen, wird der Cantilever entweder mit einem Permanentmagneten oder einem in magnetischen (Gradienten-) Feldern liegenden Supraleiter ausgestattet. Diese Arbeit beschreibt die theoretischen Grundlagen, die Implementierung, Charakterisierungen und Optimierungen dieses Aufbaus in einer Gleichstromschaltung und in einer Schwingkreis-Schaltung im Mikrowellenbereich. Im Rahmen dieser Arbeit wird der Aufbau erstmals untersucht um den Weg für weitere Experimente zu ebnen, die vielleicht in den Bereich der starken Einzelphotonkopplung vordringen können.

Contents

Abstract/Kurzfassung	iii
1 Introduction	1
1.1 Overview of thesis	3
1.2 Work not covered in this thesis	3
2 Superconducting Quantum Magnetomechanics	5
2.1 Superconducting quantum circuits	5
2.1.1 Superconductivity	5
2.1.2 Josephson junction (JJ)	12
2.1.3 DC-SQUIDs	15
2.1.4 Microwave resonators/circuits	21
2.1.5 SQUID resonators	27
2.2 Mechanical systems	30
2.2.1 Cantilever	31
2.2.2 Effective harmonic oscillator	32
2.2.3 Power spectral density (PSD) of a harmonic oscillator	34
2.2.4 Quantum regime	36
2.3 Coupling between superconducting circuits and mechanical systems	38
2.3.1 Cavity optomechanics in superconducting circuits	38
2.3.2 Classical response of mechanics to a cavity	40
2.4 Magnetic coupling	42
2.4.1 Backaction mechanism	44
2.4.2 Cavity optomechanics with the magnetic cantilever setup	47
2.4.3 Meissner effect setup	53
3 DC-SQUID setup	59
3.1 Practical DC-SQUIDs	59
3.2 Experimental setup	63
3.2.1 Sample packaging	63
3.2.2 Cryostat setup	67
3.2.3 SQUID Readout	67
3.2.4 Noise optimization	68
3.3 Samples and characterizations	71
3.3.1 Innsbruck 1st generation	71
3.3.2 Tübingen 1st generation	73
3.3.3 HYPRES	76
3.3.4 Tübingen/PTB 2nd generation	84
3.3.5 In-house Nb constriction	84
3.4 Adding mechanics: the cantilever	87
3.4.1 Design and fabrication	87
3.4.2 Preparation and alignment	90

3.4.3	Measurements of the complete setup	90
4	Microwave setup	93
4.1	Experimental setup	93
4.2	Granular Aluminium (grAl) SQUID resonators	96
4.2.1	Design and Fabrication	97
4.2.2	Characterizations	98
4.2.3	Behavior with magnetic cantilevers	103
4.2.4	Hybrid grAl SQUID resonators	105
4.3	Niobium constriction SQUID resonators	106
4.3.1	Designs	107
4.3.2	Fabrication	108
4.3.3	Characterizations	109
4.3.4	Behavior with magnetic cantilevers	109
4.4	Hybrid Nb/Ta-Al SQUID resonators	110
4.4.1	Design	110
4.4.2	Fabrication	111
4.4.3	Characterizations	112
4.4.4	Behavior with magnetic cantilevers	115
5	Conclusions and Outlook	119
	Bibliography	121
	Publication list	139
	Appendix A Fabrication recipes	141
A.1	Wafer cleaning	141
A.2	grAl SQUID resonators	141
A.3	Nb constriction SQUID resonators	143
A.4	Nb-grAl hybrid SQUID resonators	145
A.5	Nb/Ta-Al hybrid SQUID resonators	145
	Appendix B Programming	149
B.1	Instruments class	149
B.2	Experiments class	150
B.3	Datamodule	150
B.4	Monitoring	150
B.4.1	Webapp backend: flask	151
B.4.2	Webapp frontend: Vue.js	151
	Acknowledgements	153

Introduction

Erwin Schrödinger posed an intriguing question in a 1935 article: How does quantum mechanics - a theory that works well at the atom scale - effect macroscopic objects [5]. He exemplified this problem a bit provocatively in form of a cat in combination with radioactive decay that triggers poison to kill the cat, all embedded in a closed box and ensured that the cat does not accidentally trigger the mechanism itself. This stimulating gedankenexperiment troubled many physicists ever since [6], and in its honor, the superposition of coherent states is called a (Schrödinger) cat-state today. In the last paragraph of his article, Schrödinger clarified that the vagueness (today we call it a superposition state) should extend (become entangled) from the atom-scale to a bigger scale at which the state gets *decided* (measured) by observation. The process of the measurement is what troubles many physicists¹, which is somehow the connection between classical physics and quantum physics [7]. Another open question is how big can we make this cat; is there a fundamental limit on the size of a quantum system? Impressive experimental efforts over the last 50 years extended the size from electrons [8, 9], to atoms [10], molecules [11], gigantic molecules [12], macroscopic currents [13], towards living organisms [14]. Mechanical systems offer an excellent platform to investigate this topic [15]. Can we excite the collective motion of billions of atoms to a quantum state? And at some point, if the system gets heavy enough, and if we can create a big displaced quantum state, gravity has to effect the system. To this day, we do not have a conclusive answer to the question how gravity effects quantum mechanics. Mechanical systems have the potential to reach this exciting regime [1, 16, 204] and explore these exciting frontiers of quantum mechanics.

Moreover, developments of mechanical systems over the past decade showed sublime results [15, 17–21]. These systems reach now quality factors above $Q \geq 10^9$ [17], corresponding to a mechanical coherence time $\gamma^{-1} \approx 1$ ms at 10 K, which even rises when going to lower temperatures. Such long lived systems offer the potential as a quantum memory for quantum information processing. However, the biggest application in quantum information processing would be using mechanical systems as transducers to establish quantum networks [22]. Mechanical systems have the potential to coherently up-convert microwave signals to optical frequencies, allowing the transfer of information between superconducting circuits, propagating light fields and for example trapped ion qubits [22–27]. Another application lies in metrology, as full quantum control over mechanical systems would boost the sensitivity of acceleration and force sensors [28].

¹Known as the measurement problem

(Quantum) control over mechanical systems requires an auxiliary system to detect and manipulate mechanical motion. In this work we use superconducting circuits, a powerful platform that offers a high compatibility for hybrid systems [29, 30], including the coupling to mechanical systems [15, 19, 31, 32]. Over the last two decades superconducting circuits have become one of the leading platforms for quantum simulation and quantum information processing [33, 34], in the beginning with coherence times around nanoseconds [35], and today reaching milliseconds [36–38]. This great progress could enable to enter a regime, in which the coupling rate between superconducting circuits and a mechanical system is larger than the loss rates, i.e. inverse of the coherence times, of the two systems

$$g_0 > \kappa \wedge g_0 > \Gamma, \quad (1.1)$$

where g_0 is the coupling rate between mechanical system and microwave circuit, $\kappa = 1/T_2$ is the loss/decoherence rate of the microwave circuit and Γ is the loss/decoherence rate of the mechanical system. This regime is called strong-single-photon coupling and would allow to efficiently swap a quantum state from a well controlled microwave circuit to a mechanical system. Moreover, in this regime the interaction becomes intrinsically nonlinear, allowing further protocols to generate non-classical mechanical states [15].

There are only three fundamentally different ways of coupling mechanical systems to superconducting circuits, since we can always come up with an equivalent circuit schematic consisting of resistance R , inductance L , and capacitance C . The first way is to modulate R by a displacement of the mechanical system, which is the typical configuration of a DC-SQUID setup. While sending a constant current through the resistive element, a modulation in R due to mechanical displacement leads to a modulation in V that we can detect and digitize. This setup has the disadvantage of being intrinsically dissipative, which is typically unwanted for fragile quantum systems. However, such a setup allows real-time detection of the mechanical motion, gives detailed insight about the system, which may be useful for debugging, and offers applications as ultra-sensitive force or acceleration sensor. To enter the world of quantum states, one has to switch gears and remove all dissipative elements (another possibility could be to engineer a quantum bath). We are left with two further possibilities: a mechanical sensitive capacitance $C(x)$ and a mechanical sensitive inductance $L(x)$. The former has been proven to be the prizewinning highflier, demonstrating groundstate cooling [39], coherent state-transfer [26], entangling motion to propagating microwaves [27], reaching ultra-strong coupling [40], and ultimately stabilization of a mechanical quantum state [20, 41]. However, the single photon coupling is given by the change of capacitance with displacement, which is highest when the plates are as close together as possible. Recent setups already optimized this down to 50 nm [40–42], which cannot be reduced further without risking the collapse of the capacitance due to van-der-Waals forces. For the generation of quantum states, the researchers developed clever methods using either piezoelectric materials or boosting the sensitivity of a cooper pair to mechanical motion by applying a voltage to the mechanical sensitive capacitance. However, both approaches come at cost of a decreased coherence time for the microwave circuit. Inductive coupling on the other hand had a slow start after early pioneering work [32] but may reach stronger coupling regimes [1]. Difficulties arose since strong magnetic fields and superconductors are not very compatible. Nevertheless, recently there were breakthroughs by integrating this coupling mechanism to circuit QED architecture [43–46]. In this work, we investigate the coupling scheme proposed by Refs. [1, 2], which is theoretically able to

reach the strong single-photon coupling regime. We further investigate a slightly modified setup using permanent magnets [3, 4] to relax the experimental requirements.

1.1 Overview of thesis

This thesis has three main chapters. The first main chapter, Chapter 2, is an introduction to our toolbox: superconducting circuits, the cantilever (our mechanical system of choice), and the coupling between these two systems. After introducing and deriving the basic equations to describe superconducting circuits and mechanical systems, we develop a model to describe the magnetic coupling between a superconducting quantum interference device (SQUID) and a magnetic cantilever.

The next main chapter, Chapter 3, presents the DC-SQUID setup. In this first step we want to detect the mechanical motion by a DC-SQUID. On our way to establish the setup, we learned that the DC regime is actual a world full of noise that requires a careful designed setup and filtering. The chapter discusses practical DC-SQUID setups, and shows how to make a cantilever magnetically visible. At the end of the chapter I present a characterization of optimized setups.

In the last main chapter, Chapter 4, we switch to a microwave setup where the SQUID is embedded into a microwave resonator. The chapter is about finding good materials and architectures to allow strong coupling to magnetic cantilevers (requiring high magnetic fields close to the superconductor), while preserving a high quality factor (low loss rates) under these high fields. We investigate the materials granular Aluminum, Niobium, Tantalum, and hybrid structures consisting out of Nb/Ta resonators together with Al Josephson junctions far away from the high field regions.

1.2 Work not covered in this thesis

I had the honor of participating in two further projects that I would like to mention here, but which are beyond the scope of this thesis. For the first project, I joined Paul Heidler to assist measurements and analyze the results of his record Niobium cavity. We applied our knowledge about microwave resonators together with an exhaustive two-level-system (TLS) model developed by K. Kustura *et al.* [47] to fit the power decay of the coaxial cavity. We could explain the observed long-term dynamics by coherent scattering of the cavity field by the TLS, which we recently published [38].

For the second project I joined the lab of Prof. Konrad Lehnert at JILA² in Boulder, Colorado, USA. This stay abroad was made possible by the doctoral program Atom, Lights, and Molecules (DK-ALM). I joined the project of Eric I. Rosenthal, and we developed a new way of single shot qubit readout that does not require ferrite circulators, offering improved scalability together with high fidelity and high-efficient readout. The resulting

²<https://jila.colorado.edu/lehnert/>

device showed excellent performance and we published our results [48] and filed for a patent application. Even though this project is not part of this thesis, I gained a lot of expertise in qubit design, readout and potential problems, which helped a lot for the fabrication of high quality microwave resonators in Chapter 4.

Superconducting Quantum Magnetomechanics

This chapter is about the toolbox for our experiments: superconducting quantum circuits, mechanical systems, and the magnetic coupling mechanisms between the two. In the first section, I will briefly introduce superconductivity, the nonlinear circuit element Josephson Junction, the superconducting quantum interference device (SQUID), LC circuits and $\lambda/2$ resonators, as well as magnetic-flux-sensitive resonators. Section 2 is about our mechanical system of choice, the cantilever. I will describe the fundamental properties of this element and introduce basic equations to understand its properties and behavior. In the final section of this chapter, I will discuss how to couple the two systems and motivate the magnetic coupling approach. I will give a detailed description of the coupling mechanism and present calculation and simulation results for the optimization of the setup.

2.1 Superconducting quantum circuits

Superconducting quantum circuits emerged with the discovery of the Josephson Effect in 1962 [49, 50] and the first demonstration of macroscopic quantum effects in 1985 [51–54]. However, it was only after the first demonstration of coherent Rabi oscillations by Nakamura *et al.* [35] in 1999, that many groups started to investigate and exploit quantum circuits as a resource for quantum simulation and quantum information processing. It is therefore a very young, but explosively developing field. In this section, I will introduce the fundamentals of superconductivity and all the required components to understand the great potential of such circuits-

2.1.1 Superconductivity

Superconductivity was a surprise discovery by H. Kamerlingh Onnes, who found in 1911 that the resistance for mercury dropped abruptly to zero below a critical temperature T_c [55, 56]. Today the microscopic origin is well understood and explained by an attractive interaction among conduction electrons mediated by phonons of the metal lattice, which causes electrons to pair up in *Cooper pairs* with opposite momentum [57–59]. The resulting collective state is bosonic with spin 1 leading to the collapse of the Fermi sea and the condensation into a new ground state with an energy gap $\Delta = 1.76k_B T_c$ below the Fermi

energy [58–60], with the Boltzmann constant $k_B = 1.38 \cdot 10^{-23}$ J/K and the material-specific critical temperature T_c . The ground state of BCS theory (named after J. Bardeen, L. Cooper, and J. R. Schrieffer) has no fixed particle number and is not localized at a single point, in contrast to a Bose-Einstein-Condensate (BEC). Instead it is described by an average density of cooper pairs $n_s(r, t)$ in the superconductor. Macroscopically, the condensate can be described by a single macroscopic wave function for the center of mass motion

$$\Psi(\mathbf{r}, t) = \sqrt{n_s(\mathbf{r}, t)} e^{i\theta(\mathbf{r}, t)} \quad (2.1)$$

which solely depends on a phase $\theta(\mathbf{r}, t)$ and the density of cooper pairs [58, 59, 61, 62].

Inserting Eq. (2.1) into the Schrödinger equation for a charged particle in electromagnetic fields

$$\frac{1}{2m_s} \left(\frac{\hbar}{i} \nabla - q_s \mathbf{A}(\mathbf{r}, t) \right)^2 \Psi(\mathbf{r}, t) + [q_s \phi(\mathbf{r}, t) + \mu(\mathbf{r}, t)] \Psi(\mathbf{r}, t) = i\hbar \frac{\partial \Psi(\mathbf{r}, t)}{\partial t}, \quad (2.2)$$

leads after some calculation and making use of the continuity equation, to the current-phase relation [63]

$$\Lambda \mathbf{J}_s(\mathbf{r}, t) = -\mathbf{A}(\mathbf{r}, t) - \frac{\hbar}{2e} \nabla \theta(\mathbf{r}, t) \quad (2.3)$$

with the London parameter $\Lambda = m_e/2n_s e^2$. The equation describes that currents in a superconductor can be created by electromagnetic fields or a phase gradient. We will now use this relation to derive some properties for superconductors in magnetic fields.

Superconductors in magnetic fields This thesis is about coupling a mechanical system magnetically to superconducting circuits - a scheme that critically requires high magnetic fields in the proximity of superconductors. Therefore we have to consider the impact of magnetic fields on superconductors. One characteristic feature is that superconductors completely expel magnetic fields. This can be derived by taking the curl of Eq. (2.3)

$$\nabla \times \Lambda \mathbf{J}_s = -\mathbf{B}. \quad (2.4)$$

Where we used that the curl of a gradient is zero and $\mathbf{B} = \nabla \times \mathbf{A}$. This equation describes that a magnetic field will induce screening currents orthogonal to \mathbf{B} and is called the **2. London Equation**. We can take another curl and make use of Maxwell equations $\mathbf{J}_s = \nabla \times \mathbf{B}/\mu_0$ (we omit the term $\propto \partial E/\partial t$ as there is no electric field inside the superconductor) and $\nabla \cdot \mathbf{B} = 0$ to obtain

$$\Delta \mathbf{B} = \frac{1}{\lambda_L^2} \mathbf{B}, \quad (2.5)$$

with the Laplace operator $\Delta = \nabla \cdot \nabla$. The magnetic field inside a superconductor decays exponentially with the **London Penetration depth**

$$\lambda_L = \sqrt{\Lambda/\mu_0} = \sqrt{\frac{m_e}{2\mu_0 n_s e^2}} \quad (2.6)$$

as illustrated in Fig. 2.1(a). Typical values for λ_L are between 30 nm and 300 nm. This behavior for superconductors is called the *Meissner effect* and directly dependent on magnetic field \mathbf{B} . In contrast, a perfect conductor is only susceptible to magnetic field changes over

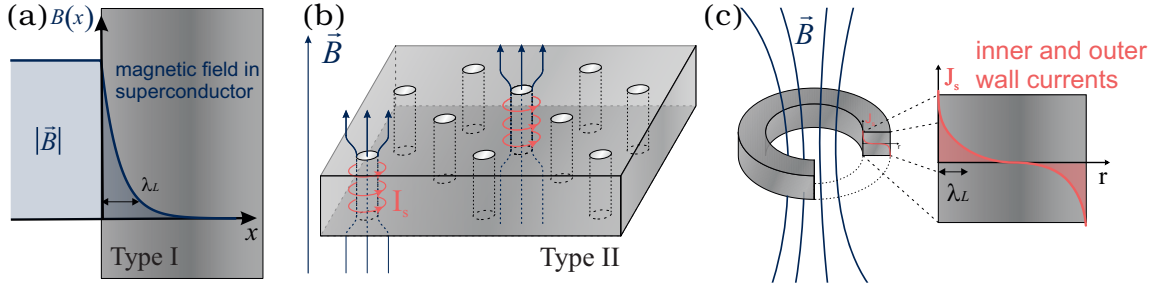


Figure 2.1: (a) Meissner effect in type I superconductors. Magnetic fields decay exponentially with λ_L inside the superconductor. This is caused by screening currents on the surface. (b) Abrikosov vortices in type II superconductors. Above a critical field B_{c1} , we will observe flux vortices penetrating through the superconductor. Each vortex has a core with size of the coherence length ξ and a magnetic flux of Φ_0 . Around each core form superconducting screening currents that decay over a length scale λ_L , focusing the magnetic field. Above a second critical field B_{c2} superconductivity breaks down. The figure is adapted from Ref. [64]. (c) Flux quantization in a thick superconducting loop. In-field cooling of a thick (above λ_L for all dimensions) loop will lead to a quantized magnetic flux value inside the loop $\Phi = n\Phi_0$. This is caused by fluxoid quantization: Using Eq. (2.10) and choosing a contour integral deep inside the superconductor where no currents are flowing results in a quantized flux in the loop. If the loop is separated by a weak link or is thinner than λ_L , we have to consider the currents in the loop and the loop flux can have arbitrary values.

time since Faraday's law of induction states that a time-varying flux through a conductive loop creates an electromotive force $\mathcal{E} = -d\Phi/dt$, which creates circulating currents. If the loop is resistive, the currents decay over time, however if the loop is a perfect conductor, the currents will persist, creating a magnetic flux which is exactly opposite to the applied flux. Therefore, in-field cooling of a perfect conductor leads to a magnetic field inside the perfect conductor, since the induced currents decay when the perfect conductor is not yet perfect conducting at high temperatures where the field is applied. This is different to a superconductor, which always expels the magnetic field. Therefore, the Meissner effect is a distinct feature of superconductors, or in other words a superconductor is an ideal diamagnet.

However, continuously increasing the applied magnetic field leads to very high screening currents. At some point, the system's energy would be higher than the condensation energy, and Cooper pairs break. The condensation energy is released by the formation of Cooper pairs and is the difference between Fermi energy and BCS ground state. The BCS prediction for a critical field at $T = 0$ is [59]

$$|\mathbf{B}_c| = \sqrt{\mu_0 n_s} \Delta_0, \quad (2.7)$$

with the magnetic field constant μ_0 , the density of Cooper pairs n_s and the energy gap at zero temperature Δ_0 . It is therefore given by material dependent parameters.

Ginzburg and Landau developed a phenomenological theory to describe superconductors in non-equilibrium conditions before BCS theory [58, 59, 65]. This theory was later derived

from BCS theory by *Gor'kov* [66]. In this formalism, the critical field is related to two other material-specific parameters [58, 59]

$$|\mathbf{B}_c| = \frac{\Phi_0}{2\pi\sqrt{2}\xi\lambda_L}, \quad (2.8)$$

namely the London penetration depth λ_L and the coherence length ξ . ξ quantifies the locality of the superconductor: A perturbation inside the condensate wavefunction will decay exponentially with ξ . Typical values of ξ range from 1 nm to 1 μm . Φ_0 is the magnetic flux quantum $\Phi_0 = h/2e$ and independent of the material. We will discuss the relevance of this parameter later in this subsection.

One remarkable deduction of Ginzburg-Landau theory was the prediction of possible flux vortices in superconductors when the ratio

$$\kappa_{\text{GL}} = \frac{\lambda_L}{\xi} \quad (2.9)$$

is larger than $1/\sqrt{2}$ [58, 59, 67]. The vortices are sometimes called *Abrikosov* vortices in honor of its discoverer. They are sketched in Fig. 2.1(b) and caused by an energy favorable state where the magnetic field penetrates through the superconductor. Flux vortices have been experimentally verified with various imaging methods [58, 59, 64].

We can then separate superconductors into different types.

Type I for superconductors with $\kappa_{\text{GL}} \leq 1/\sqrt{2}$. This type will never allow magnetic fields inside and will therefore always be in a Meissner state until a critical field B_c at which cooper pairs will break up.

Type II for superconductors with $\kappa_{\text{GL}} \geq 1/\sqrt{2}$. Below a critical field B_{c1} they behave the same as type I, but above B_{c1} flux vortices as shown in Fig. 2.1(b) will penetrate through the superconductor until a second critical field B_{c2} at which superconductivity breaks down. Each vortex has a core at its center with dimension ξ . The core is normal conducting, allowing the field to penetrate through the metal. Screening currents form around the core that decay at length scale λ_L .

Intertype (IT) A special case are thin films of superconductors for which the thickness is comparable to λ_L and ξ . Here, stray magnetic fields outside the sample create non-local interactions between vortices. This regime often shows type II characteristics [68] but can exhibit more complex features and is sometimes referred to as an intertype (IT) regime [69]. It is common for thin films but can also be achieved in bulk superconductors with non-local interactions.

The presence of vortices changes the transport properties of the superconductor since an applied current results in a Lorentz force $\mathbf{F} = \mathbf{I} \times \mathbf{B}$. The resulting motion of vortices leads to dissipation because the normal conducting electrons in the core scatter at defects and phonons [64]. Therefore, high magnetic fields close to superconductors cause a new dissipation channel as soon as the magnetic field is high enough to create vortices.

Fluxoid quantization By integrating Eq. (2.3) along a closed ring and using that the integral of the phase of a wave function along a closed loop must be a multiple of 2π ¹ results in the *fluxoid quantization* condition

$$\oint_{\partial S} \Lambda \mathbf{J}_s d\mathbf{l} + \Phi_{\text{loop}} = n\Phi_0. \quad (2.10)$$

Here $n \in \mathbb{Z}$ is an integer, $\Phi_0 = \hbar\pi/e$ is the magnetic flux quantum and $\Phi_{\text{loop}} = \int_S \mathbf{B} ds$ is the actual magnetic flux through the closed contour ∂S . Since the magnetic field inside a superconductor vanishes, there will be no circulating currents inside. However, if we make a loop out of a superconductor as illustrated in Fig. 2.1(c), magnetic flux inside the loop is allowed. Fluxoid quantization tells us that this flux is exactly a multiple of Φ_0 when there is no weak link and the superconductor is thicker than λ_L . If this is the case, we can choose a contour integral deep inside the superconductor where the superconducting current is zero. The same is true for vortices in type II superconductors.

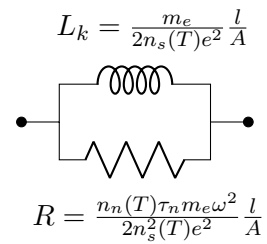
Two fluid model At zero temperature all the conduction electrons condense into the BCS ground state and the Cooper pair density approaches $n_s = n_{\text{tot}}/2$, where n_{tot} is the total density of conduction electrons. Finite temperatures can break up cooper pairs when the bath's energy exceeds the binding energy. The broken cooper pairs are electrons that interact via coulomb and lattice vibrations with cooper pairs. They become dressed and don't behave like free electrons. Therefore the excitation is called a *quasiparticle*. Higher quasiparticle densities change the superconducting gap energy due to the interaction with the cooper pair condensate. Therefore, we obtain a a temperature dependence of $\Delta = \Delta(T)$. Moreover, the unpaired conduction electrons contribute to dissipation when applying alternating electromagnetic fields². We can describe the effective conductivity with a *two-fluid model* in which we assume an ohmic/normal conducting channel with conductivity σ_n in parallel to the superconducting channel [58, 59]:

$$\mathbf{J}(\omega, t, T) = [\sigma_n(\omega, T) + \sigma_s(\omega, T)] \mathbf{E}e^{i\omega t}. \quad (2.11)$$

It is illustrative to use the AC *Drude* model

$$\sigma(\omega) = \frac{nq^2\tau}{m} \left(\frac{1}{1 + \omega^2\tau^2} + i \frac{\omega\tau}{1 + \omega^2\tau^2} \right) \quad (2.12)$$

with the density of conduction electrons n , the scattering time τ , the charge q , and the effective mass of charge carriers m for each channel. For a superconductor we assume $\tau_s \rightarrow \infty$ leading to a vanishing real part for $0 < \omega < 2\Delta$. On the other hand, we can assume a very high scattering rate for the normal conducting channel, much higher than frequencies of interest ($\omega \ll 1/\tau_n$).



¹The wave function must be single valued.

²The DC component will always be dissipation-less, which can be illustrated by a simple argument: The first London equation $d\mathbf{J}_s/dt = (n_s e^2/m)\mathbf{E}$ shows that an applied electrical field would lead to a steadily increasing current. However, if we assume a constant current $\partial\mathbf{J}/\partial t = 0$, the electric field inside the superconductor must be zero, and therefore the normal current density must be zero - a normal conducting current always requires an applied voltage/electric field (Ohm's law).

This leads to a purely resistive response for the normal conducting channel. Eq. (2.11) can then be simplified to

$$\mathbf{J}(\omega, t, T) = \left[\frac{n_n(T)e^2\tau_n}{m_e} - i \frac{n_s(T)2e^2}{m_e\omega} \right] \mathbf{E}e^{i\omega t}. \quad (2.13)$$

Where we used that for the superconducting channel $q = -2e$, $m_s = 2m_e$, i.e. the effective mass of a cooper pair is the one of two electrons, n_n is the density of normal conducting charge carriers ($n_{\text{tot}} = n_s/2 + n_n$), and m_e the effective mass of normal conducting charge carrier.

We get two main results from this picture. First, we see that the superconductor's response is the one of an inductance $\sigma_s = 1/i\omega L_k$. This is purely caused by the inertia of cooper pairs with mass $2m_e$ and not due to a counteracting magnetic field. Such an inductance is called *kinetic inductance*. Secondly, we get for the resistive channel

$$R = \text{Re} \left(\frac{1}{\sigma} \right) = \frac{\sigma_1}{\sigma_1^2 + \sigma_2^2} \approx \frac{\sigma_1}{\sigma_2^2} = \frac{n_n(T)\tau_n m_e \omega^2}{2n_s^2(T)e^2} \quad (2.14)$$

where σ_1 labeled the real part and σ_2 the imaginary part of the complex conductivity. Increasing frequency causes more and more current to flow in the resistive channel as expected for a parallel RL circuit. However, the characteristic frequency above which the dominant current will flow in the resistive channel is typically much higher than our operating frequencies $\omega_0 \approx (n_s/n_n)(1/\tau_n) \approx 10^{11}$ Hz [59]. Moreover, we see that R rises if $n_n(T)$ rises. We can use a result from BCS theory for the quasiparticle density [57, 70–72]

$$n_n = 2N_0 \sqrt{2\pi k_B T \Delta} \exp \left(-\frac{\Delta}{k_B T} \right). \quad (2.15)$$

Here N_0 is the single spin density of states at the Fermi energy. Therefore, we expect an exponential increasing resistance R for increasing temperature.

Mattis and Bardeen derived a more thorough relation for the real and imaginary part of the conductivity $\sigma = \sigma_1 - i\sigma_2$ based on BCS theory [73]. In the dirty limit³ and for $\hbar\omega < 2\Delta$ they got the result

$$\frac{\sigma_1}{\sigma_n} = \frac{2}{\hbar\omega} \int_{\Delta}^{\infty} \frac{[f(E) - f(E + \hbar\omega)] (E^2 + \Delta^2 + \hbar\omega E)}{\sqrt{E^2 - \Delta^2} \sqrt{(E + \hbar\omega)^2 - \Delta^2}} dE, \quad (2.16a)$$

$$\frac{\sigma_2}{\sigma_n} = \frac{1}{\hbar\omega} \int_{\Delta - \hbar\omega}^{\Delta} \frac{[1 - 2f(E + \hbar\omega)] (E^2 + \Delta^2 + \hbar\omega E)}{\sqrt{E^2 - \Delta^2} \sqrt{(E + \hbar\omega)^2 - \Delta^2}} dE, \quad (2.16b)$$

where $f(E) = 1/(e^{E/k_B T} + 1)$ is the Fermi function and σ_n is the normal state conductivity close to T_c . In the limit $\hbar\omega \ll k_B T \ll \Delta$ it is possible to evaluate the integrals [59, 70, 75, 76]

$$\frac{\sigma_1}{\sigma_n} = \frac{4\Delta}{\hbar\omega} e^{-\frac{\Delta}{k_B T}} \sinh \left(\frac{\hbar\omega}{2k_B T} \right) K_0 \left(\frac{\hbar\omega}{2k_B T} \right), \quad (2.17a)$$

$$\frac{\sigma_2}{\sigma_n} = \frac{\pi\Delta}{\hbar\omega} \tanh \left(\frac{\Delta}{2k_B T} \right), \quad (2.17b)$$

³The notion dirty superconductor was introduced by P. W. Anderson [74] and is the limit where the mean-free path l is smaller than the coherence length ξ . This limit allows a local description of the superconducting wavefunction. Most experimental realizable superconductors fall in this limit.

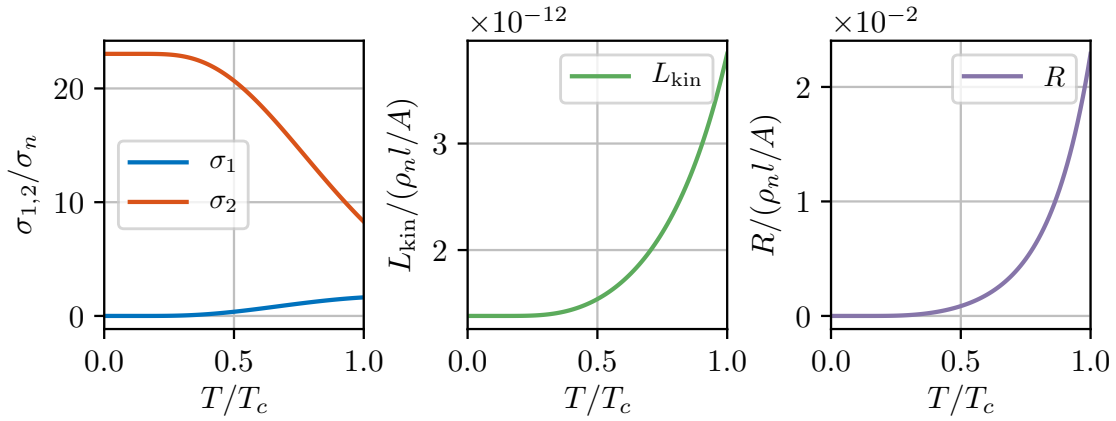


Figure 2.2: Behavior of $\sigma_{1,2}/\sigma_n$, L_{kin} and R in normalized units over temperature. Note that these plots are just correct for $T \ll T_c$ because of approximations. For increasing temperature, we observe increasing kinetic inductance and resistance.

with the modified Bessel functions of second kind $K_0(x)$ and the temperature dependent gap $\Delta = \Delta(T)$. We can evaluate the equations using the approximation [70]

$$\Delta \approx \Delta_0 \left(1 - \sqrt{\frac{2\pi k_B T}{\Delta_0}} e^{-\frac{\Delta_0}{k_B T}} \right), \quad (2.18)$$

for the temperature dependence of the superconducting gap, which is valid for $k_B T \ll \Delta$. These results give a more accurate formula for the kinetic inductance $L_{\text{kin}} = 1/\omega\sigma_2$

$$L_{\text{kin}} = \frac{\hbar}{\sigma_n \pi \Delta \tanh\left(\frac{\Delta}{2k_B T}\right)} \frac{l}{A}, \quad (2.19)$$

of a superconductor with length l and cross section A . For temperatures $T \ll T_c$ and using the *Residual Resistance Ratio* (RRR)⁴ we can relate the kinetic inductance of superconductors to room temperature resistance measurements [77]

$$L_{\text{kin}} = \frac{\hbar \rho_{RT}}{\pi} \frac{1}{\text{RRR}} \frac{l}{A} \approx 0.18 \frac{\hbar \rho_{RT}}{k_B T} \frac{1}{\text{RRR}} \frac{l}{A} \quad (2.20)$$

This relation is beneficial when working with high kinetic inductance superconductors like granular Aluminum. Here RRR is close to 1, and the room temperature measurements will help to calibrate the designed kinetic inductance value.

Fig. 2.2 depicts the temperature dependence of $\sigma_{1,2}$, L_{kin} and R predicted by Eq. (2.17). We observe an exponential increase for L_{kin} and R with increasing temperature similar to the simple Drude model. In Sec. 2.1.4 we will use the two fluid model to characterize the loss of microwave resonators.

⁴The residual resistance ratio (RRR or "triple R") is the ratio between the resistivity close to T_c and the room temperature resistivity, $\text{RRR} = \rho_{RT}/\rho_{Tc}$. At high temperatures, the conduction electrons scatter at lattice vibrations (phonons). Cooling down close to absolute zero will freeze the lattice vibrations and the electrons will only scatter at residual defects in the metallic crystal. The RRR therefore quantifies the purity/quality of the metal and has typically values between 10 and 300.

Table of superconductors used in this thesis The list of available superconductors is long. Starting from pure elements, scientists discovered many new ways of creating superconductors in alloys and ceramics, some with remarkably high critical temperatures reaching recently even room temperature superconductivity under very high pressures [78]. However, BCS theory only holds for low temperature superconductors. Due to our fabrication possibilities and material properties, we will focus on Aluminium (Al), Niobium (Nb), Tantalum (Ta) and granular Aluminum (grAl) in the course of this thesis. Table 2.1 is a list of the characteristic parameters for these superconductors. A special case is granular Aluminum (grAl), a compound of Aluminum spheres with small oxide layers. This material shows a higher critical temperature than pure Aluminum and a much higher magnetic field resilience. The reason for the changed properties is still investigated.

Material	Type	T_c (K)	$\Delta(0)$ (meV)	$2\Delta/\hbar$ (GHz)	B_c (mT)	λ_L (nm)	ξ_{GL} (nm)
Al	I	1.18	0.180	87.0	10.5	50	1550
Ta	I	4.47	0.650	314	82.9	35	
Nb	II	9.25	1.45	701	206	32-45	39
grAl	II	1.2 - 2.2	0.2 - 0.3	90-160	$\rightarrow 1$ T	-	6-27.2

Table 2.1: Table of superconductors used in this thesis. Parameters are critical field T_c , superconducting gap Δ in units of meV and GHz, critical magnetic field $B_c = \mu_0 H_c$, London penetration depth λ_L , and the Ginzburg-Landau coherence length ξ . Data taken from [58, 79–83].

2.1.2 Josephson junction (JJ)

B. D. Josephson derived on pen and paper that for superconductors separated by a weak link you can observe a tunneling current. This current will depend on the phase difference of the macroscopic wave functions [49]. Feynman later gave a simplified, intuitive derivation for this phenomenon [62, 84] that we use here to get more intuition about the system. Let's assume two superconductors are separated by a thin barrier so that the two superconductor wave functions can overlap, illustrated in Fig. 2.3. Moreover, we assume that there is no electromagnetic field. The Schrödinger equations for the two superconductors then read as

$$\begin{aligned} i\hbar\partial_t\Psi_1 &= E_1\Psi_1 + \zeta\Psi_2 \\ i\hbar\partial_t\Psi_2 &= E_2\Psi_2 + \zeta\Psi_1 \end{aligned} \quad (2.21)$$

where ζ is a constant which quantifies the overlap of the wave function and therefore depends on the geometry of the junction and coherence length of the superconductor.

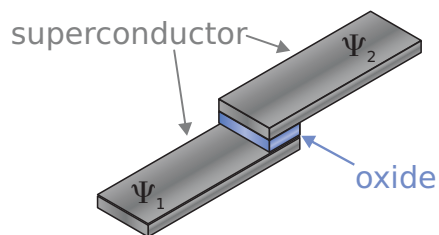


Figure 2.3: Sketch of a typical Josephson junction.

Inserting $\Psi_i = \sqrt{n_i}e^{i\theta_i}$ in Eq. (2.21) and assuming $\zeta \in \mathbb{R}$ for simplicity, we get

$$-\hbar\dot{\theta}_1 = \zeta\sqrt{\frac{n_2}{n_1}}\cos(\theta_2 - \theta_1) + E_1 \quad (2.22)$$

$$-\hbar\dot{\theta}_2 = \zeta\sqrt{\frac{n_1}{n_2}}\cos(\theta_1 - \theta_2) + E_2 \quad (2.23)$$

for comparing the real parts and

$$\dot{n}_1 = \frac{2\zeta}{\hbar}\sqrt{n_1 n_2}\sin(\theta_2 - \theta_1) = -\dot{n}_2 \quad (2.24)$$

for comparing the imaginary parts. Since qn_i is the electrical current through the junction, we arrive at the two **Josephson equations**

$$I = I_0 \sin(\varphi) \quad (\text{Josephson Eq. 1})$$

$$\dot{\varphi} = 2eV/\hbar \quad (\text{Josephson Eq. 2})$$

with the phase difference $\varphi = \theta_2 - \theta_1$, the *critical current* $I_0 = 4e\zeta\sqrt{n_1 n_2}/\hbar$, and the voltage across the junction $V = (E_1 - E_2)/2e$. We further used that cooper pairs carry a charge of $-2e$. I_0 is called the *critical current* since it quantifies the maximum current you can send through a junction before cooper pairs will break and the junction becomes normal conducting.

A more general approach allowing magnetic and electric fields ($\mathbf{A} \neq 0$) leads to the same equations but with a modified phase difference [58, 59]

$$\varphi = \theta_2 - \theta_1 + \frac{2\pi}{\Phi_0} \int_1^2 \mathbf{A}(\mathbf{r}, t) d\mathbf{l}, \quad (2.26)$$

with an integration contour going from superconductor 1 to superconductor 2. This was already discovered by Josephson who mentioned that the effect should be quite sensitive to magnetic fields [49, 50].

The Josephson effect was a big triumph for theoretical physics since it was first predicted theoretically and later observed experimentally by P. W. Anderson and J. M. Rowell in the same year [50]. Josephson received the Nobel Prize in Physics in 1973 for this work, and in his honor, the circuit element of two superconductors connected by a weak link is called Josephson junction (JJ).

Nonlinear inductance Taking the time derivative of Josephson Eq. 1 and inserting Josephson Eq. 2 leads to the following current-voltage characteristic

$$V = \frac{\hbar}{2e} \frac{1}{I_0 \cos(\varphi)} \dot{I} = L(\varphi) \dot{I}. \quad (2.27)$$

Thus, a Josephson junction acts as a dissipation-less inductance L . However this inductance is nonlinear since φ depends on the current through the junction.

To get an explicit equation for the inductance depending on I , we use the branch flux defined by $\Phi_b(t) = \int_{-\infty}^t V(t') dt'$ (see Sec. 2.1.4). We can then rewrite the first Josephson equation by using the second Josephson equation as

$$I(t) = I_0 \sin\left(\frac{2e}{\hbar} \Phi_b(t)\right). \quad (2.28)$$

Now we can use the defining equation of an inductance

$$I(t) = \frac{1}{L} \Phi_b(t), \quad (2.29)$$

to obtain [85, 86]

$$L(I) = \frac{\Phi_b(t)}{I(t)} = \frac{\hbar}{2e} \frac{\arcsin \frac{I}{I_0}}{I} \approx L_J \left[1 + \frac{1}{6} \left(\frac{I}{I_0} \right)^2 \right], \quad (2.30)$$

where we introduced the **Josephson inductance**

$$L_J = L(0) = \frac{\hbar}{2eI_0}. \quad (2.31)$$

For increasing current, the inductance increases until the junction gets normal conducting ($I = I_0$), making it a nonlinear dissipationless inductor. This is used to construct low loss nonlinear LC -circuits like the *transmon*, which can serve as a qubit.

Note that in contrast to a coil, a Josephson junction does not build up a magnetic field. The inductive behavior arises completely out of the kinetic energy of cooper pairs tunneling through the junction.

Current voltage characteristic Applying a slowly increasing DC current to a Josephson junction will lead to the characteristic current-voltage dependence seen in Fig. 2.4. There is no DC voltage drop across the junction below the critical current I_0 , which means that all cooper pairs tunnel dissipationless through the junction. At I_0 the DC voltage will abruptly jump, and we observe an ohmic behavior. The slope here corresponds to the normal state resistance of the weak link. Moreover, allowing vector fields, we have to use Eq. (2.26) in Josephson Eq. 1. This leads to a magnetic sensitive Josephson current. In fact, this feature was used to verify the measurement of the Josephson effect [50, 87].

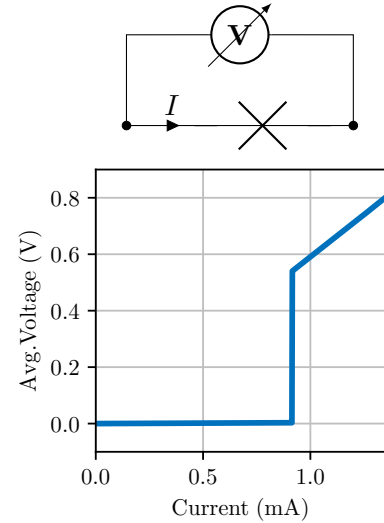


Figure 2.4: Measured IV characteristic of a Josephson junction.

2.1.3 DC-SQUIDS

We can further increase the magnetic sensitivity by increasing the area in which the vector field contributes to a phase change φ . One of the simplest geometry to achieve this is the parallel connection of two Josephson junctions illustrated in Fig. 2.5. This geometry is called a direct current superconducting quantum interference device (DC-SQUID)[58, 59, 89]. By using Kirchhoff's law and introducing α_I , which characterizes the asymmetry of critical currents for the two junctions, we can describe the total current as

$$\begin{aligned} I &= I_0(1 - \alpha_I) \sin(\varphi_1) + I_0(1 + \alpha_I) \sin(\varphi_2) \\ &= 2I_0 \cos\left(\frac{\varphi_1 - \varphi_2}{2}\right) \sin\left(\frac{\varphi_1 + \varphi_2}{2}\right) + 2\alpha_I I_0 \cos\left(\frac{\varphi_1 + \varphi_2}{2}\right) \sin\left(\frac{\varphi_2 - \varphi_1}{2}\right) \end{aligned} \quad (2.32)$$

We now use the fluxoid quantization condition, Eq. (2.10), and assume that the superconductor is thicker than the London penetration depth λ_L . Then we can choose a contour integral Γ , illustrated with the red dashed line in Fig. 2.5(b), deep inside the superconductor (from top and bottom, too). Here the superconducting currents are zero ($J_s = 0$) and we just have to integrate over the current contribution through the Josephson junctions

$$n\Phi_0 = \oint_{\Gamma} \Lambda \mathbf{J}_s d\mathbf{l} + \Phi_{\text{loop}} = \int_{1,\text{top}}^{1,\text{bot}} \Lambda \mathbf{J}_s d\mathbf{l} + \int_{2,\text{bot}}^{2,\text{top}} \Lambda \mathbf{J}_s d\mathbf{l} + \Phi_{\text{loop}}. \quad (2.33)$$

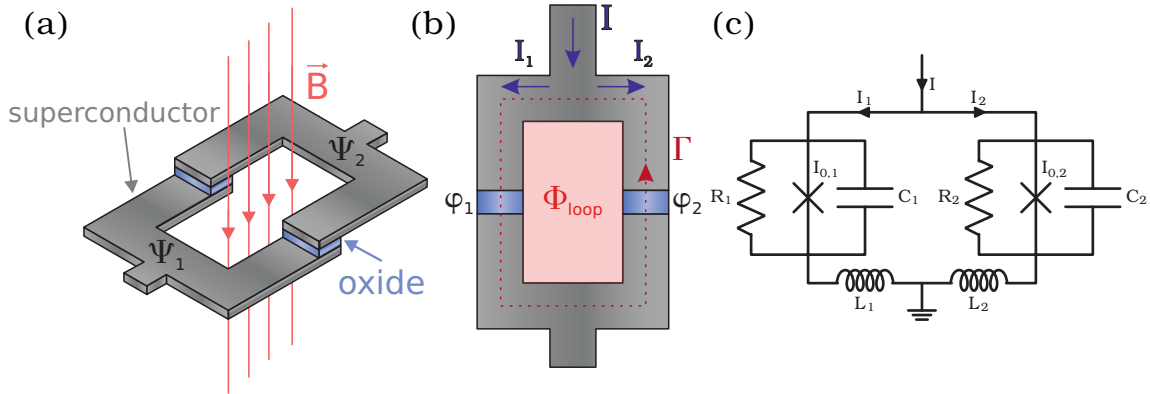


Figure 2.5: (a) and (b) illustrate a typical DC-SQUID: two Josephson junctions are connected in parallel. The whole device can be regarded as a single Josephson junction with a magnetic field tunable critical current. This is an interference effect and arises due to fluxoid quantization: The macroscopic superconducting wave function must be single valued when we integrate along the loop Γ in (b). A magnetic flux in the loop will create a phase shift similar to the Aharonov-Bohm effect [88] that must be canceled by phase changes $\varphi_{1,2}$ caused by Josephson currents across the junctions. (c) A SQUID is typically modeled by the resistively and capacitively shunted junction (RCSJ) model. Each branch also has a geometric inductance, which affects the SQUID's performance, as discussed in the main text.

To solve this integral we integrate over the current phase relation Eq. (2.3):

$$\begin{aligned}
\int_{1,top}^{1,bot} \Lambda \mathbf{J}_s d\mathbf{l} &= -1 \int_{1,top}^{1,bot} \left(\mathbf{A} + \frac{\hbar}{2e} \nabla \theta \right) d\mathbf{l} \\
&= -\frac{\Phi_0}{2\pi} \left(\int_{1,top}^{1,bot} \frac{2\pi}{\Phi_0} \mathbf{A} d\mathbf{l} + \theta_{1,top} - \theta_{1,bot} \right) \\
&= -\frac{\Phi_0}{2\pi} \varphi_1,
\end{aligned} \tag{2.34}$$

where we used the definition of the gauge invariant phase (2.26) for the last equality. When we do the same for junction 2 and evaluate Eq. (2.33), we end up with

$$2\pi \left(n - \frac{\Phi_{loop}}{\Phi_0} \right) = \varphi_2 - \varphi_1. \tag{2.35}$$

This states that the difference of the phase differences must be an integer multiple of $2\pi \frac{\Phi_{loop}}{\Phi_0}$. Inserting this result in Eq. (2.32) and dropping n due to periodicity of sin and cosine leads to the current-phase relation for a DC-SQUID

$$\begin{aligned}
I &= 2I_0 \cos \left(\pi \frac{\Phi_{loop}}{\Phi_0} \right) \sqrt{1 + \alpha_I^2 \tan^2 \left(\pi \frac{\Phi_{loop}}{\Phi_0} \right)} \\
&\cdot \sin \left(\frac{\varphi_1 + \varphi_2}{2} + \arctan \left[\alpha_I \tan \left(\pi \frac{\Phi_{loop}}{\Phi_0} \right) \right] \right).
\end{aligned} \tag{2.36}$$

If we define the argument of the sin function as a new phase-change φ' , we get a relation that looks very similar to the one of a single junction (Josephson Eq. 1) with a magnetic flux dependent **critical SQUID current**

$$I_0^{\text{SQUID}} = 2I_0 \left| \cos \left(\pi \frac{\Phi_{loop}}{\Phi_0} \right) \right| \sqrt{1 + \alpha_I^2 \tan^2 \left(\pi \frac{\Phi_{loop}}{\Phi_0} \right)}, \tag{2.37}$$

with the critical current of a single junction I_0 , the total flux through the SQUID loop Φ_{loop} , the critical current asymmetry α_I and the magnetic flux quantum Φ_0 . Fig. 2.6(a) shows the flux dependence of (2.37) for different α_I . Using an external magnetic field, we can tune the critical current with a Φ_0 periodicity. The strong dependence on magnetic flux makes DC-SQUIDS the most sensitive magnetometers, with many applications in research and medicine [89, 90]. An asymmetry in critical currents ($\alpha_I \neq 0$) leads to a decreased I_0 tunability. In the next paragraph, we will observe that a decreased tunability can be further caused by a nonzero geometric inductance of the SQUID.

Screening parameter In general, Φ_{loop} differs from the applied external flux Φ_{ext} due to flux generated by currents flowing in the geometric inductance of the SQUID. In this paragraph, we will now investigate the effect of the geometric inductance on the SQUID behavior. Two new effects arise: First, the circulating screening current will create a flux $\Phi_{screen} = L_{geo} I_{loop}$ inside the loop. Moreover, in typical setups, there will also be an AC or DC current across the SQUID. If we look at the geometric inductance of each branch (each side of the SQUID loop, cf. Fig. 2.5) $L_{geo} = L_1 + L_2$, we see that an applied bias current will lead to an induced flux inside the loop, if the inductances of each SQUID loop side are

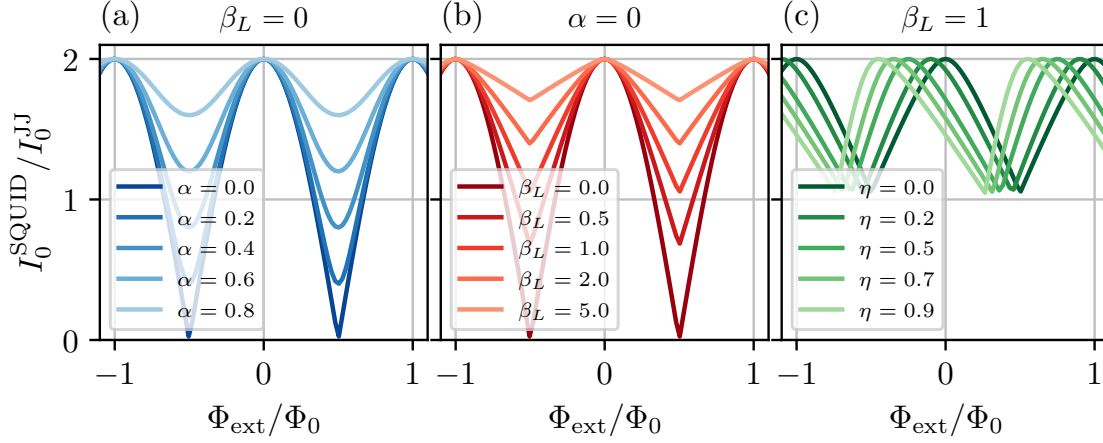


Figure 2.6: Effect of external magnetic flux on the critical current for various junction asymmetries α_I , screening parameters β_L and geometric inductance asymmetries η . At zero field, the critical current is twice the critical current of a single junction as expected for a parallel circuit. However, for finite fields, the critical current drops until it reaches a minimum at half a flux quantum inside the loop and goes up again with Φ_0 periodicity. For an ideal SQUID with perfect symmetry and negligible geometric inductance the critical current goes down to actually zero. Asymmetries and higher β_L values will lift the degeneracy and cause finite critical currents at this point. Finite inductance asymmetries cause a skewed dependence.

different $L_1 \neq L_2$. Following *C. Tesche and J. Clarke* [91], we quantify the asymmetry of the inductances, including mutual inductance by a factor $0 \leq \eta \leq 1$. $\eta = 0$ means perfect symmetry, and the field generated by branch 1 will exactly cancel the field generated by the other branch current. Deviations, however, will lead to a finite field in the loop. We can then write the following relation for the total flux inside the loop

$$\Phi_{\text{loop}} = \Phi_{\text{ext}} + LI_{\text{loop}} + \eta L \frac{I}{2}, \quad (2.38)$$

where $L = L_1 + L_2 - 2M$ is the total inductance of the SQUID loop including the mutual inductance M between the two branches, Φ_{ext} is the flux through an area of the SQUID loop created by the external magnetic field, I_{loop} is the circulating current in the loop and I is the total current across the SQUID. Inserting this result in Eq. (2.35) and taking $n = 0$ for simplicity gives

$$\varphi_2 = \varphi_1 + 2\pi \frac{\Phi_{\text{ext}}}{\Phi_0} + \pi\beta_L \frac{I_{\text{loop}}}{I_0} + \pi\eta\beta_L \frac{I}{2I_0} \quad (2.39)$$

where we introduced the **screening parameter**

$$\beta_L = \frac{2LI_0}{\Phi_0} = \frac{L}{\pi L_J}, \quad (2.40)$$

which characterizes the inductance ratio of a SQUID. Note that we include a π in the definition to be consistent with common literature [89, 92]. We can eliminate I_{loop} by

looking at the current through each junction. If we define the direction of I_{loop} in the same direction as the contour integral Γ in Fig. 2.5(b) we get

$$\frac{I}{2} + I_{\text{loop}} = I_0(1 - \alpha_I) \sin(\varphi_1) \quad (2.41a)$$

$$\frac{I}{2} - I_{\text{loop}} = I_0(1 + \alpha_I) \sin(\varphi_2) \quad (2.41b)$$

Solving Eq. (2.41a) for I_{loop} and inserting the result into Eq. (2.39) results in

$$\varphi_2 = \varphi_1 + 2\pi \frac{\Phi_{\text{ext}}}{\Phi_0} + \frac{\pi\beta_L I}{2I_0} (\eta - 1) + \pi\beta_L(1 - \alpha_I) \sin(\varphi_1) \quad (2.42)$$

We can further solve Eq. (2.41a) and Eq. (2.41b) for I and I_{loop}

$$I = I_0(1 - \alpha_I) \sin \varphi_1 + I_0(1 + \alpha_I) \sin \varphi_2 \quad (2.43a)$$

$$I_{\text{loop}} = \frac{I_0}{2} (1 - \alpha_I) \sin \varphi_1 - \frac{I_0}{2} (1 + \alpha_I) \sin \varphi_2 \quad (2.43b)$$

Note that these are both implicit equations, as φ_2 depends on the current and circulating current. The critical current of the SQUID can then be obtained only numerically by finding the maximum current I where Eq. (2.43a) still has a solution. This means finding the root of the function

$$F = \frac{I}{I_0} - (1 - \alpha_I) \sin(\varphi_1) - (1 + \alpha_I) \sin(\varphi_2) \quad (2.44)$$

with respect to φ_1 and I by inserting Eq. (2.42). In contrast to *Tesche and Clarke*, [91] we are not using the second derivative and a Newton-Raphson solver. Instead, we use a least square solver while calculating hundreds of F values for $0 \leq \varphi_1 \leq 2\pi$ and picking the minimum. This turned out to be more robust and is easily possible with the speed of modern computers. Figure 2.6(b) and Fig. 2.6(c) show numerical evaluations for increasing screening parameter β_L and inductance asymmetry η . The first leads to a decreased I_0 tunability while the latter causes a skewed saw-tooth like behavior.

Hysteresis Moreover, a nonzero β_L could lead to a hysteretic behavior if the system is probed with sufficiently low powers. Low power here means that the bias currents across the SQUID is close to zero $I \ll I_0$. The hysteresis arises because the implicit equations Eq. (2.43a) and Eq. (2.43b) have multiple allowed solutions for $\beta_L \neq 0$, leading to metastable states. The general case can only be solved numerically, but the case without applied bias current $I = 0$ can be simplified, as shown in the following. For simplicity, we further assume identical junctions $\alpha_I = 0$. Setting Eq. (2.43a) to zero results in the condition $\sin \varphi_1 = -\sin \varphi_2$, and Eq. (2.43b) becomes $I_{\text{loop}} = I_0 \sin \varphi_1$. Moreover, fluxoid quantization for the SQUID [Eq. (2.35)] states that the difference between φ_1 and φ_2 must be an integer multiple of $2\pi \frac{\Phi_{\text{loop}}}{\Phi_0}$. Together with the condition $\sin \varphi_1 = -\sin \varphi_2$ for zero

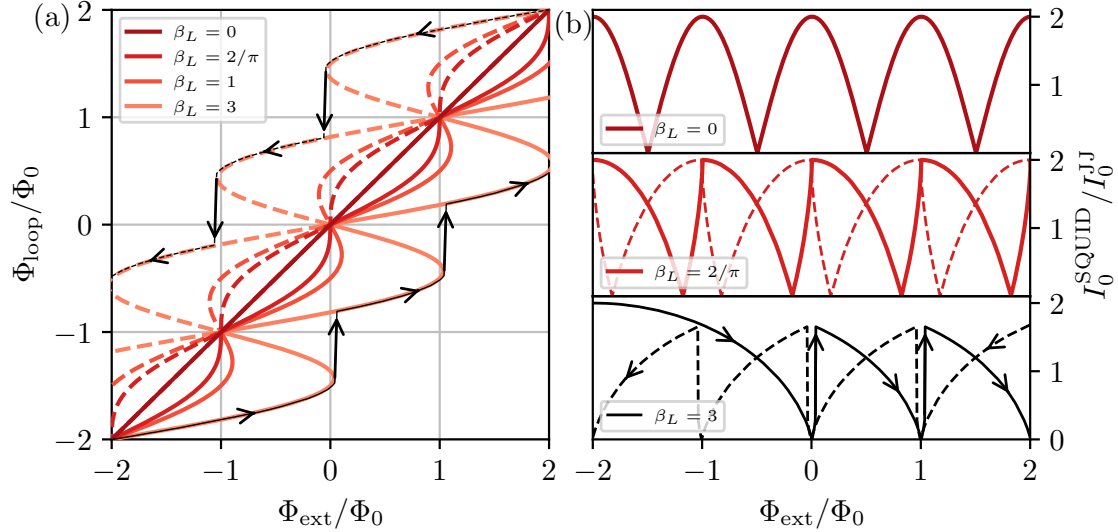


Figure 2.7: Magnetic flux in the SQUID loop (a) and critical SQUID current (b) for increasing (solid lines) and decreasing (dashed lines) external magnetic flux. The bias current is set to zero for all shown traces. For $\beta_L = 0$ the curves lie on top of each other. (a) For $\beta_L \neq 0$, applying an external flux leads to a smaller total flux in the loop due to the magnetic field generated by the induced superconducting screening currents and finite geometric inductance of the SQUID loop. The SQUID becomes hysteretic, i.e. different behavior is observed for increasing flux bias and decreasing flux bias, which is typically observed for hysteretic SQUID resonators (e.g. Fig. 4.6). $\beta_L > 2/\pi$ leads to discrete jumps for flux bias sweeps, illustrated by the black solid (dashed) line for increasing (decreasing) external flux. In this regime, there could be many metastable states (multiple allowed Φ_{loop} values for a single Φ_{ext} value). (b) shows that there are now at least two possible critical currents of the SQUID if $\beta_L \neq 0$. However, only the solution with the highest critical current is stable. When probing with low powers, one can follow the SQUID into the metastable regions. If one biases the SQUID strongly (typical for DC-SQUID operation) it always follows the stable solution (the solution with the highest critical current), recovering the behavior from Fig. 2.6(b).

bias current, this gives $\varphi_1 = n\pi\Phi_{\text{loop}}/\Phi_0$. Substituting these simplifications into Eq. (2.38) and solving for Φ_{ext} yields

$$\frac{\Phi_{\text{ext}}}{\Phi_0} = \frac{\Phi_{\text{loop}}}{\Phi_0} \pm \frac{\beta_L}{2} \sin\left(\pi \frac{\Phi_{\text{loop}}}{\Phi_0}\right) \quad (2.45)$$

Note that in contrast to [92, 93], we have a \pm to account for all solutions (n can be a negative integer, too). The intuition for this can be given by looking how fluxoid quantization can be achieved in a DC-SQUID loop: an applied magnetic flux can be compensated with clockwise or counter-clockwise circulating currents. The currents generate a flux within the loop due to $\beta_L \neq 0$, which either increases or decreases the total flux within the loop. Also note that this equation is only valid for $I = 0$, a nonzero applied bias current requires numerical evaluations, but leads to a very similar behavior for low bias currents.

Figure 2.7(a) shows the behavior of Eq. (2.45). The axes are inverted, as we normally apply external magnetic fields. A nonzero β_L leads to multiple (at least 2) allowed values for the magnetic flux within the SQUID loop Φ_{loop} for a given external flux Φ_{ext} . Since the critical current is given by the total flux within the loop [see Eq. (2.37)], we observe the same for the critical current of the SQUID. The values now depend on the sweep direction of the applied magnetic field, as shown in Fig. 2.7, solid lines show the behavior for increasing magnetic fields, and dashed lines for decreasing magnetic field. When $\beta_L > 2/\pi$, there exist even more solutions, where the number of possible Φ_{loop} values increases with increasing β_L . For example, a $\beta_L = 3$ leads to 6 possible Φ_{loop} values at $\Phi_{\text{ext}} = 0.5$, which can be seen in Fig. 2.7(a). The stable solution is the always the one where Φ_{loop} is closest to a multiple of a flux quantum, or in other words, the solution with the highest critical current. However, for low probe powers this solution may never be reached. For example, we can look at what happens if we continuously increase (decrease) the magnetic field for a SQUID with $\beta_L = 3$, as illustrated by the solid (dashed) black lines in Fig. 2.7(a) and Fig. 2.7(b). We set the initial condition to $\Phi_{\text{loop}} = -2$ and Φ_{ext} , and increase the magnetic field to $\Phi_{\text{ext}} = 3\Phi_0$, before decreasing it again to $\Phi_{\text{ext}} = -2\Phi_0$. If we probe with sufficiently low power, we follow the lowest Φ_{loop} solution to a point, where a further increase in external flux requires a jump. After that point, all jumps are Φ_0 periodic. Once we get a little above $3\Phi_0$, we decrease the magnetic field and follow now the maximum loop flux branch until we reach the external flux we started from. But now the flux inside the loop $\Phi_{\text{loop}} \approx -0.4\Phi_0$ is not the same as the value we started with $\Phi_{\text{loop}} = -2\Phi_0$. This is a hysteretic behavior, and can be observed for resonance frequencies of SQUID resonators, which depend on the critical current of the SQUID (see Sec. 2.1.5 and for an example Fig. 4.6). In contrast, typical DC-SQUID are always biased with high powers (close to or above the critical current), which causes the system to follow the stable solution, and we recover the behavior of Fig. 2.6(b). For high β_L samples, one can follow the metastable states very deeply and go up to many Φ_0 of applied external flux without observing a jump [94]. Therefore, the first flux lobe of the SQUID can have a width of many Φ_0 .

Tunable non-linear inductance Similar to a single junction, a SQUID acts as a nonlinear inductance

$$L = \frac{\hbar}{2e} \frac{\arcsin(I/I_{\text{SQUID}})}{I} \approx L_{\text{SQUID}} \left[1 + \frac{1}{6} \left(\frac{I}{I_{\text{SQUID}}} \right)^2 \right], \quad (2.46)$$

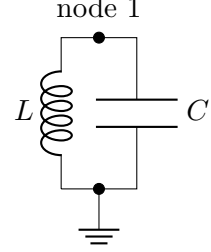
but now with a critical current $I_{\text{SQUID}}(\Phi)$ which depends on the flux in the SQUID loop given by Eq. (2.37). We define the minimum (no applied bias current) inductance again as

$$L_{\text{SQUID}} \approx \frac{\hbar}{4eI_0^{JJ} \cos\left(\pi \frac{\Phi_{\text{loop}}}{\Phi_0}\right) \sqrt{1 + \alpha_I^2 \tan^2\left(\pi \frac{\Phi_{\text{loop}}}{\Phi_0}\right)}}, \quad (2.47)$$

which is now tunable by external magnetic flux $\Phi_{\text{loop}}(\Phi_{\text{ZPFext}})$. Note that the flux in the SQUID loop Φ_{loop} can differ quite a lot from the applied magnetic flux for $\beta_L \gg 0$ as shown in Fig. 2.7(a). I_0^{JJ} denotes the critical current of a single junction. The dependence on magnetic field is used to build frequency tunable (nonlinear) LC circuits [33, 93, 95]. We later use this feature to couple a magnetic mechanical oscillator to a microwave resonator.

2.1.4 Microwave resonators/circuits

Resonant systems offer many advantages in the investigation of quantum physics. They are typically only sensitive in a small spectral range around the resonance frequency, filtering unwanted noise sources. They increase coupling strengths to other multipoles by enhancing the electromagnetic field strength. And they enhance interference effects that allow very sensitive measurements. In superconducting quantum circuits, we typically operate in the microwave regime. Microwave resonators can be described by LC circuits, consisting of an inductance L and a capacitance C as illustrated on the right. We will now shortly sketch the derivation of the Hamiltonian for such a system, following *U. Vool and M. Devoret* [96]. For more details, I kindly refer the reader to their manuscript. The main concept for a thorough description is introducing the formalism of *branch currents* and *branch voltages*



$$\begin{aligned}\Phi_b(t) &= \int_{-\infty}^t v_b(t') dt', \\ Q_b(t) &= \int_{-\infty}^t i_b(t') dt'.\end{aligned}\tag{2.48}$$

The *branch voltage* v_b and *branch current* i_b are defined as the voltage across each branch and the current through each branch, i.e., across L and C in the case of a LC circuit. It is then useful to introduce *node fluxes* Φ and *node charges* Q defined at nodes between branches. The shown LC circuit just has a single node besides the mandatory ground. We now use the equations from electrodynamics for the energy stored by capacitance and inductance

$$E_c = \frac{1}{2C} \delta Q^2,\tag{2.49a}$$

$$E_L = \frac{1}{2L} \delta \Phi^2,\tag{2.49b}$$

where δQ and $\delta \Phi$ are the node charge difference and flux difference across the capacitor and inductor. Setting Q and Φ to zero at the ground, we can write the total Hamiltonian then as

$$H = \frac{Q^2}{2C} + \frac{\Phi^2}{2L},\tag{2.50}$$

where Q and Φ are the node charge and flux at node 1. In this definition, Φ is not necessarily linked to magnetic flux [compare Eq. (2.48)], and we can include kinetic inductances (cf. Sec. 2.1.2), too. Once we excite the LC circuit, we observe an oscillation of energy between charges stored in the capacitor and (magnetic and/or kinetic) flux stored in the inductance with an angular frequency $\omega_r = 1/\sqrt{LC}$. This is the well-studied system of a Harmonic Oscillator. We often translate more complex circuits into LC circuits to allow a simple theoretical description. This Hamiltonian can be translated to a quantum formalism by replacing the classical variables with their corresponding operators and commutation relations

$$\begin{aligned}\Phi &\longrightarrow \hat{\Phi}, \quad Q \longrightarrow \hat{Q}, \quad H \longrightarrow \hat{H}, \\ [\hat{\Phi}, \hat{Q}] &= i\hbar.\end{aligned}\tag{2.51}$$

We can then introduce creation and annihilation operators and rewrite

$$\hat{\Phi} = \Phi_{\text{ZPF}} (\hat{a} + \hat{a}^\dagger), \quad (2.52a)$$

$$\hat{Q} = -iQ_{\text{ZPF}} (\hat{a} - \hat{a}^\dagger), \quad (2.52b)$$

where we introduced the zero point fluctuations of flux and charge

$$\Phi_{\text{ZPF}} = \sqrt{\frac{\hbar Z_0}{2}}, \quad (2.53a)$$

$$Q_{\text{ZPF}} = \sqrt{\frac{\hbar}{2Z_0}}. \quad (2.53b)$$

Here $Z_0 = \sqrt{L/C}$ is the characteristic impedance of the circuit. For quantum circuits, the zero point fluctuation can reach macroscopic values as pointed out by A. Blais *et al.* [33]: Taking a typical capacitance value of $C \approx 0.4$ pF and a resonance frequency of $\omega_r = 2\pi \cdot 8$ GHz we will get $Q_{\text{ZPF}} = \sqrt{\hbar\omega_r C/2} \approx 6e$. The ground state has already an uncertainty of 6 electrons across the capacitance, which equals around $V = Q/C \approx 3$ μ V in voltage!

Using creation and annihilation operators, we can rewrite the Hamiltonian in default form for a quantum harmonic oscillator

$$\hat{H} = \hbar\omega_r \left(\hat{a}^\dagger \hat{a} + \frac{1}{2} \right). \quad (2.54)$$

In this basis, the eigenstates $|n\rangle$ fulfill the condition $\hat{a}^\dagger \hat{a} |n\rangle = n |n\rangle$ for $n \in \mathbb{N}_0$, meaning that the eigenenergies are infinitesimal sharp and separated by $\hbar\omega_r$ as illustrated in Fig. 2.8. The model is very theoretical because it assumes no coupling to an environment and no internal losses. As we have seen in Sec. 2.1.1, a superconductor should be rather modeled by a two-fluid model for finite temperature and nonzero frequencies. This would lead to a resistive element in the LC circuit. Typically there are additional loss channels due to fabrication and coupling to the environment. This leads to a finite linewidth κ of the energy levels that we can now probe by sweeping a probe tone across the resonance and observing absorption. To characterize the performance of a resonator, it is useful to define the quality factor

$$Q = \frac{\omega}{\kappa}, \quad (2.55)$$

which relates the oscillator frequency ω to the linewidth κ . High quality factors mean low unwanted losses that limit the coherence time $T_2 = 1/\kappa$.

But dissipation has an advantage, too. By simply cooling down microwave resonators in dilution refrigerators, we can initialize them in the quantum ground state. The bath at a base temperatures of 20 mK has lower energy then the energy level spacing of the LC

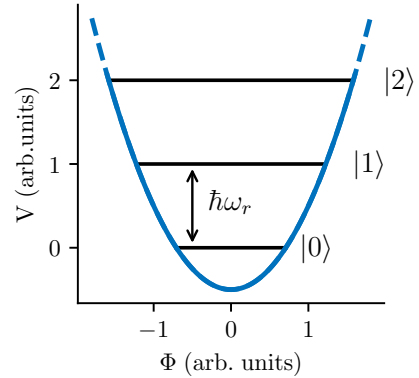


Figure 2.8: Potential and energy levels of a LC circuit.

oscillator: $k_B T_{\text{bath}}/\hbar = 2\pi \cdot 0.2 \text{ GHz} \ll 2\pi \cdot 8 \text{ GHz}$. However, since LC circuits have a linear response, we will always excite coherent states when applying coherent tones from signal generators. Nevertheless, microwave resonators could operate as a long-lived quantum memory, or even as qubits when applying quantum signals created by auxiliary nonlinear elements [97–99].

Half-wave ($\lambda/2$) resonators Half-wave or $\lambda/2$ resonators are among the most commonly used resonators in superconducting quantum circuits. They are easy to design and fabricate, and show high coherence times [100, 101]. The name arises from the fact that the device’s length is half the length of the resonator’s fundamental mode $l = \lambda/2$ (cf. Fig. 2.9). These resonators do not have a single mode, such as lumped element LC circuits, but all higher modes that satisfy the boundary conditions are also allowed. The theoretical description is more complex but still possible by modeling the resonator as a continuum of LC circuits with fixed boundary condition as illustrated in Fig. 2.9. This model is called transmission line model, and voltage-current dynamics can be calculated using the telegraphers equations. Using the formalism of branch charges and fluxes from before and assuming a uniform transmission line ($L_i = L_0$ & $C_i = C_0 \forall i, i = 0 \dots N$), we can write the Hamiltonian of this system as

$$\hat{H} = \sum_{i=0}^N \left[\frac{\hat{Q}_i^2}{2C_0} + \frac{(\hat{\Phi}_i - \hat{\Phi}_{i-1})^2}{2L_0} \right]. \quad (2.56)$$

Taking the continuum limit ($\Delta l = l/N \rightarrow 0$), following A. Blais *et al.* [33], we can rewrite the Hamiltonian after some steps in the basis of normal modes

$$\hat{H} = \sum_{j=0}^{\infty} \hbar \omega_j \left(\hat{a}_j^\dagger \hat{a}_j + \frac{1}{2} \right), \quad (2.57)$$

with the creation (\hat{a}^\dagger) and annihilation (\hat{a}) operators for each mode with number j and resonances frequencies

$$\omega_j = (j + 1)\omega_0 = (j + 1)2\pi \frac{v_0}{2l}, \quad (2.58)$$

which are harmonics of the fundamental mode ω_0 . The speed of light in the transmission line is given by $v_0 = 1/\sqrt{l_0 c_0}$ with the inductance and capacitance per unit length $dL/dx = l_0$ and $dC/dx = c_0$. The electric field distributions for the first three modes are sketched in Fig. 2.9. The depicted geometry is for usage in rectangular waveguides. A hairpin shape allows a more compact design together with the possibility of tuning the coupling by varying the leg length or position in the waveguide (see Sec. 4.1) and Refs. [102–104].

Note that Eq. (2.57) is the sum over independent harmonic oscillators. We can therefore regard each mode as a separate LC oscillator. This will not be true as soon as we insert nonlinear elements like Josephson junctions, leading to a coupling between the modes [105–108].

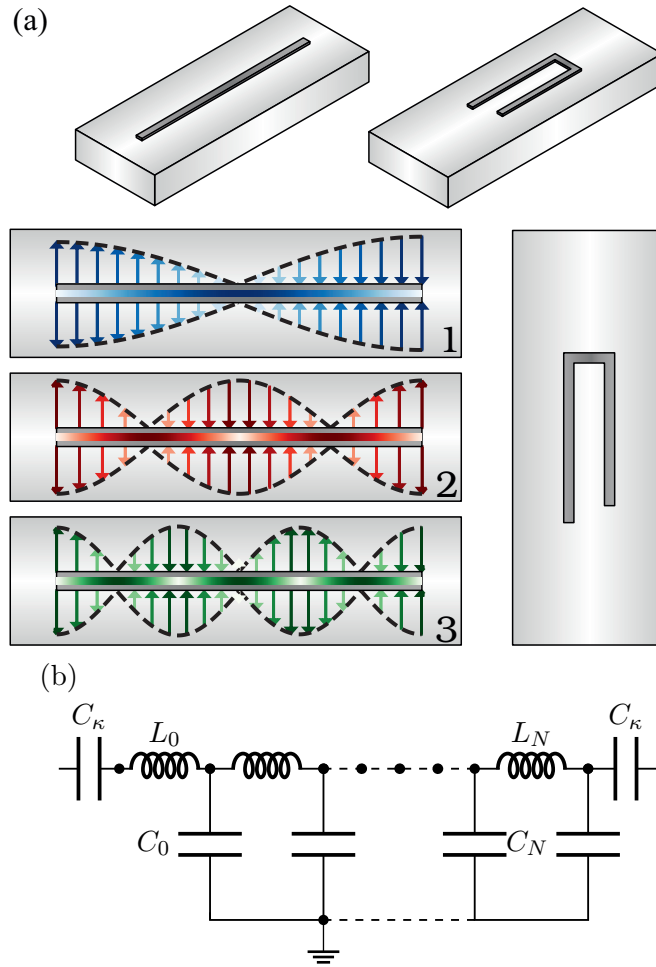


Figure 2.9: (a) Microstrip $\lambda/2$ resonators. A strip of superconductor is patterned on top of a silicon or sapphire substrate. The open boundary condition at the ends of the strip sets the resonance condition. Bottom left is a top view of the electric field (vectors) and magnitude of current (colored bar in the middle of the strip) for the first three modes. Increasing color intensity means increasing magnitude of electric field or current. Not shown is the required ground plane, which is typically far away at the walls of a waveguide. A U-shape or *hairpin* geometry allows a more compact design and allows to design the coupling to the mode of the waveguide (cf. Sec. 4.1). (b) Circuit model of a $\lambda/2$ resonator. The strip of length l can be modeled as a series of N infinitesimal LC circuits each with lengths $\Delta l = l/N$. This is the model of a transmission line of length l , which is described by the telegrapher's equation. Boundary conditions at the ends and coupling to the waveguide mode are modeled by a coupling capacitance C_κ . Nodes are marked as dots where each node has a node flux and node charge. The inductance L_i and capacitance C_i per unit length are set by geometric and material properties and characterize the transmission line. A useful quantity to describe this is the characteristic impedance $Z_i = \sqrt{L_i/C_i}$. Typically L_i and C_i do not vary over the transmission line. We can therefore characterize the transmission line by the characteristic impedance $Z_0 = \sqrt{L_0/C_0}$.

Mattis-Bardeen theory for microwave resonators For finite temperatures, we should use the two-fluid model to describe the response of a superconductor to AC fields (cf. Sec. 2.1.1). We get an additional kinetic inductance and a resistive element for the LC circuit. It is useful to define the **kinetic inductance ratio**

$$\alpha = \frac{L_{\text{kin}}}{L}, \quad (2.59)$$

as the ratio of the kinetic inductance L_{kin} over the total inductance L of the circuit. Note that this α has nothing to do with the critical current asymmetry α_I from Sec. 2.1.3.

Since the LC circuit's resonance frequency is given by $\omega_r = \sqrt{LC}$ we expect a decrease in resonance frequency for increasing quasiparticle density (e.g. due to temperature), as the kinetic inductance rises. It is useful to look at the normalized frequency change directly

$$\frac{\delta\omega_r}{\omega_r^0} = \frac{\omega_r(T) - \omega_r(0)}{\omega_r(0)} = \sqrt{\frac{LC}{(L + \delta L)C}} - 1 = \frac{1}{\sqrt{1 + \frac{\delta L}{L}}} - 1 \approx -\frac{\delta L}{2L}, \quad (2.60)$$

where δL is the change in inductance from 0 to temperature T . Inserting Eq. (2.59) for L , using that $L_{\text{kin}} = 1/\omega\sigma_2$, and assuming that all change of inductance is caused by kinetic inductance we get the result

$$\frac{\delta\omega_r}{\omega_r^0} = \alpha \frac{\sigma_2(T) - \sigma_2(0)}{2\sigma_2(T)}, \quad (2.61)$$

with σ_2 from Eq. (2.17). This allows to extract α and Δ_0 by fitting Eq. (2.61) to measurements. In Fig. 2.10 we show predictions of the normalized frequency change for typical values. A more thorough derivation of this relation can be found in the literature on microwave kinetic inductance detectors (e.g. Refs. [76, 109]).

Moreover, in Sec. 2.1.1 we saw that an increase in temperature leads to increased resistance of the superconductor. This should lead to a decrease in quality factor Q for LC circuits. To derive this condition, we use an alternative definition for the quality factor [59]

$$Q = \frac{\text{stored energy}}{\text{loss per radian}}. \quad (2.62)$$

For an LC circuit the energy in the circuit is $E = LI^2$ while the energy lost per radian is $\delta E/\omega_r = RI^2/\omega_r$. Inserting Eq. (2.59) for L gives

$$Q = \omega_r \frac{L_{\text{kin}}}{\alpha R} \approx \frac{\sigma_2}{\alpha\sigma_1}, \quad (2.63)$$

where we have used that $L_{\text{kin}} \approx 1/\omega_r\sigma_2$ and $R \approx \sigma_1/\sigma_2^2$.

Following *Tinkham* [59], we can further derive a relation for cavities and microstrip resonators where the energy of the field is mostly stored in vacuum and/or dielectric. The model assumes that the fields of the mode are totally reflected at the cavity wall by induced screening currents. These AC currents will exponentially decay with the *skin depth*

$$\delta = \sqrt{\frac{2}{(|\sigma| + \sigma_2)\omega\mu_0}}. \quad (2.64)$$

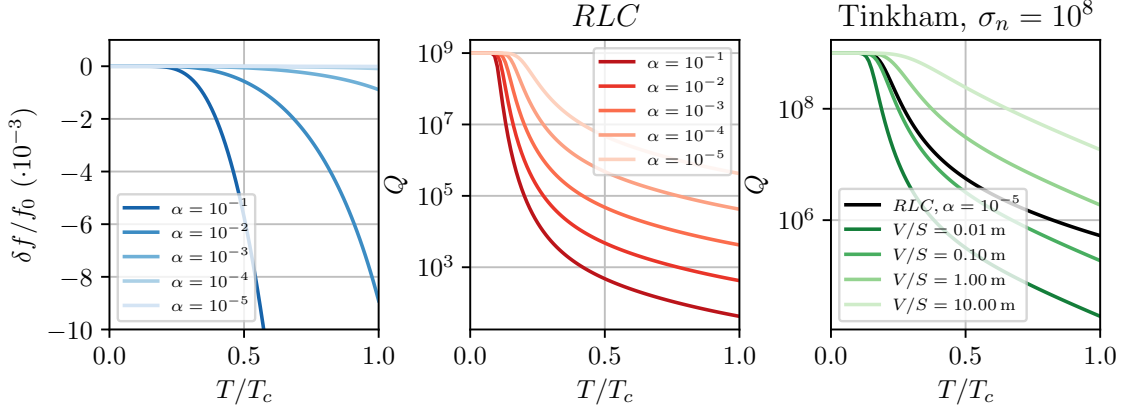


Figure 2.10: Mattis-Bardeen theory prediction of normalized frequency shift $\delta f/f_0$ and quality factor Q as a function of temperature. For the quality factor plots we added an additional loss channel to limit the quality factor to a maximum of 10^9 . Increasing temperature leads to a decreasing resonance frequency and decreasing quality factor. Higher kinetic inductance ratios α lead to stronger effects. The model by Tinkham for cavities shows the same behavior as the *RLC* model but gives access by fixing the Volume to Surface V/S from the design to the normal state conductivity σ_n instead of kinetic inductance ratio α .

Interestingly, we get a skin depth for low temperatures, which does not depend on frequency since $\sigma \approx \sigma_2 \propto 1/\omega$. This is called the anomalous skin effect [59, 73, 110]. The skin depth solely depends on the superconducting gap Δ and the conductivity σ_n just above T_c . It ranges between 1 nm to 100 nm for typical impurity values for Al and Nb.

By relating the energy stored in the mode over the power dissipated at the cavity walls, we get the relation

$$Q = \sqrt{\frac{\mu_0 \omega_0 V}{128 S} \frac{|\sigma|^2}{\sigma_1 \sqrt{|\sigma| + \sigma_2}}} \approx \frac{\sqrt{\mu_0 \omega_0 V} \sigma_2^{3/2}}{16 S \sigma_1}, \quad (2.65)$$

where V is the mode volume, S the superconductor surface, and μ_0 the magnetic constant. The two models should qualitatively agree since we can model a lower V/S ratio by a lower kinetic inductance ratio. Indeed this is the case as seen in Fig. 2.10, for a specific set of values, we can nearly overlap the two curves. However, the model by Tinkham gives access to the relevant parameters of the cavity: normal state conductance σ_n and volume to surface ratio.

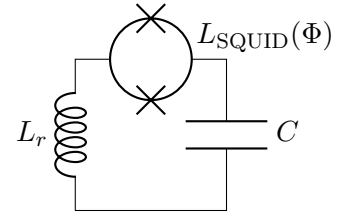
Losses in microwave resonators The source of losses in superconducting circuits is still an open question in the circuit QED community. It is unclear what limits transmons and resonators. However, research has shown that one can improve the quality factors by reducing the electromagnetic field strength at surfaces of the superconductor [111–116]. In fact, reducing the mode surface to volume ratio (S/V) leads to an increased quality factor in Eq. (2.65). But this fact alone cannot explain the drastic improvements of Q

for lower participation ratios, especially for low temperatures where quasi-particles should be negligible. For low temperatures and excitation powers there is another dominating additional loss channel: *two-level systems* (TLS) sitting in oxide layers on the surface of metals and substrates [117–121]. We observed a strong effect of TLS coherence on the time dynamics of a cavity, described in Ref. [38]. However it is still unclear if this is the only or dominating loss mechanism at low temperatures. We will model microwave losses only by TLS and thermal quasiparticles in the course of this thesis.

2.1.5 SQUID resonators

We can make the resonance frequency ω_r of an LC circuit tunable by adding a SQUID. The additional inductance will depend on the flux through the SQUID, and the resonance frequency is then obtained by

$$\omega_r = \frac{1}{\sqrt{[L_r + L_{\text{SQUID}}(\Phi)] C_r}}, \quad (2.66)$$



where L_r and C_r are the linear inductance and capacitance of the LC circuit, and L_{SQUID} can be evaluated numerically using Eq. (2.44). To estimate the tunability of the resonator, we now have to consider the ratio between L_{SQUID} and L_r , too. We quantify this by introducing a new **resonator-junction inductance ratio** parameter

$$\beta_R = \frac{L_r}{L_J}, \quad (2.67)$$

which relates the resonator inductance L_r to the Josephson inductance of a single junction L_J , Eq. (2.31). In Fig. 2.11 we show numerical evaluations of Eq. (2.66) for experimental relevant parameters. The behavior is very similar to the critical current of a SQUID (cf. Sec. 2.1.3). However, the additional dependence on β_R shows that L_J must be less than a hundred times L_r to achieve good tunability. Furthermore, higher L_J values reduce the resonance frequency of the bare LC circuit, which must be taken into account in the designs.

Note that for $\lambda/2$ resonators, the position of the SQUID plays a crucial role, too. We get the maximum effect at current anti-nodes and nearly no tunability if we place the SQUID at a node. Moreover, if we place the SQUID in the center of a $\lambda/2$ resonator, we get maximum tunability for the first mode, but nearly no tunability for the second mode, which has a node at the center (cf. Fig. 2.9).

When making the Josephson inductance the dominant inductance ($\beta_R \rightarrow 0$) we get a nonlinear circuit tunable by magnetic fields. In fact, the non-linearity can be so large that even a single excitation in the LC circuit will cause a large enough inductance change that the circuit is no longer resonant to the excitation signal - a system that acts similar to a two-level system (qubit).

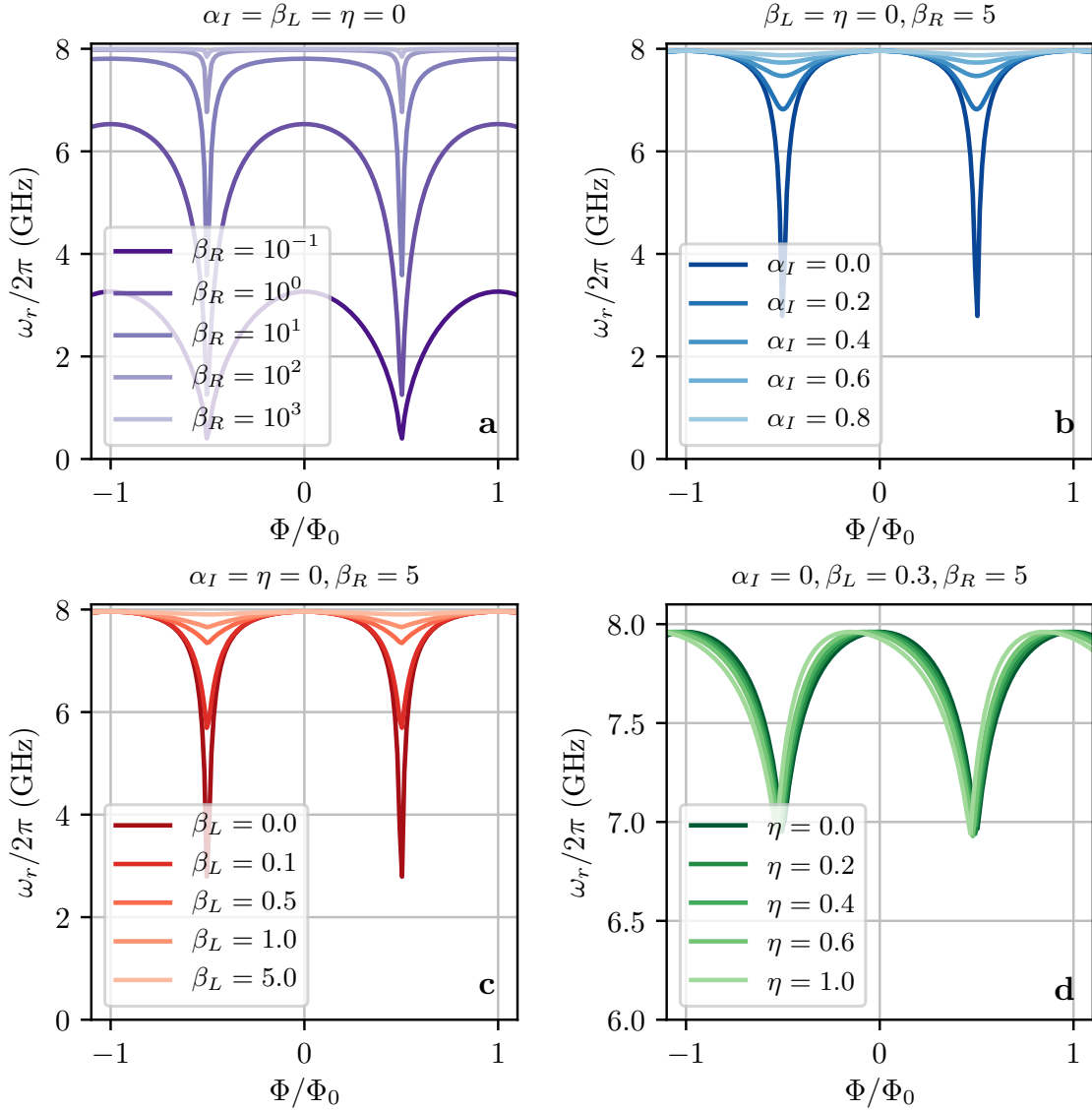


Figure 2.11: Numerical evaluations of the magnetic flux dependent resonance frequency of a SQUID LC circuit obtained by minimizing Eq. (2.44) for different values of β_R , α_I , β_L and η . We use experimental relevant parameters $\omega_r = 2\pi \cdot 8$ GHz, $L_r = 1$ nH (obtained by *HFSS* simulations), and $C = \omega_r^2/L$. For **b**, **c**, **d** we normalized the resonator frequency to 8 GHz by adapting C . A good tunability requires β_R to be smaller than 100, meaning that the junction critical current has to be chosen to match the resonator inductance. Symmetrical junctions $\alpha_I = 0$ show higher tunability, and the geometric inductance of the SQUID loop should be minimized ($\beta_L \rightarrow 0$). An asymmetry in the SQUID loop inductance leads to a skewed flux dependence as seen in **b**, which could be useful to increase flux sensitivity in situations where β_L could not be decreased.

Non-linear RLC circuit response We now introduce a simplified circuit-model to describe the change in power/photon number in the cavity as a function of drive detuning. A Josephson junction makes the LC circuit inherently non-linear, which leads to additional effects: The inductance of the circuit increases as the current through the junction increases (see Eq. (2.47)). Thus, when we add power/excitation to the circuit, the resonance frequency shifts to lower values. This results in a very asymmetric line-shape of the cavity. Suppose we drive the cavity at a frequency below the cavity resonance ($\omega < \omega_r$, red detuned). The excitation we introduce in the cavity causes the resonance to shift to lower frequencies. Now our drive is more resonant, which increases the cavity population. This in turn causes again a shift to lower frequencies, make the cavity again more resonant, and so on. As a result the resonance gets pulled to the drive. Exactly the opposite happens for a drive with a frequency above the cavity resonance ($\omega > \omega_r$, blue detuned). Once we put excitation in the circuit at this frequency, the resonance frequency gets shifted to lower values. The drive is now less resonant, leading to a decrease in excitation in the circuit, which shifts the resonance slightly higher again. In steady state this leads to a push of resonance frequency to lower values, and therefore to a lower excitation in the circuit as we would expect for that given frequency. In total, we get the line-shape illustrated in Fig. 2.13.

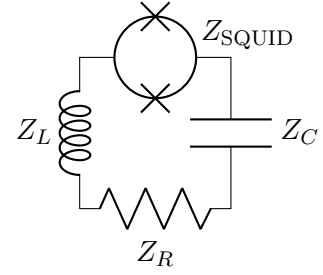


Figure 2.12: Non-linear SQUID LC model.

To model this behavior, we consider the circuit illustrated in Fig. 2.12. It consists of four elements in series, where the total impedance is simply given by the sum of the individual impedances

$$Z = Z_L + Z_C + Z_R + Z_{\text{SQUID}}. \quad (2.68)$$

We describe energy loss to an external coupling together with internal losses as a resistive element R . The linear inductance L_r and capacitance C_r characterize the circuit without a SQUID. We get the following impedances for the linear part of the circuit

$$Z_L(\omega) = i\omega L_r, \quad Z_C(\omega) = \frac{1}{i\omega C_r}, \quad Z_R = R. \quad (2.69)$$

The nonlinear part is fully given by the SQUID (see Sec. 2.1.3)

$$Z_{\text{SQUID}}(\omega, I) = i\omega L_{\text{NL}} = i\omega \frac{\hbar}{2e} \frac{\arcsin(I/I_{\text{SQUID}})}{I}, \quad (2.70)$$

with the critical current of a SQUID I_{SQUID} , depending on junction parameters and magnetic flux in the SQUID loop (that means finding the root of Eq. (2.44)).

We are interested in the current response I of the circuit for a fixed applied voltage U , which represents the drive strength. This is given by

$$I = Z^{-1}U, \quad (2.71)$$

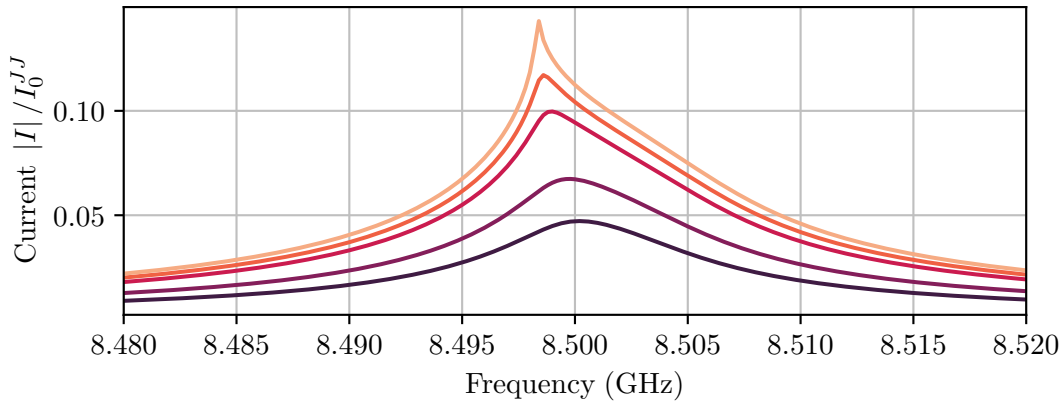


Figure 2.13: Current in the SQUID nonlinear RLC circuit as a function of drive frequency. The different colors indicate different average population on resonance in the RLC circuit, $\langle n \rangle = 5, 10, 20, 25, 30$. We use experimental relevant parameters $L_r = 1$ nH, $C_r = 315$ fF, $\beta_L = 0.01$, $Q_{\text{tot}} = 10^3$ leading to $R = 63$ m Ω , and $I_J = 3$ μ A. Increasing the oscillator population leads to a shift to lower resonance frequencies and an increasingly asymmetric lineshape.

where Z is the complex impedance of the circuit. For the nonlinear circuit, this equation becomes implicit as Z itself depends on current $Z(I)$. We can solve this numerically by finding the root of

$$f(I, U) = I - \frac{1}{Z_L + Z_C + Z_R + Z_{\text{SQUID}}(I)} U \quad (2.72)$$

using Python's scientific library⁵. Figure 2.13 shows the numerical evaluation as a function of frequency for various drive strengths. As soon as the drive is strong enough to create a high enough current that the resulting inductance change $\delta L_{\text{SQUID}}(I)$ is similar to the linear inductance L_R , we observe a shift in resonance frequency and an asymmetric lineshape. Note that R (Q_{tot}) plays a crucial role now, as it is the dominant limitation of the currents around the resonance. We will use this model in Sec. 2.4.2 to describe how a non-linear cavity effects the backaction on the mechanical system.

2.2 Mechanical systems

Mechanical systems are intriguing. Often physicists use mechanical analogues to gain an intuition for more complex systems. This works because everyone played with mechanical systems already as a child, e.g., with a swing. We have a good feeling about how they behave, even without understanding the physics behind it. Complex systems can be modeled for low excitation often as a harmonic oscillator, which we can grasp. Adding a tiny bit of complexity leads to unintuitive behavior, like chaos in a double pendulum. However, even the simple model of a harmonic oscillator becomes very unintuitive at a quantum level. It

⁵<https://docs.scipy.org/doc/scipy/reference/generated/scipy.optimize.fsolve.html>

is hard for us to imagine how a Fock state of a mechanical oscillator looks like. We never saw one and will never see one, because the excitation is much too small. Even if our eyes could see deflections much below the wavelength of visible light, we would distort/measure the state only by looking at it. We can ask the stimulating open question of how big a quantum system can be. A system that we need to completely isolate from its environment and be able to excite it to a quantum state. Today, we achieved this for single atoms [122] and much bigger molecules [12], but also for lattice vibrations of $\approx 10^{20}$ atoms [20] and a macroscopic drum [41].

But besides our fascination for mechanical systems, there is even more physics to discover. Today we do not have a verified model of how gravity interacts with quantum mechanics [123]. Making quantum systems massive and excite it to a quantum state with large delocalizations will inevitably lead to decoherence by gravity. These systems can then be used to falsify predictions by theory models.

The way to get quantum control over mechanical objects is to couple it strongly to systems that we can control well on a quantum level. This can be optical or microwave cavities like in the field of cavity optomechanics [15] or detectors that can detect motion down to the ground state (e.g., SQUIDs) [21, 124]. There exists a variety of mechanical systems that are suited for these types of experiments. We follow the proposal by *G. Via, G. Kirchmair and O. Romero-Isart* [1] and use a cantilever since it is simple, shows high enough quality factors, and is commercially available [15, 21].

2.2.1 Cantilever

A cantilever is a beam that is supported only at one end. We label the beam's dimensions as length l , width w , and thickness t . Material properties and boundary conditions give rise to torsional and bending modes of the beam. Fig. 2.14 depicts the first two bending modes. In this thesis, we are only interested in the first bending mode and assume that other modes are decoupled and far enough away in frequency.

Cantilevers are relatively simple mechanical devices that are described exhaustively in literature [21, 125]. The **resonance frequency of the first cantilever mode** can be calculated as

$$\Omega = 1.02 \frac{t}{l^2} \sqrt{\frac{E}{\rho}}, \quad (2.73)$$

with the Young's modulus E , the material density ρ , and the dimensions t and l as defined in Fig. 2.14. Note that the width of the cantilever cancels out and gives us a free parameter. In the course of this thesis, we are only using cantilevers made out of silicon with material parameters $\rho = 2330 \text{ kg/m}^3$ and $E = 170 \text{ GPa}$. Inserting these values gives

$$\Omega = 8669 \left[\frac{\text{m}}{\text{s}} \right] \frac{t}{l^2}. \quad (2.74)$$

All the cantilever used for this thesis are designed or acquired with frequencies $f = \Omega/2\pi$ between 100 kHz and 1 MHz and have typical dimensions $t = 1 \mu\text{m}$ to $5 \mu\text{m}$, $L = 30 \mu\text{m}$ to $150 \mu\text{m}$, $w = 20 \mu\text{m}$ to $50 \mu\text{m}$. Normally, we are just interested in the dynamics

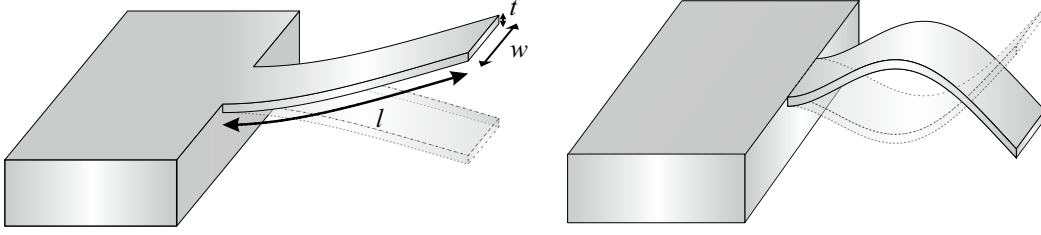


Figure 2.14: Illustration of the first two bending modes of a cantilever. We label dimensions as length l , width w and thickness t . The first mode (left) has an anti-node at the open end and a node at clamping point. The second mode (right) has an additional node and anti-node. The frequency of the second mode is typically a factor 6.3 higher than the fundamental frequency.

of small displacements. In this regime, a cantilever can be approximated by an effective harmonic oscillator.

2.2.2 Effective harmonic oscillator

When pushing the cantilever at the tip upwards or downwards, we will observe in first order a restoring force given by *Hooke's law* $F = k\Delta z$, depending on the displacement Δz of the tip. The constant k is the stiffness of the free end of the cantilever and can be calculated as [125]

$$k = \frac{Ewt^3}{4l^3}. \quad (2.75)$$

Hooke's law describes an harmonic oscillator, therefore we can define an effective mass for the cantilever mode by comparing

$$\Omega = \sqrt{\frac{k}{m_{\text{eff}}}} \quad (2.76)$$

to Eq. (2.73), resulting in

$$m_{\text{eff}} \approx \frac{m_{\text{beam}}}{4} = \frac{\rho l w t}{4}. \quad (2.77)$$

The effective mass is a quarter of the total mass of the beam. For typical cantilever parameters of this thesis ($\rho_{\text{Si}} = 2330 \text{ kg/m}^3$, $t = 5 \mu\text{m}$, $w = 50 \mu\text{m}$, $l = 100 \mu\text{m}$) we get $m_{\text{eff}} \approx 10^{-11} \text{ kg}$. To allow a magnetic coupling between cantilever and superconducting circuits we add either a permanent magnet or a superconductor on the tip. This will change the effective mass and therefore change the resonance frequency slightly

$$\Omega_+ = \sqrt{\frac{k}{m_{\text{eff}} + m_+}} = \Omega \sqrt{\frac{m_{\text{eff}}}{m_{\text{eff}} + m_+}}. \quad (2.78)$$

Now the width w of the cantilever affects the frequency, since wider cantilevers will have higher effective masses. Note that this formula will get inaccurate for $m_+/m_{\text{eff}} \geq 3$ [126].

Another important parameter is the damping rate Γ , which quantifies the loss of mechanical energy. Similar to microwave resonators, we can define a quality factor [16]

$$Q_{\text{mech}} = \frac{\Omega}{\Gamma}. \quad (2.79)$$

The damping is dependent on material parameters but can also be optimized by strain, clamping, and phononic bandgap engineering, reaching Q values as high as 10^8 at room the temperature [18, 127, 128]. Moreover, temperature has an impact on losses, too. Cooling down to cryogenic temperatures will typically lead to an increase in quality factor [129–132].

We can now write the equation of motion for the open end of the cantilever as

$$m\ddot{z}(t) + m\Gamma\dot{z}(t) + m\Omega_+^2 z(t) = F(t), \quad (2.80)$$

where $m = m_{\text{eff}} + m_+$ is the effective total mass and $F(t)$ is a force applied on the tip. This is the equation of motion for a driven damped harmonic oscillator. We can solve it in frequency space by Fourier transform leading to

$$z(\omega) = \frac{1}{\underbrace{m(\Omega^2 - \omega^2) - i\Gamma m\omega}_{=\chi(\omega)}} F(\omega), \quad (2.81)$$

where $\chi(\omega)$ is called the susceptibility and characterizes the response of displacement z to an applied force F at frequency ω . Note that $z(\omega)$ is now a complex number. This can be understood when writing the Fourier transform in the basis of sine and cosine

$$z(\omega) = \frac{1}{\sqrt{2\pi}} \int_{-\infty}^{\infty} z(t)[\cos(\omega t) + i \sin(\omega t)]d\omega. \quad (2.82)$$

Real and imaginary z values equal to in-phase or out-of-phase response to an applied force. It is best illustrated by plotting the susceptibility. In Fig. 2.15 we plot the real, imaginary and absolute value of χ for low (left) and high (right) damping. For low frequencies, the oscillator just follows the driving force. At frequencies near Ω , the resonator's response increases in magnitude, but it becomes more and more out of phase with the applied force. Right on resonance, the real part is zero, and the resonator is oscillating exactly 90° out of phase to the applied force. For slightly higher frequencies, the response will then slowly go to 180° out of phase. Excitations at $\omega \gg \Omega$ will not cause any response or deflection of the resonator since it averages to a net-zero force. Increasing the damping will lead to a broader resonance condition but a lower deflection response. Furthermore, the maximum of the response will shift to lower frequencies, which is only visible for large damping. Since sine and cosine are orthogonal, we can span a basis in which we quantify the in-phase (I) and out-of-phase or quadrature (Q) amplitude. It is often useful to describe a resonator's response in this space, as we will see later for microwave resonators.

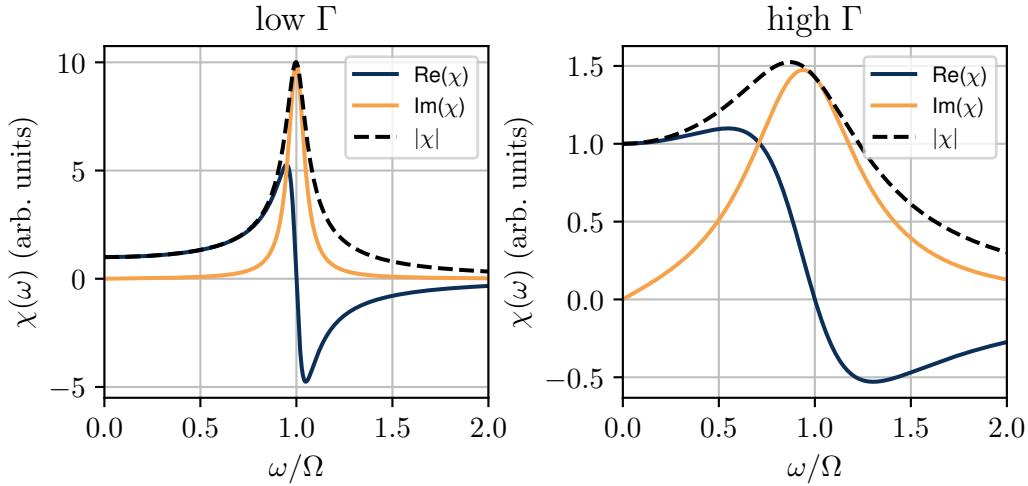


Figure 2.15: Frequency dependent susceptibility $\chi(\omega)$ of a driven damped harmonic oscillator with resonance frequency Ω for low (left) and high (right) damping Γ . The real part is plotted in blue and is one for low frequencies, zero exactly on resonance, gets negative slightly above resonance and goes again to zero for high frequencies. The imaginary part is plotted in orange and is zero everywhere but around resonance with linewidth Γ . The absolute value is plotted with a dashed black line to demonstrate the total response of the oscillator. For low damping (left), the absolute response goes to a higher value than for high damping (right).

2.2.3 Power spectral density (PSD) of a harmonic oscillator

A useful quantity for characterizing systems is the power spectral density (PSD) of a signal. It can be defined as [15]

$$S_{zz} = \int_{-\infty}^{\infty} \langle z(t)z(0) \rangle e^{i\omega t} dt, \quad (2.83)$$

where $\langle \cdot \rangle$ denotes the expectation value. We labeled the signal by a variable z in analogy to the displacement of the cantilever tip in z direction. The expectation value is required since the definition of PSD includes noise, too, which is described best by stochastic variables. The expectation value of a trajectory $z(t)z(0)$ is called *auto-correlation*. The PSD can therefore be defined as the Fourier transform of the auto-correlation. Here, the definition of power is the square of a signal $P = |z(t)|^2$. In experiments, we typically measure actual power dissipated in $50\ \Omega$ or high impedance resistances. However, the PSD is defined for other signals, too, like the motion of a harmonic oscillator. An undamped oscillator would yield a $\delta(\omega - \Omega)$ distribution in frequency space since its trajectory is deterministic and repeats every oscillation period. When the oscillator is damped by coupling it to a bath or an environment, the excitation decays, leading to a finite width. The damping Γ in Eq. (2.80) gives rise to the imaginary part of the susceptibility. Already *Einstein* deduced that dissipation always gives rise to noise. He described this insight with the example of Brownian motion [133]. Later this was shown for electrical circuits by *Nyquist* [134] and fi-

nally generalized as the **fluctuation-dissipation theorem** by *Callen and Welton* [135]. It states that the power spectral density of a thermalized resonator is related to the imaginary part of its susceptibility

$$S_{zz}(\omega, T) = \frac{2k_B T}{\omega} \text{Im}(\chi[\omega]). \quad (2.84)$$

Here k_B is the Boltzmann constant, and T is the temperature of the bath. Sloppily one can say that if one can damp energy to the bath, the bath can also randomly excite motion due to the bath's temperature. For a damped harmonic oscillator, we get

$$S_{zz}(\omega, T) = \frac{2k_B T}{m} \frac{\Gamma}{(\Omega^2 - \omega^2)^2 + (\Gamma\omega)^2}. \quad (2.85)$$

Measuring a damped harmonic oscillator with a frequency-resolved power detector (spectrum analyzer) leads to the characteristic peak illustrated in Fig. 2.16.

The actual measurement of a PSD is typically done by taking a time trace of the signal and applying a Fourier transform. For a measurement time T , we can obtain the amplitude spectral density by a truncated Fourier transform of the displacement $z(t)$

$$z(\omega) = \frac{1}{\sqrt{2\pi T}} \int_0^T z(t) e^{-i\omega t} dt. \quad (2.86)$$

Since there will always be noise in an experimental setup, we have to repeat the measurement N times to obtain the expectation value for a power spectral density

$$\langle |z(\omega)|^2 \rangle = \frac{1}{N} \sum_{k=1}^N |z_k(\omega)|^2 \quad (2.87)$$

However, S_{zz} is defined in ω space, requiring a complete Fourier transform (for all times). Therefore we have to take the limit $T \rightarrow \infty$ to be rigorous. The connection

$$S_{zz}(\omega) = \lim_{T \rightarrow \infty} \langle |z(\omega)|^2 \rangle \quad (2.88)$$

is called **Wiener-Khinchin theorem** and relates the PSD to the Fourier transform of the absolute square of $z(t)$. By integrating the PSD - which is now connected to the "variance of z " spectral density - we obtain the expectation value for the variance of a thermalized oscillator

$$\langle z^2 \rangle = \int_{-\infty}^{\infty} S_{zz}(\omega) \frac{d\omega}{2\pi}. \quad (2.89)$$

Therefore, the area below the PSD gives the variance of the displacement. Comparing it to Eq. (2.84) we see that if the system is thermalized, the area is directly proportional to

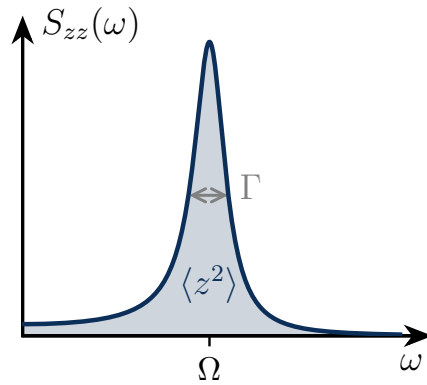


Figure 2.16: PSD of a damped harmonic oscillator. The area below gives the expectation value for the variance of displacement for a thermalized harmonic oscillator. For small dampings, the curve can be approximated by a Lorentzian with width Γ around Ω .

the bath temperature T . The specific shape of the peak will depend on the system. For a damped harmonic oscillator, it is illustrated in Fig. 2.16.

Digital measurement of mechanical motion requires a conversion of motion to an electrical signal. This can be achieved, for example, by piezoelectric materials or coupling the mechanical system magnetically to a superconducting circuit, as we will see in the next section. However, the signal's amplitude will then depend on transduction coefficients and requires calibration to allow the extraction of $\langle z^2 \rangle$ [16, 136].

2.2.4 Quantum regime

Ultimately, we want to explore the quantum regime. The quantum harmonic oscillator is one of the simplest quantum systems and treated exhaustively in literature [137, 138]. Following Ref. [15], we label the creation and annihilation operators for the mechanical mode as \hat{b}^\dagger and \hat{b}

$$\hat{z} = z_{\text{ZPF}} (\hat{b} + \hat{b}^\dagger), \quad (2.90)$$

$$\hat{p} = -iz_{\text{ZPF}} m \Omega (\hat{b} - \hat{b}^\dagger), \quad (2.91)$$

to separate them from the operators of the electromagnetic field, which we label by \hat{a} and \hat{a}^\dagger . The Hamiltonian then reads as

$$\hat{H} = \hbar \Omega \left(\hat{b}^\dagger \hat{b} + \frac{1}{2} \right). \quad (2.92)$$

The corresponding eigenvalues are discrete, non-degenerate, and equally spaced by $\hbar \Omega$. The eigenstates are called *Fock states* and labeled by their excitation number $|N = \hat{b}^\dagger \hat{b}\rangle$. They all have zero expectation value in position and momentum space [139]

$$\langle N|x|N\rangle = \langle N|p|N\rangle = 0, \quad (2.93)$$

but finite variances

$$\langle N|x^2|N\rangle = \frac{\hbar}{m\Omega} \left(n + \frac{1}{2} \right) \quad (2.94)$$

$$\langle N|p^2|N\rangle = \hbar m \Omega \left(n + \frac{1}{2} \right). \quad (2.95)$$

The explicit wave function of a Fock state in momentum and position space is given by *Hermite functions*. The square of the hermite functions, which is the probability density of measuring the cantilever at that location, is illustrated in Fig. 2.17 for the position space.

Quantum control requires discriminating the discrete level structure. In other words, we must be able to detect or couple to zero-point fluctuations of the cantilever [21, 124]. For

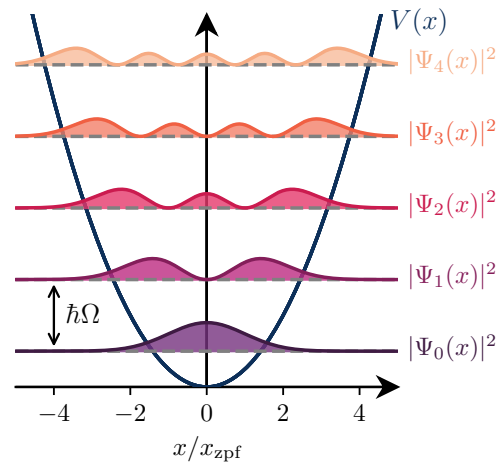


Figure 2.17: Square of position space wavefunction for the first 5 Fock states of a quantum mechanical oscillator.

a quantum harmonic oscillator the zero-point fluctuations in position space are given by [15, 21, 138]

$$z_{\text{ZPF}} = \sqrt{\frac{\hbar}{2m\Omega_+}}. \quad (2.96)$$

Typical values for cantilevers used in this thesis give a zero-point fluctuation between 10^{-15} and 10^{-14} m.

Note that we only discussed the quantum description for the undamped harmonic oscillator. The damped harmonic oscillator is an open quantum system which is more complex to describe. However, the formalism of Lindblad superoperators allows us to model this system by coupling it to a bath of harmonic oscillators [16, 140, 141].

Ground state cooling Typically, the first step towards quantum control is to cool the mechanical oscillator down to its ground state. However, modern dilution refrigerators just achieve base temperatures of around 20 mK which is much bigger than the level spacing of our cantilever modes $\hbar\Omega/k_B \approx 10 \mu\text{K}$.

One solution is to go to higher mechanical frequencies, which was demonstrated in a pioneering experiment by O’Connell *et al.* [142]. Here, the researchers investigated a bulk acoustic mode inside a piezoelectric material. Bulk and surface acoustic wave resonators can easily achieve resonance frequencies in the GHz regime [142, 143]. However, since the zero-point fluctuations scale inversely with the frequency, as seen by Eq. (2.96), it gets harder to achieve quantum control since the displacements are even smaller. However, by using piezoelectric materials, one can achieve the required high sensitivity, which led to the demonstration of ground-state cooling and single Fock state generation [142]. Recent improvements of acoustic wave systems demonstrated phonon number resolved detection [144–146] and creation of higher number Fock states [20, 143]. The downside of piezoelectric materials is that they show higher microwave losses, limiting the coherence times of close-by superconducting circuits.

The alternative is to stay with low-frequency modes but actively cool them. In particular, there are two schemes suitable for our system that have demonstrated ground-state cooling in recent years: feedback cooling and sideband cooling.

Feedback cooling to the ground state requires a quantum-limited measurement of the mechanics. In other words: If the detector can separate zero-point fluctuations, we can build a feedback loop that cools the system to the ground state or stabilizes Fock states. M. Rossi *et al.* recently demonstrated ground-state cooling of a high-Q membrane resonator in an optical setup using feedback cooling [17].

Sideband cooling is another possibility. It requires coupling of the mechanical system with an auxiliary resonant system and originates from ion-trapping [147–149]. When the linewidth of the auxiliary system is small enough to resolve the energy levels of the coupled mechanical system, we obtain separate sidebands, corresponding to the creation (blue detuned) or annihilation (red detuned) of a phonon. J. Teufel *et al.* demonstrated sideband cooling to the ground state for a macroscopic oscillator using a superconducting LC circuit

[39]. Sideband cooling actually works quite well for unresolved systems. However, in this case you will always drive a small part of the blue detuned sideband, which heats up the system. The minimum phonon number for sideband cooling (in all regimes) is [16, Chap. 2]

$$\langle n \rangle_{\min} = \left(\frac{\kappa}{4\Omega} \right)^2 \frac{2}{1 + \sqrt{1 + (\kappa^2/4\Omega^2)}}, \quad (2.97)$$

for an optimal detuning

$$\Delta = -\sqrt{\Omega^2 + \kappa^2/4} \quad (2.98)$$

with the cavity linewidth κ and the mechanical frequency Ω .

2.3 Coupling between superconducting circuits and mechanical systems

Superconducting circuits offer a variety of coupling possibilities with mechanical systems [21, 29]. We can distinguish between continuous linear detectors and cavity optomechanics. The former is, for example, a DC-SQUID setup. A magnetic flux change through the SQUID loop is directly converted to a voltage. Placing a magnet on the mechanics allows to convert a motional signal into a voltage [4, 129, 150]. We will follow this approach in the first part of this thesis. In contrast, cavity optomechanics uses optical or microwave cavities to enhance the effect of mechanical displacement on the optical or microwave signal. A displacements of the cavity mirror changes the resonance frequency, which can be detected very precisely. In addition, the cavity itself can be used directly to provide feedback to the mechanical system, e.g., for cooling or to generate a quantum state. We will use this scheme in the second part of this thesis. In the following, we give a brief introduction to cavity optomechanics in superconducting circuits. For details and information about further systems, I refer to the excellent review paper by M. Aspelmeyer, T. Kippenberg, and F. Marquardt [15].

2.3.1 Cavity optomechanics in superconducting circuits

At the heart of cavity optomechanics is an interaction of mechanical displacements with the cavity. This is typically achieved by modulating the resonance frequency $\omega(x)$ or the linewidth $\kappa(x)$ as a function of mechanical displacement. Here we will focus on the former. For LC circuits, there are two possibilities, as shown in Fig. 2.18: We can construct a displacement-sensitive capacitance $C(x)$ or a displacement-sensitive inductance $L(x)$. The resonance frequency of the cavity can then be approximated by a Taylor series as

$$\omega_r(x) = \omega_r + x \frac{\partial \omega_r}{\partial x} + \dots \approx \omega_r + \frac{x}{x_{\text{ZPF}}} g_0, \quad (2.99)$$

where we labeled the change in resonance frequency caused by a displacement of the zero point fluctuation as coupling strength $g_0 = x_{\text{ZPF}} \partial \omega_r / \partial x$. The Hamiltonian of the coupled system then reads as (neglecting zero point energies)

$$\hat{H} = \hbar \left(\omega_r + (\hat{b} + \hat{b}^\dagger) g_0 \right) \hat{a}^\dagger \hat{a} + \hbar \Omega \hat{b}^\dagger \hat{b}, \quad (2.100)$$

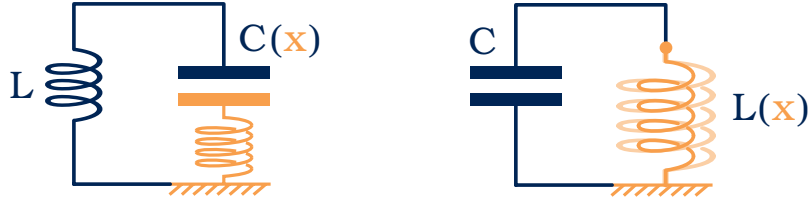


Figure 2.18: In principle, there are only two ways of coupling an LC circuit to mechanical systems. On the left hand side, one plate of the capacitor is free. Displacements lead to a change in capacitance, which results in a changed resonance frequency. The same can be achieved by making an inductor sensitive to mechanical displacements, as shown on the right.

with the creation and annihilation operators introduced in Sec. 2.2.4. We can identify the **interaction Hamiltonian** as

$$\hat{H}_{\text{int}} = \hbar g_0 (\hat{b} + \hat{b}^\dagger) \hat{a}^\dagger \hat{a}, \quad (2.101)$$

which is a nonlinear three wave mixing process where a photon and a phonon create a photon ($\hat{a}^\dagger \hat{b} \hat{a}$) or a single photon can create a photon and a phonon ($\hat{b}^\dagger \hat{a}^\dagger \hat{a}$).

Linearized Hamiltonian For typical cavity optomechanical systems, g_0 is too small to observe effects at the power level of single photon. One solution is to drive the cavity to a coherent state $\langle \alpha | \hat{a} | \alpha \rangle = \alpha e^{i\omega_r t} = \sqrt{\bar{n}} e^{i\omega_r t}$ with mean photon number \bar{n} and look at the quantum fluctuations for this state. In the frame rotating with ω_r this means

$$\hat{a} = \alpha + \delta \hat{a}. \quad (2.102)$$

The interaction Hamiltonian then reads as

$$\hat{H}_{\text{int}} = \hbar g_0 (\hat{b} + \hat{b}^\dagger) (\alpha^* + \delta \hat{a}^\dagger) (\alpha + \delta \hat{a}). \quad (2.103)$$

We get four new terms because of the two last brackets. The term $\propto |\alpha|^2$ is an average force displacing the mechanics. In the case of an optical cavity, this is the average radiation pressure force; in the case of a free capacitor LC circuit, this is the Coulomb attraction between the two oppositely charged capacitor plates. In the case of a SQUID coupled to a magnetic cantilever, it is a bit more complex, but in general attributed to circulating currents in the SQUID loop creating a magnetic field gradient [151–153]. We will discuss the latter in more detail in Sec. 2.4. In all cases, this term simply causes a static shift of the zero position.

The term $\propto \delta \hat{a}^\dagger \delta \hat{a}$ is usually neglected since it is smaller than the other terms by a factor α . Assuming with no loss of generality that $\alpha = \sqrt{\bar{n}}$ is real, we obtain the **linearized Hamiltonian**

$$\hat{H}_{\text{int}} \approx \hbar g_0 \sqrt{\bar{n}} (\delta \hat{a} + \delta \hat{a}^\dagger) (\hat{b} + \hat{b}^\dagger). \quad (2.104)$$

This resembles an XX interaction of two coupled harmonic oscillators. The excitation of one oscillator is swapped back and forth between the oscillators at the coupling rate $g_0 \sqrt{\bar{n}}$, which is enhanced by the number of photons inside the microwave cavity. This allows even

for moderate g_0 values the cooling to the ground state [39], entangling mechanical motion with microwave radiation [27], coherently swapping excitations [26], and going into the strong [19] and even ultrastrong coupling regime [40].

The strongest single-photon coupling g_0 has been achieved using piezoelectric materials to couple to acoustic waves on the surface of the substrate or into the bulk [20, 142, 143]. However, this comes at the cost of low coherence times for microwave circuits since piezoelectric materials typically show high microwave losses. Moreover, very recently the demonstration of energy squeezed states was demonstrated by strongly coupling a drum resonator to a cooper pair box [41]. The high coupling rate of $g_0/2\pi = 22$ MHz requires a charge sensitive qubit, which again has a limited coherence time due to charge fluctuations.

Coherent states It is illustrative to consider what happens for a mechanical coherent state $\alpha = \sqrt{\bar{N}}e^{-i\Omega t}$ with average phonon number \bar{N} . Insertion of the expectation value for a coherent state in position space

$$\langle \alpha | x | \alpha \rangle = 2x_{\text{ZPF}} \text{Re}(\sqrt{\bar{N}}e^{i\Omega t}) \quad (2.105)$$

into Eq. (2.99) leads to

$$\omega_r(t) = \omega_r + 2\sqrt{\bar{N}}g_0 \cos \Omega t . \quad (2.106)$$

The microwave resonance frequency is modulated by the mechanical frequency Ω with a strength of $2\sqrt{\bar{N}}g_0$. The same behavior can be observed for a displaced thermal state.

2.3.2 Classical response of mechanics to a cavity

We are now following Ref. [16] to derive an expression of how the cavity affects the mechanical system. The equations of motion for the mechanical displacement and field strength in the cavity are [16]

$$\ddot{x} = -\Omega^2 x - \Gamma \dot{x} + \frac{1}{m}(F_{\text{OM}} + F_{\text{ext}}), \quad (2.107a)$$

$$\dot{\alpha} = \left[i \left(\omega_{\text{drive}} - \omega_r - \frac{x}{x_{\text{ZPF}}} g_0 \right) - \frac{\kappa}{2} \right] \alpha + \frac{\kappa}{2} \alpha_{\text{max}}, \quad (2.107b)$$

with the optomechanical force F_{OM} and an external force F_{ext} acting on the mechanical system. The second equation describes an exponential decay with $\kappa/2$ of the cavity field together with an applied drive tone ω_{drive} and a cavity resonance frequency shift caused by a displacement of the mechanics. The notation is chosen such that on resonance ($\omega_{\text{drive}} = \omega_r$), and with no mechanical coupling ($g_0 = 0$), the external drive creates a steady state field $\alpha = \alpha_{\text{max}}$ inside the cavity, meaning that $|\alpha_{\text{max}}|^2$ is the photon number at resonance. If the system is described by the interaction Hamiltonian Eq. (2.101), the optomechanical force becomes $F_{\text{OM}} = d\hat{H}_{\text{int}}/d\hat{x} = \hbar g_0 |\alpha|^2 / x_{\text{ZPF}}$. By applying a tone to the cavity, we drive it to a coherent state $\bar{\alpha}$, causing a static displacement of the mechanical zero position to \bar{x} . These solutions can be found by setting $\dot{x} = \dot{\alpha} = 0$. We now want to look at small

oscillations around the new average solutions $x = \bar{x} + \delta x$, $\alpha = \bar{\alpha} + \delta\alpha$. Inserting the expression for F_{OM} , the equation of motions become

$$\delta\ddot{x} = -\Omega^2\delta x - \Gamma\delta\dot{x} + \frac{\hbar g_0}{m x_{\text{ZPF}}}(\bar{\alpha}^*\delta\alpha + \bar{\alpha}\delta\alpha^*) + \frac{F_{\text{ext}}}{m}, \quad (2.108a)$$

$$\delta\dot{\alpha} = i\left(\omega_{\text{drive}} - \left[\omega_r + \frac{\bar{x}}{x_{\text{ZPF}}}g_0\right]\right)\delta\alpha - \frac{\kappa}{2}\delta\alpha + i\frac{g_0}{x_{\text{ZPF}}}\bar{\alpha}\delta x, \quad (2.108b)$$

with again neglecting the term $\delta\alpha\delta\alpha^*$ since it is a factor $\bar{\alpha}$ smaller. The resonance frequency of the cavity is shifted by a static displacement of the mechanical system $\delta\omega_r = \bar{x}g_0/x_{\text{ZPF}}$. We now label the detuning of the drive by $\Delta = \omega_{\text{drive}} - [\omega_r + \bar{x}g_0/x_{\text{ZPF}}]$. The equations for the cavity field can be solved in frequency space

$$\delta\alpha(\omega) = \frac{i g_0 \bar{\alpha} / x_{\text{ZPF}}}{-i\omega - i\Delta + \kappa/2} \delta x(\omega). \quad (2.109)$$

We can insert this result into Eq. (2.108a) to obtain the response of the mechanical system to an applied cavity drive with detuning Δ . For this we are using the Fourier Transform property $\text{FT}[\delta\alpha^*(\omega)] = (\text{FT}[\delta\alpha(-\omega)])^*$ and that $(\text{FT}[\delta x(-\omega)])^* = \text{FT}[\delta x(\omega)]$ since $x(t)$ is real-valued. This results in the **optomechanical equation of motion** for the mechanical system

$$\delta x[\omega] = \frac{1}{m(\Omega^2 - \omega^2 - i\omega\Gamma) - \Sigma(\omega)} F_{\text{ext}}, \quad (2.110)$$

with the **optomechanical interaction** summarized in

$$\Sigma(\omega) = \frac{\hbar g_0^2 |\bar{\alpha}|^2}{x_{\text{ZPF}}^2} \left(\frac{1}{-\omega - \Delta - i\kappa/2} + \frac{1}{\omega - \Delta + i\kappa/2} \right). \quad (2.111)$$

Σ is complex-valued, meaning that the cavity leads to an in-phase (real) and out-of-phase (imaginary) response. The real part stiffens or softens the mechanical spring constant resulting in a shift of the mechanical frequency. This is often called the **optical spring effect** and is quantified by

$$\delta(\Omega^2) = \frac{-1}{m} \text{Re}[\Sigma(\Omega)] = 2\Omega g_0^2 |\bar{\alpha}|^2 \left(\frac{\Omega + \Delta}{(\Omega + \Delta)^2 + (\kappa/2)^2} - \frac{\Omega - \Delta}{(\Omega - \Delta)^2 + (\kappa/2)^2} \right), \quad (2.112)$$

$$\delta\Omega = -\Omega + \sqrt{\Omega^2 - \delta(\Omega^2)}. \quad (2.113)$$

In Fig. 2.19(a) we plot Eq. (2.112) as a function of detuning for various cavity linewidths κ . If the cavity has a linewidth smaller than the mechanical frequency Ω , we can resolve each of the resonance features. Higher linewidths wash out the effect, and we just observe the averaged response.

Σ has an imaginary component, which arises because the cavity has a finite linewidth κ . This leads to damping or anti-damping of the mechanical system. Specifically, we obtain for the **optomechanical damping**

$$\Gamma_{\text{OM}} = \frac{1}{m\Omega} \text{Im}[\Sigma(\Omega)] = g_0^2 |\bar{\alpha}|^2 \kappa \left(\frac{1}{(\Omega + \Delta)^2 + (\kappa/2)^2} - \frac{1}{(\Omega - \Delta)^2 + (\kappa/2)^2} \right). \quad (2.114)$$

Figure 2.19(b) shows the behavior of the damping versus cavity drive detuning for different cavity linewidths κ . When κ is smaller than the mechanical frequency Ω , we can resolve

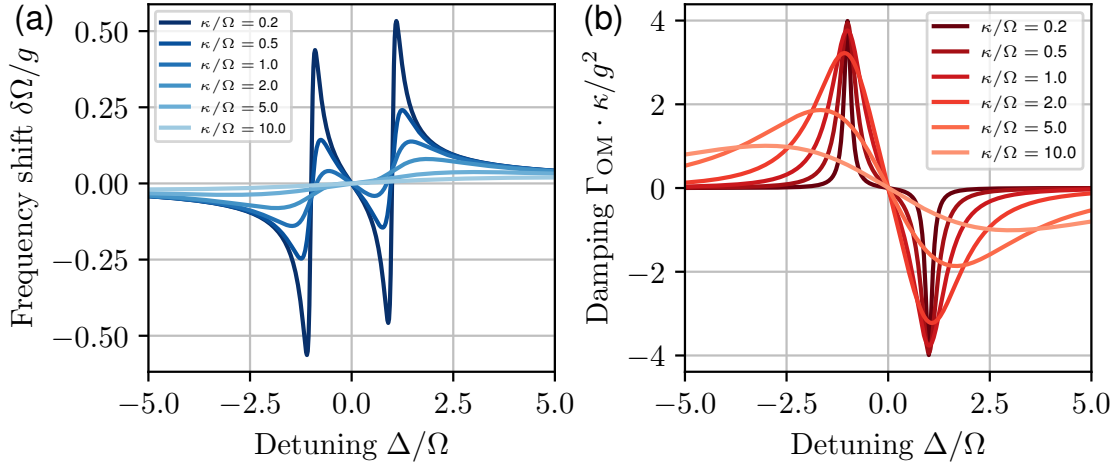


Figure 2.19: (a) Optical spring effect. Depending on the detuning of the cavity drive to the cavity resonance, the mechanical spring constant is stiffened or softened. This causes an increase or decrease in mechanical frequency. Increasing the linewidth κ of the microwave cavity blurs the sharp response at $\pm\Omega$. (b) Optical damping. The delayed cavity response leads to an out of phase response [imaginary part in Eq. (2.111)]. We observe increased damping when the cavity drive is red-detuning and anti-damping when it is blue-detuned. Decreasing the cavity linewidth results in stronger and sharper damping/anti-damping as the response becomes more out of phase. Note that the y axis is multiplied by κ instead of divided by κ for better visibility.

the terms arising from the cavity either lagging behind (negative detuning) or advancing (positive detuning) the mechanics. This is equivalent to damping and anti-damping, visible as an increased or decreased linewidth of the mechanical response. Directly at $\pm\Omega$, the damping scales as $1/\kappa$. At higher cavity linewidths, the two responses overlap, resulting in a reduced response.

2.4 Magnetic coupling

The novelty in our approach is a new magnetic coupling scheme that offers the possibility to achieve strong single photon coupling $g_0 > \kappa$ [1]. This type of setup was pioneered and demonstrated by A. Vinante *et al.* [2–4, 129, 150]. We will consider the two possible setups shown in Fig. 2.20. There are further possibilities for magnetic coupling, e.g., allowing one arm of the SQUID to oscillate inside a strong magnetic field [32, 44, 46, 153, 154], which we do not consider in this work.

Both of our two approaches use either a permanent magnet or a superconductor patterned on the tip of a separate cantilever. This chip is then aligned and attached above a SQUID. Motion of the cantilever alters the flux through the SQUID loop. This can be detected either by a DC-SQUID measurement setup or by embedding the SQUID in a resonant circuit and detecting the frequency change. The latter is the typical cavity optomechanics

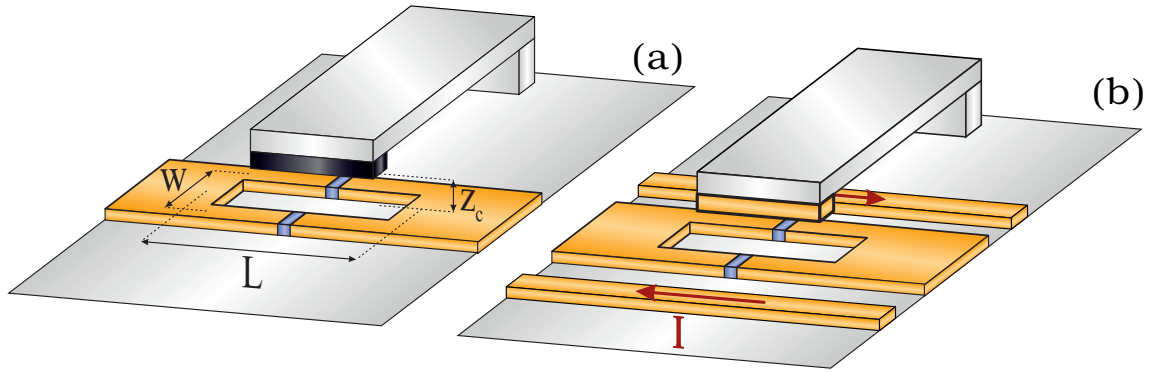


Figure 2.20: Two schemes of magnetic coupling between cantilever and superconducting circuit followed in this thesis. (a) The tip of the cantilever is equipped with a permanent magnet (black). A displacement of the tip changes the magnetic flux within the SQUID loop, resulting in a changed critical current (inductance) of the SQUID. (b) The tip of the cantilever is equipped with a superconductor (orange). Antiparallel currents (red arrows) in two close-by superconducting wires create a magnetic gradient field that induces a position-dependent dipole moment in the superconducting tip. This in turn changes the flux through the SQUID loop as a function of cantilever position.

setup. Using a permanent magnet has the disadvantage that it must be adjusted at room temperature by fixing the magnet size and the distance between the cantilever tip and the SQUID.

Another approach is not to use a permanent magnet, but to induce a magnetic dipole moment by a tunable magnetic field. Placing a superconductor on the cantilever tip and exposing it to a magnetic field results in a Meißner state response. The magnetic field induces screening currents to completely expel the magnetic field from its interior. Close to the superconducting strip, this is therefore an induced dipole moment opposing the magnetic field. We can further improve the sensitivity by placing the cantilever tip in a magnetic gradient field generated by antiparallel currents in two closely spaced superconducting wires. Now, the induced dipole moment is displacement dependent because the magnetic field strength changes with position. This boosts the sensitivity of the cantilever to displacements as discussed in Ref. [1] and in Sec. 2.4.3. In addition, the magnetic fields can be switched on and off and tuned in strength by currents. This avoids problems caused by in-field cooling of superconductors [155–160]. On the other hand, this setup requires strong currents close to the SQUID, which causes problems because one is limited by the critical current of superconductors. Moreover, the resonator may couple to the feed-line, which adds another decoherence channel. Careful filtering is required to ensure that no signal is leaking out of the high current lines.

For simplicity, we first consider the permanent magnet setup shown in Fig. 2.20(a) to discuss the general coupling mechanism. The principle is the same for the setup with a quadrupole field, shown in Fig. 2.20(b). However the additional requirement of the field generation adds complexity.

2.4.1 Backaction mechanism

At first glance, it is not clear how the resonator or the SQUID circuit can exert a backaction on the mechanics (e.g. cooling). From daily experience we know that magnets attract and repel each other. This force arises because the gradient field of one magnet acts on the magnetic moment \mathbf{m} of the other [58, 161]

$$\mathbf{F} = \nabla (\mathbf{m} \cdot \mathbf{B}). \quad (2.115)$$

Thus, applying a feedback on the cantilever requires a magnetic gradient field. Circulating currents in the SQUID loop, as illustrated in Fig. 2.21, generate such a gradient field. They occur as soon as we apply a magnetic flux to the SQUID and make it flux-sensitive. This is all very consistent: To detect a displacement, the SQUID must be flux biased. The steeper the voltage or resonance change, the more sensitive the SQUID circuit becomes to mechanical displacements. On the other hand, increasing the flux bias increases the circulating currents, see Fig. 2.22(a), increasing the force on the mechanics.

To describe this quantitatively, we calculate the **circulating current** in the SQUID loop by subtracting Eq. (2.41b) from Eq. (2.41a)

$$\frac{I_{\text{loop}}}{I_0} = \frac{1}{2} [(1 - \alpha_I) \sin \varphi_1 - (1 + \alpha_I) \sin \varphi_2]. \quad (2.116)$$

Here, the phase differences depend on the applied external magnetic flux and bias current $\varphi_1(\Phi_{\text{ext}}, I_{\text{bias}})$. We can solve the implicit equation by finding the root of Eq. (2.44) again,

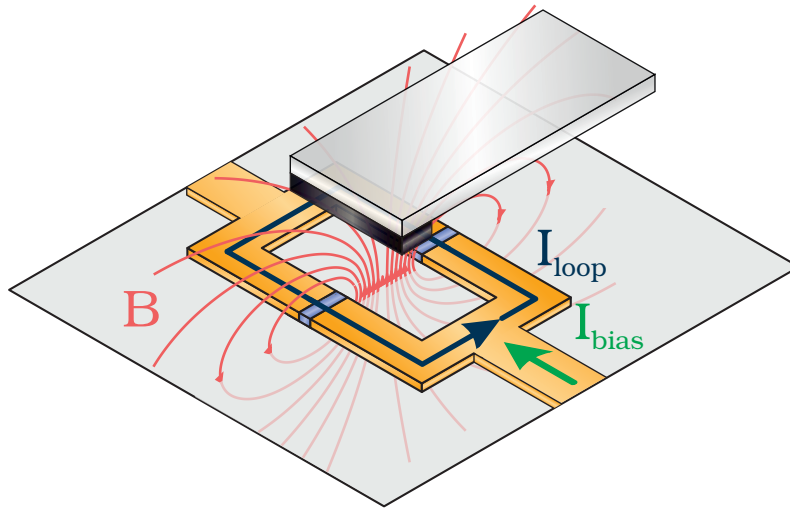


Figure 2.21: Backaction mechanism of a SQUID on a cantilever with a magnetic dipole moment. Circulating currents in the SQUID loop (I_{loop}) generate a magnetic gradient field (B) that exerts a force on the magnet attached to the cantilever (black). A bias current (I_{bias}) affects the loop currents due to the current phase relationship of Josephson junctions and fluxoid quantization, thus changing the force acting on the cantilever.

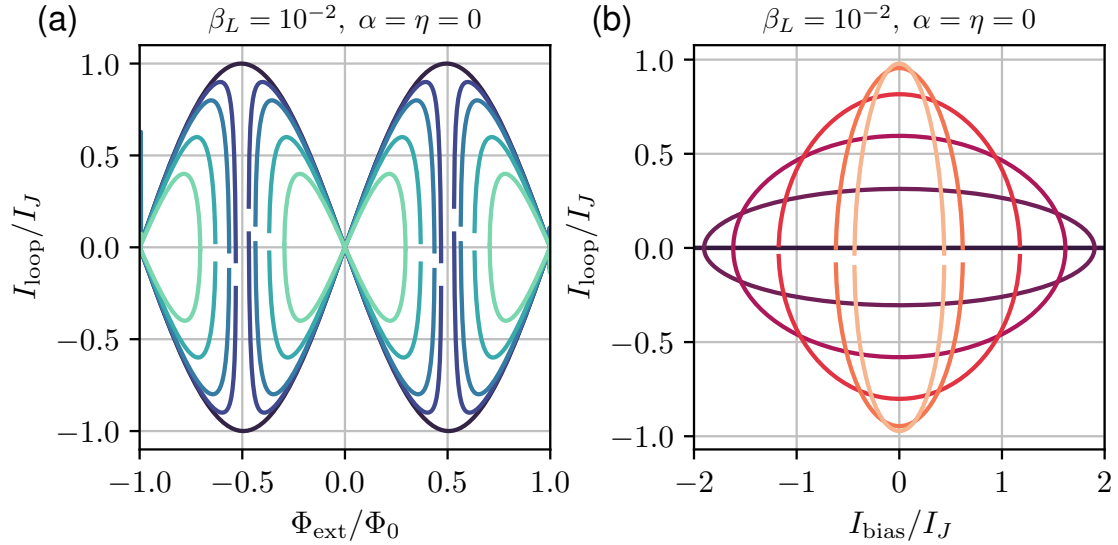


Figure 2.22: (a) Circulating SQUID loop currents as a function of normalized applied flux for various bias currents $I_{\text{bias}}/I_J = 0, 0.2, 0.4, 0.8, 1.2$. Currents are normalized by the critical current of a single junction. The implicit equation has two solutions (clockwise and counter-clockwise circulating screening currents) leading to two valid loop currents for a given flux bias point. Close to half a flux quantum, the system is very sensitive to applied bias currents because the circulating currents are already close to the critical current of the junction. The bias current then pushes the current across one of the junctions above the critical current, creating dissipation. (b) Circulating SQUID loop currents as a function of applied bias current for various applied magnetic flux points $\Phi/\Phi_0 = 0, 0.1, 0.2, 0.3, 0.4, 0.43$. Increasing the bias current magnitude $|I_{\text{bias}}| > 0$ leads to reduced loop currents. The effect gets stronger the closer the flux in the SQUID loop is to odd multiples of $\Phi_0/2$. The lines are not going to zero loop currents for high flux bias points because of numerical imprecision.

but now for a given current I_{bias} instead of finding the maximum current I_c where a solution still exists. This is achieved by using a SciPy root finding function⁶, together with providing the derivative of Eq. (2.44) with regard to φ_1 . The implicit equation has more than one solution. Numerical evaluations are shown in Fig. 2.22. The two valid solutions for a given applied external flux or bias current differ by clockwise or counter-clockwise screening currents in the SQUID loop. When the flux in the loop reaches a multiple of half a flux quantum, the circulating currents become very sensitive to applied bias currents. The reason for his behavior is that around half a flux quantum, the loop current is already close to the critical current of the junction. Adding an additional bias current pushes the current across one junction above the critical current, which leads to the breaking of cooper pairs, and therefore to dissipation.

To derive an equation for the force acting on the magnet as a function of the loop currents, we use the analytical formula for the magnetic field generated by a magnetic point

⁶https://docs.scipy.org/doc/scipy/reference/generated/scipy.optimize.root_scalar.html

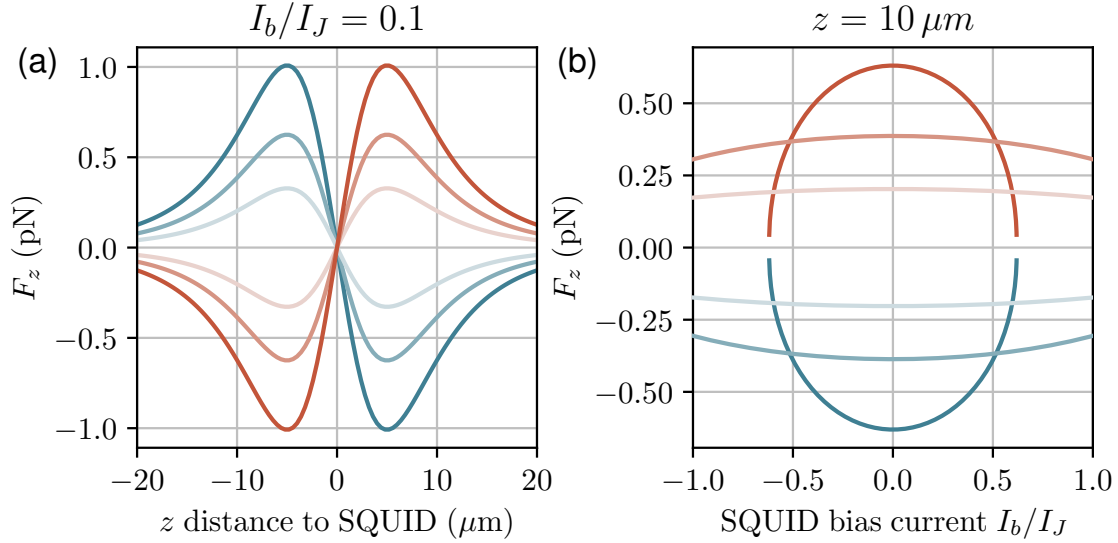


Figure 2.23: Gradient force acting on cantilever as a function of distance between SQUID and magnet (a) or as a function of applied bias current (b) for various $\Phi_{\text{ext}}/\Phi_0 = -0.3, -0.2, -0.1, 0.1, 0.2, 0.3$. The radius of the SQUID loop is fixed $R = 10 \mu\text{m}$. We pick the solution that leads to the lowest magnitude of flux within the SQUID loop out of the two possible circulating current solutions. (a) The force is either repulsive or attractive at a given distance depending on whether the currents are circulating clockwise or counter-clockwise. The magnetic gradient of a conductive loop is zero in the loop plane, therefore F_z vanishes at $z = 0$. The highest feedback force is where the gradient is highest, at a finite distance above or below the SQUID. (b) For a given flux bias point, the force decreases for increasing magnitude of bias current. This is expected as the force is directly proportional to the loop current, which shows the same behavior [see Fig. 2.22(b)].

dipole [161]. For simplicity, we assume the magnet to be a point particle and just consider the magnetic field in the center of the SQUID loop. Moreover, we model the SQUID loop as a circle with radius R . Then, the force on the cantilever at height z can be calculated as

$$F_z(z, I_{\text{loop}}) = -\frac{m_z \mu_0 I_{\text{loop}}}{2} \frac{3R^2 z}{(R^2 + z^2)^{5/2}}, \quad (2.117)$$

which depends on the magnetic moment of the magnet m_z along the z direction, on the distance between cantilever and SQUID loop z , and on the circulating currents I_{loop} . The latter we evaluate using the root finding procedure discussed in the beginning of this subsection. The magnetic moment of the permanent magnet we estimate as

$$\mathbf{m} = \frac{1}{\mu_0} \mathbf{B}_r V, \quad (2.118)$$

with the residual flux density \mathbf{B}_r , and the volume of the magnet V . Inserting estimated values for our magnets, $\mathbf{B}_r \approx 1 \text{ T}$ and $V = (5 \mu\text{m})^3$, and assuming that we can set the magnetization axis perfectly along z , results in a dipole moment of $m_z \cdot 10^{-10} \text{ Am}^2$.

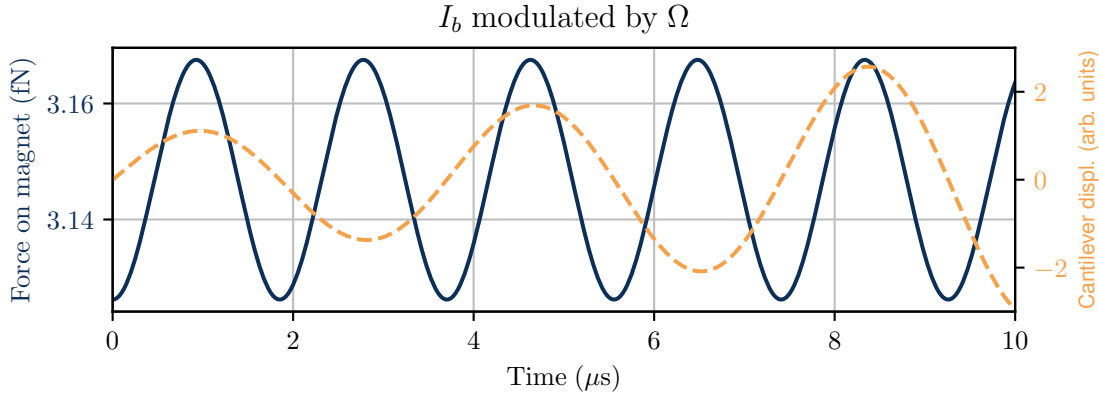


Figure 2.24: Parametric amplification of the mechanical mode (orange) by modulating the bias current of the SQUID by the mechanical frequency. The modulation of the gradient force (blue) happens with twice the bias current modulation frequency due to the dependence depicted in Fig. 2.23(b). The stiffening is always minimized when the cantilever is not deflected and maximized when its maximally deflected. This is the working principle of a parametric oscillator.

In Fig. 2.23(a), we show the numerical evaluation of Eq. (2.117) as a function of distance between SQUID and magnet for different flux bias points. We pick the solution which leads to the lowest total flux magnitude in the SQUID loop from the two valid loop current solutions. The force is either repulsive or attractive, depending on the direction of the loop currents, and location of the magnet. For a given SQUID size exists an optimum distance at which the force is strongest. However, we have to be careful with this model as we assume the magnet to be a point particle. We will later discuss the question of optimal SQUID size and distance between cantilever and SQUID in Sec. 2.4.3. Nevertheless, we see that the loop current creates a non-negligible force on the cantilever.

We further plot the force on the cantilever as a function of bias current in Fig. 2.23(b) for different flux bias points. As the force is directly proportional to the circulating currents, we observe the same dependence on bias current. The force on the cantilever will effectively increase the stiffness k of the cantilever. With a modulation of the bias current, we can therefore get a strong feedback on the mechanical system as illustrated in the following example: When we modulate the bias current by the mechanical frequency, the force will oscillate by twice the modulation frequency due to the dependence shown in Fig. 2.23(b). This leads to parametric amplification of the mechanical mode, as illustrated in Fig. 2.24. When the bias current is modulated exactly out of phase we can obtain damping, too. However, after reaching the ground state the cantilever will then be parametrically amplified as the cantilever will then lock to the bias current modulation.

2.4.2 Cavity optomechanics with the magnetic cantilever setup

Now, as we understand the backaction mechanism of the SQUID on a magnet, we can try to model the cavity optomechanics setup with a magnetically coupled cantilever. Here, the

modulation of the bias current is at microwave frequencies, multiple orders of magnitudes higher than the mechanical frequency. The cantilever cannot respond that quickly. Thus, it sees an effective average force depending on the strength of the modulation. However, to actually calculate a force, we first have to estimate the bias current through the SQUID for a given mode.

To estimate the current and therefore the gradient force as a function of average photon number in the cavity, we assume that the SQUID resonator is driven in a coherent state $\alpha = \sqrt{\bar{n}_{ph}}e^{i\omega t}$ with an average photon number \bar{n}_{ph} . The oscillating charge for a linear quantum LC circuit can then be calculated using Eq. (2.52b)

$$Q = -iQ_{ZPF}(\alpha - \alpha^*) = 2Q_{ZPF}\sqrt{\bar{n}_{ph}}\sin(\omega t). \quad (2.119)$$

The **circulating current** is then given by the derivative $I = dQ/dt$,

$$I = 2Q_{ZPF}\sqrt{\bar{n}_{ph}}\omega \cos(\omega t) = \sqrt{\frac{2\bar{n}_{ph}\hbar\omega_r}{L_r + L_{SQUID}(I, \Phi)}} \cos \omega t. \quad (2.120)$$

Here we used Eq. (2.53b) to express Q_{ZPF} in terms of inductance and resonance frequency. This is again an implicit equation, as the inductance of the SQUID depends on the current through the SQUID. For now, we will assume small excitations so that the nonlinearity is negligible. We further use the experiment relevant parameters $L_r = 1$ nH, $C_r = 250$ fF and $I_J = 1$ μ A, obtained from finite element simulations and fabrication parameters. We can now insert I as the bias current in Eq. (2.44), solve for φ_1 , calculate the loop currents according to Eq. (2.116), and obtain the gradient force by Eq. (2.117). The cantilever only sees a time average of this fast oscillating force (the force is oscillating with twice the microwave frequency). Therefore, we average over one period to obtain $\langle F_z \rangle$. Note that we cannot simply take an average of the current, since the force has a nonlinear dependence on the bias current. $\langle F_z \rangle$ is then the actual force acting on the cantilever for a given photon number in the microwave resonator. In Fig. 2.25(a) we plot numerical evaluations of the average force normalized by the maximum force (which depends on the applied external flux) as a function of resonator population for different flux bias points (dark means no applied flux bias, bright indicates that the applied flux is close to $\Phi_0/2$). Interestingly, we observe exactly the opposite behavior of typical radiation pressure: The force in our case is strongest with no excitation in the resonator and gets weaker the more we populate it. This is caused by the fact that the loop currents are strongest when there is no bias current. Applying a bias current reduces the loop currents and thus the force acting on the cantilever. A very important result is that despite the fact that the equations are nonlinear and implicit, the resulting average force for low resonator population scales linearly with the photon number. This is important because it is the same scaling as the optomechanical force $F_{OM} = \hbar g_0 |\alpha|^2 / z_{ZPF}$ resulting from the cavity optomechanics interaction Hamiltonian Eq. (2.101). Furthermore, the applied flux bias has an effect on the strength of the feedback, exactly as we would expect: The closer it is to $\Phi/\Phi_0 = 0.5$, the higher is the effect of a single quanta of excitation (meaning higher coupling g_0). Indeed we can compare the two forces by plotting the derivative of the force with respect to photon number as a function of flux bias, shown in Fig. 2.25(b). The derivative Fig. 2.25(a) close to $n = 0$ as a function of flux bias is shown in blue. For the optomechanical force, we use

$$\frac{\partial F_{OM}}{\partial n_{ph}} = \frac{\hbar g_0}{z_{ZPF}} = \hbar \frac{\partial \omega}{\partial z} = \hbar \frac{\partial \omega}{\partial \Phi} \frac{\partial \Phi}{\partial z}. \quad (2.121)$$

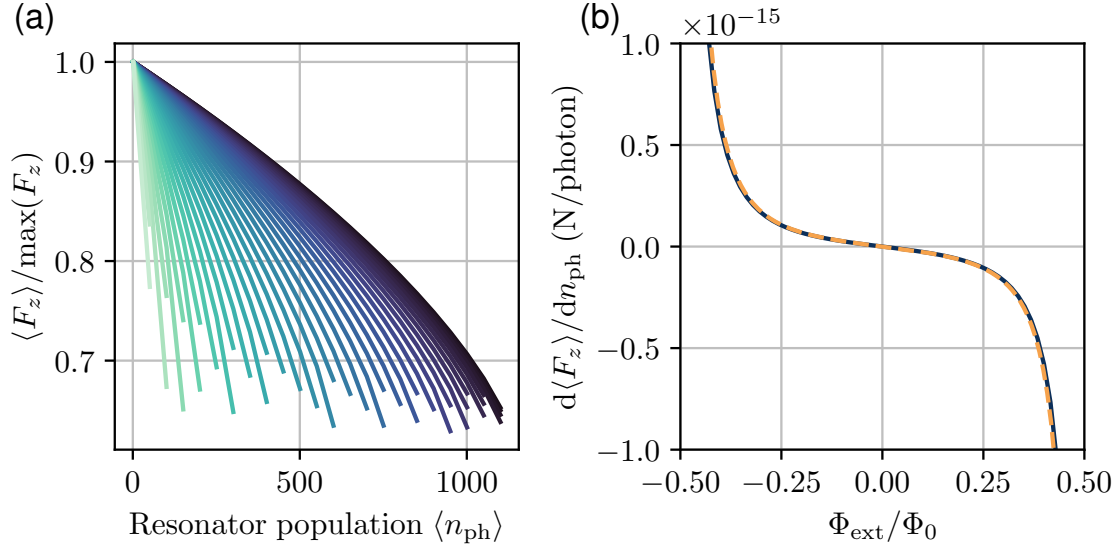


Figure 2.25: (a) Average force on the magnet at the cantilever tip as a function of average photon number in the microwave resonator. The average force is normalized to the maximum force at that flux bias point [compare right plot in Fig. 2.23] to allow a comparison. Color indicates flux bias strength, from close to 0 (blue) to $0.4\Phi_0$ (bright teal). The force is directly proportional to the photon number for low powers. This is the same scaling as for radiation-pressure. Increasing the flux bias point, leads to a stronger dependence. For high photon numbers, the force gets non-linear. All the curves stop at some point. This is the point where the current across one junction goes above the critical current. (b) Slope of the left plot close to $\langle n \rangle = 0$ as a function of flux bias point (blue). This shows the change in force resulting from adding a photon in the resonator. For increasing flux bias point, we get an increasing force change. The dashed orange line shows the behavior of the optomechanical force arising from the cavity-optomechanics interaction Hamiltonian. We observe excellent agreement, indicating that the gradient force is the dominant coupling mechanism in our cavity-optomechanics setup.

The first derivative can be calculated using Eq. (2.66). For the latter we calculate the change in magnetic flux through the SQUID loop created by a displacement of the magnet

$$\frac{\partial \Phi}{\partial z} = -\frac{3\mu_0 m_z R^2 z}{2(R^2 + z^2)^{5/2}}, \quad (2.122)$$

with the SQUID radius R , the magnetic moment of the magnet $\mathbf{m} = m_z$ and the distance between SQUID and magnet z . The dashed, orange line in Fig. 2.25(b) is the numerical evaluation of Eq. (2.121) using the same values for distance, SQUID loop and magnetic moment as for the gradient force. We observe excellent agreement, showing that the gradient force created by the circulating loop currents is really the dominant force in the interaction. This is the main result of this subsection.

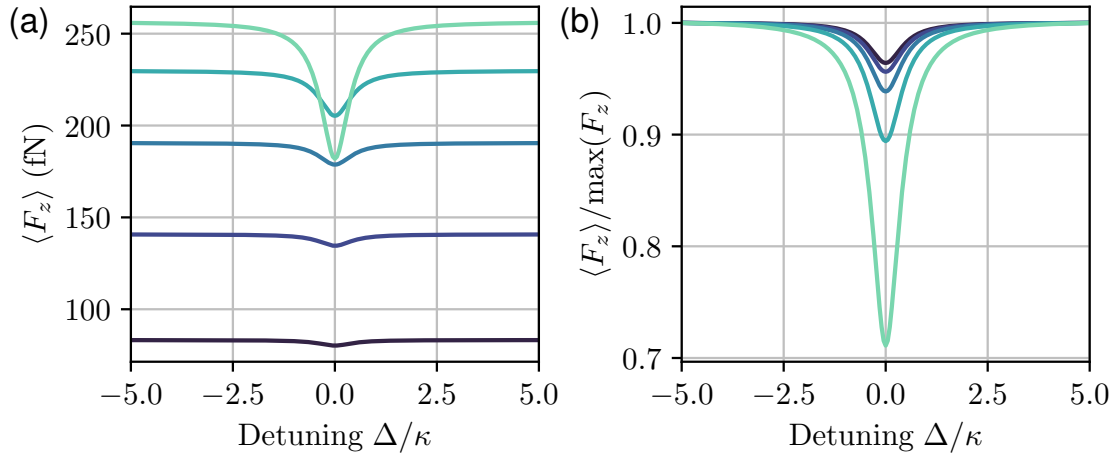


Figure 2.26: Force on magnet as a function of detuning for various flux bias points $\Phi/\Phi_0 = 0.1, 0.18, 0.25, 0.33, 0.4$ in absolute scale (a) and normalized to the maximum force (b). The drive power is fixed to the same value for all traces. We observe that the force decreases once we populate the resonator. The effect is stronger the closer the flux in the loop is to a multiple of $\Phi_0/2$.

Linear cavity regime We are now interested how the cavity will effect the mechanics. For this, we use the *RLC* model of Sec. 2.1.5 and start in the linear regime, neglecting inductance changes due to resonator population. As seen before, the force on the cantilever depends on the number of photons in the cavity, which depends on applied drive-strength and detuning between drive tone and cavity frequency. For the following we assume a drive with fixed strength, but look at the dependence on detuning. This is exactly the mechanism how the photon number changes depending on the state of the mechanics: We always pump with the same strength at the same frequency, but the mechanical displacement shifts the resonator frequency and therefore the detuning. In Fig. 2.26(a), we plot the force acting on the cantilever as a function of detuning for various flux bias points. To make it more comparable, we normalize the force again by the maximum average force for a given flux bias as shown in Fig. 2.26(b). Once we populate the cavity, we observe a strong dependence of the gradient force on detuning. When we fix the drive frequency to a point where the force change as a function of detuning is most prominent (could be slightly red detuned or blue detuned), the tone gets amplitude modulated (AM) as the mechanical system will shift the cavity resonance periodically. Thus, we observe AM sidebands at $\omega_{SB} = \omega_{\text{drive}} \pm \Omega$, which appear at plus or minus the mechanical frequency away from the drive tone. The two sidebands contain the full information about the cantilever, as the width of the sidebands is the actual width of the mechanical system, and the area is a combination of coupling and mechanical system excitation (see Sec. 2.2.3). The drive tone is therefore a probe/measurement of the mechanical motion.

However, here we are interested in the backaction of this probe tone onto the cantilever. For this we start again by the equation of motions Eq. (2.107a), but instead of using the optomechanical force coming from the interaction Hamiltonian, we use the force calculated by the loop currents. As we have seen in Fig. 2.25, the gradient force in our setup scales exactly

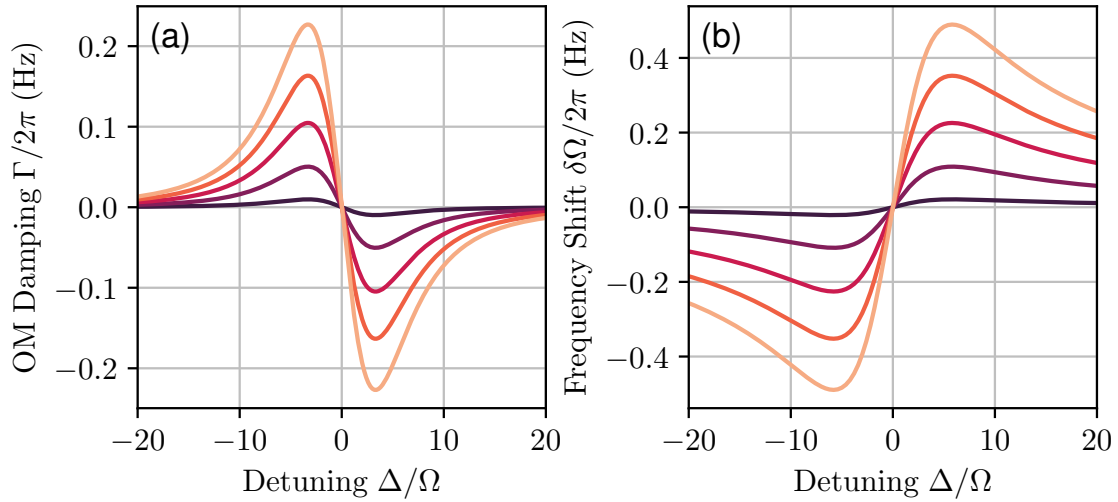


Figure 2.27: Optomechanical damping/anti-damping (a) and stiffening/softening (b) in the linear cavity regime for an effective coupling $g_0/2\pi \approx -57$ Hz and various cavity population $\langle n_{\text{cav}} \rangle = 10, 50, 100, 150, 200$. (a) Probing the resonator with a red detuned drive leads to an increased damping rate, while drive it blue detuned leads to a decreased damping. Shown here is only the optomechanical damping, meaning the effect of the cavity. To obtain the full damping of the mechanical system one has to add the intrinsic damping rate of the cantilever. (b) Probing blue detuned softens the effective spring constant of the cantilever mode, while probing red detuned stiffens it. Right on resonance there is no backaction and therefore no effect on damping or stiffness.

the same as the optomechanical force for low resonator populations. To get an expression for the optomechanical interaction, we want to do the same trick as before and expand the equations around an average photon number and look at small fluctuations at the new average solutions. Since we only have an implicit equation for the gradient force, this is hard to do. Therefore, we take the explicit $\propto |\alpha|^2$ dependence out of the model and just calculate the prefactor using the loop current model. We will get the same Eqns. (2.110) to (2.112) and (2.114), but instead of an explicit g_0 dependence, we obtain a prefactor that depends on flux bias and resonator population. The behavior is the same as before: The photon number change is not instantaneously, but happening at the decay time of the cavity ($1/\kappa$), lagging always a bit behind. It is exactly this lag that is creating a drag force (imaginary part in Eq. (2.111)), leading to cooling and amplification. If the photon number would follow instantaneously, we would only get a conservative force on the cantilever, stiffening or softening the effective spring constant. The optomechanical damping and stiffening for the gradient force is shown in Fig. 2.27 for low cavity population and flux bias point. The parameters are chosen to match the performance of a currently working setup (actual dimensions may differ): $\Omega/2\pi = 270$ kHz, $\omega_r/2\pi = 8$ GHz, $\kappa/2\pi = 3$ MHz, $z_{\text{ZPF}} = 2$ fm, $I_J = 2$ μ A, $\Phi_{\text{ext}} = 0.05\Phi_0$, $m_z = 10^{-10}$ Am², $r_{\text{SQUIDloop}} = 5$ μ m, $z_c = 10$ μ m. By using

$$g_0 = \frac{\partial F}{\partial |\alpha|^2} \frac{1}{\hbar z_{\text{ZPF}}},$$

we can calculate a corresponding coupling rate, which is $g_0/2\pi \approx -57$ Hz for the parameters above. Here we do not observe an effect of the nonlinearity and the behavior is exactly the same as Sec. 2.3.2 for the unresolved sideband regime. Red detuning of a cavity drive leads to microwave damping and softening of the cantilever, while blue detuning leads to anti-damping and stiffening. Everything is perfectly symmetric around $\Delta = 0$.

Nonlinear cavity regime We now briefly discuss the effect of the intrinsic nonlinearity in the circuit. For this purpose we use the non-linear $RLC + \text{SQUID}$ model of Sec. 2.1.5 to include the nonlinear response of the cavity. For a strong drive, the frequency of the circuit gets shifted to lower values due to the nonlinearity. When sweeping the strong drive this leads to an asymmetric lineshape: For frequencies below resonance, the resonance gets pulled to the drive, which increases the photons in the resonator, which in turn shifts the resonance frequency further. The average population follows the behavior seen in Fig. 2.13. If we fix a strong drive at a given frequency and the mechanics moves the resonator frequency, the behavior is exactly the same. This leads to stronger change in cavity population on the red side in comparison to the blue detuned drive tones. And since the change in photon number corresponds to the change in force, we should observe a different behavior for cooling and heating.

To calculate this quantitatively, we take the nonlinear response of the cavity, evaluated numerically by solving Eq. (2.72). We normalize the resulting complex currents by κ to

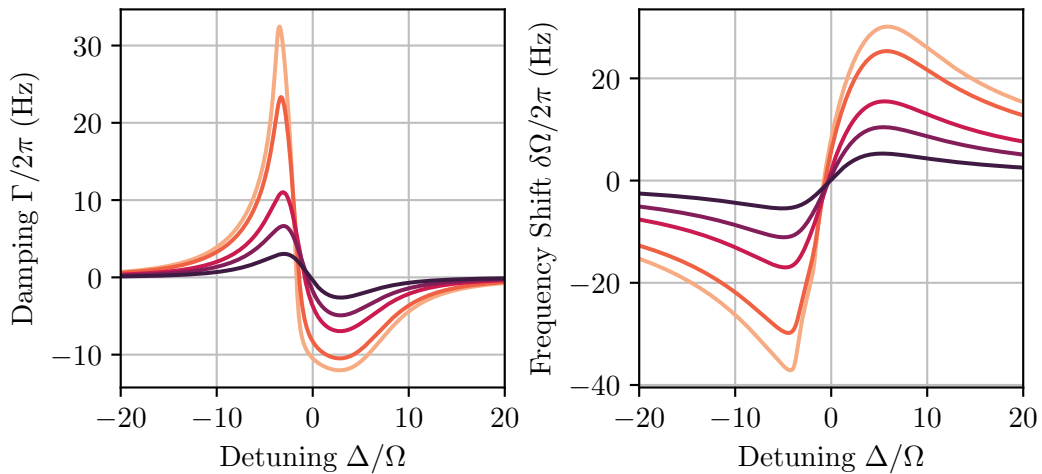


Figure 2.28: Nonlinear optomechanical damping/antidamping and stiffening/antistiffening for a coupling $g_0/2\pi = -2.9$ kHz and varied maximum cavity population $\langle n_{\text{cav}} \rangle = 1, 2, 3, 5, 6$. We observe a shift to lower microwave resonance frequencies due to the Kerr effect. Moreover, we observe an asymmetry in cooling and heating rates, showing enhanced cooling rate, and an asymmetry in mechanical frequency shift, showing enhanced softening.

convert it to the susceptibility $\chi_{\text{NL}}(\omega)$ of a nonlinear cavity to a strong drive and insert the result into the equation for the optomechanical interaction (compare Eq. (2.111))

$$\Sigma(\omega) = iA|\alpha|^2 [\chi_{\text{NL}}(\omega) - \chi_{\text{NL}}^*(-\omega)], \quad (2.123)$$

where the prefactor $A = (\partial F/\partial |\alpha|^2)^2/\hbar$ is determined using the derivative of the gradient force with respect to $|\alpha|^2$, and $*$ denotes the complex conjugate. We can then use Eqns. (2.112) and (2.114) to determine the optomechanical damping and stiffening. The predictions of the model are shown in Fig. 2.28. We used the same parameters as we used for the linear regime, but changed the flux bias point to a higher value $\Phi_{\text{ext}} = 0.4\Phi_0$, resulting in an effective coupling of -2.9 kHz. The model predicts a Kerr shift to lower frequencies and an improved cooling when the drive is red detuned (in this example the damping rate is three times the anti-damping rate). We also observe an asymmetry in the frequency shift: For a red detuning the resonance frequency of the mechanical system gets shifted stronger as for blue detuning. The nonlinearity can therefore be exploited to improve optomechanical cooling, which is currently investigated in our group.

2.4.3 Meissner effect setup

Instead of using a permanent magnet one could use a superconductor and induce a magnetic dipole moment. If a superconductor is placed inside a magnetic field, the superconductor repels the magnetic field from its inside by screening currents, effectively creating an induced dipole moment that exactly cancels the field inside the superconductor (Meissner effect). By using coils to generate the magnetic field, this offers another tuning knob for the experimental setup. This allows to precisely tune the induced magnetic dipole moment \mathbf{m} by currents through the coil. Moreover, we can actually use a magnetic gradient field, which changes in magnitude with position, leading to a position dependent magnetic dipole moment $\mathbf{m}(\mathbf{x})$. This increases the coupling between SQUID and mechanical system [1, 4]. However, such a setup requires large magnetic gradients, which can only be created by close-by coils/wires. This brings another source of noise close to the setup. Moreover the resonator couples to the wires, which requires loss-less on-chip filtering of the field generating wires to prevent energy leakage of the resonator. Fig. 2.29 depicts such a setup together with the a plot of the gradient field (top right) and the effective induced dipole moment field (bottom right).

This setup is sensitive to many parameters, but one of the most important parameters is the SQUID width relative to the superconducting strip width of the cantilever (the same is true for the permanent magnet setup). For a given strip width w and distance z_m between strip and SQUID there exist an optimal SQUID width for highest sensitivity. This is best illustrated by plotting the magnetic field lines of the induced dipole moment (Fig. 2.29(c)). For a given distance z_m , there is an optimum SQUID width that is at the point where B_z is zero. A smaller SQUID loop would miss some magnetic field going around the SQUID. On the other hand, if we make the SQUID loop bigger, the flux within the loop also decreases, as the fieldlines enter and leave the SQUID loop within its width, effectively creating no

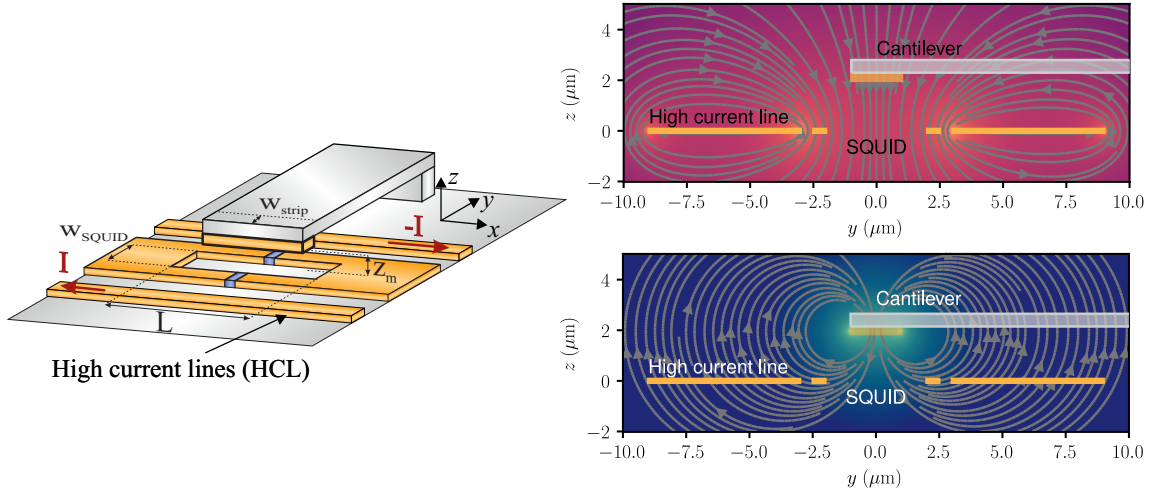


Figure 2.29: Gradient field setup. On the tip of the cantilever we place a superconductor with width w_{strip} . Right next to the SQUID we further place additional wires creating the magnetic gradient field. The field lines and magnitude (brighter red colors indicate higher magnitude) of the created magnetic field are shown on the top right. On the bottom right is the effective induced magnetic dipole moment field created by the cantilever. To achieve highest sensitivity, the SQUID loop requires an ideal width. This is the width where B_z is zero for the given distance z_m (the magnetic fieldlines turn back).

flux. The optimal SQUID width can be estimated by the condition $B_z = 0$ and using Eq. (4) of Ref. [1] together with $\mathbf{B} = \nabla \times \mathbf{A}$. After some calculations one ends up with

$$w_{\text{SQUID}} = w_{\text{strip}} \sqrt{1 + \frac{20}{3} \left(\frac{z_m}{w_{\text{strip}}} \right)^2 - \frac{4}{3} \frac{z_m}{w_{\text{strip}}} \sqrt{3 + 16 \left(\frac{z_m}{w_{\text{strip}}} \right)^2}}, \quad (2.124)$$

with parameters indicated in Fig. 2.29. Figure 2.30(a) shows the behavior for various strip widths. Increasing w_{strip} helps for decreasing the sensitivity to distance and misalignment.

To describe the magnetic coupling quantitatively, we can again calculate the flux change through the SQUID loop created by a displacement of the cantilever. The flux at the SQUID created by screening currents in the superconducting strip on the cantilever tip can be calculated as [1]

$$\Phi(z=0) = 2lB_z(z_m) \left[\frac{w_{\text{SQUID}}}{2} - \text{Re} \sqrt{\left(\frac{w_{\text{SQUID}}}{2} + iz_m \right)^2 - \left(\frac{w_{\text{strip}}}{2} \right)^2} \right], \quad (2.125)$$

with the SQUID loop being at $z = 0$, the superconducting strip of the cantilever being at $z = z_m$ seeing a magnetic field of $B_z(z_m)$, the length and width of the SQUID loop l and

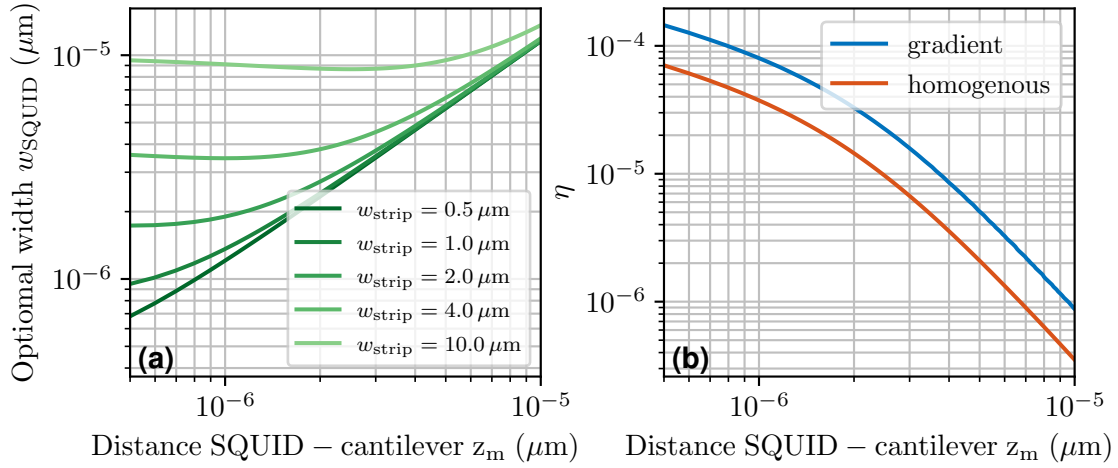


Figure 2.30: (a) There exists an optimal SQUID loop width for a given distance between SQUID and cantilever, and width of superconducting strip on cantilever. To be less sensitive to distance, one could maximize w_{strip} . (b) Magnetomechanical coupling parameter $\eta = \frac{z_{\text{zpf}}}{\Phi_0} \frac{\partial \Phi}{\partial z_m}$ for the optimal width (a) for a given distance between SQUID and cantilever. The strip width is set to 2 μm , the current for the gradient field is fixed to 100 mA, and the magnetic field for the homogeneous field is chosen to be the same as the field generated by the gradient field setup for that given distance. We observe an improvement by factor 4-5 when using the gradient setup.

w_{SQUID} , and the width of the superconducting strip on the cantilever tip w_{strip} . The flux change by a mechanical displacement is then given by

$$\begin{aligned} \frac{\partial \Phi}{\partial z_m} = & 2l \left. \frac{\partial B_z}{\partial z} \right|_{z=z_m} \left[\frac{w_{\text{SQUID}}}{2} - \text{Re} \sqrt{\left(\frac{w_{\text{SQUID}}}{2} + iz_m \right)^2 - \left(\frac{w_{\text{strip}}}{2} \right)^2} \right] + \\ & + 2l B_z(z_m) \text{Re} \frac{iw_{\text{SQUID}} - 2z_m}{\sqrt{(w_{\text{SQUID}}/2 + iz_m)^2 - (w_{\text{strip}}/2)^2}}. \end{aligned} \quad (2.126)$$

The second part of the sum is the flux change generated by the changing distance between SQUID and cantilever for a magnetic field $B(z_m)$ at the cantilever. This factor would be the same when using a homogeneous field instead of a gradient field. The first factor is the additional signal we gain by using a gradient field $\partial B / \partial z|_{z=z_m} \neq 0$. Due to the beneficial scaling with distance, one could use an external coil to shift the magnetic field zero position close to the cantilever. This would allow to get a bigger gradient while staying below the critical field of the superconductor [1]. However, in typical experimental setups we are limited by the maximum current through the wires.

A good dimensionless parameter to characterize the magnetically coupled setup is [1]

$$\eta = \frac{z_{\text{zpf}}}{\Phi_0} \frac{\partial \Phi}{\partial z_m}, \quad (2.127)$$

with the cantilever zero point fluctuation in position space z_{zpf} . This parameter quantifies the flux change in the SQUID loop per ground state size in units of magnetic flux quanta

Φ_0 . Figure 2.30(a) shows the dependence of η on distance between SQUID and cantilever, where we use a SQUID loop of optimal width for each distance. We observe a factor of 4 gain by using the gradient field in comparison to a homogeneous field for a given distance. To be able to detect the groundstate of the mechanical oscillator, the noise floor of the experiment has to be below η . The experimental characterizations will be discussed in Sec. 3.4.3.

Magnetic gradient field generation To increase the magnetic coupling, we have to maximize the magnetic field and gradient. However, superconductors have a limited maximum current. When using multiple windings, one can increase the field and gradient for the same current, as typically done for coils. However, since we are using planar on-chip wires, we have to separate them in a plane, the outer lines will therefore contribute less and less. Using finite element simulations for superconducting wires⁷, we can estimate the field and gradient by multiple number of close-by wires. The results are summarized in Fig. 2.31. Increasing the number of wires leads to increased fields and gradients. However, this behavior saturates since the wires are further and further away from the center. We decided to use $n = 5$ lines on each side for the HYPRES design, see Sec. 3.3.3.

⁷We use the London equation as boundary for the superconducting regions. Many thanks to J. Prat-Camps and Martí Gutierrez-Latorre for helping in the implementation and discussions.

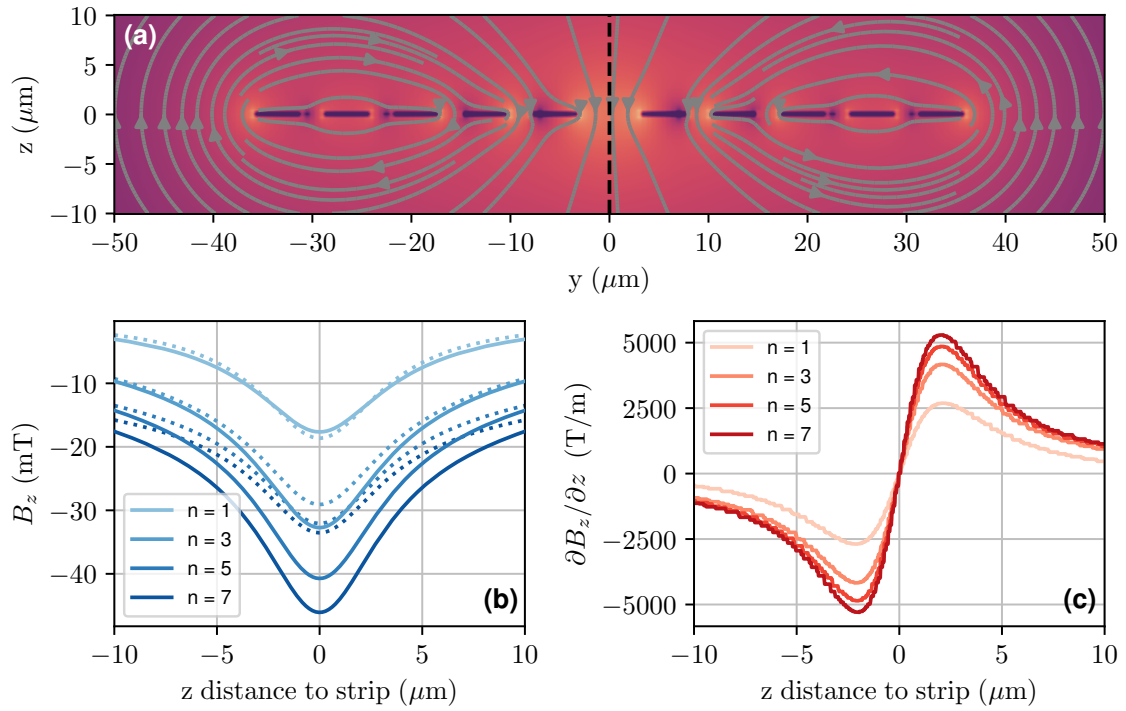


Figure 2.31: (a) Simulation results of magnetic field generated by $n = 5$ strips on each side. Brighter colors indicate higher field magnitude, field direction is illustrated by gray fieldlines. The other two plots are a cut along $y = 0$, indicated by the black dashed line. (b) Magnitude of magnetic field along $y = 0$. Solid lines are superconducting finite element simulations, the dashed lines is an analytical model. We observe that the model fits the simulations for $n = 1$ quite well, but differs more and more for increasing number of strips due to flux focusing effects. (c) Gradient of magnetic field along $y = 0$ for various number of strip. We gain by using multiple lines for the same current as expected for a coil configuration.

DC-SQUID setup

Exploring the dead end
of the frequency spectrum

In a first approach we want to detect the mechanical system using a DC SQUID setup. This chapter is about the design, experimental setup and characterizations of DC-SQUID read out with a bias current. In the first section, practical DC-SQUIDs are discussed. The second section discusses the experimental setup and noise considerations. Multiple iterations of setup improvements allowed us to go to the intrinsic noise floor of the SQUID. In the third section, I will introduce and motivate our circuit design and present characterization measurements. The last section is about adding the cantilever to the setup. We discuss design, preparation, alignment and expected signals.

3.1 Practical DC-SQUIDs

Practical DC-SQUIDs require some modifications to function optimally as a magnetic flux to voltage converter [89, 90]. I will now discuss the most important concepts to optimize DC-SQUIDs for applications in the lab.

Shunt resistor A DC-SQUID is a flux to voltage transformer. However, without adding a shunt resistance we will get an unwanted hysteretic behavior. To understand this, we can look at what happens to a SQUID when we vary a magnetic field. If the DC-SQUID is biased slightly below the critical current and we apply the field, the magnetic-flux-dependent critical current [Eq. (2.37)] decreases and we observe a high voltage drop as soon as the critical current is shifted below the bias current. However, a voltage across the SQUID creates a time-varying phase difference φ (Josephson Eq. 2). If we now decrease the magnetic flux in the SQUID loop again, the time-varying phase difference creates an ac current (Josephson Eq. 1) that effectively increases the bias current for the SQUID. This leads to an hysteretic effect: When we reach the magnetic field at which we started and had no voltage drop before, we now observe a voltage drop. This can be prevented by shunting the Josephson junctions by a resistor. Together with the natural capacitance of a Josephson junction (without the tunneling supercurrent a Josephson junction would just be a parallel plate capacitor) the resistance forms an RC circuit. The characteristic time scale at which a voltage decays in an RC circuit is $\tau_{RC} = RC$. We can compare this

to the Josephson current oscillation period, which is given by $\tau_{\text{RL}} = L_J/R$ and define the Stewart-McCumber parameter

$$\beta_C = \frac{\tau_{\text{RC}}}{\tau_{\text{RL}}} = \frac{RC}{L_J/R} = \frac{2eI_0}{\hbar} R^2 C. \quad (3.1)$$

A $\beta_C \leq 1$ means that the oscillating Josephson current decays already in a single oscillation period and vanishes. However, reducing β_C means shunting the SQUID with a low resistance that diminishes the voltage across the SQUID, and therefore our signal. We have to find an optimum between available bandwidth and signal strength. If we want to detect fast flux changes, we need to ensure that we have no hysteretic effects on this time scale and decrease the resistance. On the other hand, increasing the resistance increases the Johnson-Nyquist noise created by this dissipative element. Numerical optimizations show that $\beta_C \approx 1$ is optimal for best noise performance [89]. For a practical DC-SQUID, we have to add a matched resistor in parallel to each junction of the SQUID. Matched means here, that the resistor together with the capacitance of a junction, which is given by fabrication parameters and geometry, gives $\beta_C = 1$.

Gradiometer SQUIDS are the most sensitive magnetic field detectors in the world, even able to detect the magnetic field created by currents in the brain [63, 89, 90]. If already thinking close to your experimental setup will distort your measurement, it is understandable that we have to protect SQUIDS from unwanted noise signals. Of course, for such weak signals like the ones coming from our brains a small distance is already protection enough, however in a typical lab environment we will find much stronger signals. In addition to using mu-metal and superconducting shields, we can use a geometric trick to make the SQUID completely insensitive to spatially homogeneous magnetic fields. By twisting

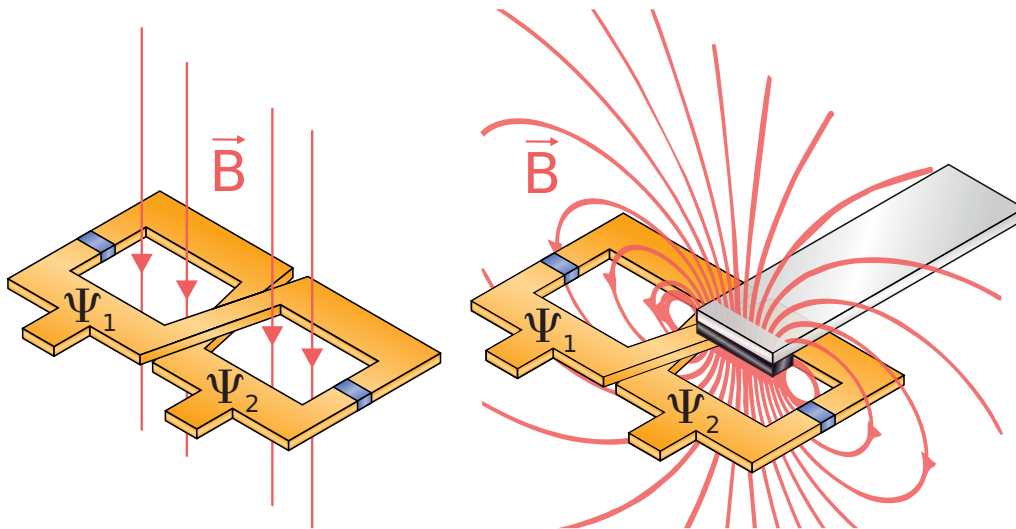


Figure 3.1: Gradiometric SQUID loop. **left:** In a figure eight loop a homogeneous field creates zero magnetic flux in the loop, as the flux in one loop cancels the flux in the other loop. **right:** The local field of the cantilever tip instead leads to finite magnetic flux and therefore an effect on the critical current of the SQUID

the SQUID loop to obtain a figure eight geometry with two equal loop areas, as shown in Fig. 3.1, a spatially homogeneous magnetic field creates zero magnetic flux within the SQUID loop. We are therefore not susceptible to noise sources that create a homogeneous field across the two SQUID loops. However, a magnetic field gradient causes unequal fields across the two loops, leading to a finite magnetic flux within the loop. For our setup, we can place the cantilever above only one loop, achieving high sensitivity to the mechanical signal but canceling homogeneous external fields.

Low signal DC-SQUID operation DC-SQUIDs are typically operated in constant current mode, which is illustrated in Fig. 3.2. Fixing a bias current at I_b (indicated by the gray dashed line in the center of Fig. 3.2) and sweeping the magnetic flux through the SQUID loop gives the nonlinear voltage response displayed on the right in Fig. 3.2. As long as the critical current of the SQUID is above the bias current, the SQUID is superconducting and we observe no voltage signal. Once the flux inside the loop is big enough to shift the critical current below the bias current, we get a sharp voltage signal. For small magnetic signals ($\delta\Phi \ll \Phi_0$), we can pick an ideal flux bias point Φ_b at which we achieve highest sensitivity $\partial V/\partial\Phi$. Small changes in magnetic flux are directly converted to a voltage that we can read out and digitize using an amplifier chain.

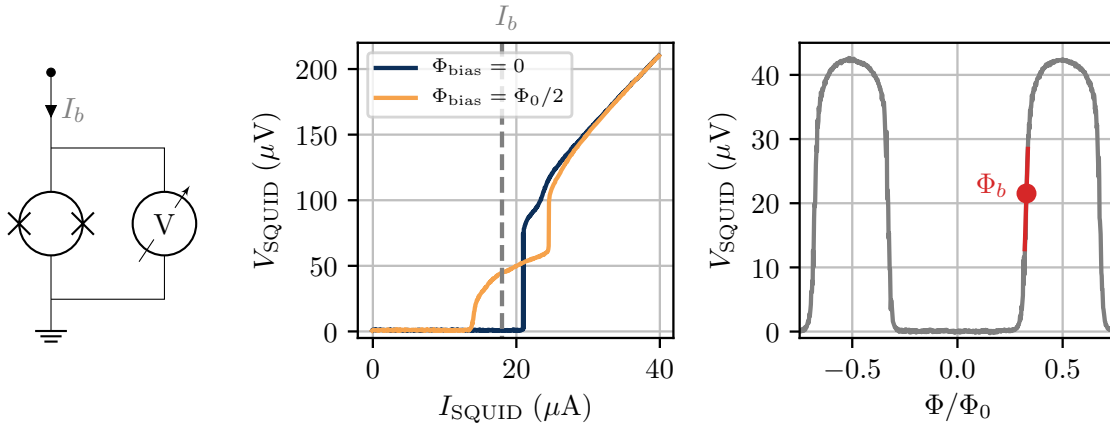
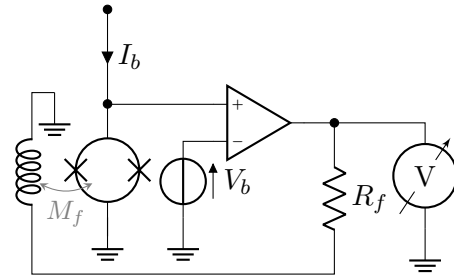


Figure 3.2: Default DC-SQUID operation. On the left is a circuit diagram of a typical operation: A bias current is applied through the SQUID and the voltage drop across the SQUID is detected. In the center, we show measurements of the voltage response as a function of applied bias current for an optimized DC-SQUID. The SQUID has a similar IV characteristic as a single Josephson junction, but the critical current is strongly dependent on the magnetic flux within the SQUID loop [see Eq. (2.37)]. On the right hand side we show the measured voltage response of a SQUID for a fixed bias current (that is indicated by the dashed line in the center figure). The voltage response is very nonlinear with applied flux. For small signals, we can pick an optimal flux bias point Φ_b with highest sensitivity, indicated by the red dot. The red line indicates the flux to voltage transfer function for the bias point.

Fluxed Locked Loop (FLL) The response of a DC-SQUID to magnetic field is very nonlinear (see Fig. 3.2). If the magnetic signal is strong $\Phi \gtrsim \Phi_0$ we must use a feedback coil to keep the flux inside the loop at the highest sensitivity point Φ_b , to obtain a linear flux to voltage transduction. For this we must track how much flux we need to feed back to keep the bias point the same. Since the voltage as a function of flux is periodic with Φ_0 , we have to track this fast, as skipping some periods leads to a wrong flux measurement. The feedback circuit is implemented by an operational amplifier as illustrated in the circuit on the right and already implemented in typical SQUID electronics. The required coil for the feedback must have a fast response and is therefore typically implemented by an on-chip flux bias line (which has to be considered in the design process). Note that a magnetically coupled cantilever on top of the SQUID is actually cooled by the flux locked loop, if the applied feedback is fast enough. This was observed experimentally in Ref. [129].



Design routine For the design process of DC-SQUIDS, we need to find a compromise between the requirements for the experiment and the limitations due to fabrication. The following is a typical design routine for DC-SQUIDS:

1. **Design SQUID loop:** In our case, the geometry has to fit the dimensions of the permanent magnet/superconductor on the cantilever. Increasing the width of the cantilever increases our signal, but there is a limit imposed by the critical current of the SQUID. Due to fabrication and readout limitations, we can only use a critical current higher than $1 \mu\text{A}$. This sets a maximum loop size to avoid hysteretic effects. Larger loops can be achieved using flux transformer circuits [89].
2. **Simulate loop inductance:** To prevent hysteretic effects and optimize the noise performance of the SQUID we have to know the geometric inductance of the SQUID loop. Since superconductors repel magnetic fields, half of the field above the superconducting strip is guided inside the loop. This is called *flux focusing* and allows to increase the effective area of the SQUID without increasing its inductance, which is given by the inner perimeter, by using wide strips for the SQUID loop. To optimize the design, this requires a full superconducting simulation of the geometry. For this we use the superconducting finite element solver *3D-MLSI*¹.
3. $\beta_L \approx 1$: Numerical simulations show that best SQUID performance regarding sensitivity is achieved for a $\beta_L = 2LI_c/\Phi_0 \approx 1$ [89]. This sets the value for the critical current, which is typically adjusted by the area of the junctions.
4. $\beta_C \approx 1$: Once the critical current is set, we can estimate the junction capacitance and add a shunt resistance to achieve $\beta_C = 2eI_0R^2C/\hbar \approx 1$. Together with the available resistivity of available shunt resonator materials, this sets the dimension of resistor.

¹<http://vmbak.cs.msu.ru/sotr/vmhap/3dmlsi/3dmlsi.htm>

5. **Finalize and check design:** With all the free parameters set, we can finalize the design. This includes adding vias for connecting multiple layers, checking that all layers are correct, and checking that all fabrication limitations regarding distance between geometries are fulfilled. It is normally better to be conservative but have a running device.

SQUID loop self-resonance Optimized DC-SQUIDS ($\beta_L = \beta_C = 1$) typically show a double step characteristic IV curve, depicted in the center of Fig. 3.2. This feature is caused by the LC resonance of the SQUID loop, which gets excited by ac Josephson currents, as described in Ref. [89, p. 47] and Refs. [162–165]. The fundamental mechanism for this is the following: Josephson Eq. 2 together with Josephson Eq. 1 state that an applied voltage across the junction causes oscillating currents at frequency

$$\omega_J = \frac{2e}{\hbar}V, \quad (3.2)$$

with V being the voltage applied to the Josephson junction. When ω_J matches the resonance frequency of the SQUID loop $\omega_{\text{loop}} = 1/\sqrt{L_{\text{loop}}C/2}$ ($C/2$ because the two capacitances of the junctions are in series), we can excite the circuit. However, when no flux is applied to the SQUID loop, the generated Josephson currents at the two junctions oscillate in-phase, resulting in no circulating loop current. Only if the two Josephson currents differ we can excite circulating loop currents. This occurs for finite applied flux and is strongest when we apply half a flux quantum to the loop. At this point the ac Josephson currents oscillate exactly out of phase and the excitation of the loop resonance is strongest. Averaged over time there is now always one arm of the SQUID that has a current opposite to the applied bias current, resulting in an effective decreased bias current and thus a lower voltage at the SQUID loop, which is visible in the IV characteristic. This is also the explanation why the $V - \Phi$ characteristic [e.g. Fig. 3.15(c)] flips when the applied bias current is high enough to create a high enough bias voltage that excites the loop resonance.

3.2 Experimental setup

DC-SQUIDS require a well shielded and well thermalized measurement environment together with a sensitive and low noise measurement electronics for optimal operation. In this section, I will discuss therefore sample packaging, the wiring and electronic requirements for sensitive measurements, the cryostat setup, and some considerations about noise.

3.2.1 Sample packaging

DC-SQUIDS are typically fabricated on 5 mm × 5 mm or 10 mm × 10 mm silicon microchips, too small to directly solder connections on them. We are using printed circuit boards (PCBs) to connect the microchips via Aluminum wire-bonds. On the PCB we solder surface mount connectors to connect the packaged sample to our measurement setup. During the course of this thesis we started from scratch and went through two main generations

of designs. We typically design PCBs with *Altium Designer*² and order them commercially at *Beta Layout*³. The metal parts are designed with *Solidworks*⁴ and fabricated in our excellent in-house IQOQI workshop.

Magnetic shielding A DC-SQUID requires good screening of magnetic fields. For this purpose we use a cryogenic mu-metal *Amumetal 4K* (A4K)⁵ that shows a very high magnetic permeability ($\mu_r = 8 \cdot 10^4$) at 4K. Due to this high permeability, magnetic fields are guided around the sample space as illustrated in Fig. 3.3. We can enhance the shielding factor S by using a dual layer (DL) instead of a single layer (SL) mu-metal shield. The gain in attenuation factor due to the use of two layers can be calculated as follows⁶

$$S_{DL} = S_1 + S_2 + S_1 S_2 \left(1 - \left(\frac{R_1}{R_2} \right)^2 \right), \quad (3.3)$$

where S_i is the shielding factor for a single mu-metal layer

$$S_i = \frac{\mu_i t_i}{2R_i}, \quad (3.4)$$

with the thickness of mu-metal t_i and inner radii of the first and second shield R_i . In the center of Fig. 3.3 we show the scaling of a single shield versus multiple shields. By using two layers we directly gain a full order of magnitude of screening. One could gain even

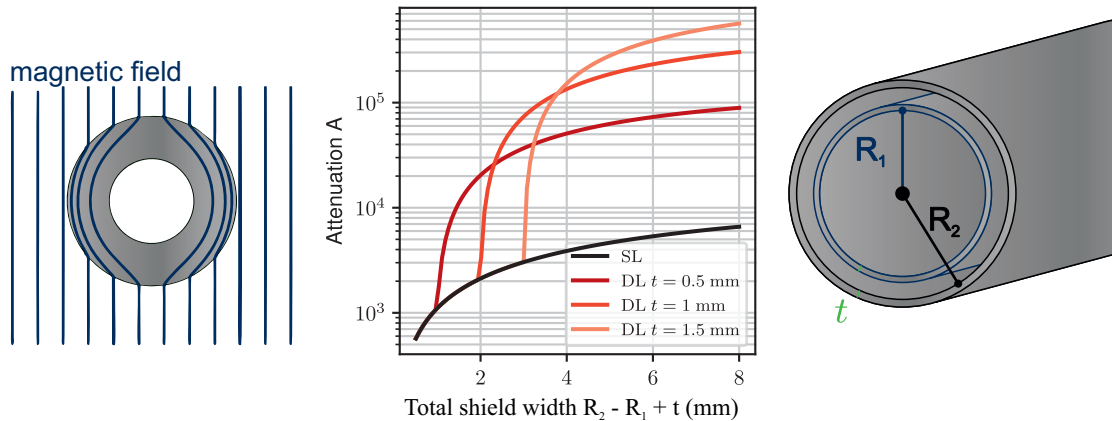


Figure 3.3: Magnetic shielding. **left:** A high magnetic permeability material (silver) guides the magnetic field lines (blue) around the sample space in the center. Figure adapted from [166]. **center:** Attenuation of magnetic field for single layer (SL) and dual layer (DL) magnetic shields as a function of total shield thickness $R_2 - R_1 + t$. We gain a factor 10 to 100 of attenuation by using two layers instead of one. **right:** Sketch of multi-layer mu-metal shield. Two cylinders with inner radius R_i are combined.

²<https://www.altium.com>

³<https://de.beta-layout.com>

⁴<https://www.solidworks.com>

⁵<https://www.amuneal.com>

⁶<https://www.amuneal.com/magnetic-shielding/theory-design/formulas-calculations>

more attenuation by combining superconducting layers together with layers of mu-metal. Details about this can be found in the PhD thesis by *Jordi Prat-Camps* [166]. Due to limited space in the cryostat we could not include a superconducting inner-shield.

1st generation For the optimal operation of the quadrupole field setup, an additional requirement arises: we need a big coil to generate a strong homogeneous field to shift the zero field position close to the cantilever tip. For this purpose, we wind superconducting coils with up to 4000 windings using a mechanical winding machine or a lathe. The whole packaging is designed to be compact for being able to put it at different stages of the dilution refrigerator. Figure 3.4 shows the PCB, sample box and mu-metal shield for the first generation. Details about this setup can be found in the Master's thesis of M. Schmid [154].

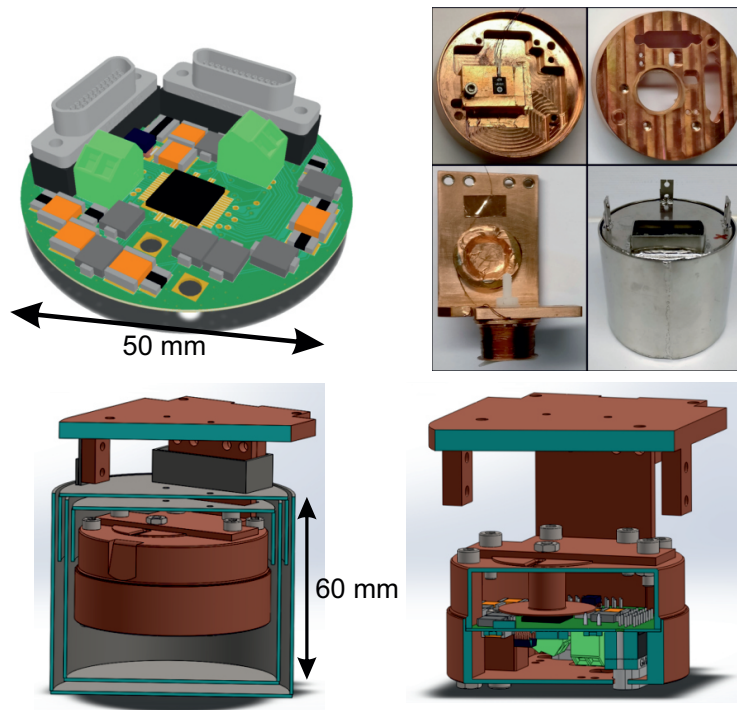


Figure 3.4: First generation sample packaging. **top left:** PCB design. The microchip is illustrated in the center (black). Two Micro-Sub-D surface mount connectors (black/silver) allow the operation of up to 8 DC-SQUIDS. Two screw terminals (green) are used to connect the superconducting wire for the magnetic field generation high current lines. Cryogenic surface mount capacitances, inductances and resistors are used for filter circuits. **top right:** Copper sample box, cover, angled sample holder with coil, and cryoperm mu-metal shield. A cryogenic hall-probe is added below the chip position to characterize the coil. **bottom left:** CAD drawing of packaged sample box inside mu-metal shield. The design is chosen to be as compact as possible to put it at higher temperature cryostat plates. **bottom right:** Closed sample box without mu-metal shield. The coil is positioned right above the microchip while the connectors are plugged from below.

2nd generation For the second generation, we moved the coil under the PCB for better access from the top as shown in Fig. 3.5. This proved useful for wirebonding, and mounting and fixing the cantilever chip. We also removed the filter circuits from the PCB to decrease complexity and make the filter optional and modular. Additional filters are designed with their own boxes that can be plugged in front of the setup. The connectors are soldered to the bottom to provide a flat surface for wire-bonding on the top. To shield the setup from magnetic fields, we use the same cryoperm mu-metal shielding. For fixing the cantilever chip we use two Copper-Beryllium springs.

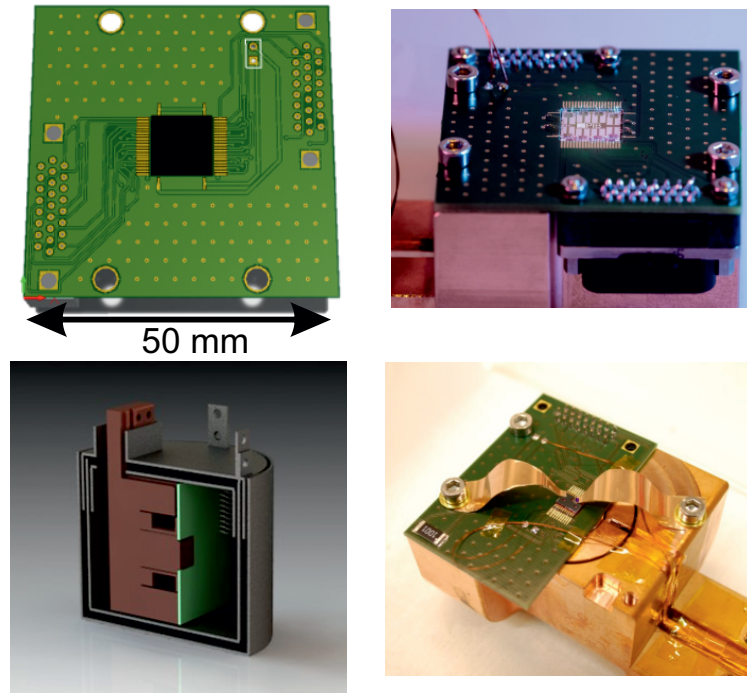


Figure 3.5: Second generation sample packaging. **top left:** New PCB design. Filter circuits are removed, the connectors are soldered from the back-side. The micro-chip is again centered. We removed the solder-stop resist from the backside for a good thermalization. **top right:** Photograph of the composed setup. The SQUID chip is wire-bonded to the PCB which is screwed to the sample holder. A coil is embedded below the PCB. **bottom left:** Cut through CAD drawing of design. The coil is embedded in a notch below the PCB. The chip is directly glued to copper to ensure good thermalization. **bottom right:** Assembled setup with cantilever chip in flip-chip configuration clamped with two Copper-Beryllium clamps. One can see a part of the coil embedded below the PCB.

3.2.2 Cryostat setup

For the cryogenic setup, we are using commercial *Oxford Instruments Triton*⁷ dilution refrigerators. The open cryostat without radiation and vacuum shields is shown on the right in Fig. 3.6. The setup is designed for maximum flexibility so that we can mount the packed sample at different temperature stages. This is a safety measure for the high current lines of the quadrupole setup. If the heat load due to the high conductivity of the thick wires is too high, we can move the setup to a stage with higher cooling power as illustrated in Fig. 3.6. One of our cryostats is also equipped with a small vibration isolation system, where the cryostat sits on air buffers (see Fig. 3.6). Special care is taken to ensure good thermalization of samples, wiring and filters following the recommendations by J. W. Ekin [167].

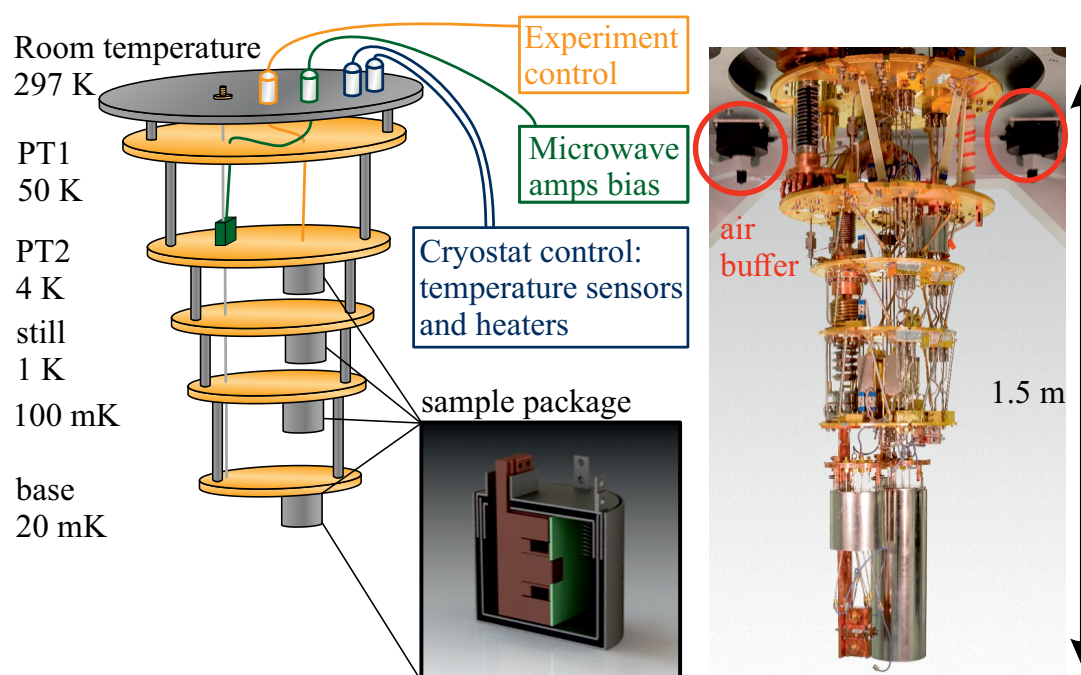


Figure 3.6: Cryostat setup. On the left we show a schematic of the cryostat plates while on the right we show an actual photograph of the open cryostat. The sample packaging is designed that it can be mounted at the PT2, still, 100 mK or base plate. One of our cryostats has air buffers, which are highlighted red on the right picture. Typically, the cryostats are shared with microwave experiments of colleagues. Together with the cryostat control this leads to multiple DC and microwave connections into the cryostat that could potentially couple in noise.

3.2.3 SQUID Readout

In principle, DC SQUIDs are simple to operate and read out. We just need to apply a bias current and measure the voltage across the SQUID. Typical shunt resistances are in the

⁷<https://nanoscience.oxinst.com/>

range between 1 and 10 Ω , which is similar to the resistance of the leads. Therefore, to read the actual voltage of the SQUID, a four-point measurement setup is recommended. In the beginning, we used a relatively simple setup using a Labjack UE9⁸ for applying current and measuring voltage. At a later stage, we decided to switch to the commercial Magnicon XXF-1⁹ SQUID electronics, because of much better noise characteristics. In addition, the new electronics allows the operation in flux locked loop. XXF-1 is a complete SQUID setup box, which comes with a graphical user interface to control and readout the SQUID. For optimal noise performance, it is best plugged directly at the top of the cryostat to the connector. We use a laptop (to prevent ground loops) for the control and developed a Python library, which allows talking to the control software and integration in our default data analysis setup.

3.2.4 Noise optimization

Since typical setups in our group are optimized for microwave experiments, it was a long way to get a direct current setup running and measuring the first good IV characteristic of a DC-SQUID. Moreover, it turned out that it is not really feasible running microwave and DC experiments at the same time due to noise carried into the cryostat by additional DC wiring required for microwave experiments (coils, cryogenic amplifiers, switches, etc...). We improved the noise level by filtering, ground loop reduction and learning about the various noise sources. In this subsection, I briefly discuss some of the main results.

Thermalization and wiring Good thermalization is critical for DC-SQUID performance. First of all, the superconductor needs to be cooled below the critical temperature. Moreover, as the shunt resistor is a Nyquist noise source, we have to cool down the resistor as much as possible. The resulting currents created by the Nyquist noise generate flux noise, which sets the limit for the flux sensitivity of the SQUID.

In Fig. 3.7 our first measured IV curve is plotted in blue, which barely resembles the expected behavior of a SQUID Sec. 2.1.2. Following the recommendations by J. Ekin [167], we improved our wiring and thermalization by clamping the wire to each cryostat plate, using grease and varnish to increase the thermal connections between sample, wires and cryostat, and increased wire length between cryostat plates. This led to increasingly better IV curves, as seen in Fig. 3.7.

Cryogenic amplifiers We discovered that the largest noise source is our cryogenic microwave amplifier. These commercial low noise amplifiers (LNA) from *Low Noise Factory*¹⁰ come standard with a switching power supply. As soon as we connect the amplifier to the power supply we observe excessive noise that completely washes out the IV curve, as shown in Fig. 3.8. We have replaced the standard power supplies with linear power

⁸<https://labjack.com/products/ue9>

⁹<http://www.magnicon.com/squid-electronics/xxf-1>

¹⁰<https://www.lownoisefactory.com/>

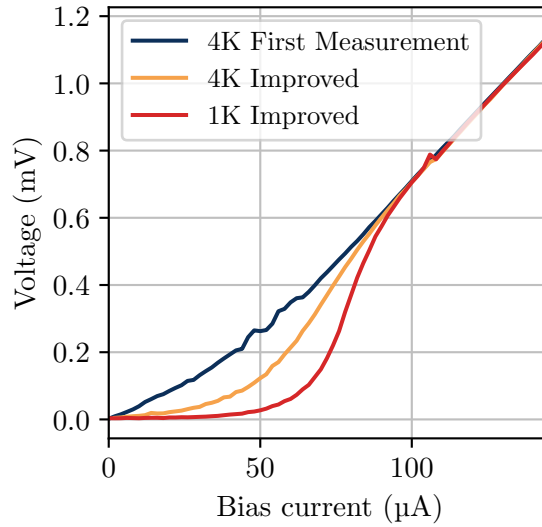


Figure 3.7: First measured IV curve in our cryostat (blue) and improvements due to better thermalization (orange and red). A RuOx temperature sensor mounted to the sample holder indicated $T = 6.7\text{ K}$, $T = 5.2\text{ K}$ and $T = 1.8\text{ K}$ for the blue, orange and red setups, respectively. In the first measurement, hardly any SQUID characteristic is observed, while the red line already shows the typical dependence. There is still excess noise rounding off the expected sharp rise at the critical current.

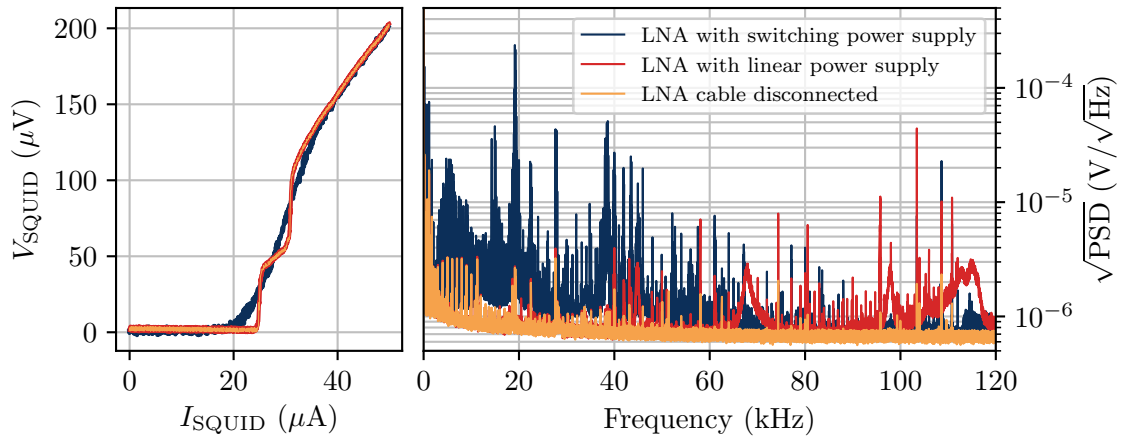


Figure 3.8: IV curve and voltage spectral density of the same DC-SQUID for either no cable connected to the cryogenic amplifiers (orange), for supply with a linear power supply (red), and for supply with the standard switching power supply (blue). The latter generates so much excess noise that even the IV curve is washed out. Using a linear power supply helps a lot, but the best noise level is achieved when all DC connections to the cryostat are disconnected.

supplies, resulting in a dramatic reduction in noise. However, the best noise floor is still only achieved when the additional cables are completely disconnected.

Faraday cage and preventing ground loops DC experiments are susceptible to broad noise sources and require a careful experiment design [168, 169]. The optimal setup for DC experiments in a cryostat is illustrated in Fig. 3.9. All parts that require a DC connection to the inside of the cryostat are placed in the same Faraday cage, which is grounded at a single point. If we use multiple single shielded wires to connect the instruments to the cryostat, magnetic fields could induce circulating currents in the shields. Due to induction, these currents transfer to the wiring going inside the cryostat and therefore bring the noise back into the Faraday cage. The same happens for multiple grounding points. For most experiments this means that there is a whole shielding chamber around the cryostat with space for the required instruments. In our case, we do not have such a chamber and creating a Faraday cage including the commercial cryostat control would require a lot of effort. However, we can create a simplified version of this ideal setup by unplugging all DC connections including the whole cryostat control and just connecting the DC-SQUID control and readout box, ensuring everything is shielded and isolated correctly (we are connecting the XXF-1 SQUID electronics solely to an isolated Laptop). With this setup we achieved the best noise floor without any parasitic noise spikes. It requires however to disconnect all other DC wiring and cryostat control, which prevents temperature stabilization or running other experiments in parallel.

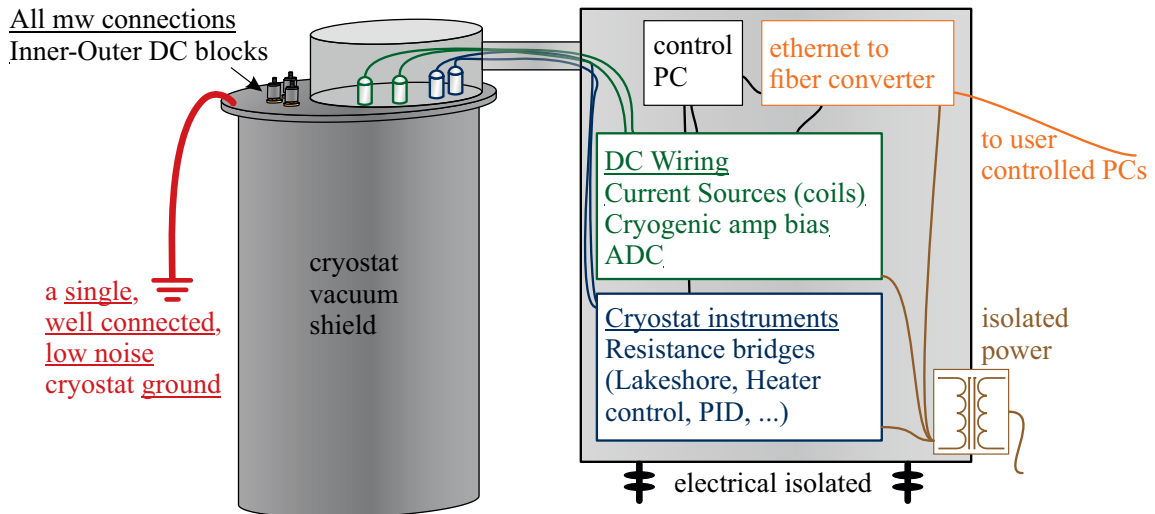


Figure 3.9: Ideal setup for low noise DC cryogenic experiments. All the DC connections are placed in the same Faraday cage. Connection to the outside is isolated and guided over optical links. The whole system is grounded at a single point to prevent circulating currents on the Faraday cage which can be induced to the wiring.

Filtering Another solution is to use filters to prevent noise from reaching the sample. They are best placed directly in front of the sample box. We tried a variety of filter

architectures, ranging from PCB lumped element filters at room temperature and cryogenic temperatures [170] to filter designs directly on the microchip itself. Although we did not obtain a conclusive answer about the optimal filtering strategy, we obtained the best results with homemade steel-powder filters similar to those in Ref. [171], but with a self-wound coil embodied in Stycast-steel-powder mixture. For the most sensitive measurements, we still remove any extra wiring going into the cryostat.

3.3 Samples and characterizations

DC-SQUIDS are an established technology that has been greatly optimized over the past 50 years. However, fabrication typically requires a complex multilayer Niobium process that only a few facilities worldwide have mastered. Moreover, we had no experience in DC-SQUIDS. We have therefore collaborated with the experts Prof. R. Kleiner and Prof. D. Koelle from the University of Tübingen¹¹, who in turn have a collaboration with PTB Braunschweig, where the samples are fabricated. We also ordered a sample from HYPRES Inc.¹², a commercial foundry that offers multilayer SQUID fabrication. The experiment requires a specific SQUID design, which we optimized through calculations and simulations with guidance from our collaborators. We designed some of the designs ourselves, which we label with Innsbruck. Other designs come from our experienced collaborators Matthias Rudolph and Kevin Uhl from the University of Tübingen, which we label with Tübingen. The microchips ordered commercially from HYPRES are designed by us. All samples are fabricated on silicon substrates.

3.3.1 Innsbruck 1st generation

Our first generation design is shown in Fig. 3.10 together with optical images and a scanning electron microscope (SEM) image of a fabricated sample. Our collaborators from Tübingen recommended a chip size of $1\text{ cm} \times 1\text{ cm}$. We could fit 8 gradiometric SQUIDS on the available space, each with its SQUID control and flux bias lines. The SQUID loop consists of two $50\text{ }\mu\text{m}$ long loops in a figure eight geometry. We vary the width of the loops between 2 and $6\text{ }\mu\text{m}$ for the different SQUIDS to have an optimal width depending on the distance between SQUID chip and cantilever chip (see Sec. 2.4.3). In the beginning, we were not sure how close we could get the chips together and estimated that 1 to $2\text{ }\mu\text{m}$ should be feasible.

In close proximity to the SQUID loop are two wires for generating the magnetic quadrupole field. Since we want to maximize the gradient, these wires must be as close together as fabrication allows. Unfortunately, this proved to be too close, as all of our first generation designs are shorted (visible in the photograph of the samples). We were unable to measure any SQUID characteristic, only resistive behavior caused by the lead wires to the SQUID. Furthermore, some of the SQUID structures have an additional loop around

¹¹<https://uni-tuebingen.de/fakultaeten/mathematisch-naturwissenschaftliche-fakultaet/fachbereiche/physik/institute/physikalisches-institut/bereiche/festkoerperphysik/>

¹²<https://www.hypres.com/>

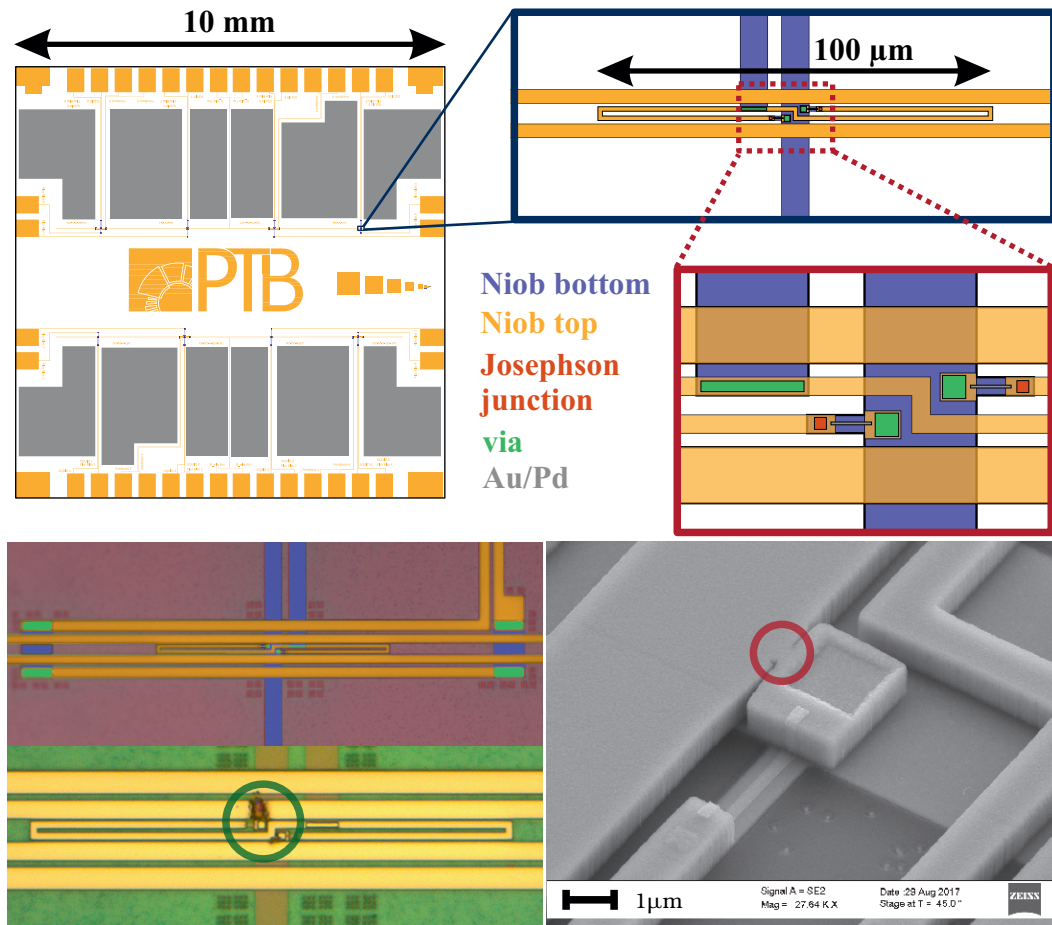


Figure 3.10: Innsbruck first generation DC-SQUID design. We designed $10\ \mu\text{m} \times 10\ \mu\text{m}$ microchips equipped with a total of 8 SQUID designs each. We place anti-parallel current strips near to the gradiometric SQUID loop to generate the magnetic gradient field. To make connections efficient, we use the same high current line for the top 4 SQUIDs, and add another one for the bottom 4 SQUIDs. Some of the SQUIDs have an additional feedback loop around the entire gradiometric SQUID loop to apply a feedback to the cantilever that is not visible in the gradiometric SQUID loop. Each SQUID is optimized using the design routine (see Sec. 3.1). The image below the full chip shows a photo of a SQUID design with the additional feedback loop. At the bottom right is a scanning electron microscope (SEM) image showing that most of the designs are shorted by the high current lines (red circle). However, even the samples with no obvious connection got damaged when a current was applied in the high current lines (see green circle in bottom left image).

the entire gradiometer to apply feedback to the cantilever. To test the high current lines for magnetic gradient generation, we applied currents up to 10 mA. We examined the samples after warming up again with an optical microscope and observed some sort of disruptive breakdown at the high current lines even at these low currents (see bottom left in Fig. 3.10).

Summarizing, none of the first generation Innsbruck designs worked because of fabrication problems. We learned that we should be more conservative in new designs or vary the design parameters to have at least one very conservative design that is sure to work.

3.3.2 Tübingen 1st generation

The first generation design by Matthias Rudolph is depicted in Fig. 3.11 and consists of 8 SQUID setups on a $1\text{ cm} \times 1\text{ cm}$ chip. In contrast to the Innsbruck design, each setup is independent and can in principle be cut out separately. Again, the SQUID loop is in a gradiometric figure eight geometry and its size is varied on each design to sweep different β_L values. Matthias added a dedicated flux bias loop above one arm of the loop for SQUID control. He also added on-chip low-pass RLC filters. Details on the design, fabrication, and the filters can be found in Ref. [154]. The microchips also exhibited fabrication difficulties such as lift-off problems and interconnections between SQUID and high-current lines. These problems are likely due to the very thick Nb top layer, which is required to support high currents for magnetic gradient field generation.

In contrast to the Innsbruck design, we were able to measure our first SQUID IV curve for one of the Tübingen designs (see Fig. 3.12(a)). This first signal finally allowed us to optimize the setup. By repeatedly cooling down the same sample, we optimized the thermalization, wiring, and eliminated noise sources as discussed in Sec. 3.2.4. We also observed a weak dependence on magnetic flux, shown in Fig. 3.12(b) when sweeping the current through an external coil.

In the end, we decided to try another chip of the same batch. This one fortunately had no connection between the high current line and the SQUID, resulting in a lower critical current. However, due to holes in the shunt resistance, likely caused by the thick Nb top layer, the SQUID was hysteretic, as can be seen in Fig. 3.12(c): The voltage jumps at two different critical currents depending on increasing or decreasing bias current. However, the jump is now very sharp and not rounded as we observed in our first IV curves, which shows that we were able to get rid of most of the noise sources in our setup.

The high current lines seemed to work reliably up to 10 mA, however we did not have compliant cantilevers with superconducting tips at that time. We therefore decided not to increase the currents too much in order to have at least one working SQUID for optimizing the setup and for setups with cantilevers equipped with permanent magnets.

In summary, the first Tübingen generation allowed us to optimize our experimental setup and to become familiar with SQUID characterizations and measurements. However, the SQUIDs seemed to be hysteretic and showed a low sensitivity to magnetic flux. We also

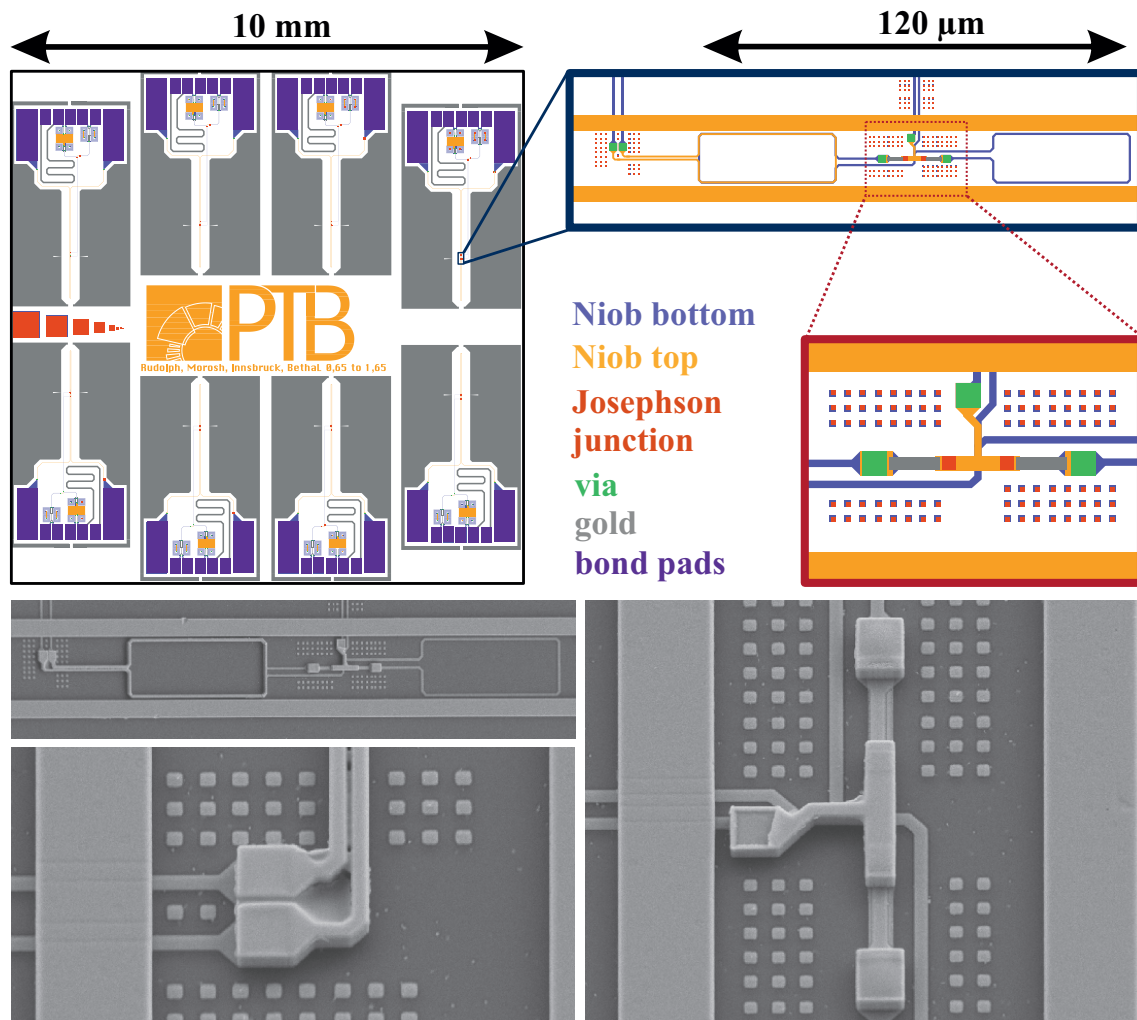


Figure 3.11: First generation Tübingen DC-SQUID design. 8 independent setups are packed together on a 1 cm × 1 cm microchip. Each design has a gradiometric SQUID loop with a feedback flux loop above one part of the loop. Right next to the SQUID loop are two Nb strips for the generation of the magnetic quadrupole field. The size of the gradiometric SQUID loop is varied over the chip to have designs with different β_L . The three bottom SEM images show the actual design, problems with lift-off, and the thick Nb top layer. The chip has on-chip low-pass filters not shown here, but described in Ref. [154].

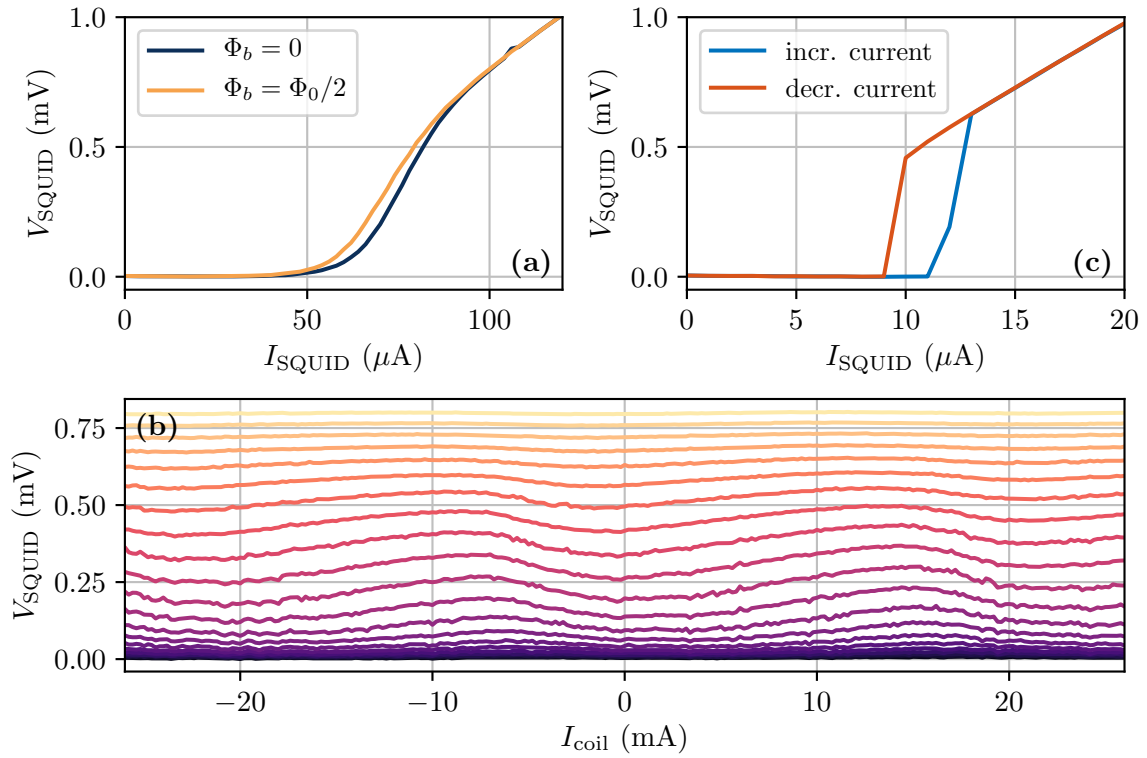


Figure 3.12: Characterizations of Tübingen 1st generation DC-SQUIDs. (a) IV-curve of our first working sample. We used this sample to optimize the setup. The SQUID showed a connection to the high current lines used for magnetic field generation what increased the critical current. (b) Measured voltage across the SQUID as a function of applied magnetic flux for the same SQUID as in (a). The different colors indicate different bias currents (dark to bright equal low to high bias currents). We observe a flux dependence, however it only shows a small slope and therefore low magnetic field sensitivity. (c) IV curve of another SQUID of the same batch after setup improvements. We now observe a sharp critical current at which the voltage across the SQUID jumps. The SQUID is hysteretic as increasing currents and decreasing currents lead to voltage jumps at a different bias current. This is likely due to holes in the shunt resistor that are caused by the high height of the superconducting Niobium top layer.

placed a cantilever chip with deposited nanomagnets on top of this SQUID in a flip-chip configuration. Unfortunately, we observed no verified evidence of a mechanical signal. Details about this setup can be found in the Master's thesis of Michael Schmid [154].

3.3.3 HYPRES

We further ordered a batch of micro-chips from the foundry HYPRES Inc. This time, we chose three very distinct SQUID designs, depicted in Fig. 3.13. Since HYPRES has a mandatory chip size of $5\text{ mm} \times 5\text{ mm}$, we decided to place only three setups on one chip. All SQUIDS share the same high-current line for magnetic gradient field generation. To achieve this, this time we used five thin, closely spaced strips instead of a single wide strip to increase the magnetic field gradient (see Sec. 2.4.3). Since HYPRES has a three-layer process by default, we could even pattern the field generation lines on top of the SQUID. This generates a greater gradient, as the distance between opposing current wires is smaller. Moreover, the field generation lines are the most top layer, and are therefore closer to the cantilever chip. However this makes the designs a bit messy since there are many layers on top of each other.

The three designs are named H-Innsbruck, Flux-Transformer (FluxTra), and JuanJo. Table 3.1 lists the design parameters for each design. H-Innsbruck is again a gradiometric

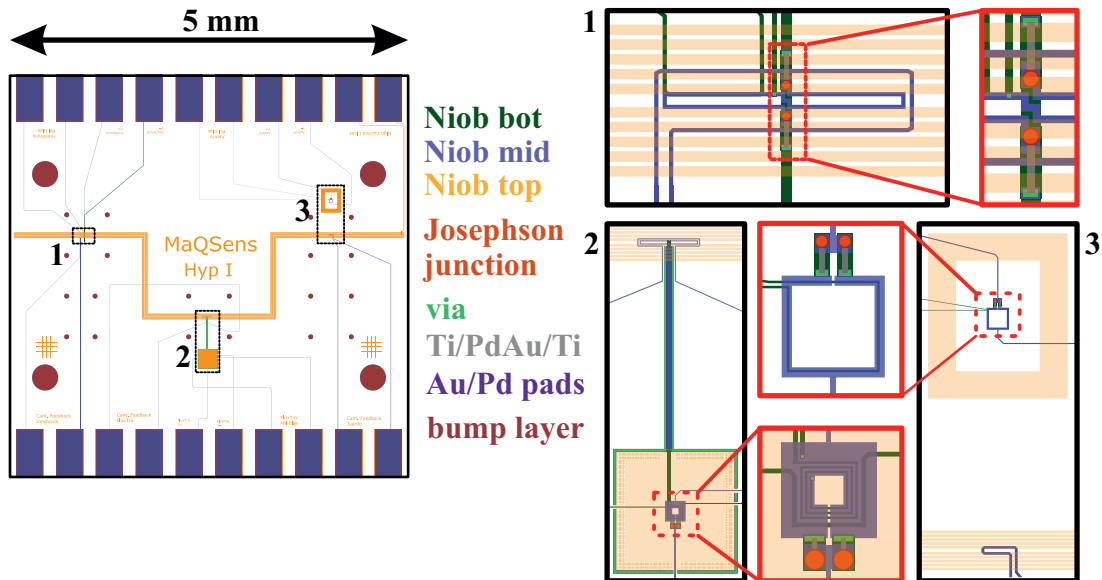


Figure 3.13: HYPRES design. The chip size is fixed to $5\text{ mm} \times 5\text{ mm}$. We design three different setups: 1 H-Innsbruck, 2 FluxTra, 3 JuanJo. All three designs share the same high current lines (orange lines in the center) to generate the magnetic gradient field. Only 1 has a SQUID directly at these lines, the others use a gradiometric pick-up loop on the same chip (2) or a normal pick-up loop on the cantilever chip (3) to pick up the signal and route it to the SQUIDS, which are placed $500\text{ }\mu\text{m}$ away. The black boxes show the entire setup, and the red boxes are a zoom in on the SQUID/Josephson junction.

SQUID design, while Flux-Transformer and JuanJo are normal SQUIDs far away from the high magnetic gradient field. The latter two receive the magnetic signal from the cantilever via a (gradiometric) pick-up loop. We will now go through the individual designs and present their characterizations.

Table 3.1: Design values for all three HYPRES designs.

Parameter	1. Innsbruck	2. FluxTra	3. JuanJo
Type	gradiometric	flux transformer	default
SQUID loop	$2 \times 54 \mu\text{m} \times 4 \mu\text{m}$	$12 \mu\text{m} \times 12 \mu\text{m}$	$32 \mu\text{m} \times 32 \mu\text{m}$
L_{loop}	54.6 pH	22.6 pH	78.0 pH
β_L	1	1	1
β_C	1	1	1
I_0	$19 \mu\text{A}$	$45.7 \mu\text{A}$	$13.2 \mu\text{A}$
C	820 fF	1900 fF	530 fF
R	4.6Ω	1.9Ω	6.9Ω
$\omega_p/2\pi$	43.9 GHz	43.9 GHz	43.9 GHz

Design 1 - H-Innsbruck The first design is very similar to our first PTB design: a gradiometric SQUID loop in figure eight configuration, matched Josephson junctions and shunt resistors, a flux bias line for the SQUID loop away from the cantilever and a cantilever feedback line surrounding the whole gradiometer (to not perturb SQUID operation). An optical and SEM image of the fabricated device is show in in Fig. 3.14. The SQUID sits directly below the high current lines used for generation of the magnetic gradient field. This allows to decrease the distance between the high current lines, which increases the magnetic field gradient. We further used this time 5 thinner lines than a single wide strip, as simulations showed that this also increases the magnetic gradient (see Sec. 2.4.3). Moreover, we used circular Josephson junctions, as this was required by HYPRES.

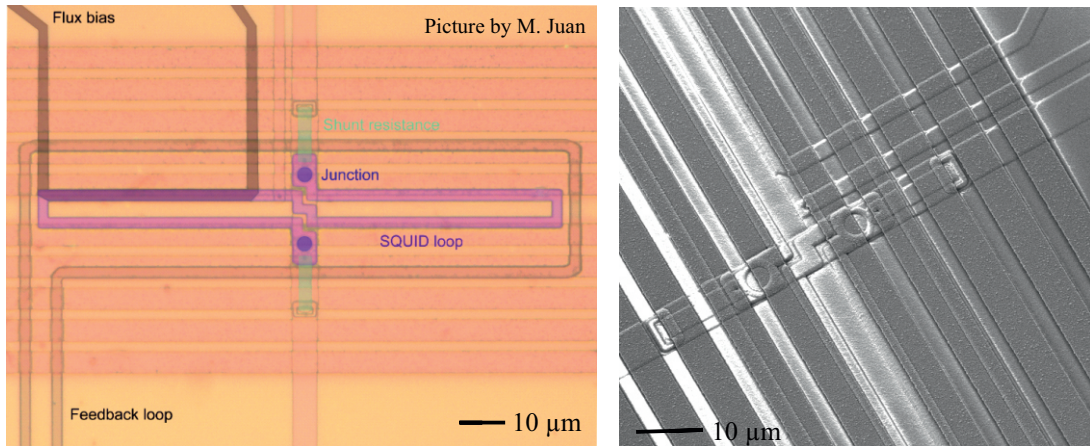


Figure 3.14: Optical image (left) and scanning electron microscope (right) image of a fabricated H-Innsbruck design. The gradiometric SQUID loop sits below the high current lines that generate the magnetic gradient field. A flux bias line is at one loop of the gradiometer.

This time, the SQUID was not shorted and we were able to characterize it. Figure 3.15 shows an IV curve, the critical current as a function of applied flux bias, and the voltage response as a function of applied flux for various bias currents indicated by different colors. The SQUID operates as expected and we observe no hysteric effects and a high magnetic field sensitivity. Table 3.2 summarizes the experimental obtained parameters. The values do not match the design values precisely, which is probably attributed to the high current lines going directly above the junctions. Nevertheless, the SQUID performs well and we have a working device for the mechanical setup.

Table 3.2: Summary of experimental characterization of the H-Innsbruck design.

Parameter	Fit value	Comment
β_L	1.6 ± 0.1	Screening parameter (design: 1)
I_0	$10.9 \mu\text{A}$	Critical current of a single junction (design: $19 \mu\text{A}$)
α	0.06	Critical current asymmetry, should be 0
R	11.8Ω	Shunt resistance (design: 4.6Ω)

Design 2 - FluxTra The second design is very different and illustrated in the black box labeled 2 in Fig. 3.13. An optical microscope image of the design is shown in Fig. 3.16. In this setup, the SQUID is placed 500 μm away from the high current lines and cantilever. To get the magnetic signal to the SQUID we use a gradiometric pick-up loop on the same chip. The whole SQUID is placed inside a Nb on-chip box, constructed by a bottom and top Nb layer together with vias. The SQUID itself is not gradiometric, but has a washer geometry to make use of flux focusing while reducing the geometric inductance.

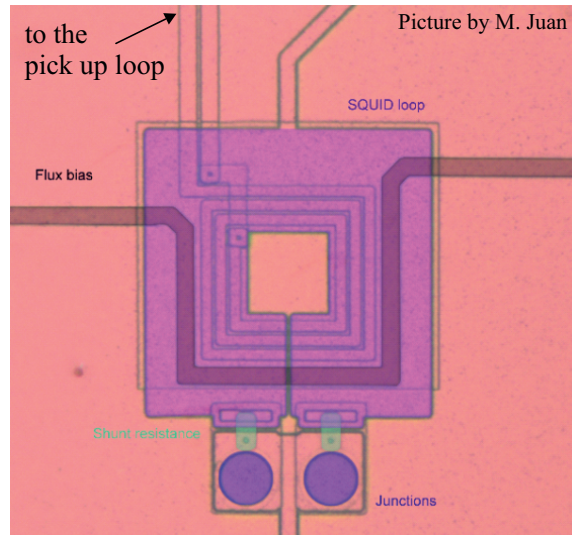


Figure 3.17 and Table 3.3 summarize the characterization of this design. The design showed some difficulties that led us to not investigate this SQUID further. First, we were only able to tune the flux-bias by at most half a flux quantum [see right in Fig. 3.17] within the available bias current range of the XXF-1 electronics. Moreover, the SQUID voltage as a function of flux bias dependence looks strange: It shows a flat plateau and a single sharp edge. We attribute this behavior to screening/mirror currents in the Nb box around the SQUID. This probably also causes the deformation of the IV curve. The critical current and shunt resistance are close to the design values. However, due to limited time, we decided not to invest more time in characterizing this setup and better focus on the other two designs.

Figure 3.16: Optical image of the FluxTra design.

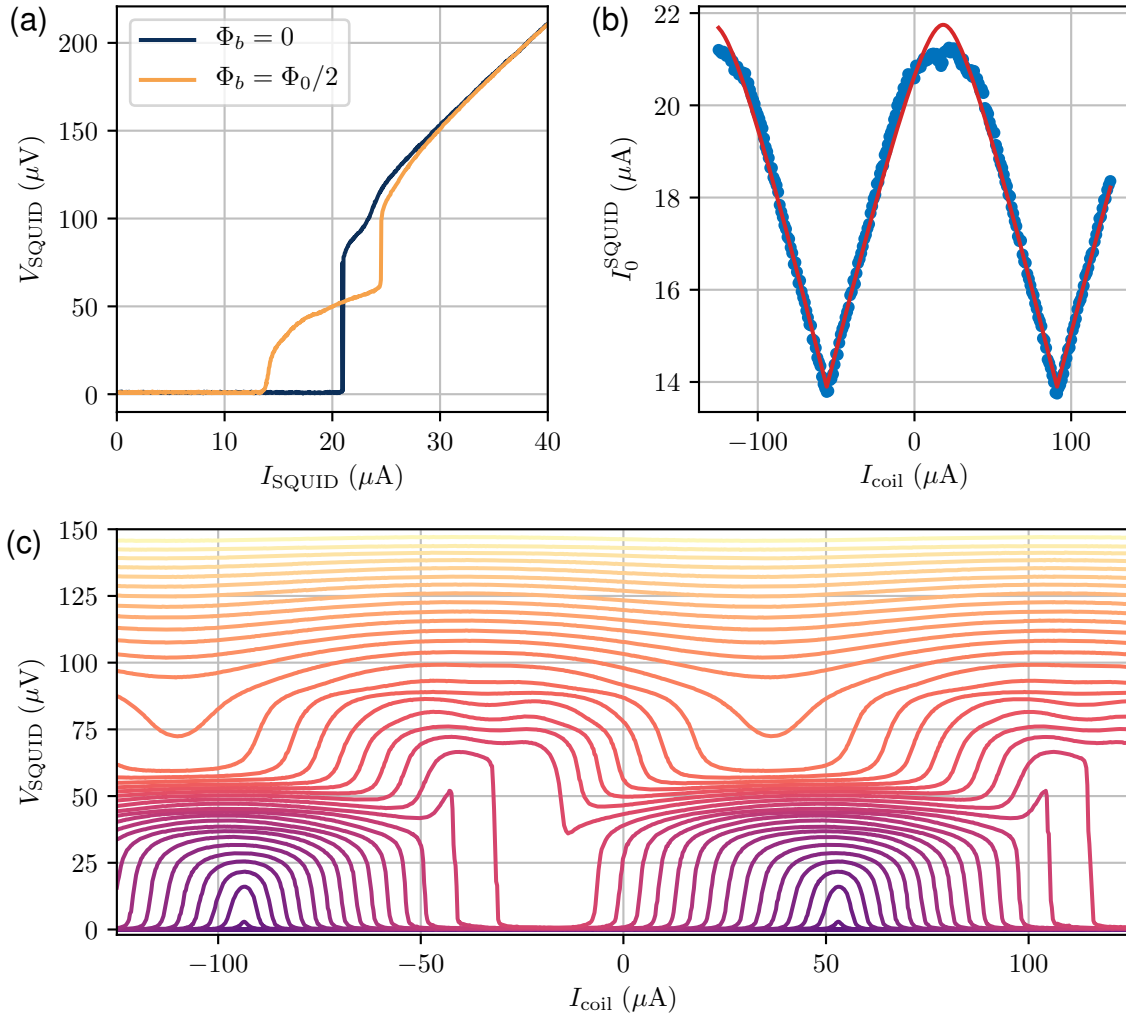


Figure 3.15: Characterization of H-Innsbruck DC-SQUID. (a) IV curve for zero applied magnetic flux (blue) and for half a flux quantum of applied magnetic flux (orange). We observe sharp jumps and a good flux tunability. The double step shape arises from the excitation of the self resonance, as discussed in Sec. 3.1. (b) Critical current as a function of coil current (which is directly proportional to magnetic flux in the loop). The red line is a fit of the SQUID model to extract $\beta_L = 1.6$ and $\alpha = 0.06$. We have trapped flux inside the loop causing the maximum shift away from $I_{\text{coil}} = 0 \mu\text{A}$. (c) SQUID voltage as a function of coil current for varied bias current (0: purple to 28 μA : yellow). The highest sensitivity is achieved for intermediate bias currents and tuning flux bias point to the steepest slope. Due to the double step behavior from the IV curve, the voltage behavior flips for a critical current around 20 μA .

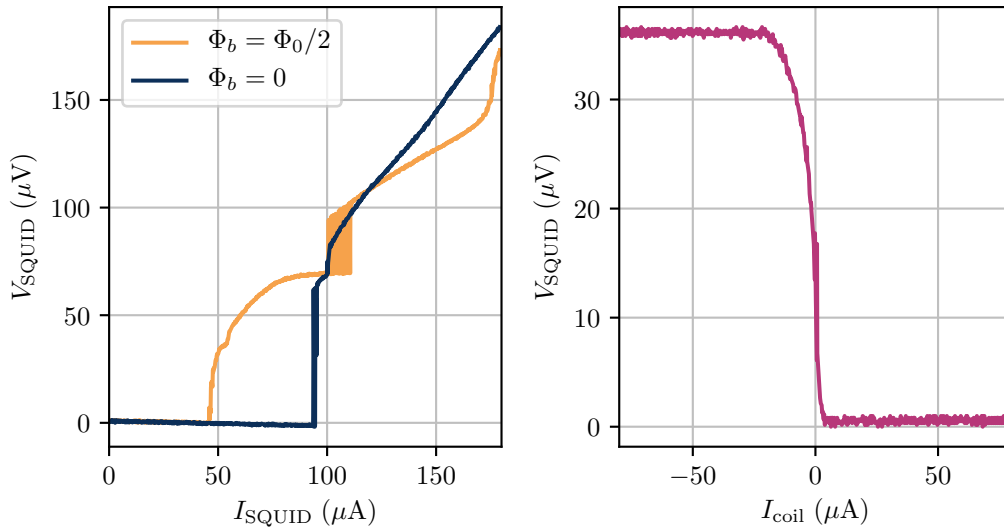


Figure 3.17: Characterization of FluxTra design. **left:** IV characteristic, showing a noisy second edge and a slight deformation above the second edge, and even the beginning of a third edge. This is likely caused by screening currents in the Nb shield box and/or another resonance of the whole system. The critical current is right at the design value. **right:** SQUID voltage as a function of current applied to the bias wire. We do not observe a periodic pattern but only a single edge, with plateaus before and after. This behavior is again likely caused by screening currents in the Nb box surrounding the SQUID.

Table 3.3: Experimental characterization of FluxTra design

Parameter	Fit value	Comment
I_0	$46.9 \mu\text{A}$	Critical current. (design: $45.7 \mu\text{A}$)
R	2.6Ω	Shunt resistance. (design: 1.9Ω)

Design 3 - JuanJo The third design is similar to FluxTra and illustrated in the black box with label 3 in Fig. 3.13. However, instead of having a pick-up loop on the same chip, we fabricate the loop on the cantilever chip. When the cantilever oscillates in the gradient field, the flux through this loop changes, which we can detect at the SQUID position. To achieve this, we cannot place the SQUID inside a box, because it has to pick up the field from the other chip. Therefore, the SQUID is a standard single-loop SQUID. In this setup, we do not gain in sensitivity as compared to using a permanent magnet (discussed in Sec. 2.4.3). But we can tune the gradient field, allowing to precisely set the flux change caused by the displacement of the can-

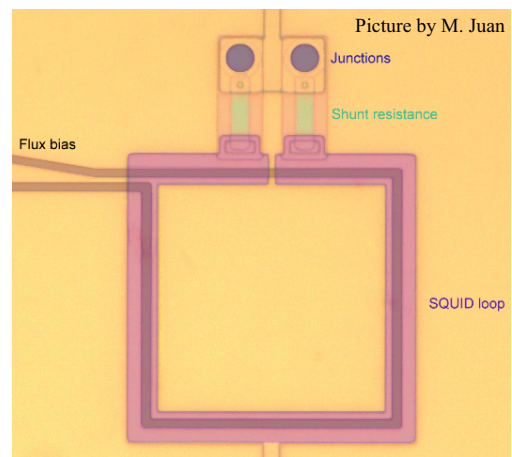


Figure 3.18: Optical image of the JuanJo design.

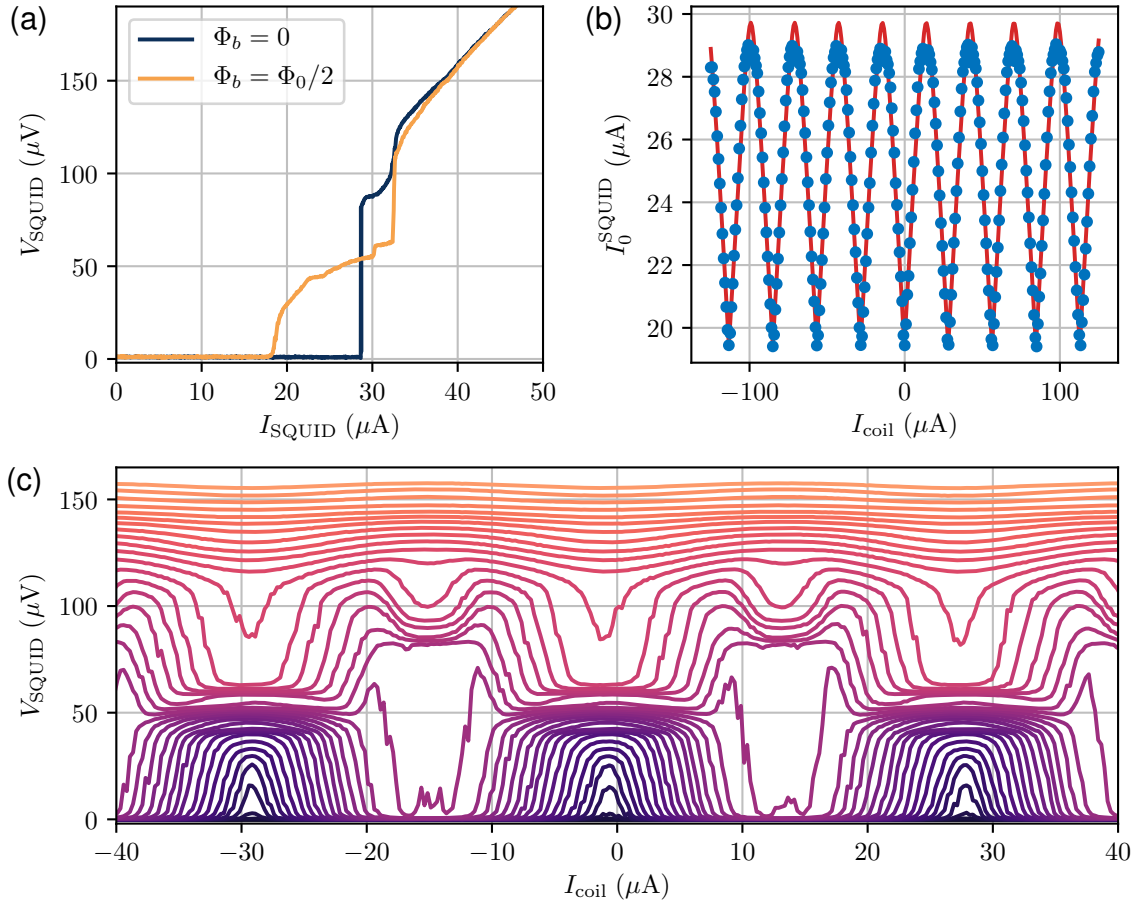


Figure 3.19: Characterization of a JuanJo DC-SQUID. (a) IV curve for zero applied magnetic flux (blue) and for $\Phi_{\text{ext}} = 0.5\Phi_0$ (orange). We observe a second edge, likely caused by another resonance of the circuit. (b) Critical current as a function of coil current. The red line is a fit of the SQUID model with an extracted $\beta_L = 1.65$. We have trapped exactly half a flux-quantum inside the loop causing the maximum shift away from $I_{\text{coil}} = 0 \mu\text{A}$. (c) SQUID voltage as a function of coil current for varied bias current (15 μA : purple to 40 μA : yellow).

Table 3.4: Experimental characterization for JuanJo design.

Parameter	Fit value	Comment
β_L	1.65 ± 0.02	Higher than design value 1.
I_0	$14.8 \mu\text{A}$	Critical current. Close design value of $13.2 \mu\text{A}$.
R	8.9Ω	Shunt resistance. Design value is 6.9Ω .

tilever. This idea and therefore the name comes from Juan José García-Ripoll¹³. During one of his visits at our group, we had a discussion and came up with this design. This design can also be used to read out a cantilever equipped with a permanent magnet (the same is possible with the H-Innsbruck design).

¹³<https://juanjose.garciaripoll.com/>

The characterization of the JuanJo SQUID is summarized in Fig. 3.19 and Table 3.4. This is a standard SQUID that works as expected (nevertheless we are happy!). The higher value for β_L arises likely due to a mutual inductance to a larger Niobium loop surrounding the SQUID, which we added to screen external homogeneous fields (see Fig. 3.13).

Spectral response We do not want to detect static magnetic fields, but fields oscillating with at mechanical frequency, in the range of 100 kHz to 1 MHz. Therefore, we must consider the noise floor in this range. For this purpose we use a spectrum analyzer that we connect to the Magnicon setup. Figure 3.20 shows the magnetic flux sensitivity in the cantilever frequency range for three different flux bias points. We observe a forest of noise peaks, which however decreases for the point of highest sensitivity (orange). To investigate this further, we sweep the applied magnetic flux for a fixed bias current and integrate over each noise spectrum. The resulting curve is plotted in purple in Fig. 3.21 along with the voltage transfer function (red) and the differential resistance (salmon). We observe a clear minimum in integrated power spectral density (PSD) at the point of highest

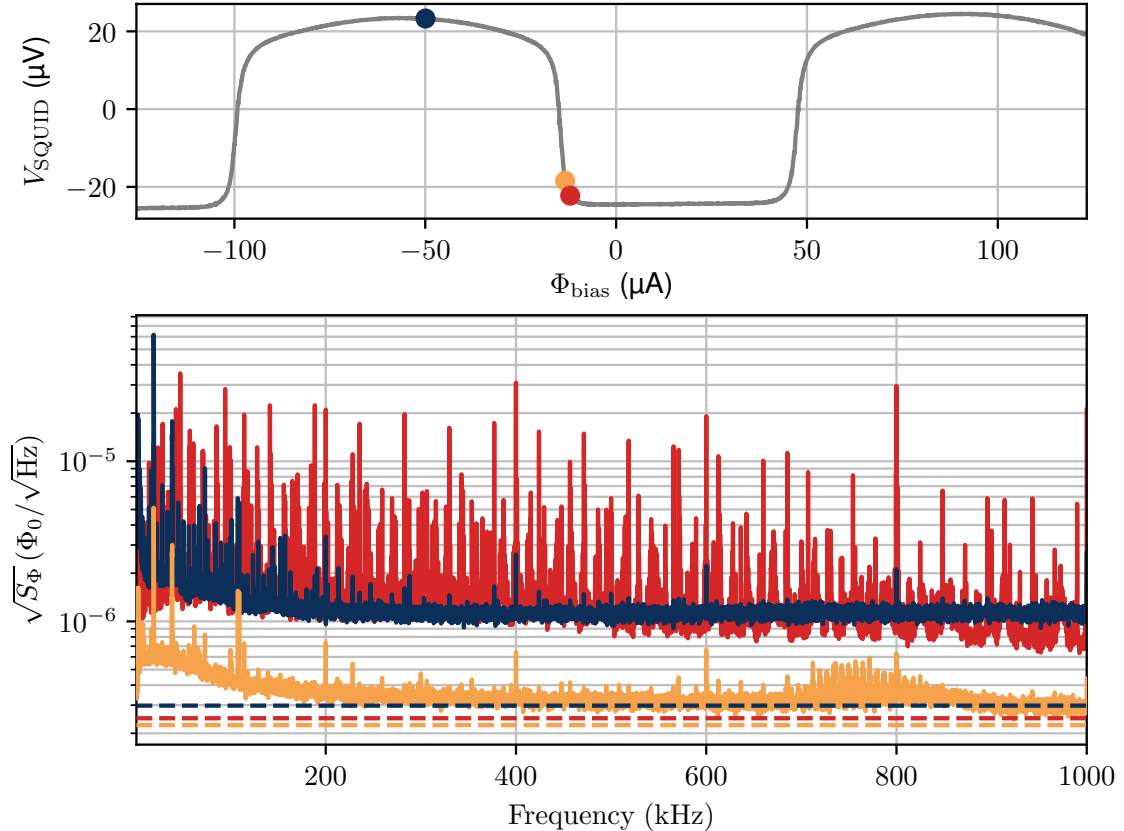


Figure 3.20: Spectral flux sensitivity of H-Innsbruck SQUID for three different flux bias points (blue, orange, red) indicated by dots in the top plot. The three dashed lines indicate the flux noise level created by Nyquist noise of the shunt resistance, which is given by Eq. (3.5). The three bias points have different noise floors, as the intrinsic flux noise depends on the voltage transfer function and differential resistance.

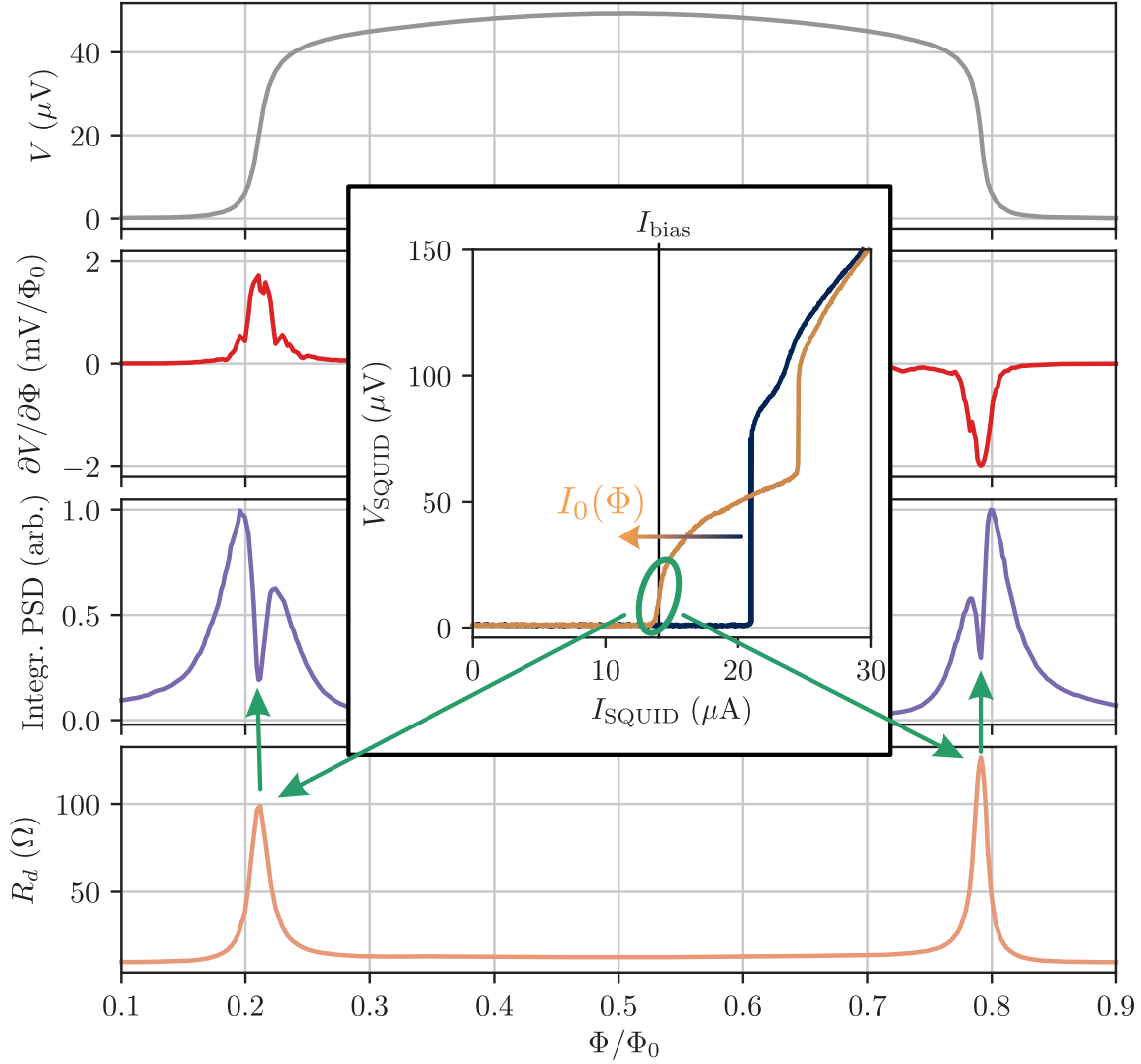


Figure 3.21: Voltage across SQUID (gray), voltage transfer function (red), integrated power spectral density from 100 kHz to 1 MHz (purple), and differential resistance (salmon) as a function of magnetic flux through the H-Innsbruck SQUID loop. For the highest sensitivity to magnetic flux (red) at around 0.21 and $0.79 \Phi/\Phi_0$, we observe a minimum in noise power (purple). As explained in the main text, this is due to impedance mismatching of a noise source in the SQUID control wiring: By increasing the flux, we decrease the critical current of the SQUID, illustrated in the central inlet. When the critical current is around the bias current (illustrated by green circle), $R_d = \partial V/\partial I$ is highest, resulting in a high impedance and thus lower noise power at the SQUID.

sensitivity ($\partial V/\partial \Phi$). This can be explained by picked up voltage noise in the SQUID control lines. The resistance seen by the noise is the differential resistance $R_d = \partial V/\partial I$ at the set bias current I_{bias} of the SQUID. By increasing the magnetic flux, we change the differential resistance from 0, to a maximum at $I_0(\Phi) = I_{\text{bias}}$, and to a finite value for $I_0(\Phi) < I_{\text{bias}}$ (see inlet of Fig. 3.21). If the SQUID becomes the dominant resistance in the bias current circuit, the voltage created by the noise source will almost completely

drop at the SQUID. Increasing the resistance even further, decreases the current in the circuit, therefore decreasing the voltage across the SQUID created by current fluctuations. This is actually impedance mismatching: The noise source has a specific impedance Z_{noise} . All of the noise power will be transmitted to the SQUID, if the impedances are matched ($Z_{\text{SQUID}} = Z_{\text{noise}}$). Increasing the impedance of the SQUID further, lowers the power dissipated at the SQUID. Therefore, for optimal SQUID performance, we should always operate at the point of highest sensitivity (equals highest differential resistance) when limited by low impedance noise.

Note that the noise floor for the optimal point of the H-Innsbruck design (see orange spectrum in Fig. 3.20) is close to the limit given by Nyquist noise of the shunt resistances [92, 172, 173] indicated by the dashed line. This limit can be calculated by

$$S_{\Phi}(f) = \frac{4k_B T}{V_{\Phi} R} R_d^2 \left[1 + \frac{1}{2} \left(\frac{I_0}{I_{\text{bias}}} \right)^2 \right]. \quad (3.5)$$

Where $R_d = \partial V / \partial I$ is the differential resistance, $V_{\Phi} = \partial V / \partial \Phi$ is the flux to voltage transfer coefficient, R is the shunt resistance, T is the temperature of the shunt resistance, I_0 is the critical current of a single junction, and I_{bias} is the bias current. Reaching this limit shows that we optimized our setup and are able to use the SQUID at its full potential, detecting flux changes as small as $\delta\Phi = 3 \cdot 10^{-7} \Phi_0$.

3.3.4 Tübingen/PTB 2nd generation

The designs for the second generation of Tübingen/PTB designs are shown in Fig. 3.22. We increased the distance between high current lines and SQUIDs to prevent short circuits, and we added a parallel gradiometric design together with a JuanJo design, similar to the HYPRES one, but with a gradiometric SQUID. In addition, Kevin Uhl designed a second generation chip of the Tübingen design. However, the PTB Braunschweig had a change in the fabrication process, which caused problems. None of ours and none of the Tübingen designs showed a characteristic IV curve of a Josephson junction. Instead, all designs showed a flat response indicative of short circuits. Inspection of the microchips with an optical microscope and a with a SEM revealed some collapsing and detached features, shown in Fig. 3.22. Despite these problems, we were able to improve the maximum current of the high current lines. We were now able to apply up to 100 mA without heating or increase in resistance. At this point, due to time constraints, we decided to focus on the microwave setup and stopped investigating further DC setups.

3.3.5 In-house Nb constriction

In the course of this thesis, we got our own cleanroom for nanofabrication and started to fabricate our own samples. However, we did not have the time or capabilities to develop the multilayer Niobium process used at PTB and HYPRES. Instead we tried Niobium constriction junctions [93, 174–178]. In this approach, the junction is not created by an insulator between two superconducting areas. Instead, the superconductor is narrowed to

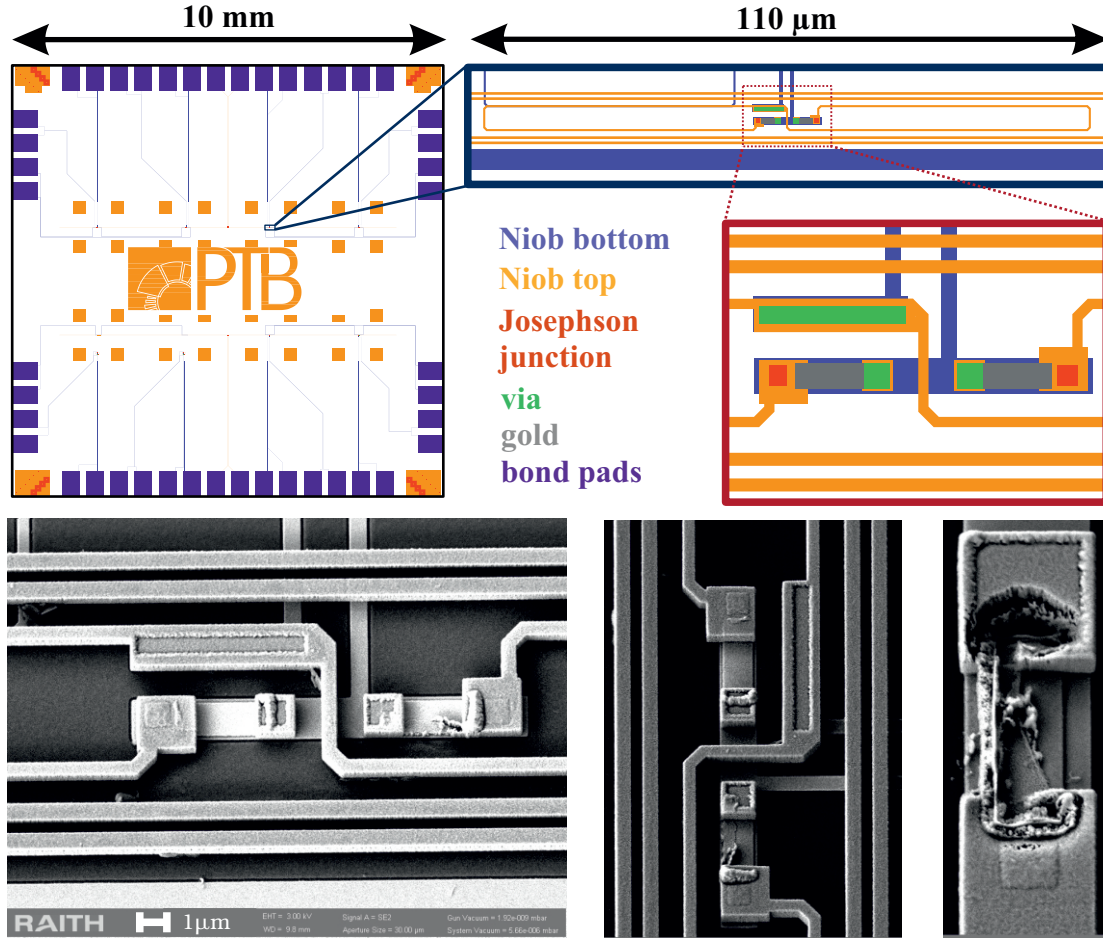


Figure 3.22: 2nd generation PTB Innsbruck design. We increased the distance between high current lines and SQUIDs, added a parallel SQUID and JuanJo gradiometric setup (both not shown) and added niobium pads close to the SQUID designs to define the distance between SQUID and cantilever chip (which is equipped with pillars). None of the fabricated designs were working due to fabrication problems, caused by a new fabrication process. In the lower scanning electron microscope images, one can see the detached and collapsed structures.

a width less than or close to the coherence length $w \lesssim \xi$ (see Fig. 3.23), leading to a weak link and a very similar current phase relation as for the insulator Josephson junctions, Josephson Eq. 1. However, increasing the length of the weak link leads to an increasingly deformed current phase relation [174, 177].

By using the lift-off process discussed in Sec. 4.3, we are able to fabricate reliable 50 nm wide Niobium constrictions (see Fig. 3.23). To characterize the junction properties, we fabricated a micro-chip with 6 DC-SQUIDs, for which we varied the SQUID loop size and constriction widths, illustrated in Fig. 3.23. Unfortunately, due to a fabrication error (stitching error) in the feed-lines, only two of the SQUIDs worked.

We characterized the samples by measuring the switching currents [83] at 1 K. The switching current is twice the critical current of a single junction only for zero temperature.

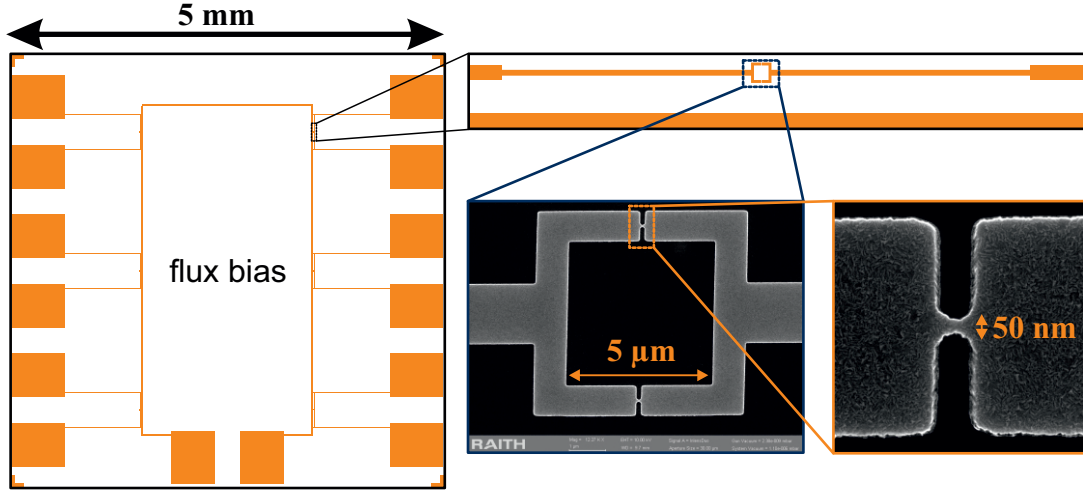


Figure 3.23: In-house fabricated niobium constriction junctions. We used the same dimensions of the HYPRES design to use the same setup. The chip has just a single layer of Niobium (orange) in which we pattern 6 SQUID setups with varied loop size and constriction widths. The junction itself is a constriction of Niobium to about 50 nm. The chip is fabricated using the process developed in Sec. 4.3.

Increasing temperature causes earlier switching due to fluctuations, which can be best explained by oscillations in the tilted washboard potential [92, Chap. 2]. In Fig. 3.23 we plot a single trace for increasing and decreasing currents. As expected, the SQUIDs are very hysteretic. Due to the different constriction widths, the resistance and switching current are different. Table 3.5 summarizes the parameters of the two working SQUIDs. Our fabrication process only allows to fabricate a reliable minimum constriction width of 50 nm, which imposes a lower limit for the critical current $I_c \gtrsim 500 \mu\text{A}$. This is unfortunately too high for most of our applications, since we could only use very small SQUID loops to still achieve $\beta_L \lesssim 1$.

Table 3.5: Design values and experimental results for the characterized in-house Nb constriction DC-SQUIDs.

Parameter	SQUID5	SQUID6	Description
w_{design}	50 nm	60 nm	Design width of constriction
L_{geo}	12.8 pH	12.8 pH	Simulated geometric inductance of $(5 \mu\text{m} \times 5 \mu\text{m})$ SQUID loop
I_{sw}	0.93 mA	3.1 mA	Measured switching current, roughly twice the critical current.
β_L	5.8	19	Screening parameter
R	299 Ω	74.4 Ω	Resistance per junction.

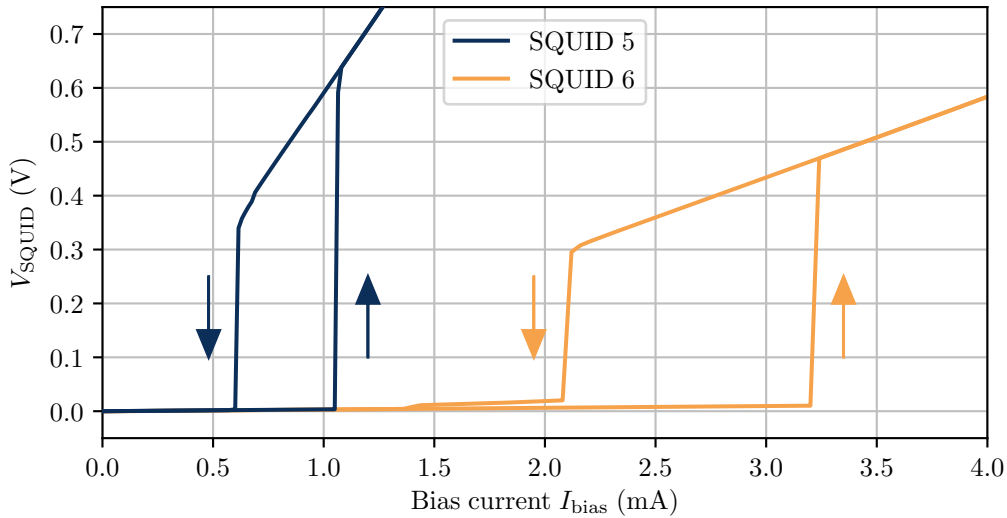


Figure 3.24: IV characteristic for Nb in-house fabricated Nb constriction SQUIDs. We observe a difference between increasing and decreasing current (indicated by arrows) as a consequence of the high normal state resistance of the constriction. The two SQUIDs differ in the width of the constriction. SQUID5 (blue) has a lower width leading to a lower critical current and a higher normal state resistance.

3.4 Adding mechanics: the cantilever

Now that we have a working DC-SQUID setup, we can think about adding the mechanical counterpart. For the fabrication of cantilevers with superconducting tip, we collaborated with Michael Trupke and Stefan Minniberger from the University of Vienna¹⁴. We also equipped cantilevers from Vienna and commercially available cantilevers with nanomagnets and micromagnets. In the following, I will briefly discuss our cantilever design, how we prepare and align them on top of the SQUIDs, and present noise spectra of the assembled setup. However, we could not observe a validated mechanical signal with any of the DC setups.

3.4.1 Design and fabrication

Our designs for the different SQUID setups are shown in Fig. 3.25. We choose silicon as a material and fix the thickness of the cantilever to $t = 5 \mu\text{m}$. To do this, we use Silicon on Insulator (SOI) wafers to etch the cantilever structure from the top and use a Bosch process to etch through the bulk of substrate from the back. Details about the process can be found in Ref. [154]. The fabrication was entirely

Table 3.6: Common properties.

Parameter	Value
Material	Silicon
Wafer type	SOI
Crystal axis	(100)
Cantilever Thickness	$5 \mu\text{m}$
Cantilever Width	$50 \mu\text{m}$
Niobium Thickness	200 nm
Titanium Thickness	$2 \mu\text{m}$

¹⁴<https://walther.quantum.at/>

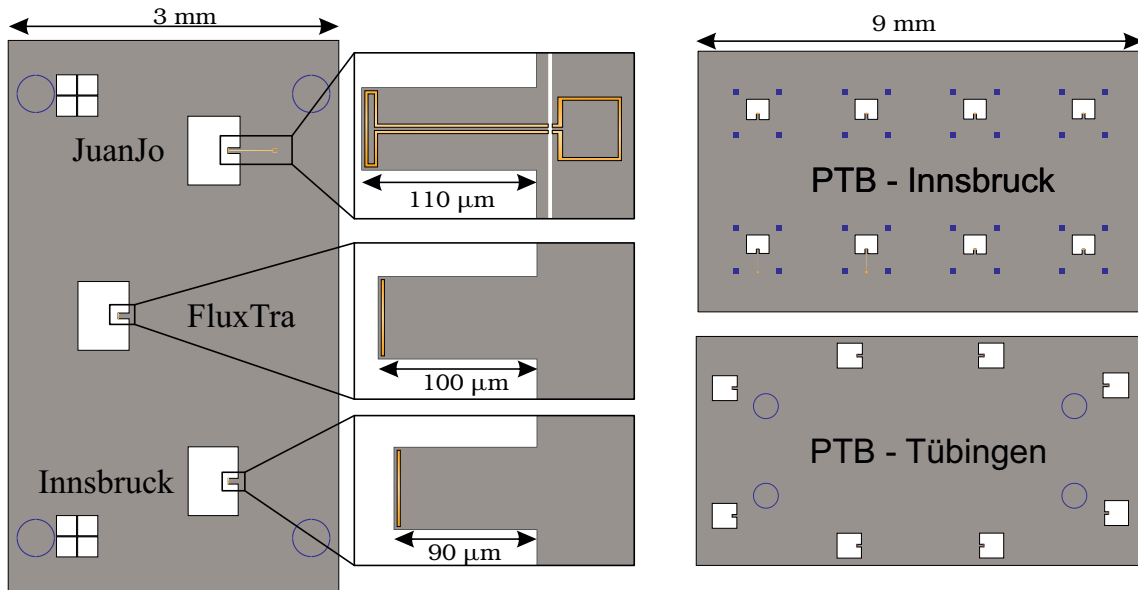


Figure 3.25: Cantilever designs with superconducting strips/loops at the tip (orange). On the left is the design for the HYPRES chip. The three cantilevers have different lengths to separate them in frequency. The JuanJo design has the pick-up loop on the cantilever chip. We have also designed chips for the Innsbruck and Tübingen PTB samples, as shown on the right. The idea is to have the two micro-chips in a flip-chip configuration. The distance between the two chips is set by Titanium columns/pillars (blue).

developed and performed by M. Trupke and S. Minniberger at the "Zentrum für Mikro- und Nanostrukturen (ZMNS)" of the Vienna University of Technology (TU Wien). Table 3.6 summarizes the cantilever parameters defined for the entire wafer.

We vary the mechanical frequency by varying the length of the cantilever, see Eq. (2.74). The fabrication process may create an under-etched area around the cantilever, which may also oscillate and contribute to the cantilever mode, effectively decreasing the resonance frequency. To account for this, we use finite element simulations to obtain a value for the frequency with underetching. We assume a worst-case under-etched width of $40\ \mu\text{m}$. The resulting frequencies together with analytical predictions and simulations without underetching, Eq. (2.74) are presented in Table 3.7 for the various cantilever designs. The actual frequency of the cantilevers should be somewhere in between the simulated values, depending on the actual under-etched width. Scanning electron microscope images of the fabricated samples, see Fig. 3.26, show that there is hardly an under-etched region. We therefore expect the frequencies to be close to the calculated/simulated values. All cantilevers have either a Niobium strip, Niobium loop or a Niobium flux transformer loop patterned on top. The mass of the strip or the loops has a negligible effect on the resonance frequency.

Table 3.7: Cantilever length, calculated frequency f_0 using Eq. (2.74), and simulated resonance frequency without and with using a $40\ \mu\text{m}$ under-etch width for the different setups.

Design	Length	f_0 Calc.	f_0 Sim.	f_0 Sim. (under)	m_{eff}
H-Innsbruck	$90\ \mu\text{m}$	852 kHz	827 kHz	517 kHz	1.3×10^{-11} kg
H-FluxTra	$100\ \mu\text{m}$	689 kHz	673 kHz	441 kHz	1.45×10^{-11} kg
H-JuanJo	$110\ \mu\text{m}$	570 kHz	558 kHz	379 kHz	1.6×10^{-11} kg
PTB-I (min)	$80\ \mu\text{m}$	521 kHz	511 kHz	353 kHz	1.2×10^{-11} kg
PTB-I (max)	$115\ \mu\text{m}$	1077 kHz	1041 kHz	618 kHz	1.7×10^{-11} kg
PTB-T (min)	$80\ \mu\text{m}$	521 kHz	511 kHz	353 kHz	1.2×10^{-11} kg
PTB-T (max)	$115\ \mu\text{m}$	1077 kHz	1041 kHz	618 kHz	1.7×10^{-11} kg

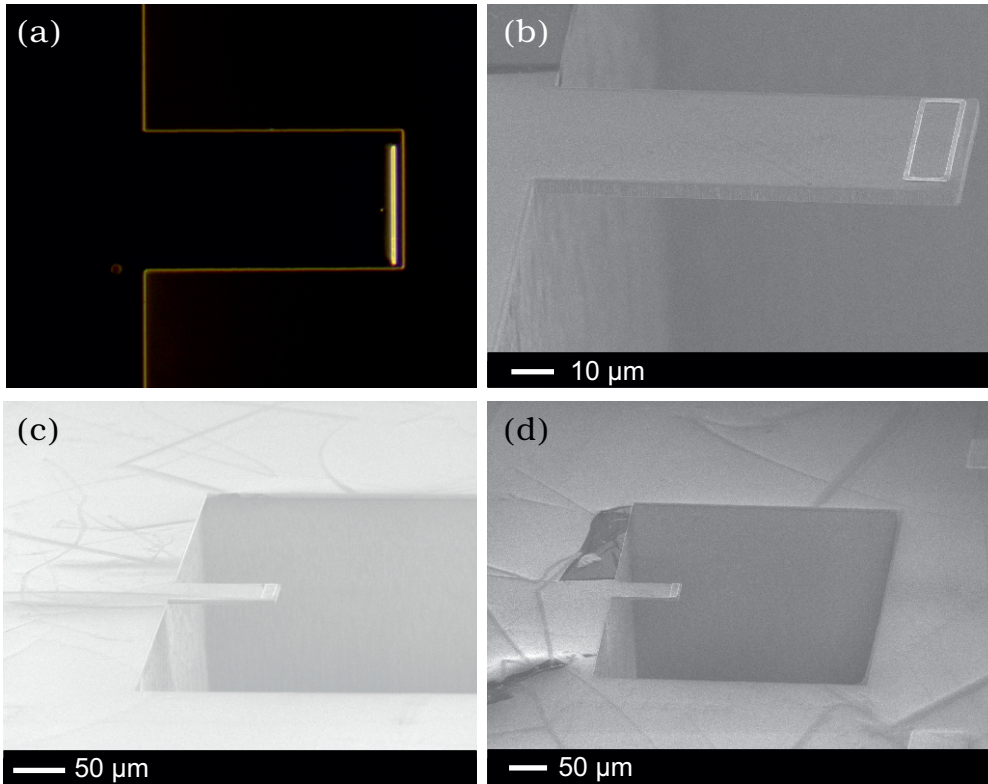


Figure 3.26: Dark field microscope image (a) and scanning electron microscope images (b), (c), (d) of Vienna fabricated cantilevers. The samples in (b)-(d) have a loop instead of a strip to account for the wider SQUID loop size in the Tübingen designs. We see on the tilted SEM pictures that the fabrication process has nearly no under-etched-regions. In (d) we see a bit of resist left-over close to the cantilever.

In addition to the fabricated cantilevers, we buy commercially available tipless AFM cantilevers¹⁵ and equip them with small micromagnets obtained by grinding NdFeB powder. We typically use particles with diameters between 5 and 30 μm .

3.4.2 Preparation and alignment

We equipped the commercial and some of the Vienna fabricated cantilevers with nanomagnets (Fe_3O_4) and micromagnets (Nd-Fe-B). The nanomagnets come in an aqueous solution and are deposited using a nebulizer (see Ref. [154] for details). In contrast, the coarser grained micromagnets (1 to 30 μm in diameter) are glued to the tip with an epoxy¹⁶. To do this, we put a small drop of epoxy on the tip where we place the magnet with a probe station. We then magnetize the magnet along the soft cantilever axis, which is the axis it deflects, by placing it in a strong magnetic field ($B \gtrsim 1T$). Figure 3.27 shows microscope images of the three cantilever variants with either a superconducting strip, deposited nanomagnets, or glued micromagnet.

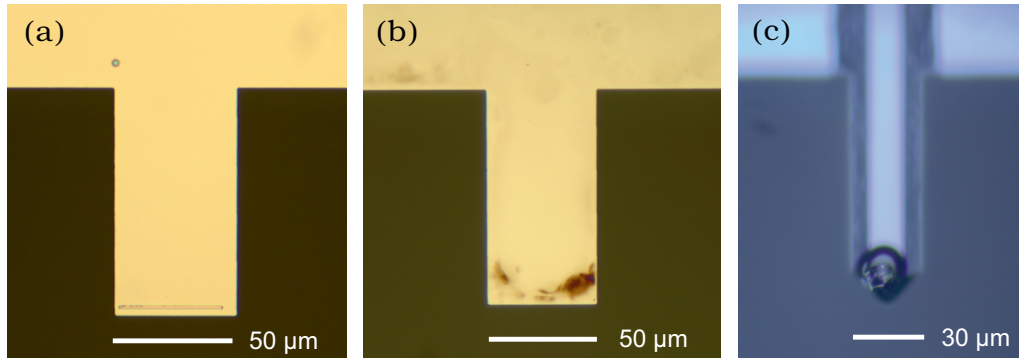


Figure 3.27: Cantilevers with superconducting strip (a), nanomagnets (b) and micromagnet (c) on the tip. (a) and (b) are Vienna fabricated cantilevers, whereas (c) is a commercial cantilever.

Once the cantilevers are prepared, we assemble the setup in a flip-chip configuration. For this, we flip the cantilever chip and align the cantilevers on top of the SQUIDs by using tweezers. We then fix the two chips with either glue¹⁷ or Copper-Beryllium springs (see Fig. 3.5). The distance between cantilever tip and SQUID chip is set either by additional pillars on the chips or by the glue in between the two chips. With the help of tweezers, an optical microscope, and some patience, we were able to achieve micrometer-level alignment, as shown in Fig. 3.28.

3.4.3 Measurements of the complete setup

With the assembled setup, we can start to look for mechanical signatures. Using deposited nanomagnets on a cantilever together with the Tübingen SQUID design did not

¹⁵<https://www.budgetsensors.com/multipurpose-afm-probe-no-tip-all-in-one-tipless>

¹⁶Henkel Loctite Stycast 1266

¹⁷GE 7031 varnish

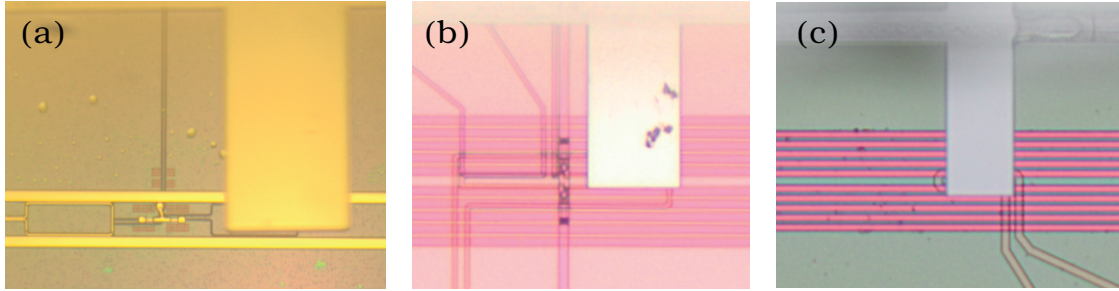


Figure 3.28: Examples of cantilever alignment for the Tübingen design (a), the HYPRES-Innsbruck design (b) and the HYPRES-JuanJo design (c). We are able to look through the etched hole in the cantilever chip, which allows us to align the cantilever on top of the SQUID loop by using tweezers.

lead to a verified mechanical signature (see M. Schmid [154]). Furthermore, we cooled down HYPRES samples equipped with superconducting-tip and micromagnet-on-tip cantilevers. Unfortunately, we were unable to apply higher currents than 12 mA for the generation of the magnetic gradient field without breaking superconductivity. At this point we are not sure what is limiting the maximum current, but it is likely due to either the $25\ \mu\text{m}$ thin Aluminum wire bonds or a problem with the microchip itself, such as the required on-chip vias for the high current line. A wire-bonded setup with multiple $50\ \mu\text{m}$ thin wire-bonds increased the current only slightly (15 mA).

We can compare the estimated signal to the noise floor of the DC-SQUIDs. For simplicity, we consider only the case of the H-Innsbruck design. The other Innsbruck designs, Tübingen designs and the FluxTra design behave very similarly. By using Eq. (2.126) we can estimate the flux change per unit displacement of the cantilever. Moreover, using the equipartition theorem, we can estimate the displacement of a thermalized harmonic oscillator by

$$\langle x^2 \rangle = \frac{k_B T}{m_{\text{eff}} \Omega^2}, \quad (3.6)$$

with the Boltzmann constant k_B , the bath temperature T , the effective mass of the harmonic oscillator m_{eff} and the mechanical resonance frequency Ω . In Fig. 3.29 we plot the noise-floor, ground state levels and estimated signal for thermal states for the complete H-Innsbruck setup. Unfortunately, we were never able to observe a mechanical signature. Moreover, we do not know what limits the maximum current for the magnetic gradient field generation. To be able to detect the ground state we would need at least a further increase of the current by a factor of 20, see Fig. 3.29, which seemed to be hopeless at that time. Since the microwave setup worked, we decided to focus on the microwave setup directly, instead of trying another generation of a DC-setup, where we would optimize the magnetic field generation. It further turned out to be beneficial to increase the width of the superconducting strip on the cantilever, for example, covering a third of the entire cantilever with superconductor. This would drastically improve the behavior in case of possible alignment errors and distance variations between SQUID chip and the cantilever.

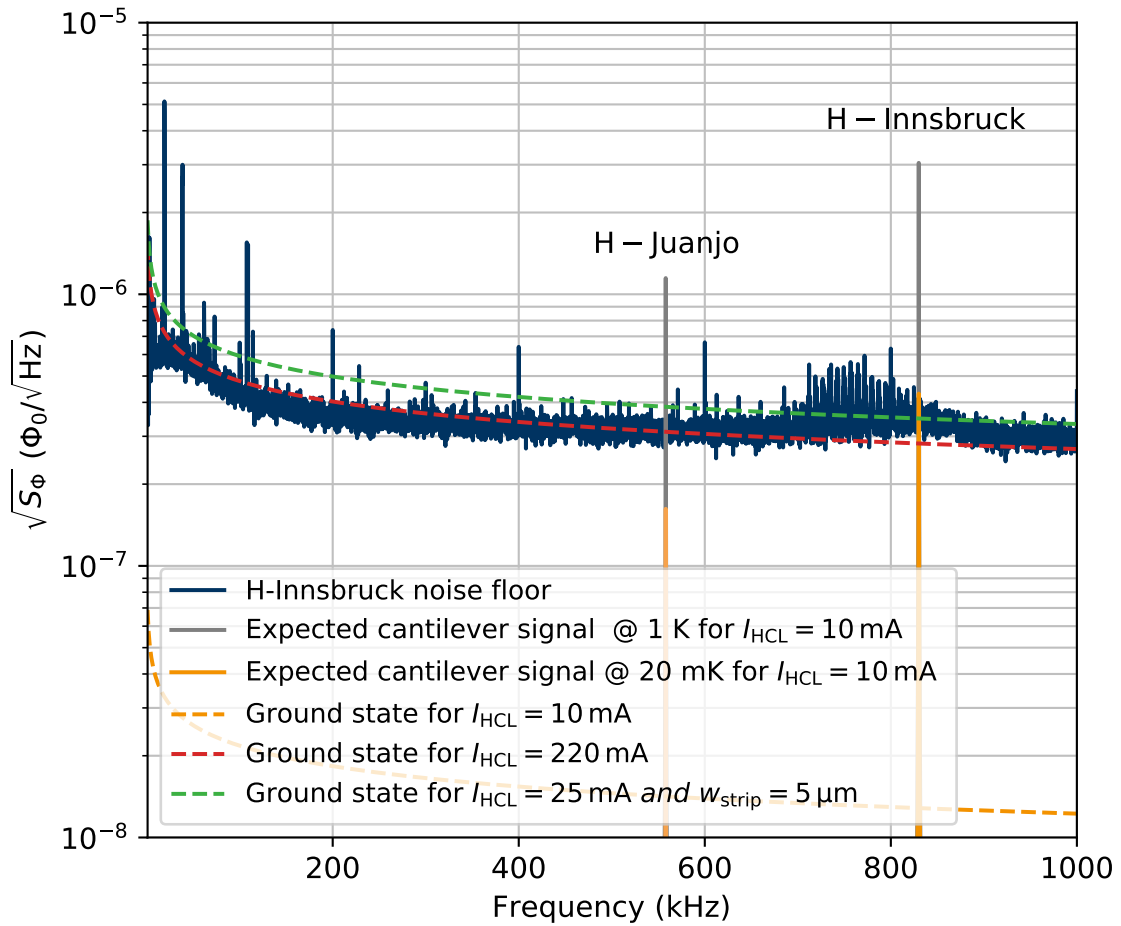


Figure 3.29: Noise floor and expected signal for the composite H-Innsbruck + cantilever setup. In blue we illustrate the noise-floor of the SQUID setup. Gray and orange solid peaks indicate the expected signal for a bath temperature of 1 K and 20 mK. Ground-state cooling would require detection down to a level of $10^{-8} \mu\Phi_0$ for 10 mA in the high current lines (orange dashed line). We would need to send 200 mA to be able to detect the ground-state with our current setup (red dashed line). The high requirements for the current can be decreased when increasing the size of the superconducting area on the cantilever (green).

Microwave setup

If we knew what we were doing, it wouldn't be called research, would it?

(Unknown, commonly attributed to Albert Einstein)

In the meantime, David Zöpfl and Mathieu Juan pushed the microwave setup and made it work by glueing a micromagnet to a commercially available cantilever and aligning this setup on top of the SQUID of a SQUID-resonator. As discussed in Sec. 2.4, this is the typical cavity-optomechanics setup, allowing control over the mechanics through the cavity. However, unlike previous setups, the single photon coupling rate could be tuned up to 3 kHz, allowing efficient cooling of the mechanics with an average of a single photon in the cavity. This work is published in Physical Review Letters [43]. In this chapter, I will discuss how to further improve the setup by an in-house fabrication of high- Q microwave resonators. The goal would be to get into the side-band resolved regime, where the cantilever frequency is higher than the loss rate of the microwave resonator, allowing cooling to the ground state. To achieve this, we tried several materials, which will be discussed in separate sections. In the first section however, I will outline the experimental setup for all characterizations. The next section, Sec. 4.2, will focus on granular Aluminum (grAl). This disordered superconductor has a high critical field [82, 179–181], and great developments from the Karlsruhe Institute of Technology showed that it can be used for quantum circuits [80, 81, 83, 182–186]. Unfortunately, the combined setup with a magnetic cantilever does not seem to work for us. We therefore attempted to fabricate in-house Niobium constriction junctions [93, 174, 176, 178, 187], discussed in Sec. 4.3. However, our fabrication capabilities limited us to too high critical currents. That's why we tried hybrid structures, consisting out of Tantalum or Niobium for the strong magnetic field regions, together with Aluminum junctions far away from the high magnetic fields, discussed in Sec. 4.4.

4.1 Experimental setup

The basic microwave setup is sketched in Fig. 4.1. A SQUID resonator can be equipped with a micromagnet cantilever chip by using glue. We use $\lambda/2$ resonators in a hairpin/U-shape to adjust the coupling to the waveguide [102–104]. The assembled sample is placed in a copper rectangular waveguide, which in turn is connected to the measurement chain via

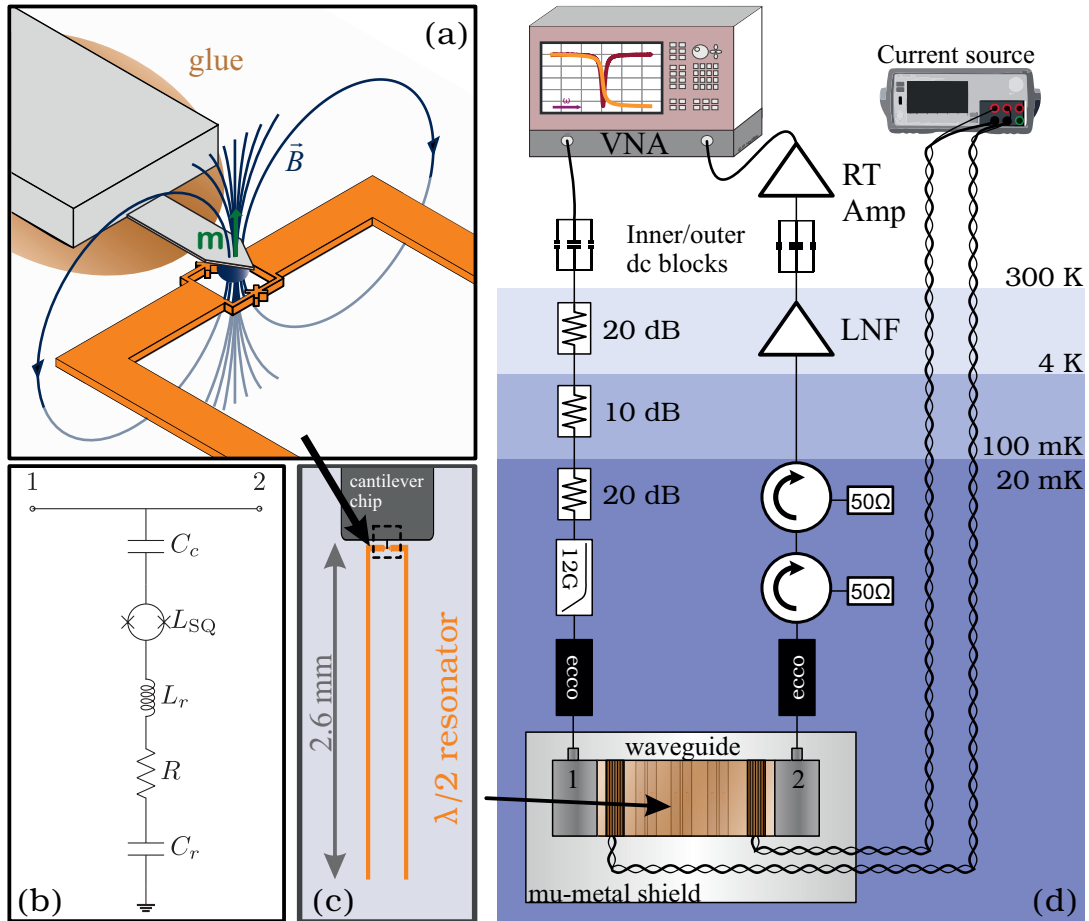


Figure 4.1: Microwave measurement setup. (a) A cantilever with a permanent magnet is glued to the SQUID resonator chip. This setup is the typical cavity optomechanics setup, where a deflection of the cantilever changes the resonance frequency of the SQUID resonators, see Sec. 2.4. (b) Circuit model of the resonator placed inside a rectangular waveguide. This is a notch type resonator configuration, in which the resonator is capacitively coupled to a transmission line (the rectangular waveguide) (c) We use $\lambda/2$ resonators in a hairpin shape, where we place the SQUID in the center, to achieve highest flux sensitivity for the first mode. (d) The prepared samples are mounted in a copper rectangular waveguide, around which we wind superconducting coils to control the flux bias point. We then use a typical Vector Network Analyzer (VNA) setup to characterize the resonators by transmission measurements. Thermalization of the resonator mode is ensured by using multiple attenuators for the input line, a 12 GHz low-pass filter, home-built eccosorb filters, and two isolators for the output line. To increase the signal-to-noise ratio we use a cryogenic amplifier along with a room temperature amplifier. We also use inner/outer dc blocks for every microwave line to avoid ground loops that would cause noise.

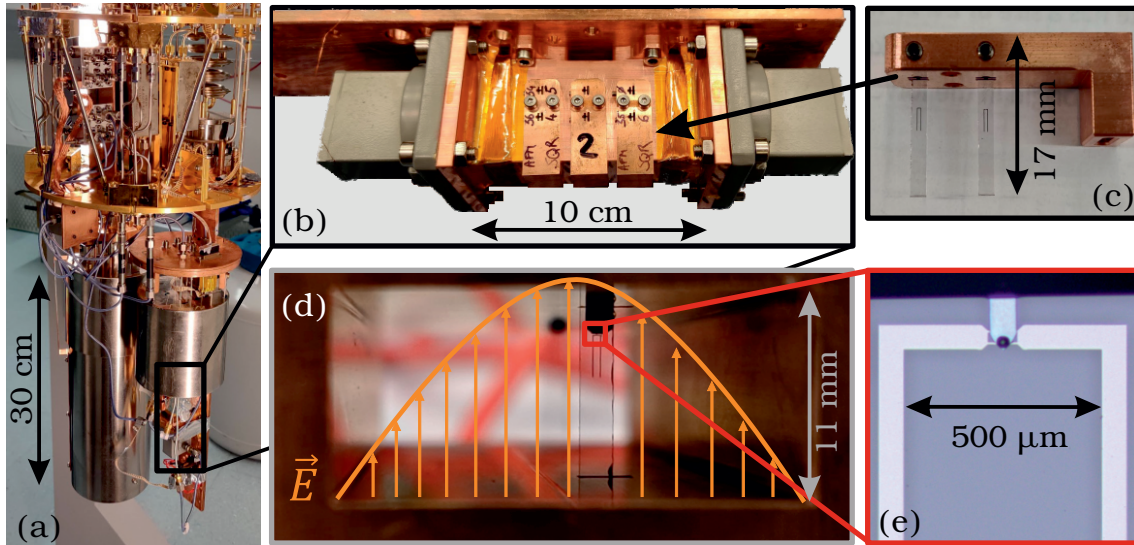


Figure 4.2: Photographs of waveguide setup. (a) The setup is placed inside mu-metal shields at the base plate of a dilution refrigerator. (b) We use commercial couplers (gray) to connect the copper rectangular waveguide to our measurement chain. The resonator and cantilever chips are glued together and attached with screws to a copper fixture (c), which we slide into the waveguide and fix by screws. (d) The electric field (orange) of the propagating waveguide mode is strongest in the center and decreases towards the walls in a cosine behavior. Hairpin shaped resonators couple to the gradient of the field. (e) Zoom into the SQUID area of the resonator. The cantilever is aligned on top of the SQUID by using tweezers and fixed with GE varnish.

commercially available waveguide couplers. To characterize the microwave resonators, we use a standard Vector Network Analyzer (VNA) setup. By measuring the complex transmission parameters through the waveguide as a function of frequency, we obtain complete information on the internal losses and the coupling, using a circlefit routine [70, 103, 188–190]. To ensure that the sample is thermalized to the bath temperature, we use a series of attenuators for the input line and two isolators for the output line. Moreover, we add a 12 GHz low-pass filter and home-built eccosorb filters to prevent infrared radiation reaching our sample. Furthermore, we increase the signal to noise ratio by using a cryogenic amplifier¹, along with an additional amplifier at room temperature. To be able to tune the SQUID resonator, we wind superconducting (NbTi) coils directly around the waveguide, and control the current through them with programmable current sources. Images of the actual setup are shown in Fig. 4.2. We fix the samples using screws inside a copper holder [Fig. 4.2(c)] and slide them into the waveguide [Fig. 4.2(d)]. The waveguide is connected to our measurement chain by coaxial cables and commercially available waveguide couplers. Furthermore, the waveguide is placed inside mu-metal to shield magnetic fields and is mounted to the mixing chamber plate of our dilution refrigerator [Fig. 4.2(a)] using several screws to ensure good thermalization.

¹Low Noise Factory

Resonator coupling A hairpin-shaped half-wave resonator couples only to the gradient of the waveguide mode, illustrated in Fig. 4.2(d): Capacitive-coupling requires a potential difference across the antenna. If we place the U-shape in the center of the waveguide, the potential at the left and right leg would be exactly the same; it would not couple to the propagating waveguide mode at all. If we move it towards a side wall, the coupling increases more and more. The same can be achieved by an asymmetry in leg length, i.e. making the right leg longer than the left leg. Thus, with help of finite element simulations, we can adjust the coupling precisely. Furthermore, we have to differentiate between energy lost in a nonradiative decay of the LC circuit (modeled by a resistor R), which we describe with a loss rate κ_{int} , and energy coupled out of the resonator (modeled by the coupling capacitance C_c), which we describe with a coupling rate κ_c . When we mount the resonator inside the rectangular waveguide, we obtain a notch-type or hanger configuration [see Fig. 4.1(b)] that allows to extract both loss rates independently. Typically, these rates are characterized in form of quality factors $Q_{\text{int}} = \omega_r / \kappa_{\text{int}}$ and $Q_c = \omega_r / \kappa_c$.

4.2 Granular Aluminium (grAl) SQUID resonators

Granular Aluminum has a huge potential as high kinetic material for quantum circuits [80, 81, 182, 183]. This material consists of Aluminum grains covered by aluminum oxide, which have dimensions around 10 nm, depending on oxidation parameters. The resulting disordered superconductor can be thought of a network of Josephson junctions [81, 191]. Moreover, early measurement demonstrated a very high critical field [179–181], which still holds for high in-plane fields of high quality microwave resonators [82]. However, this is not true for perpendicular magnetic fields due to flux trapping as we will observe in this section and as discussed in Ref. [82].

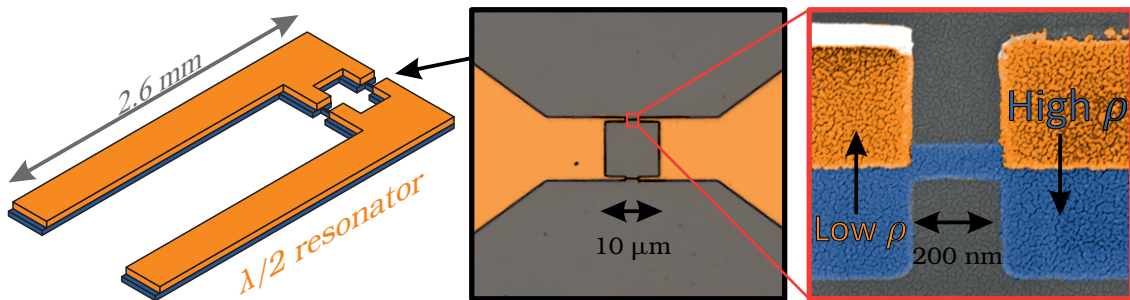


Figure 4.3: SQUID resonators using high-resistance (blue) and low-resistance (orange) grAl. We use the standard $\lambda/2$ resonator in hairpin-shape to define the coupling to the waveguide. The center shows an optical microscope image of the SQUID loop. On the right is a SEM picture of the junction area, showing that the actual Josephson junction is defined only by the high-impedance grAl. Everywhere else, the resonator is covered with low-resistance grAl.

4.2.1 Design and Fabrication

We want high sensitivity to magnetic fields around the cantilever position, but the rest of the $\lambda/2$ resonator should be insensitive, while still showing a high resilience to magnetic fields. Therefore, we use high resistivity grAl to define the Josephson junction area and shunt it everywhere else by low resistivity grAl. Figure 4.3 shows a sketch of such a resonator design, together with optical and SEM images of the SQUID and Josephson junction area. The critical current for a fixed geometry can then be approximately tuned by the resistivity of the high resistive grAl layer [81, 186]. To achieve a good flux sensitivity we have to minimize the critical current to obtain $\beta_R \ll 1, \beta_L \ll 1$, see Sec. 2.1.5. This is a hard task, as increasing the resistivity of grAl too much can lead to a purely insulating behavior [80]. Since we were not sure about the actual critical current, we designed different SQUID loops sizes to vary β_L .

Fabrication process In Fig. 4.4 we illustrate the fabrication process. It is intentionally kept very simple, which allows us to fabricate the resonators in a one-step evaporation process. We pattern the resonator and SQUID structure using electron beam lithography and a single layer of resist. The junctions are defined by a 50 nm wide and 200 nm long constriction. After developing the resist, we place the sample inside a commercial electron beam evaporator Plassys MEB 550STM². We use a mild descum to remove resist residuals

²<https://plassys.com/evaporation-hv-uhv/>

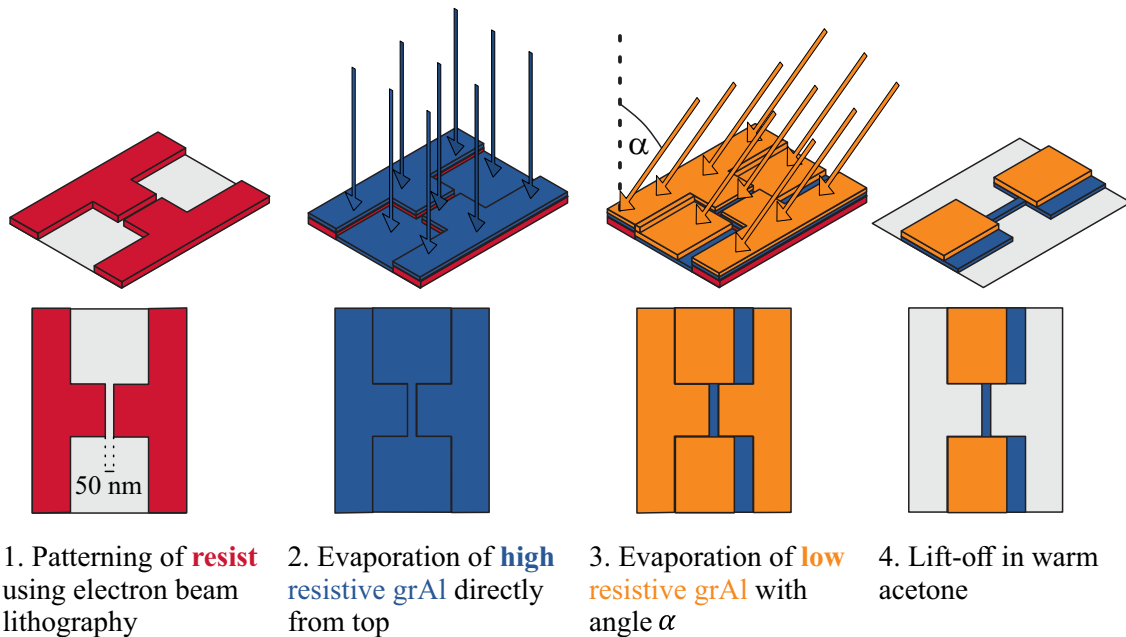


Figure 4.4: Fabrication sketch of grAl SQUID resonators. We use a minimal constriction width of 50, nm that works reliably with our electron beam lithography system. The gist is to use high resistivity grAl from the top to cover the whole resonator structure, while shunting it everywhere but the constriction using an angle for the second evaporation.

and dirt on the substrate. During a first evaporation of 20 nm Aluminum directly from top, we add a controlled high flow of 4.5 sccm oxygen to the chamber, resulting in a highly resistive grAl layer. We adapted the process from the Karlsruhe Institute of Technology with help, feedback and discussions from Lukas Grünhaupt, Patrick Winkel and Ioan Pop. Details on the calibration of the process can be found in I. Pietka Master's thesis [192]. In a second Al evaporation step (40 nm), now with angle $\alpha = 35$ deg, we reduce the oxygen flow to 3.2 sccm and therefore shunt the high resistive grAl everywhere except the constriction (where we evaporate the walls of the resist). Finally, we perform a lift-off of the resist in warm acetone.

4.2.2 Characterizations

We characterized two grAl SQUID resonators with a $10 \mu\text{m} \times 10 \mu\text{m}$ loop size (*SQR1*) and $60 \mu\text{m} \times 20 \mu\text{m}$ loop size (*SQR2*). By placing the resonators in the waveguide as discussed in Sec. 4.1, we obtain a notch-type configuration and can extract internal resonator properties using a circle-fit routine [70, 103, 189, 190, 193]. An example trace is shown in Fig. 4.5 for *SQR2* at the single-photon drive power level. The extracted parameters are summarized in Table 4.1. Both samples show internal quality factors above 10^5 , leading to total linewidths of around 130 kHz (dominated by the coupling to the waveguide). We can compare this to the frequencies of the cantilevers $\Omega/2\pi \approx 300$ kHz and see that these samples would be in the resolved sideband regime $\kappa_{\text{tot}} < \Omega$. Moreover, these samples are now completely limited by the coupling linewidth, as the internal linewidth is a factor three smaller. We can easily adjust the coupling rate by the location of the resonator inside the waveguide.

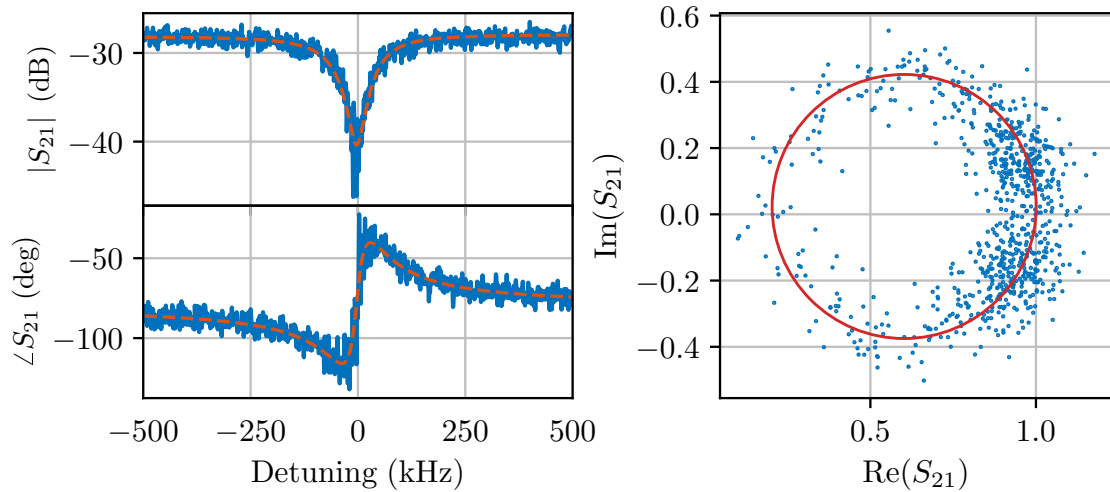


Figure 4.5: Complex data from VNA measurement for *SQR2* at the single-photon power level (blue). On the left we plot magnitude and phase as a function of frequency. The right plot is a scatter plot showing the real and imaginary part of the scattering parameter. An *LC* resonator has a linear response, leading to a circle. The prediction by the circle-fit routine for the values listed in Table 4.1 is shown as red lines. We observe excellent agreement between data and model.

Table 4.1: Single-photon power level fit results for *SQR1* and *SQR2*.

Parameter	SQR1	SQR2	Description
Q_{int}	$(1.98 \pm 0.05) \times 10^5$	$(3.1 \pm 0.1) \times 10^5$	Internal quality factor
Q_c	$(9.9 \pm 0.1) \times 10^4$	$(8.1 \pm 0.1) \times 10^4$	Coupling quality factor
f_0	8.704 GHz	8.725 GHz	Resonance frequency
$\kappa_{\text{tot}}/2\pi$	(131 ± 2) kHz	(136 ± 3) kHz	Total linewidth/loss rate
$\kappa_{\text{int}}/2\pi$	(44 ± 1) kHz	(27 ± 1) kHz	Internal loss rate

Magnetic field sensitivity We further have to check that the resonators are sensitive to magnetic fields. For this purpose, we sweep the magnetic field generated by coils around the waveguide, while for each coil current value we take a VNA trace. The resulting data can be illustrated using a color scale as shown on the left in Fig. 4.6, what is often called *fluxmap*. We observe that the resonance frequency of both resonators is changing as a function of coil current. *SQR2* shows a higher sensitivity because it has a bigger SQUID loop, as both resonators are in a similar distance to the coil. The abrupt jumps in the curve indicate hysteresis due to a high geometric inductance of the bigger loop (see Sec. 2.1.3). And indeed we observe a different behavior for increasing and decreasing currents, shown on the right in Fig. 4.6.

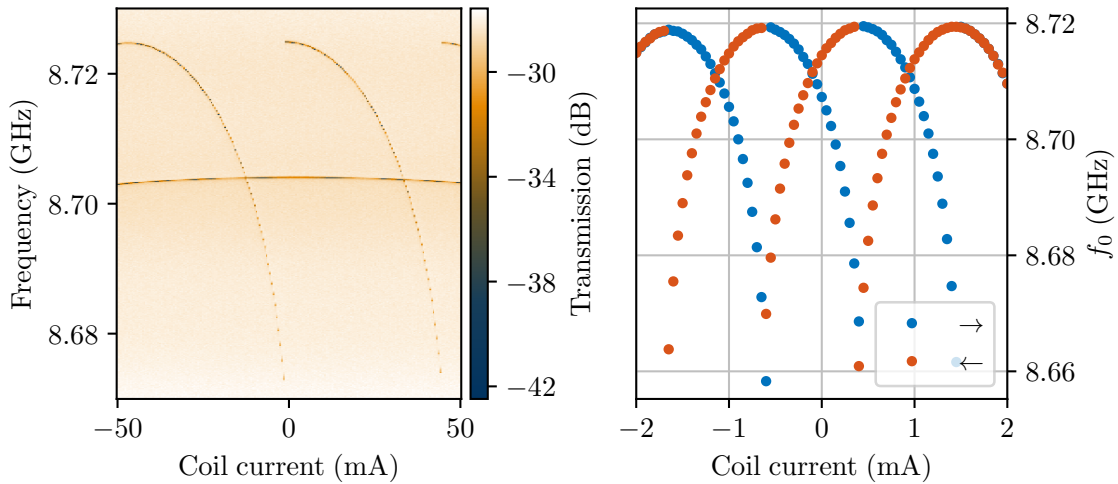


Figure 4.6: **left:** Fluxmap of the two grAl SQUID resonators. Shown are VNA traces for varied coil currents, where the transmission signal is indicated by a color scale. Dark colors mean low transmission, indicating the position of the two resonators (energy is reflected and lost in nonradiative resonator decay). *SQR2* has a bigger SQUID loop, leading to a stronger dependence on magnetic field, but also to hysteresis, which is visible as abrupt jumps. **right:** Extracted resonance frequency for *SQR2* in a second cool-down with a bigger coil. The maximum resonance frequency is slightly lower due to aging effects. We observe a different behavior for increasing (blue) and decreasing (red) currents. This hysteretic behavior is caused by the geometric self-inductance of the SQUID loop.

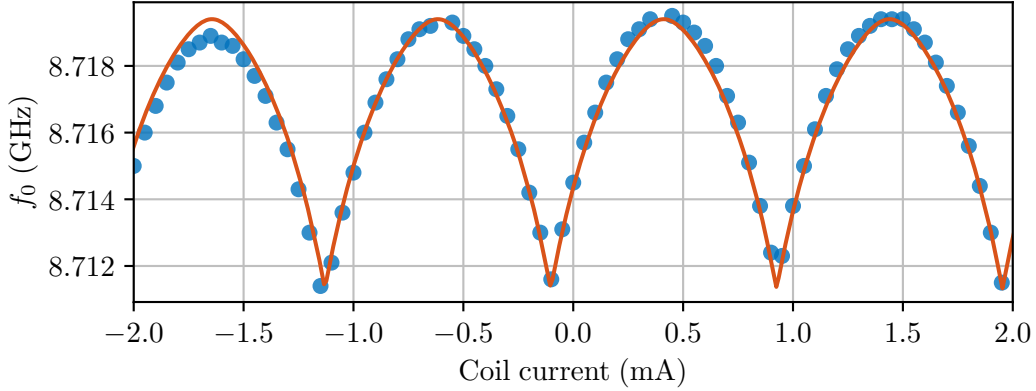


Figure 4.7: SQUID resonator fit for *SQR2*. As seen in Fig. 4.6, there can be two solutions for a given coil current. We pick the maximum since it is the stable solution. We can now fit the SQUID resonator model to the data. The resulting fit parameters are listed in Table 4.2. We observe very good agreement between model prediction and measurements.

We can extract more information about the resonator by fitting the SQUID resonator model from Sec. 2.1.5 to the measurements. Since there are two solutions for a given coil current, we only pick the higher frequency value, which is the stable solution. The resulting curve together with the prediction from a least-squares fit is shown Fig. 4.7. We fixed L_r and C_r to values obtained by finite element simulations. Table 4.2 summarizes the obtained parameters from the fit. The geometric inductance is a factor π larger than the Josephson inductance, explaining the observed hysteresis. Moreover, the linear resonator inductance is two orders of magnitude higher, explaining the low tunability. Due to the smaller SQUID loop, *SQR1* should perform better in terms of hysteresis. Unfortunately, the coil used for this cool-down was too small to achieve a single flux quantum inside the SQUID loop.

Table 4.2: Flux dependence fit

Parameter	SQR2	Description
I_{Φ_0}	1.02 mA	Coil current to change the flux by Φ_0
I_{offset}	0.4 mA	Offset current due to trapped flux.
β_L	1.03 ± 0.05	Screening parameter
β_R	235 ± 13	Resonator/Josephson junction ratio L_r/L_J
I_J	$(19 \pm 1) \mu\text{A}$	Critical current of Josephson junction
L_J	$(17 \pm 1) \text{pH}$	Josephson inductance $L_J = \hbar/2eI_J$
L_{geo}	56 pH	Geometric inductance of SQUID loop
L_r	4.0 nH	Linear resonator inductance. Obtained from HFSS
C_r	82 fF	Resonator capacitance. Obtained from HFSS

Powersweep and temperature ramp To further investigate what limits the quality factor, we conduct power sweeps and a temperature ramp. For the power sweep we take VNA traces while varying the output power and extract Q_{int} , Q_c and f_r with the circle-fit routine.

By using the definition of Q_{int} Eq. (2.62) and an equation for the absorbed power in a notch configuration [113, 194]

$$P_{\text{abs}} = P_{\text{int}} - P_{\text{refl}} - P_{\text{trans}} = \frac{2Q_{\text{tot}}^2}{Q_c Q_{\text{int}}} P_{\text{in}}, \quad (4.1)$$

we can estimate the average resonator population $\langle n_{\text{ph}} \rangle$ (stored energy in the resonator in units of photons) as

$$\langle n_{\text{ph}} \rangle = \frac{2}{\hbar\omega_0^2} \frac{Q_{\text{tot}}^2}{Q_c} P_{\text{in}}, \quad (4.2)$$

with the total quality factor $Q_{\text{tot}}^{-1} = Q_c^{-1} + Q_{\text{int}}^{-1}$, the resonator frequency $\omega_0 = 2\pi f_0$, and the input power at the resonator P_{in} . We can only approximate the latter by estimating the losses in the setup. Therefore, the photon numbers should be taken with care and can easily vary by factors 2-5. In Fig. 4.8 we show the normalized frequency shift, together with internal quality factor and coupling quality factor as a function of resonator population. For photon numbers around 1000, the resonator nonlinearity due to the Josephson junctions becomes apparent, causing the resonance frequency to shift to lower values (Kerr effect). Q_c stays constant over the power range, as expected since the coupling rate should not depend on power. Moreover, we observe that Q_{int} is only slightly increasing with increasing power. This indicates that either a lot of two level systems (too many to saturate, or they

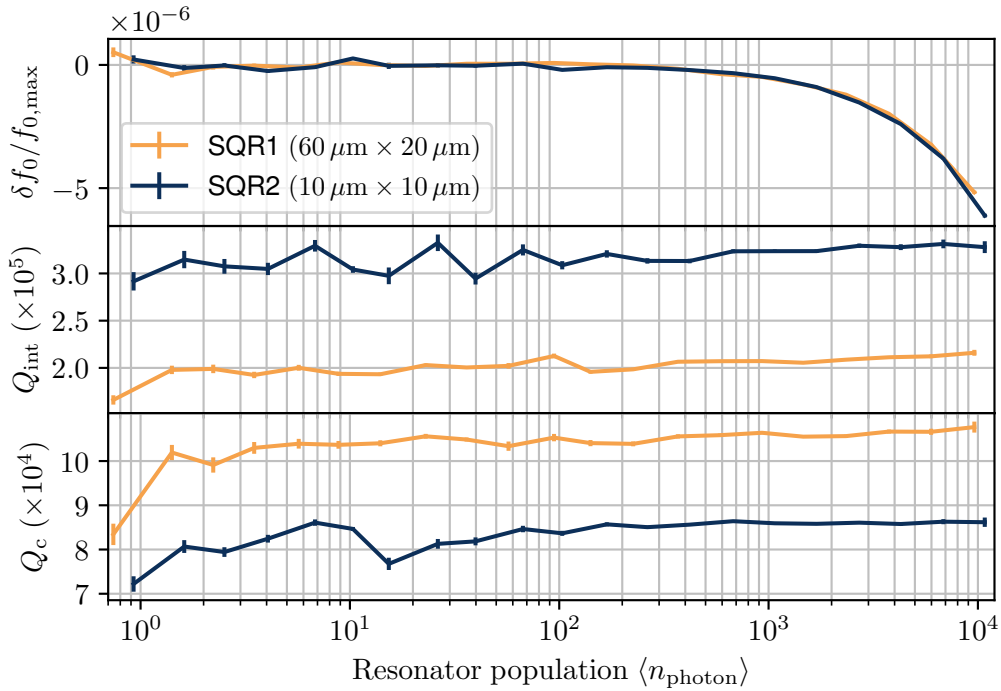


Figure 4.8: VNA power sweep for *SQR1* (orange) and *SQR2* (blue) as a function of photons in the resonator. Both resonators are nonlinear due to Josephson junctions, visible in a power dependent shift of resonance frequency (Kerr effect), visible for photon numbers higher than 1000. Q_c does not change with power as expected. Q_{int} shows no, or at most a slight increase with power. Indicating that the resonators are either limited by a lot of two level systems or another unknown loss source.

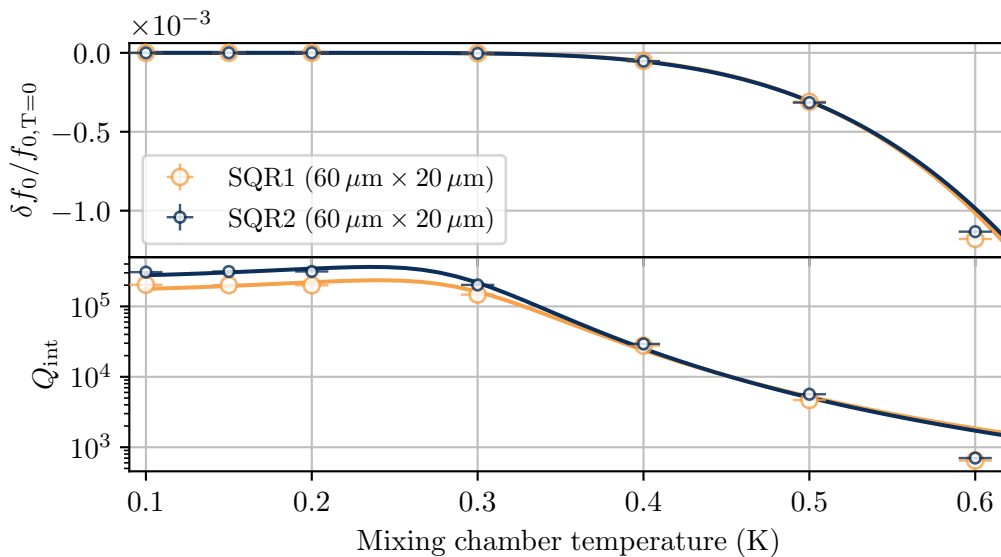


Figure 4.9: Normalized frequency shift (top) and internal quality factor (bottom) as a function of cryostat temperature, for *SQR1* (orange) and *SQR2* (blue). Measurements are indicated by dots, while the predictions of the Mattis-Bardeen and combined loss model are indicated by solid lines. We observe a decreasing resonance frequency due to a thermal quasi-particle population, leading to a higher kinetic inductance (see Sec. 2.1.1). The increased quasiparticle population leads further to more loss, visible as a lower internal quality factor. For low temperatures, the resonator is limited by another loss channel. Here we assume that the loss is arising completely from two level system.

decay too fast) are limiting us, or we have another loss channel, e.g. eddy currents in the waveguide wall [113–119, 121, 195, 196].

We further take VNA traces with a low power level for different mixing chamber temperatures. The measurement results of the normalized frequency shift and internal quality factor are shown in Fig. 4.9. We fit the frequency shift using Eq. (2.61) to extract α and Δ , summarized in Table 4.3. For Q_{int} we assume two loss channels, quasi-particles (QP) and two-level-systems (TLS)

$$Q_{\text{int}}^{-1} = Q_{\text{TLS}}^{-1} + Q_{\text{QP}}^{-1}, \quad (4.3)$$

where we use the Mattis-Bardeen *RLC* model [Eq. (2.63)] for Q_{QP} and a saturable TLS model [113, 114]

$$Q_{\text{TLS}}^{-1} = \delta_{\text{TLS}} \tanh\left(\frac{hf_0(T)}{2k_B T}\right), \quad (4.4)$$

with the TLS loss tangent δ_{TLS} . The fit results are summarized in Table 4.3. We get high values for α . This makes sense for a disordered superconductor like grAl, which has a lot of kinetic inductance. The values obtained for T_c agree well to our dc measurements of the critical current for this resistivity discussed in Ref. [192].

In summary, we could fabricate low-loss and magnetic-sensitive grAl-SQUID resonators, which are likely limited by TLS for low temperatures. The next step is to check the per-

Table 4.3: Temperature ramp fit results

Parameter	SQR1	SQR2	Description
α	0.21 ± 0.04	0.17 ± 0.03	Kinetic inductance ratio L_k/L_{tot}
Δ	$(299 \pm 7) \mu\text{eV}$	$(290 \pm 6) \mu\text{eV}$	Superconducting gap
T_c	$(1.97 \pm 0.04) \text{ K}$	$(1.92 \pm 0.04) \text{ K}$	BCS: $T_c = \Delta/1.76k_B$
δ_{TLS}	$(5.6 \pm 0.5) \times 10^{-6}$	$(3.5 \pm 0.5) \times 10^{-6}$	TLS Loss tangent $\delta_{\text{TLS}} = Q_{\text{TLS}}^{-1}$

formance of these resonators in high magnetic fields, generated by the permanent magnet of the cantilever.

4.2.3 Behavior with magnetic cantilevers

In a next step we equipped *SQR1* and *SQR2* with the two micromagnet-cantilevers shown in Fig. 4.10. The magnet on *SQR1* turned out to be much bigger and closer to the SQUID than the one for *SQR2*. Once the sample were cold, we observed a three orders of magnitude drop in quality factor for *SQR1*, shown in Fig. 4.11 and summarized in Table 4.4. This behavior is likely caused by trapped flux vortices that generate loss when moved around by the ac magnetic field of the microwave mode. Recently, KIT researchers observed the same, that the quality factor drops in a strong perpendicular magnetic field [82]. *SQR2* suffers similarly by the magnetic field, however the resonance is still visible (see Fig. 4.12). Due to the smaller magnet and the further spacing between magnet and SQUID, Q_{int} only dropped by a factor 10. However, the coupling between mechanics and microwave resonator seemed to be low, leading to the fact that we could not detect sidebands or any other mechanical characteristic in the microwave signal.

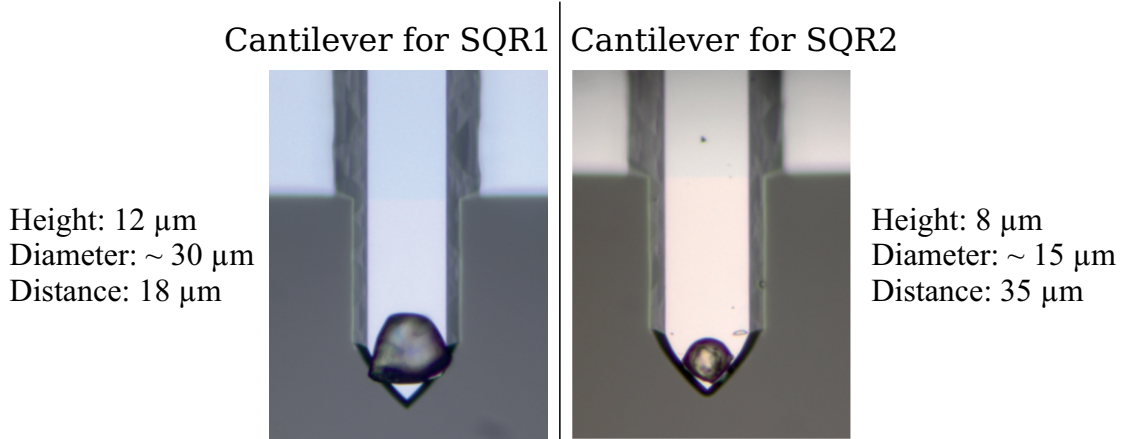


Figure 4.10: Cantilever glued micromagnets at the tip. The magnet for *SQR1* is much bigger. Moreover, when assembling the cantilever chip with the SQUID resonator chip, the cantilever for *SQR1* turned out to be much closer to the SQUID (distance between end of magnet and top of SQUID) than the one for *SQR2*.

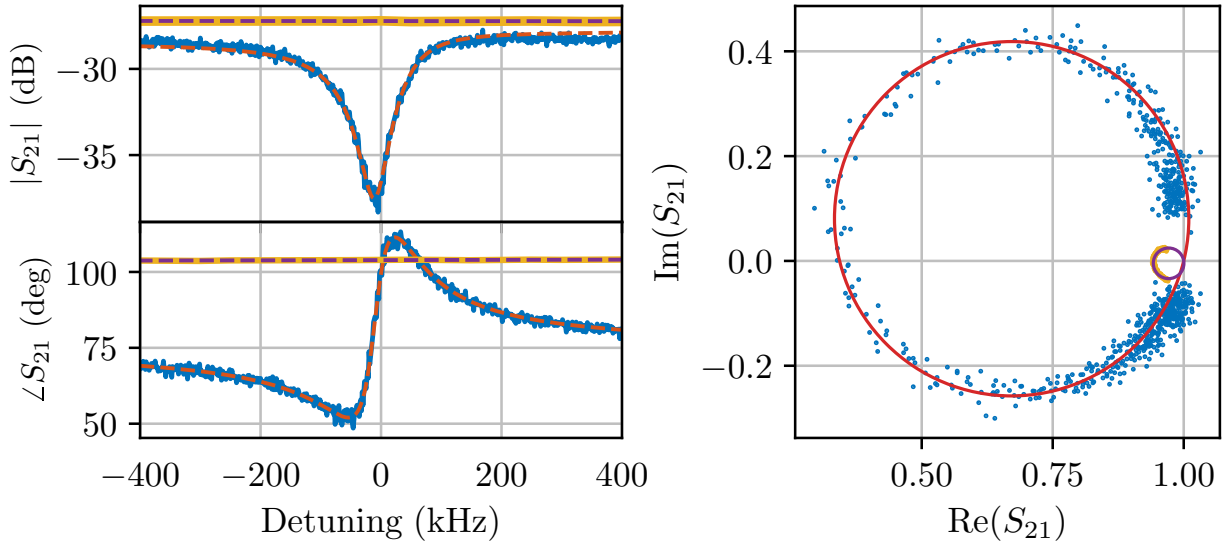


Figure 4.11: Scattering parameters for $SQR1$ without (blue) and with the cantilever (yellow). The huge magnet is causing the resonance to nearly disappear, it is only barely visible in the circle representation. In red and violet we show the prediction for the notch model with the fitted parameters summarized in Table 4.4.

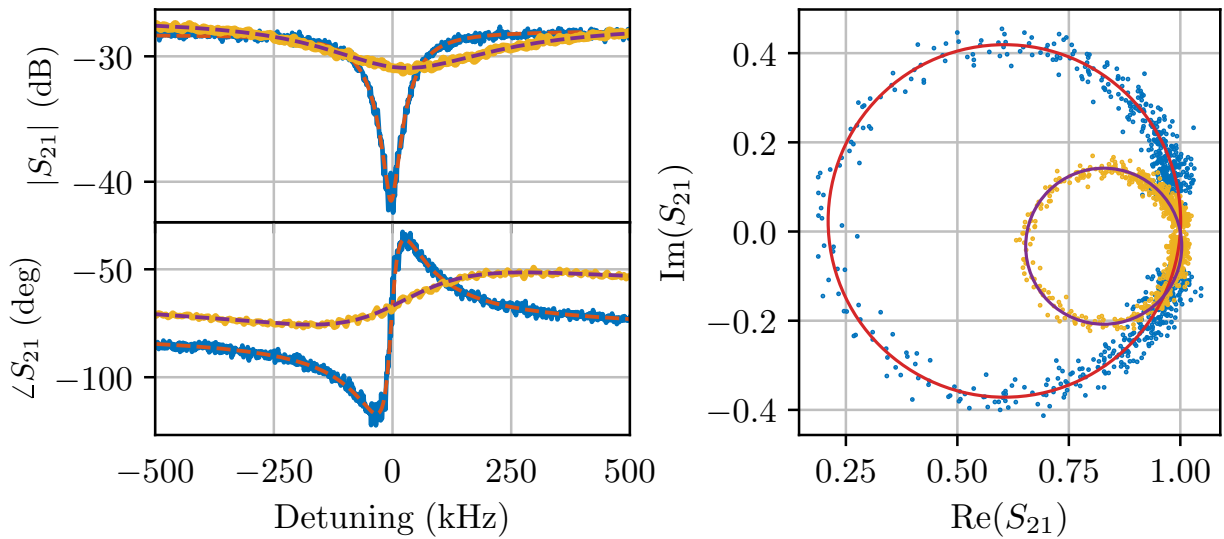


Figure 4.12: Scattering parameters for $SQR2$ without (blue) and with the cantilever (yellow). Prediction by the notch model are shown by dashed red and violet lines. In contrast to $SQR1$ we still observe a resonance feature, however the internal quality factor decreased by a factor 10.

Par.	SQR1	SQR1+Cant	SQR2	SQR2+Cant
Q_{int}	$(1.98 \pm 0.05) \times 10^5$	473 ± 15	$(3.1 \pm 0.1) \times 10^5$	$(2.4 \pm 0.02) \times 10^4$
Q_c	$(1.0 \pm 0.1) \times 10^5$	$(8.2 \pm 0.5) \times 10^3$	$(8.5 \pm 0.1) \times 10^4$	$(4.6 \pm 0.03) \times 10^4$
f_0	8.704 GHz	8.672 GHz	8.725 GHz	8.720 GHz
$\kappa_{\text{tot}}/2\pi$	(128 ± 1) kHz	(18.3 ± 0.6) MHz	(130 ± 1) kHz	(546 ± 3) kHz
$\kappa_{\text{int}}/2\pi$	(43.9 ± 0.1) kHz	(17.3 ± 0.5) MHz	(27.2 ± 0.1) kHz	(359 ± 2) kHz

Table 4.4: Single-photon power level fit results for *SQR1* and *SQR2* equipped with magnetic cantilevers.

4.2.4 Hybrid grAl SQUID resonators

Furthermore, we tried a hybrid SQUID resonator, using high-resistance grAl for the Josephson junction and shunting it everywhere else by Niobium, as shown in Fig. 4.13. The resonators behaved very similar to the pure grAl resonators. Table 4.5 summarizes the VNA characterizations at the single-photon level. In addition, we fabricated a resonator without a SQUID or any Josephson junction for comparison, which we label *NbR1*. The quality factor for the resonator without Josephson junctions is similar to those with SQUIDs, indicating that the resonator is limited by another loss channel, most likely TLS.

When equipped with magnetic cantilevers, the resonances completely disappeared. At high probe powers, one of the three resonances that disappeared reappeared. However the resonance frequency ($f_0 = 11.8$ GHz) was much higher than the design frequency (between 7.4 and 8.5 GHz). Since we had three samples with different SQUID sizes equipped with cantilevers in the same waveguide we cannot identify the sample.

The flux tunability is depicted in Fig. 4.14. All resonators have a hysteretic behavior, created by the geometric self-inductance of the SQUID loop. To decrease this effect we have to decrease the critical current of the junctions by using a narrower constriction or higher resistivity grAl. We moreover observe a strange flux dependence for *HSQR2*. There seem to be multiple Φ_0 conditions, which we could not explain.

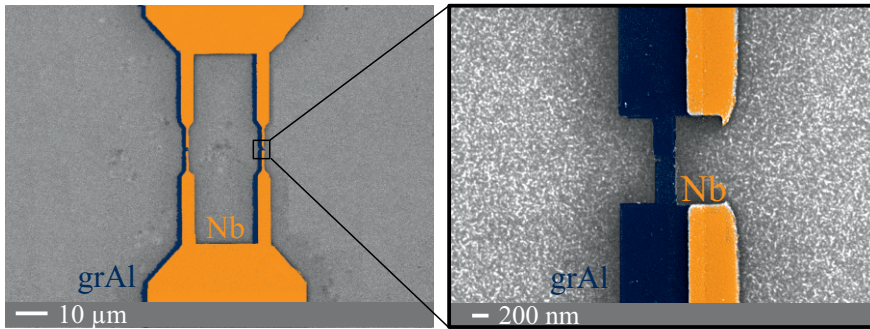


Figure 4.13: False color (blue: high resistive grAl, orange: Nb) scanning electron microscope photographs of a hybrid Nb-grAl resonators. The design is similar to the one of pure grAl resonators, however we use evaporated Nb instead of low resistive grAl for the second layer.

Sample	SQUID size ($\mu\text{m} \times \mu\text{m}$)	f_0 (GHz)	Q_{int}	Substrate	Δf_0 (MHz)
NbR1	No junctions	7.761	3.7×10^5	Sapphire	-
HSQR1	10×10	8.061	3.8×10^5	Sapphire	0*
HSQR2	60×20	8.526	1.1×10^5	Sapphire	8.3
HSQR7	10×10	8.031	1.0×10^5	Sapphire	2.1
HSQR8	60×20	8.892	3.2×10^5	Sapphire	1.2
HSQRX+C	-	11.776	1.5×10^4	Sapphire	-

Table 4.5: Characterization results for hybrid Nb-grAl resonators. *One SQUID loop arm was disconnected. The last sample was equipped by a cantilever (+C). This sample was only visible by probing with high power. The resonance frequency is much higher than expected. Since there were three samples with cantilevers in the same waveguide, we could not identify the sample.

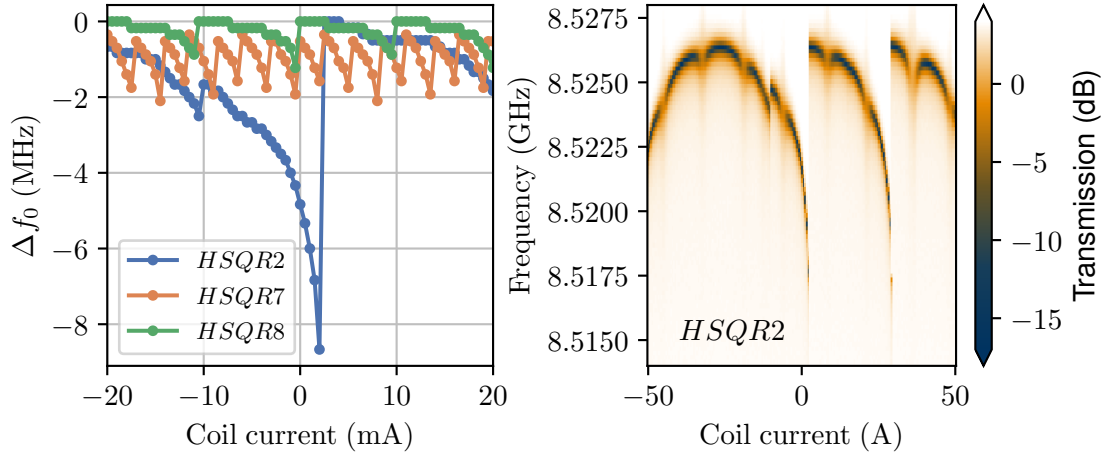


Figure 4.14: Flux tunability of hybrid Nb-grAl resonators. We observe a tunability of up to 8 MHz. All of the resonators however are hysteretic. Moreover we observe additional lobes in in the fluxmaps, shown in the right plot, which are normally caused by multiple SQUID loops.

4.3 Niobium constriction SQUID resonators

Since the setups with Niobium [43] seem to suffer less we decided to try in-house Niobium fabrication. However, we had no way to sputter dielectrics, so we could not copy the Niobium trilayer process for junctions. Instead, we tried Niobium constriction junctions [93, 174–178, 187, 197–201]. We started to try it directly in a single layer process with our electron beam lithography and decided to add eventually a focused ion beam step later.

4.3.1 Designs

The design is fairly simple. To achieve a Josephson junction like behavior, one has to constrict Niobium to a width $w_{\text{const}} \lesssim \xi$ below the coherence length of Niobium $\xi \approx 39$ nm. Unfortunately, our lithography only allows a reliable minimum width of $w_{\text{const}} \approx 50$ nm. Therefore, we expect high critical currents for the junctions. To prevent hysteresis we consequently have to decrease the SQUID loop size, which in turn decreases the coupling to the magnetic signal from the cantilever (lower area means lower picked up flux). To increase the magnetic sensitivity again, we thought about multiple designs, shown in Fig. 4.15. We tried large single SQUID loops (which will very likely be hysteretic), small SQUID loops with a flux focusing superconductor nearby (b), arrays of small SQUID loops in series (c) and (d), SQUID loops in parallel (not shown) and a grid of SQUID loops [series of parallel SQUID loops, shown in (e) and (f)]. Moreover, we observed for the working setups that the magnetic field of the cantilever reduces the critical current of the Nb/AlO_x/Nb junctions. This would help in this case further to reduce hysteretic effects and increase magnetic sensitivity.

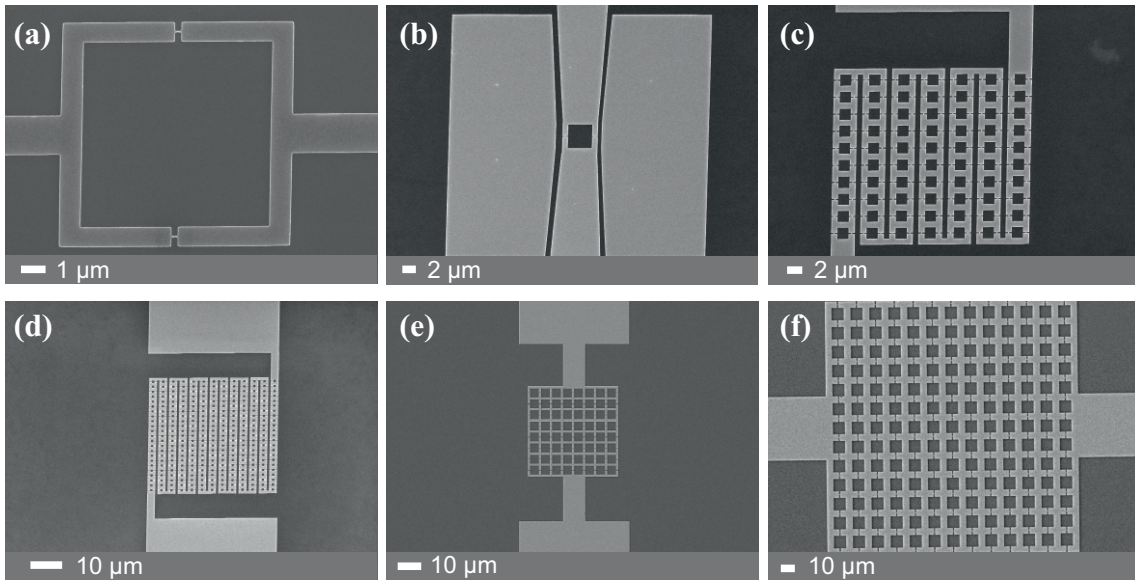


Figure 4.15: To increase the sensitivity to magnetic field changes created by the cantilever we tried various Niobium constriction SQUID resonator designs. Shown are scanning electron microscope photographs of fabricated Niobium samples. Bright areas indicate Niobium, dark areas in the background indicates the silicon substrate. (a) a large single SQUID loops, expected to be hysteretic. (b) Small SQUID loop with a flux focusing superconductor nearby. (c),(d) Array of 70, 169 small SQUID loops in series. (e), (f) Grid of SQUID loops, series connection of parallel SQUIDs.

4.3.2 Fabrication

In the beginning, we only had the possibility to evaporate Niobium in our cleanroom, a sputtering chamber was only added later. We adapted the process from Ref. [202] and modified it to match the parameters of our evaporation machine. Niobium has a very high boiling point (4744°C), which results in very hot Niobium reaching the sample when using electron beam evaporation. We observed that this leads to interactions with the resist that wash out structures and result in defective samples. Our solution was to evaporate a thin layer (10 to 20 nm) of grAl prior to Niobium evaporation. This creates a grAl hardmask that protects the resist and results in very well defined structures, as shown in Fig. 4.16.

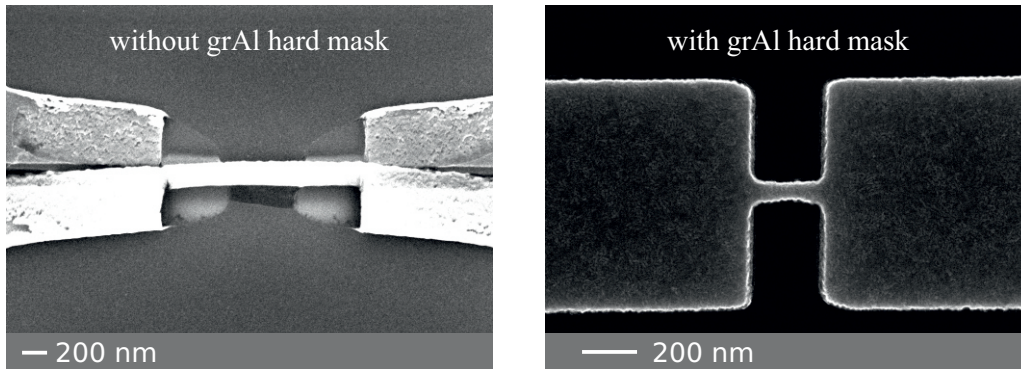


Figure 4.16: Effect of grAl hardmask on fabricated Niobium structures. Shown are scanning electron microscope photographs of the junction area for a sample without grAl hardmask and a sample with grAl hardmask. Bright is Niobium, dark in the background is silicon.

The grAl layer below the Niobium layer does not seem to have a strong impact on the losses of the resonators. We optimized the minimum reliable constriction width we could fabricate with our setup to $w_{\text{const}} = 50$ nm, limiting the critical current to around 1 mA. The main result of this section is the robust one layer Niobium lift-off process, sketched in Fig. 4.17, which allows to fabricate constriction junctions in the mA range. One can also

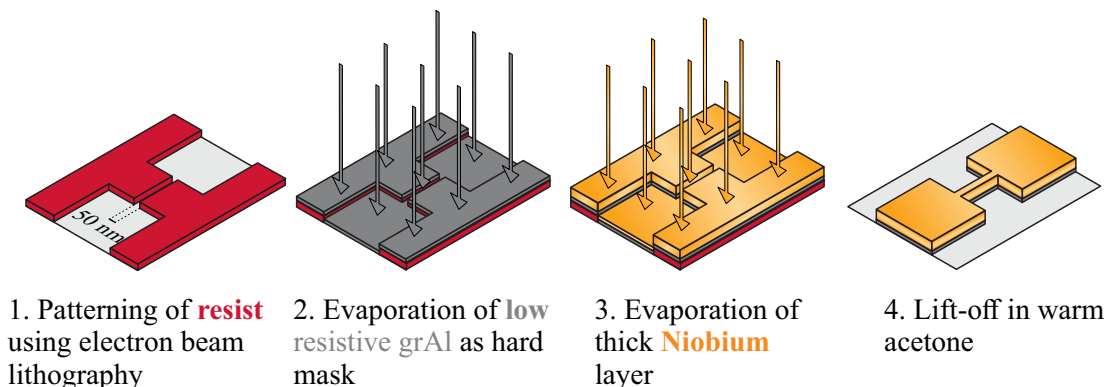


Figure 4.17: Fabrication of Niobium constriction junctions using a lift-off process.

add another layer of Al or grAl over the Niobium to prevent oxidation of the Niobium, which typically has high loss oxides, e.g. Nb_2O_5 [121].

4.3.3 Characterizations

VNA characterizations of the samples without a magnetic cantilever are summarized in Table 4.6. We observe good internal quality factors up to 5.6×10^5 . However the problem with these samples is the flux tunability/sensitivity, illustrated further in Fig. 4.18. We either get hysteretic samples if the SQUID loop is too large, or we cannot tune them far enough because we cannot generate high enough magnetic fields. Power sweeps show that the resonators behave linearly up to 10^7 photons. For higher powers we observe a frequency shift to lower frequencies (Kerr effect). The internal quality factor slowly rises, indicating that we are limited by saturable two level systems.

Table 4.6: Characterized Niobium constriction resonators without cantilevers. Types are SSQ: single SQUID, TSQ: thin single SQUID, WSQ: washer single SQUID, 70SQA: SQUID array with 70 SQUIDs in series, 300SQA: SQUID array with 300 SQUIDs, FSQ: single SQUID with focusing plane, 19×19 19 times 19 grid of SQUIDs. *One junction was open. The flux tunability of colored samples is shown in Fig. 4.18.

Sample	Type	w_{const} (nm)	SQUID size ($\mu\text{m} \times \mu\text{m}$)	f_0 (GHz)	Q_{int}	Substrate	Δf_0 (MHz)
NbC1	SSQ	50 nm	10×10	7.74	5.6×10^5	Sapphire	-
NbC2	SSQ	100 nm	10×10	8.12	5.2×10^5	Sapphire	-
NbC3	SSQ	80 nm	60×20	7.41	1.3×10^5	Sapphire	-
NbC4	SSQ	150 nm	60×20	8.32	4.5×10^5	Sapphire	-
CoNbRe3	TSQ	50 nm	20×20	7.92	1.5×10^5	Silicon	2.04
CoNbRe5	TSQ	50 nm	10×10	8.03	1.3×10^5	Silicon	0.40
CoNbRe6	WSQ	50 nm	20×20	8.68	2.0×10^5	Silicon	0.75
CoNbRe13	TSQ	50 nm	10×10	6.87	2.3×10^5	Silicon	2.96
CoNbRe15	TSQ	50 nm	20×20	6.93	4.3×10^5	Silicon	0*
CoNbSA1	70SQA	50 nm	2×2	8.42	5.6×10^4	Silicon	0.06
CoNbSA4	FSQ	50 nm	5×5	7.19	5.8×10^4	Silicon	0.02
CoNbSA6	300SQA	50 nm	1×1	7.53	6.2×10^4	Silicon	0.50
CoNbSA19	70SQA	50 nm	2×2	7.20	4.6×10^4	Silicon	0.45
CoNbG1	19×19 G	50 nm	2×2	8.752	2.9×10^5	Sapphire	0.89
CoNbG2	13×13 G	50 nm	2×2	8.668	1.7×10^5	Sapphire	0.99

4.3.4 Behavior with magnetic cantilevers

When adding a magnetic cantilever we observe again a drop in internal quality factor down to around 10 000. Table 4.7 lists the important parameters for the four samples that we equipped with a cantilever. We suspect that the loss behavior arises due to trapped vortices that are moved around by the current from the resonator mode. Unfortunately, with the

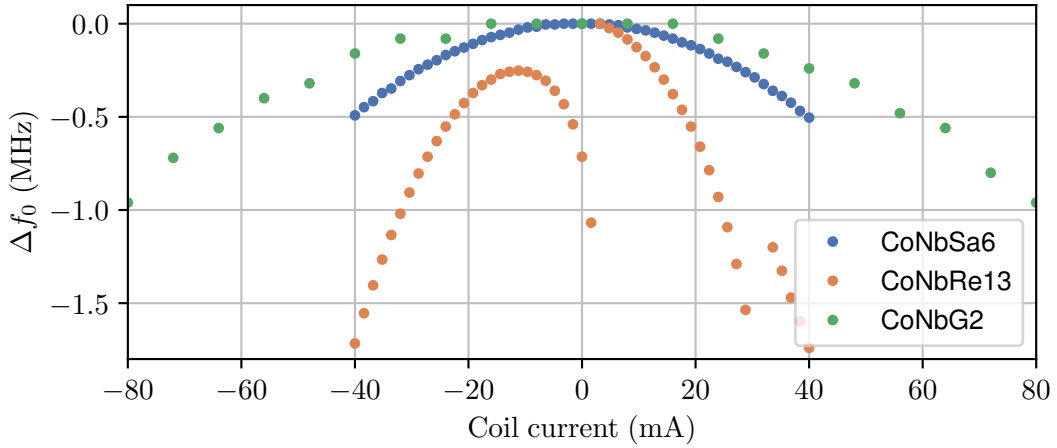


Figure 4.18: Flux tunability of selected Nb constriction resonators. Plotted is the change in resonance frequency from the maximum frequency as a function of coil current.

coil of the waveguide, we were not able to get into a more sensitive coupling range and detect a mechanical signal.

Table 4.7: Characterized Niobium constriction resonators with magnetic cantilevers.

Sample	Type	w_{const} (nm)	SQUID size ($\mu\text{m} \times \mu\text{m}$)	f_0 (GHz)	Q_{int}	Substrate	Δf_0 (MHz)
CoNbSA5+C	FSQ	50 nm	2×2	8.389	4.2×10^4	Silicon	0.5
CoNbSA16+C	SA	50 nm	1×1	7.385	4.1×10^3	Silicon	2.3
CoNbG3+C	$19 \times 19\text{G}$	50 nm	1×1	8.738	9.5×10^3	Sapphire	1.9
CoNbG4+C	$13 \times 13\text{G}$	50 nm	2×2	8.663	9.3×10^3	Sapphire	1.3

4.4 Hybrid Nb/Ta-Al SQUID resonators

We finally decided to try another hybrid approach: Use Tantalum or Niobium for the microwave resonator and SQUID loop, and use our standard Aluminum process for the Josephson junctions. This should combine the best of both worlds: highly magnetic field resilient materials together with high quality and tailored Al Josephson junctions.

4.4.1 Design

We have two main designs, shown in Fig. 4.19. On the left you can see a design with "ears". The Nb or Ta SQUID loop (red) is at the center and kept thin to pick up as few vortices as possible. The Al junctions (blue) are designed to be away from the center (top

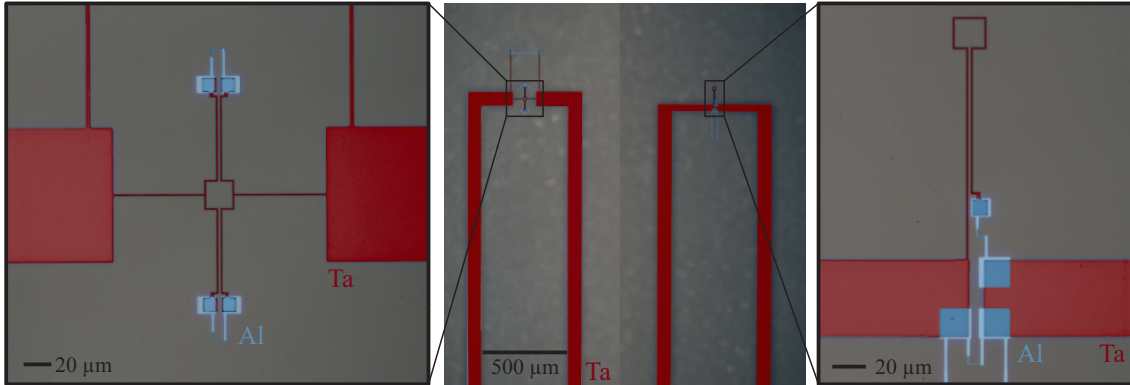


Figure 4.19: Two main hybrid Nb/Ta-Al SQUID resonator designs. In the center is a false-color (Ta/Nb:red, Al: blue) optical microscope image of the half-wave resonator. In the middle of the resonator is the SQUID loop. We decided to try two different designs: On the left is a zoom-in of the "ear" design, in which the SQUID loop has two ears going away from the high magnetic field region to the Aluminum junctions. The other design, which is illustrated on the right, has an asymmetric SQUID loop that goes further away from the resonator. The junctions are close to the resonator. Both designs comprise an Aluminum shunt to protect the junctions during the dicing process.

and bottom) where the magnet is aligned. Therefore, the Aluminum structures should be far away from the areas of high magnetic field. Another design, shown on the right in Fig. 4.19, uses an asymmetric SQUID loop with the cantilever placed above the top part of the loop. Again the SQUID loop is kept as thin as possible in the high field region to prevent vortex trapping. This is now a two-layer process, requiring two lithography steps and thus alignment with each other. To relax the alignment requirements we use larger pads to ensure a good overlap between the Nb/Ta layer and the Al layer. Because of the ears or the top loop, the SQUID loop has become larger. However, we can compensate for this by now using tailored critical current values for the Josephson junctions down to about 30 nA. Unlike our Al samples, many Ta-Al samples were shorted during dicing in our laser-cutter. We therefore added a short to prevent this for future designs and we are working on optimizing the dice process.

4.4.2 Fabrication

In a first lithography step we fabricate the resonator and SQUID loop geometries using electron beam lithography. We either use a negative mask and reactive ion etching (RIE) process to etch the Tantalum structures, or a positive mask and a lift-off process to evaporate Niobium. After that, we use our Al shadow evaporation process, developed by M. Zanner, to fabricate the Josephson junctions. The process is illustrated in Fig. 4.20. We use two layers of resist, 730 nm of a highly sensitive copolymer³, and 275 nm of a less sensi-

³MicroChem MMA-EL13

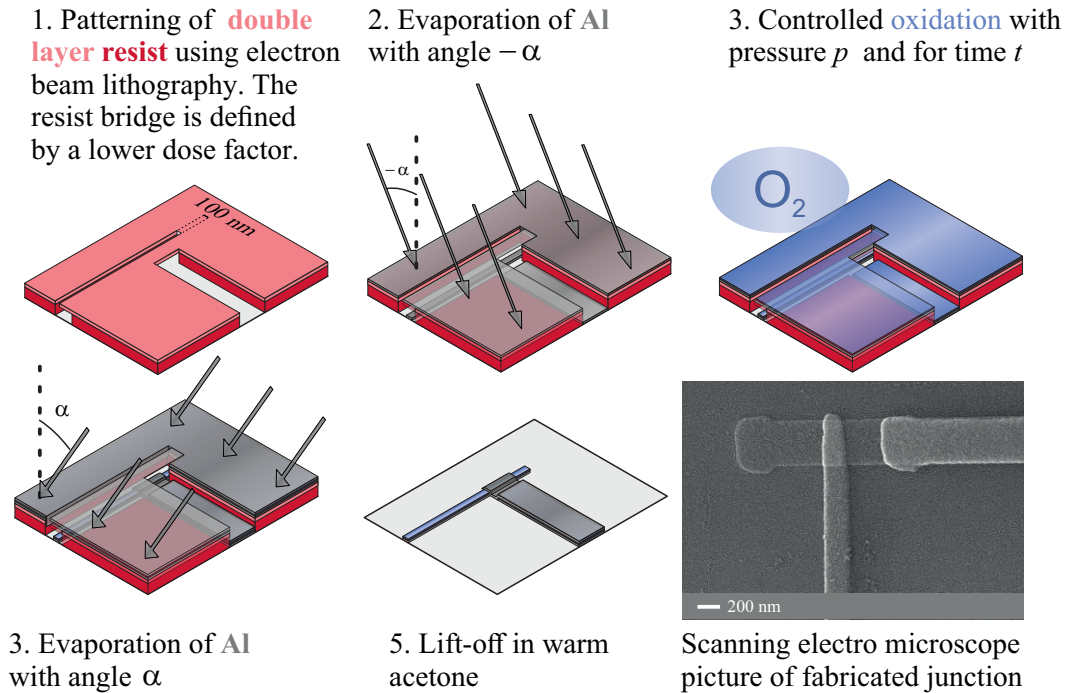


Figure 4.20: Sketch of Al junction fabrication. We use a standard double layer process to define a Dolan bridge, followed by evaporation with angle $-\alpha$, oxidation at chamber pressure P for time t , evaporation with angle $+\alpha$ and a final lift-off in warm acetone.

tive polymer⁴ on top of it. The bridge is defined by an area written with a lower dose of the electron beam lithography. Before evaporation, we use Argon milling to remove the oxide on the Nb/Ta layer to get a good contact between the layers. After that, we use two angles (typically -25° and $+25^\circ$) to evaporate Aluminum. Before the second evaporation, we add oxygen with a defined pressure and time duration into the chamber to oxidize the first Aluminum layer. This creates the insulator in between the two superconductors, which together with the area of the overlap sets the critical current of the Josephson junction. In a final step, we lift off the resist so that only the structures directly on the substrate remain. Transmon qubits [95] fabricated by this process reached coherence times above $100 \mu\text{s}$, which should be good enough for all our purposes.

4.4.3 Characterizations

We characterized two generations of Nb-Al and two generations of Ta-Al hybrid resonators. The first generation Nb resonators showed low and very power dependent quality factors of around 4000, increasing with increasing power. This was likely caused by an oxygen plasma step after Nb lift-off (meant to clean resist residuals), which we removed for the second generation. Due to limited space in the waveguide we could only characterize two samples, one Nb-Al, and one Ta-Al, two other mounted samples did not seem to work

⁴MicroChem PMMA-A4

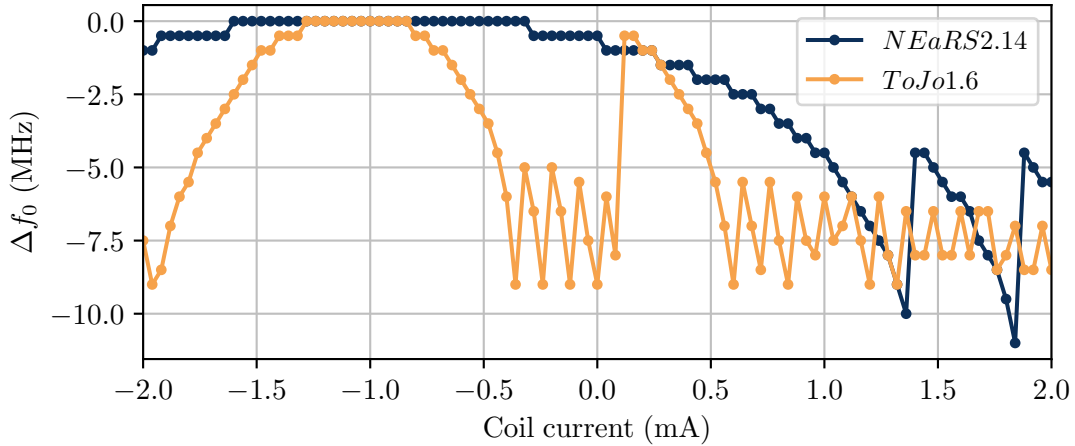


Figure 4.21: Flux tunability of Nb-Al (blue) and Ta-Al (orange) hybrid resonators. We observe a hysteretic behavior for both resonators. It further looks like we are following a flux lobe deep into the metastable regime, and observe a jump by multiple Φ_0 for ToJo1.6. The behavior can be fully explained by the model of Sec. 2.1.3 and is typical for $\beta_L > 2/\pi$.

and two further samples had cantilevers mounted on them, which will be discussed in the next section. A summary of the single-photon power level properties is listed in Table 4.8 for the two working samples. The internal quality factors are very promising. However, the flux tunability is bad and hysteretic, as shown in Fig. 4.21. The reason for this is probably a too short oxidation time for the junctions, resulting in a higher critical current as designed. Another possibility is, that the junctions got shorted and the thin wire of Aluminum acts as a constriction junction with a high critical current. The dependence further looks like we are going into multiple Φ_0 bistable states [94] for the first lobe. After that the jumps should be Φ_0 periodic. This behavior is expected for resonators with a high β_L (see Sec. 2.1.3).

Table 4.8: Summary of two Nb/Ta-Al hybrid resonators without cantilevers.

Sample	Type	SQUID size ($\mu\text{m} \times \mu\text{m}$)	f_0 (GHz)	Q_{int}	Substrate	Δf_0 (MHz)
<i>NEaRs2.14</i>	Nb-Ears	20×20 +connection	8.468	7.0×10^5	Sapphire	11
<i>ToJo1.6</i>	Ta-Ears	20×20 +connection	8.75	1.3×10^6	Sapphire	8.9

We further conducted a power sweep, shown in Figure 4.22. The sample *NEaRs2.14* behaves normally, showing a shift in resonance frequency for high powers (Kerr), while the quality factors stay constant. *ToJo1.6* instead shows fluctuations. The reason for this is that the resonator was unfortunately not biased at its flux sweet spot for the power sweep. The fluctuations are therefore a consequence of flux noise moving the resonator. When averaging outliers, we can still observe a similar behavior as for the Niobium sample. The flat Q_{int} dependence indicates that the resonator is either limited by a lot and short lived TLS that we cannot saturate, or another unknown loss channel.

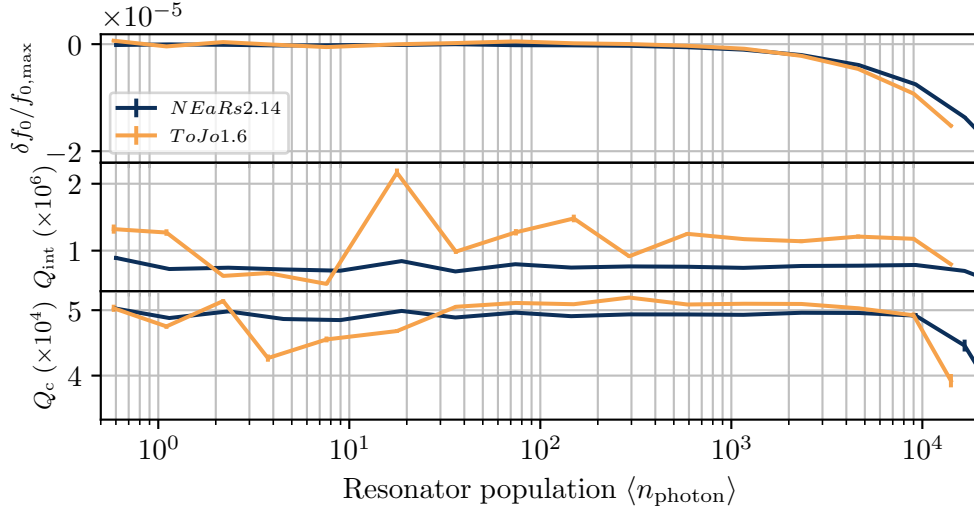


Figure 4.22: Normalized frequency shift, internal quality factor, and coupling quality factor as a function of resonator population. For high photon numbers in the resonators we observe the characteristic Kerr shift to lower frequencies. The fluctuations for *ToJo1.6* are likely caused by flux noise, as the resonator was not biased at its maximum frequency for this power sweep. The overall constant behavior of Q_{int} indicates that the resonators are either limited by a lot or very short lived TLS, which we cannot saturate, or another unknown loss source.

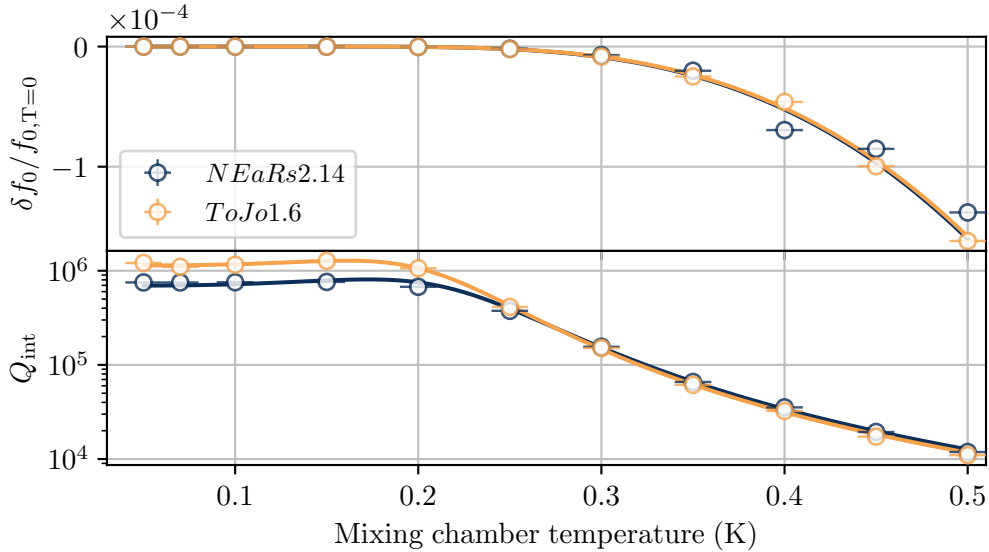


Figure 4.23: Normalized frequency shift and internal quality factor as a function of cryostat temperature. Dots indicate measurements and solid lines prediction by the Mattis-Bardeen and our loss model. Increasing temperature leads to a thermal population of quasiparticles, thus a rising kinetic inductance that shifts the resonance frequency. Moreover, the increased losses due to quasiparticle scattering decrease the quality factor. Both resonators are limited by the Al part of the resonator for high temperatures. In our model we assume that all losses at low temperatures are caused by two level systems.

Table 4.9: Temperature ramp fit results for Nb/Ta-Al hybrid resonators.

Parameter	<i>NEaRs2.14</i>	<i>TEaRsoJ1.6</i>	Description
α	$(5.6 \pm 0.9) \times 10^{-3}$	$(5.5 \pm 0.3) \times 10^{-3}$	Kinetic inductance ratio L_k/L_{tot}
Δ	$(178 \pm 5) \mu\text{eV}$	$(176 \pm 20) \mu\text{eV}$	Superconducting gap. Both samples limited by Al part ($\Delta_{\text{Al}} = 180 \mu\text{eV}$)
T_c	$(1.17 \pm 0.03) \text{ K}$	$(1.16 \pm 0.13) \text{ K}$	BCS: $T_c = \Delta/1.76k_B$
δ_{TLS}	$(1.4 \pm 0.2) \times 10^{-6}$	$(0.9 \pm 0.1) \times 10^{-6}$	TLS Loss tangent $\delta_{\text{TLS}} = Q_{\text{TLS}}^{-1}$

Finally we swept the base temperature of the dilution refrigerator to investigate the behavior with temperature. The results for the normalized frequency shift and internal quality factor are plotted in Fig. 4.23. Both resonators show a similar shift in resonance frequency and decreasing quality factor for temperatures above 200 mK. This indicates that both resonators are limited by thermal quasiparticles in the Al part of the resonator for higher temperatures. We use again Eq. (2.61) to fit the frequency shift and we use the same loss model as we used for grAl [Eq. (4.3)] to fit the internal quality factor dependence on temperature. Again, we model all the losses for low temperatures arising from TLS. The resulting parameters of the least-squares fit are summarized in Table 4.9. The extracted parameters for the gap, and therefore the critical temperature, are close to the literature values for Aluminum, $\Delta_{\text{Al}} = 180 \mu\text{eV}$, $T_c = 1.19 \text{ K}$ [58]. This shows that both samples are limited by thermal quasiparticle excitations in the Aluminum part.

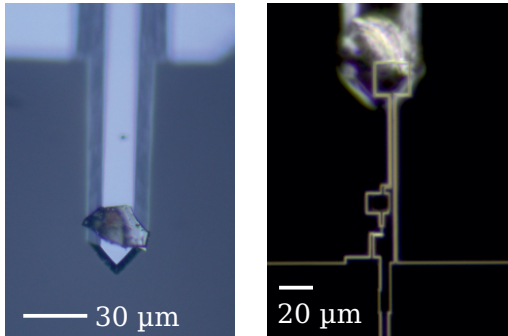
Moreover, we cooled down a second generation of Ta-Al hybrid resonators. However, we could not detect any resonances. This was likely caused by too low critical currents, shifting the resonance frequencies below the waveguide cut-off frequency. For the next generation samples, we will design the frequencies higher to have enough room for uncertainties in Junction resistance due to oxidation variations.

4.4.4 Behavior with magnetic cantilevers

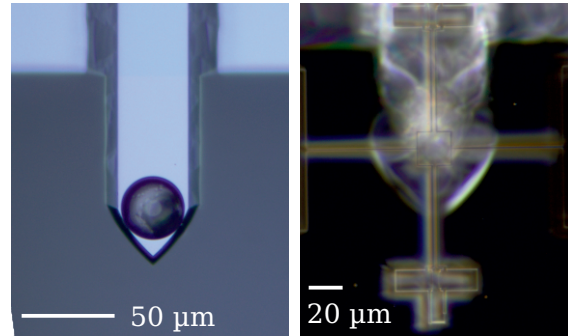
In the same cooldown we equipped two samples with magnetic cantilevers. The cantilevers with the prepared magnets, and the alignment between magnet and SQUID are shown in Fig. 4.24. Inspection of sample *Noop2.20 + C* after warming up the sample showed that the upper loop was broken. This probably happened during the assembly of the cantilever. We therefore focus on sample *ToJo1.1 + C* in this section. The summary for single-photon power level VNA characterizations of the two samples are listed in Table 4.8.

Table 4.10: Summary of two Nb/Ta-Al hybrid resonators with cantilevers. * is likely caused by a broken SQUID loop.

Sample	Type	SQUID size ($\mu\text{m} \times \mu\text{m}$)	f_0 (GHz)	Q_{int}	Substrate	Δf_0 (MHz)
<i>Noop2.20</i>	Nb-Loop	20×20 +connection	8.313	1.2×10^4	Sapphire	0*
<i>ToJo1.1</i>	Ta-Ears	20×20 +connection	9.152	3.4×10^4	Sapphire	21

Magnetic Cantilever for *Noop 2.20*

Magnet height: 7 μm
 Magnet size: 33 μm x 18 μm
 Distance: 23 μm

Magnetic Cantilever for *ToJo1.1*

Magnet height: 11 μm
 Magnet diameter: 30 μm
 Distance: 33 μm

Figure 4.24: Cantilevers with magnets for *Noop2.20* and *ToJo1.1* hybrid SQUID resonators. An optical photograph of the cantilever is shown for each sample on the left. On the right is a dark field image of the composed setup from the backside of the Sapphires resonator chip showing the alignment. The cantilever with the big magnets can be seen in the back.

Both samples show internal quality factors at least a factor 10 lower than the samples without cantilevers. Sample *ToJo1.1* shows a strong dependence on whether the pulse tube is switched on or off, when flux biased away from the sweet-spot. In Fig. 4.25 we show VNA traces for pulse tube on (PT ON) and pulse tube off (PT OFF) for *ToJo1.1 + C* at a magnetic sensitive flux bias point ($f_0 = 9.132$ GHz). We obtain values around $Q_{\text{int}} = 27\,500$ when switching off the pulse tube, which drop to 11 500 when it is switching back on. This is a first indication that we are sensitive to vibrations caused by the pulse tube head.

To check if we are coupled to the cantilever mode we use the setup from Ref. [43]. We apply a slightly blue detuned probe tone. Periodic displacements of the cantilever modulate the resonance frequency of the resonator, which becomes visible as AM-modulated sidebands of the probe tone. One can further extract the coupling strength by comparing the sideband generated by a known modulation to the mechanical sideband. This is a calibration method developed by Gorodetsky *et al.* [136]. This method requires knowledge of the average phonon number in the mechanics, and thus that the cantilever is well thermalized to the bath provided by the cryostat.

We observe sidebands that only occur when the PT is on or when we knock against the cryostat, illustrated in Fig. 4.26. However, all the resonances are very broad and we do not observe a sideband in the frequency range where we expect the first cantilever mode (between 200 kHz and 500 kHz). We therefore attribute this behavior to other mechanical modes that deflect the cantilever/magnet. For example when the two chips vibrate against each other. However, we cannot explain why we do not see the first cantilever mode.

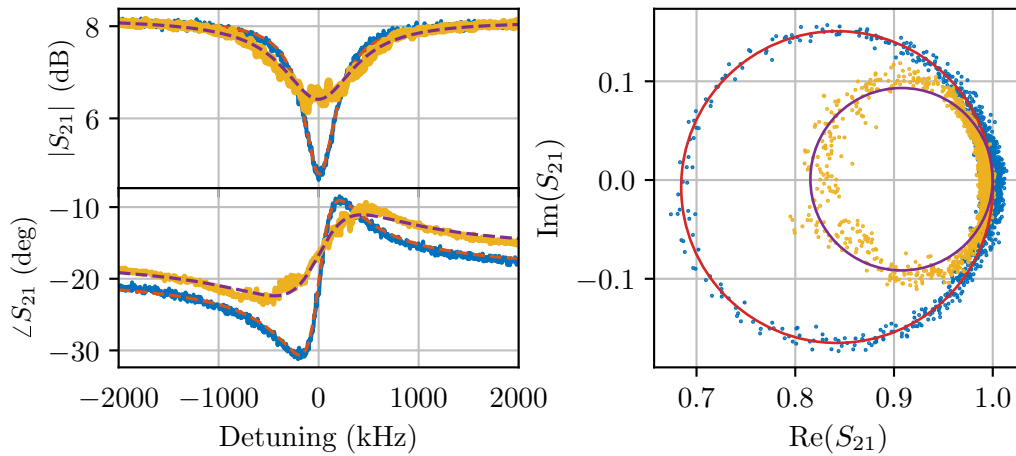


Figure 4.25: Dependence of scattering parameters for $ToJo1.1 + C$ on pulse tube cooler at a flux sensitive bias point ($f_0 = 9.132$ GHz). Blue (yellow) lines are measurements for pulse tube off (on). Red and purple show the fitted prediction by the notch model. Q_{int} decreases from 27 500 for PT off to 11 500 when switching the PT on. The circle is distorted for PT on, indicating that the resonance is pulled around by vibrations caused by the PT head.

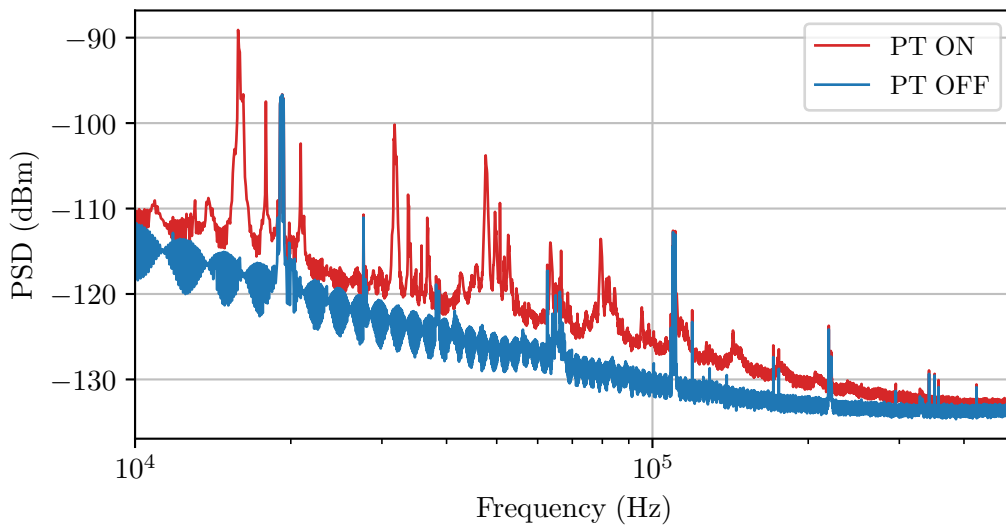


Figure 4.26: Power spectral density of $ToJo1.1 + C$ probed by a blue detuned probe tone. We observe a variety of broad peaks appearing when the pulse tube is on (PT on) or when we knock against the cryostat. However, we do not observe a signature of the cantilever mode, which is expected to be between 200 kHz and 500 kHz.

Nevertheless, we demonstrated that the Nb/Ta-Al hybrid architecture can improve the internal quality factor by at a factor of 10 compared to our current setup [43]. The internal loss rate of the microwave resonator ($\kappa/2\pi = 153$ kHz) is close to the mechanical linewidth, which opens the door to the sideband-resolved regime. I am optimistic that an improved version of the latest generation Nb/Ta-Al hybrid resonators with improved Josephson junctions and vortex-trapping features [159] will be able to achieve this.

Conclusions and Outlook

In this thesis, we have developed a new setup for coupling mechanical systems to superconducting circuits: A magnetic coupling between a cantilever and a SQUID circuit. Based on the theoretical foundations developed in Ref. [1], and the pioneering and concurring work by A. Vinante *et al.* [2–4, 129, 150], we realized the setup with the possibility of mechanical ground state detection in the dc domain, and progressed to a microwave setup. This setup has the potential of quantum state engineering of macroscopic mechanical objects, which I hope we will be able to exploit in the future.

In Chapter 2, I introduced the building blocks of the setup, superconducting circuits and a magnetic cantilever, and further discussed the coupling mechanisms between the two. We developed a model to describe the system and gain intuition how the SQUID circuit can exert a force on the cantilever. This allows further optimization of the setup and explore the full potential of this intrinsically nonlinear setup.

Chapter 3 showed the difficulties of the experimental implementation of the dc setup and the importance of a carefully designed setup and filtering. We learned that limitations of the measurement environment and fabrication may require a redesign of the setup, e.g. to adjust for current limitations. Despite the difficulties, we were able to optimize the setup and reach the intrinsic noise floor of the DC-SQUIDs, which is given by the shunt resistances. Although we did not observe a mechanical signature, with some modifications this setup could allow a continuous measurement of cantilever motion and resolve the ground state fluctuations, allowing feedback cooling to the ground state.

We switched to the microwave setup in Chapter 4 and tried several approaches to decrease the losses of half-wave SQUID resonators in magnetic fields. It turned out that the out-of-plane field created by the magnets was too strong for the granular Aluminum resonators. Another possibility for the malfunction could be that problems arose from in-field cooling of the samples. Switching to all-Niobium structures did not solve the problem because we could not sufficiently decrease the critical current for the constriction Josephson junction process. The final solution, a hybrid approach by using Tantalum or Niobium for the high field regions and fabricating Josephson junctions using Aluminum shadow evaporation, appears to be a promising approach. We have shown that these hybrid SQUID resonators are compatible with high magnetic fields and were able to observe mechanical signals. Despite the fact that we were unable to detect the first cantilever mode, I see a lot of potential in these devices. In particular, by incorporating vortex-trapping features [159] and adjusting the critical current of the Al junctions, we should be able to achieve the sideband resolved regime that enables ground state cooling.

Currently, quantum magnetomechanics is a heavily investigated area of research with major advances during the time of my PhD. In recent years, several researchers have developed a working setup in which they magnetically couple a superconducting circuit to a mechanical oscillator [4, 32, 43–46]. However, ground state cooling has not yet been demonstrated and would be a milestone towards quantum control. Currently, the lowest average phonon number $\langle n_{\text{phonon}} \rangle = 1.6$ is achieved in a four-wave mixing scheme by D. Bothner *et al.* [203]. D. Zöpfl and M. Juan currently exploit the nonlinearity of our working setup and achieve a minimal average phonon occupation of 11 phonons. Remarkably, the detection of these low phonon states is possible without the use of an additional quantum-limited amplifier, which is due to transduction gain of the SQUID resonator itself. All current setups achieve single photon coupling rates in the kHz range, rapidly advancing towards the strong single-photon coupling regime $g_0 > \kappa$, where we can efficiently engineer mechanical quantum states. Together with ground state cooling or by directly stabilizing a quantum state, as in Ref. [41], this could allow us to study the influence of gravity on quantum mechanics [204]. A promising approach for such a setup is to use levitated massive superconducting spheres [205, 206] coupled to a superconducting SQUID circuit. The large zero-point fluctuations together with the high mass of such systems could make it possible to investigate the gravitational decoherence of a quantum state - one of the greatest unknowns in our current knowledge of physics.

Bibliography

- [1] G. Via, G. Kirchmair, and O. Romero-Isart, “Strong Single-Photon Coupling in Superconducting Quantum Magnetomechanics”, *Physical Review Letters* **114**, 143602 (2015).
- [2] O. Usenko, A. Vinante, G. Wijts, and T. H. Oosterkamp, “A superconducting quantum interference device based read-out of a subattonewton force sensor operating at millikelvin temperatures”, *Applied Physics Letters* **98**, 133105 (2011).
- [3] A. Vinante and P. Falferi, “Feedback-Enhanced Parametric Squeezing of Mechanical Motion”, *Physical Review Letters* **111**, 207203 (2013).
- [4] A. Vinante, “Superconducting inductive displacement detection of a microcantilever”, *Applied Physics Letters* **105**, 032602 (2014).
- [5] E. Schrödinger, “Die gegenwärtige Situation in der Quantenmechanik”, *Naturwissenschaften* **23**, 807 (1935).
- [6] A. J. Leggett, “Testing the limits of quantum mechanics: Motivation, state of play, prospects”, *Journal of Physics: Condensed Matter* **14**, R415 (2002).
- [7] W. H. Zurek, “Decoherence, einselection, and the quantum origins of the classical”, *Reviews of Modern Physics* **75**, 715 (2003).
- [8] P. G. Merli, G. F. Missiroli, and G. Pozzi, “On the statistical aspect of electron interference phenomena”, *American Journal of Physics* **44**, 306 (1976).
- [9] C. Jönsson, “Elektroneninterferenzen an mehreren künstlich hergestellten Feinspalten”, *Zeitschrift für Physik* **161**, 454 (1961).
- [10] O. Carnal and J. Mlynek, “Young’s double-slit experiment with atoms: A simple atom interferometer”, *Physical Review Letters* **66**, 2689 (1991).
- [11] O. Nairz, M. Arndt, and A. Zeilinger, “Quantum interference experiments with large molecules”, *American Journal of Physics* **71**, 319 (2003).
- [12] Y. Y. Fein, P. Geyer, P. Zwick, F. Kiałka, S. Pedalino, M. Mayor, S. Gerlich, and M. Arndt, “Quantum superposition of molecules beyond 25 kDa”, *Nature Physics* **15**, 1242 (2019).
- [13] J. R. Friedman, V. Patel, W. Chen, S. K. Tolpygo, and J. E. Lukens, “Quantum superposition of distinct macroscopic states”, *Nature* **406**, 43 (2000).

-
- [14] O. Romero-Isart, M. L. Juan, R. Quidant, and J. I. Cirac, “Toward quantum superposition of living organisms”, *New Journal of Physics* **12**, 033015 (2010).
- [15] M. Aspelmeyer, T. J. Kippenberg, and F. Marquardt, “Cavity optomechanics”, *Reviews of Modern Physics* **86**, 1391 (2014).
- [16] M. Aspelmeyer, T. J. Kippenberg, and F. Marquardt, eds., “Cavity Optomechanics: Nano- and Micromechanical Resonators Interacting with Light” (Springer Berlin Heidelberg, Berlin, Heidelberg, 2014).
- [17] M. Rossi, D. Mason, J. Chen, Y. Tsaturyan, and A. Schliesser, “Measurement-based quantum control of mechanical motion”, *Nature* **563**, 53 (2018).
- [18] Y. Tsaturyan, A. Barg, E. S. Polzik, and A. Schliesser, “Ultracoherent nanomechanical resonators via soft clamping and dissipation dilution”, *Nature Nanotechnology* **12**, 776 (2017).
- [19] J. D. Teufel, D. Li, M. S. Allman, K. Cicak, A. J. Sirois, J. D. Whittaker, and R. W. Simmonds, “Circuit cavity electromechanics in the strong-coupling regime”, *Nature* **471**, 204 (2011).
- [20] Y. Chu, P. Kharel, T. Yoon, L. Frunzio, P. T. Rakich, and R. J. Schoelkopf, “Creation and control of multi-phonon Fock states in a bulk acoustic-wave resonator”, *Nature* **563**, 666 (2018).
- [21] M. Poot and H. S. J. van der Zant, “Mechanical systems in the quantum regime”, *Physics Reports Mechanical Systems in the Quantum Regime*, **511**, 273 (2012).
- [22] LehnertLaboratory, “MURI: Wiring Quantum Networks with Mechanical Transducers”.
- [23] A. P. Higginbotham, P. S. Burns, M. D. Urmey, R. W. Peterson, N. S. Kampel, B. M. Brubaker, G. Smith, K. W. Lehnert, and C. A. Regal, “Harnessing electro-optic correlations in an efficient mechanical converter”, *Nature Physics* **14**, 1038 (2018).
- [24] A. P. Reed, K. H. Mayer, J. D. Teufel, L. D. Burkhardt, W. Pfaff, M. Reagor, L. Sletten, X. Ma, R. J. Schoelkopf, E. Knill, and K. W. Lehnert, “Faithful conversion of propagating quantum information to mechanical motion”, *Nature Physics* **13**, 1163 (2017).
- [25] R. W. Andrews, R. W. Peterson, T. P. Purdy, K. Cicak, R. W. Simmonds, C. A. Regal, and K. W. Lehnert, “Bidirectional and efficient conversion between microwave and optical light”, *Nature Physics* **10**, 321 (2014).
- [26] T. A. Palomaki, J. W. Harlow, J. D. Teufel, R. W. Simmonds, and K. W. Lehnert, “Coherent state transfer between itinerant microwave fields and a mechanical oscillator”, *Nature* **495**, 210 (2013).

- [27] T. A. Palomaki, J. D. Teufel, R. W. Simmonds, and K. W. Lehnert, “Entangling Mechanical Motion with Microwave Fields”, *Science* **342**, 710 (2013).
- [28] C. L. Degen, F. Reinhard, and P. Cappellaro, “Quantum sensing”, *Reviews of Modern Physics* **89**, 035002 (2017).
- [29] A. A. Clerk, K. W. Lehnert, P. Bertet, J. R. Petta, and Y. Nakamura, “Hybrid quantum systems with circuit quantum electrodynamics”, *Nature Physics* **16**, 257 (2020).
- [30] Z.-L. Xiang, S. Ashhab, J. Q. You, and F. Nori, “Hybrid quantum circuits: Superconducting circuits interacting with other quantum systems”, *Reviews of Modern Physics* **85**, 623 (2013).
- [31] C. A. Regal, J. D. Teufel, and K. W. Lehnert, “Measuring nanomechanical motion with a microwave cavity interferometer”, *Nature Physics* **4**, 555 (2008).
- [32] S. Etaki, M. Poot, I. Mahboob, K. Onomitsu, H. Yamaguchi, and H. S. J. van der Zant, “Motion detection of a micromechanical resonator embedded in a d.c. SQUID”, *Nature Physics* **4**, 785 (2008).
- [33] A. Blais, A. L. Grimsmo, S. M. Girvin, and A. Wallraff, “Circuit Quantum Electrodynamics”, [arXiv:2005.12667 \[quant-ph\]](https://arxiv.org/abs/2005.12667) (2020).
- [34] M. H. Devoret and R. J. Schoelkopf, “Superconducting Circuits for Quantum Information: An Outlook”, *Science* **339**, 1169 (2013).
- [35] Y. Nakamura, Y. A. Pashkin, and J. S. Tsai, “Coherent control of macroscopic quantum states in a single-Cooper-pair box”, *Nature* **398**, 786 (1999).
- [36] M. Reagor, W. Pfaff, C. Axline, R. W. Heeres, N. Ofek, K. Sliwa, E. Holland, C. Wang, J. Blumoff, K. Chou, M. J. Hatridge, L. Frunzio, M. H. Devoret, L. Jiang, and R. J. Schoelkopf, “Quantum memory with millisecond coherence in circuit QED”, *Physical Review B* **94**, 014506 (2016).
- [37] A. Somoroff, Q. Ficheux, R. A. Mencia, H. Xiong, R. V. Kuzmin, and V. E. Manucharyan, “Millisecond coherence in a superconducting qubit”, [arXiv:2103.08578 \[cond-mat, physics:quant-ph\]](https://arxiv.org/abs/2103.08578) (2021).
- [38] P. Heidler, C. M. F. Schneider, K. Kustura, C. Gonzalez-Ballester, O. Romero-Isart, and G. Kirchmair, “Observing Non-Markovian Effects of Two-Level Systems in a Niobium Coaxial Resonator with a Single-Photon Lifetime of 10 ms”, [arXiv:2102.10016 \[cond-mat, physics:quant-ph\]](https://arxiv.org/abs/2102.10016) (2021).
- [39] J. D. Teufel, T. Donner, D. Li, J. W. Harlow, M. S. Allman, K. Cicak, A. J. Sirois, J. D. Whittaker, K. W. Lehnert, and R. W. Simmonds, “Sideband cooling of micromechanical motion to the quantum ground state”, *Nature* **475**, 359 (2011).

- [40] G. A. Peterson, S. Kotler, F. Lecocq, K. Cicak, X. Y. Jin, R. W. Simmonds, J. Aumentado, and J. D. Teufel, “Ultrastrong Parametric Coupling between a Superconducting Cavity and a Mechanical Resonator”, *Physical Review Letters* **123**, 247701 (2019).
- [41] X. Ma, J. J. Viennot, S. Kotler, J. D. Teufel, and K. W. Lehnert, “Non-classical energy squeezing of a macroscopic mechanical oscillator”, *Nature Physics*, **1** (2021).
- [42] S. Kotler, G. A. Peterson, E. Shojaei, F. Lecocq, K. Cicak, A. Kwiatkowski, S. Geller, S. Glancy, E. Knill, R. W. Simmonds, J. Aumentado, and J. D. Teufel, “Tomography of Entangled Macroscopic Mechanical Objects”, [arXiv:2004.05515 \[quant-ph\]](https://arxiv.org/abs/2004.05515) (2020).
- [43] D. Zoepfl, M. L. Juan, C. M. F. Schneider, and G. Kirchmair, “Single-Photon Cooling in Microwave Magnetomechanics”, *Physical Review Letters* **125**, 023601 (2020).
- [44] I. C. Rodrigues, D. Bothner, and G. A. Steele, “Coupling microwave photons to a mechanical resonator using quantum interference”, *Nature Communications* **10**, 5359 (2019).
- [45] P. Schmidt, M. T. Amawi, S. Pogorzalek, F. Deppe, A. Marx, R. Gross, and H. Huebl, “Sideband-resolved resonator electromechanics based on a nonlinear Josephson inductance probed on the single-photon level”, *Communications Physics* **3**, 1 (2020).
- [46] T. Bera, S. Majumder, S. K. Sahu, and V. Singh, “Large flux-mediated coupling in hybrid electromechanical system with a transmon qubit”, *Communications Physics* **4**, 1 (2021).
- [47] K. Kustura, O. Romero-Isart, and C. Gonzalez-Ballester, “Effective quantum dynamics induced by a driven two-level system bath”, [arXiv:2012.11235 \[cond-mat, physics:quant-ph\]](https://arxiv.org/abs/2012.11235) (2020).
- [48] E. I. Rosenthal, C. M. F. Schneider, M. Malnou, Z. Zhao, F. Leditzky, B. J. Chapman, W. Wustmann, X. Ma, D. A. Palken, M. F. Zanner, L. R. Vale, G. C. Hilton, J. Gao, G. Smith, G. Kirchmair, and K. W. Lehnert, “Efficient and Low-Backaction Quantum Measurement Using a Chip-Scale Detector”, *Physical Review Letters* **126**, 090503 (2021).
- [49] B. D. Josephson, “Possible new effects in superconductive tunnelling”, *Physics Letters* **1**, 251 (1962).
- [50] P. W. Anderson and J. M. Rowell, “Probable Observation of the Josephson Superconducting Tunneling Effect”, *Physical Review Letters* **10**, 230 (1963).
- [51] J. M. Martinis, M. H. Devoret, and J. Clarke, “Energy-Level Quantization in the Zero-Voltage State of a Current-Biased Josephson Junction”, *Physical Review Letters* **55**, 1543 (1985).

- [52] M. H. Devoret, J. M. Martinis, and J. Clarke, “Measurements of Macroscopic Quantum Tunneling out of the Zero-Voltage State of a Current-Biased Josephson Junction”, *Physical Review Letters* **55**, 1908 (1985).
- [53] J. M. Martinis, M. H. Devoret, and J. Clarke, “Experimental tests for the quantum behavior of a macroscopic degree of freedom: The phase difference across a Josephson junction”, *Physical Review B* **35**, 4682 (1987).
- [54] M. H. Devoret and J. M. Martinis, “Implementing Qubits with Superconducting Integrated Circuits”, *Quantum Information Processing* **3**, 163 (2004).
- [55] H. Kamerlingh Onnes, “The resistance of pure mercury at helium temperatures”, *Commun. Phys. Lab. Univ. Leiden*, b **120** (1911).
- [56] D. van Delft and P. Kes, “The discovery of superconductivity”, *Physics Today* **63**, 38 (2010).
- [57] J. Bardeen, L. N. Cooper, and J. R. Schrieffer, “Theory of Superconductivity”, *Physical Review* **108**, 1175 (1957).
- [58] R. Gross and A. Marx, “*Festkörperphysik*”, 2nd ed. (De Gruyter Oldenbourg, Berlin, Boston, 2014).
- [59] M. Tinkham, “*Introduction to Superconductivity*”, 2nd ed. (Dover Publications Inc., New York, 2004).
- [60] J. Bardeen, L. N. Cooper, and J. R. Schrieffer, “Microscopic Theory of Superconductivity”, *Physical Review* **106**, 162 (1957).
- [61] F. London, “On the Problem of the Molecular Theory of Superconductivity”, *Physical Review* **74**, 562 (1948).
- [62] R. P. Feynman, R. Leighton, and M. Sands, “*The Feynman Lectures on Physics Vol 3*” (California Institute of Technology, Berkeley, 1963).
- [63] R. Gross, “*Superconductivity and Low Temperature Physics I*” (Walther-Meißner-Institut, Garching, 2015).
- [64] P. Seidel, “*Applied Superconductivity: Handbook on Devices and Applications*” (John Wiley & Sons, 2015).
- [65] V. L. Ginzburg, L. D. Landau, M. A. Leontovich, and V. A. Fok, “J. of Exp. and Theor. Phys”, *JETP* **20**, 1064 (1950).
- [66] L. P. Gor’kov, “Microscopic derivation of the Ginzburg-Landau equations in the theory of superconductivity”, *Sov. Phys. JETP* **9**, 1364 (1959).

- [67] A. A. Abrikosov, “The magnetic properties of superconducting alloys”, *Journal of Physics and Chemistry of Solids* **2**, 199 (1957).
- [68] M. Tinkham, “Effect of Fluxoid Quantization on Transitions of Superconducting Films”, *Physical Review* **129**, 2413 (1963).
- [69] W. Y. Córdoba-Camacho, R. M. da Silva, A. A. Shanenko, A. Vagov, A. S. Vasenko, B. G. Lvov, and J. A. Aguiar, “Spontaneous pattern formation in superconducting films”, *Journal of Physics: Condensed Matter* **32**, 075403 (2019).
- [70] J. Gao, J. Zmuidzinas, A. Vayonakis, P. Day, B. Mazin, and H. Leduc, “Equivalence of the Effects on the Complex Conductivity of Superconductor due to Temperature Change and External Pair Breaking”, *Journal of Low Temperature Physics* **151**, 557 (2008).
- [71] R. Barends, J. Wenner, M. Lenander, Y. Chen, R. C. Bialczak, J. Kelly, E. Lucero, P. O’Malley, M. Mariantoni, D. Sank, H. Wang, T. C. White, Y. Yin, J. Zhao, A. N. Cleland, J. M. Martinis, and J. J. A. Baselmans, “Minimizing quasiparticle generation from stray infrared light in superconducting quantum circuits”, *Applied Physics Letters* **99**, 113507 (2011).
- [72] J. Goetz, “The Interplay of Superconducting Quantum Circuits and Propagating Microwave States”, *Ph.D. thesis*, TUM, München (2017).
- [73] D. C. Mattis and J. Bardeen, “Theory of the Anomalous Skin Effect in Normal and Superconducting Metals”, *Physical Review* **111**, 412 (1958).
- [74] P. W. Anderson, “Theory of dirty superconductors”, *Journal of Physics and Chemistry of Solids* **11**, 26 (1959).
- [75] B. T. Geilikman and V. Z. Kresin, “Kinetic and Nonsteady-state Effects in Superconductors” (J. Wiley, 1974).
- [76] B. A. Mazin, “Microwave Kinetic Inductance Detectors”, *Ph.D. thesis*, California Institute of Technology (2005).
- [77] H. Rotzinger, S. T. Skacel, M. Pfirmann, J. N. Voss, J. Münzberg, S. Probst, P. Bushuev, M. P. Weides, A. V. Ustinov, and J. E. Mooij, “Aluminium-oxide wires for superconducting high kinetic inductance circuits”, *Superconductor Science and Technology* **30**, 025002 (2016).
- [78] E. Snider, N. Dasenbrock-Gammon, R. McBride, M. Debessai, H. Vindana, K. Venkatasamy, K. V. Lawler, A. Salamat, and R. P. Dias, “Room-temperature superconductivity in a carbonaceous sulfur hydride”, *Nature* **586**, 373 (2020).
- [79] W. Martienssen and H. Warlimont, eds., “Springer Handbook of Condensed Matter and Materials Data”, Springer Handbooks (Springer-Verlag, Berlin Heidelberg, 2005).

- [80] F. Levy-Bertrand, T. Klein, T. Grenet, O. Dupré, A. Benoît, A. Bideaud, O. Bourrion, M. Calvo, A. Catalano, A. Gomez, J. Goupy, L. Grünhaupt, U. v. Luepke, N. Maleeva, F. Valenti, I. M. Pop, and A. Monfardini, “Electrodynamics of granular aluminum from superconductor to insulator: Observation of collective superconducting modes”, *Physical Review B* **99**, 094506 (2019).
- [81] N. Maleeva, L. Grünhaupt, T. Klein, F. Levy-Bertrand, O. Dupre, M. Calvo, F. Valenti, P. Winkel, F. Friedrich, W. Wernsdorfer, A. V. Ustinov, H. Rotzinger, A. Monfardini, M. V. Fistul, and I. M. Pop, “Circuit quantum electrodynamics of granular aluminum resonators”, *Nature Communications* **9**, 3889 (2018).
- [82] K. Borisov, D. Rieger, P. Winkel, F. Henriques, F. Valenti, A. Ionita, M. Wessbecher, M. Spiecker, D. Gusenkova, I. M. Pop, and W. Wernsdorfer, “Superconducting granular aluminum resonators resilient to magnetic fields up to 1 Tesla”, *Applied Physics Letters* **117**, 120502 (2020).
- [83] F. Friedrich, P. Winkel, K. Borisov, H. Seeger, C. Sürgers, I. M. Pop, and W. Wernsdorfer, “Onset of phase diffusion in high kinetic inductance granular aluminum micro-SQUIDs”, *Superconductor Science and Technology* **32**, 125008 (2019).
- [84] A. O. Caldeira, “An Introduction to Macroscopic Quantum Phenomena and Quantum Dissipation”, *Ph.D. thesis*, Cambridge University Press, Cambridge (2014).
- [85] V. E. Manucharyan, E. Boaknin, M. Metcalfe, R. Vijay, I. Siddiqi, and M. Devoret, “Microwave bifurcation of a Josephson junction: Embedding-circuit requirements”, *Physical Review B* **76**, 014524 (2007).
- [86] S. Boutin, D. M. Toyli, A. V. Venkatramani, A. W. Eddins, I. Siddiqi, and A. Blais, “Effect of Higher-Order Nonlinearities on Amplification and Squeezing in Josephson Parametric Amplifiers”, *Physical Review Applied* **8**, 054030 (2017).
- [87] J. M. Rowell, “Magnetic Field Dependence of the Josephson Tunnel Current”, *Physical Review Letters* **11**, 200 (1963).
- [88] Y. Aharonov and D. Bohm, “Significance of Electromagnetic Potentials in the Quantum Theory”, *Physical Review* **115**, 485 (1959).
- [89] J. Clarke and A. I. Braginski, “The SQUID Handbook” (Wiley-VCH, 2004).
- [90] J. Clarke and A. I. Braginski, “The SQUID handbook. Vol. 2. Applications of SQUIDs and SQUID systems” (Wiley-VCH, 2006).
- [91] C. D. Tesche and J. Clarke, “Dc SQUID: Noise and optimization”, *Journal of Low Temperature Physics* **29**, 301 (1977).
- [92] R. Gross and A. Marx, “Applied Superconductivity: Josephson Effect and Superconducting Electronics” (Walther-Meißner-Institut, Garching, 2015).

- [93] O. Kennedy, J. Burnett, J. Fenton, N. Constantino, P. Warburton, J. Morton, and E. Dupont-Ferrier, “Tunable Nb Superconducting Resonator Based on a Constriction Nano-SQUID Fabricated with a Ne Focused Ion Beam”, *Physical Review Applied* **11**, 014006 (2019).
- [94] S. T. Skacel, “Development of superconducting devices employing coherent Quantum Phase Slip”, *Ph.D. thesis*, KIT-Bibliothek, Karlsruhe (2019).
- [95] J. Koch, T. M. Yu, J. Gambetta, A. A. Houck, D. I. Schuster, J. Majer, A. Blais, M. H. Devoret, S. M. Girvin, and R. J. Schoelkopf, “Charge-insensitive qubit design derived from the Cooper pair box”, *Physical Review A* **76**, 042319 (2007).
- [96] U. Vool and M. Devoret, “Introduction to quantum electromagnetic circuits”, *International Journal of Circuit Theory and Applications* **45**, 897 (2017).
- [97] D. Gottesman, A. Kitaev, and J. Preskill, “Encoding a qubit in an oscillator”, *Physical Review A* **64**, 012310 (2001).
- [98] P. Campagne-Ibarcq, A. Eickbusch, S. Touzard, E. Zalys-Geller, N. E. Frattini, V. V. Sivak, P. Reinhold, S. Puri, S. Shankar, R. J. Schoelkopf, L. Frunzio, M. Mirrahimi, and M. H. Devoret, “Quantum error correction of a qubit encoded in grid states of an oscillator”, *Nature* **584**, 368 (2020).
- [99] R. W. Heeres, P. Reinhold, N. Ofek, L. Frunzio, L. Jiang, M. H. Devoret, and R. J. Schoelkopf, “Implementing a universal gate set on a logical qubit encoded in an oscillator”, *Nature Communications* **8**, 94 (2017).
- [100] C. R. H. McRae, H. Wang, J. Gao, M. R. Vissers, T. Brecht, A. Dunsworth, D. P. Pappas, and J. Mutus, “Materials loss measurements using superconducting microwave resonators”, *Review of Scientific Instruments* **91**, 091101 (2020).
- [101] A. Megrant, C. Neill, R. Barends, B. Chiaro, Y. Chen, L. Feigl, J. Kelly, E. Lucero, M. Mariantoni, P. J. J. O’Malley, D. Sank, A. Vainsencher, J. Wenner, T. C. White, Y. Yin, J. Zhao, C. J. Palmstrøm, J. M. Martinis, and A. N. Cleland, “Planar superconducting resonators with internal quality factors above one million”, *Applied Physics Letters* **100**, 113510 (2012).
- [102] J. Zhu and Z. Feng, “Microstrip Interdigital Hairpin Resonator With an Optimal Physical Length”, *IEEE Microwave and Wireless Components Letters* **16**, 672 (2006).
- [103] D. Zoepfl, P. R. Muppalla, C. M. F. Schneider, S. Kasemann, S. Partel, and G. Kirchmair, “Characterization of low loss microstrip resonators as a building block for circuit QED in a 3D waveguide”, *AIP Advances* **7**, 085118 (2017).
- [104] D. Zöpfl, “Characterisation of stripline resonators in a waveguide”, *Master’s Thesis*, Universität Innsbruck, Innsbruck (2017).

- [105] I. M. Pop, I. Protopopov, F. Lecocq, Z. Peng, B. Pannetier, O. Buisson, and W. Guichard, “Measurement of the effect of quantum phase slips in a Josephson junction chain”, *Nature Physics* **6**, 589 (2010).
- [106] N. A. Masluk, I. M. Pop, A. Kamal, Z. K. Mineev, and M. H. Devoret, “Microwave Characterization of Josephson Junction Arrays: Implementing a Low Loss Superinductance”, *Physical Review Letters* **109**, 137002 (2012).
- [107] Y. Krupko, V. D. Nguyen, T. Weißl, . Dumur, J. Puertas, R. Dassonneville, C. Naud, F. W. J. Hekking, D. M. Basko, O. Buisson, N. Roch, and W. Hasch-Guichard, “Kerr nonlinearity in a superconducting Josephson metamaterial”, *Physical Review B* **98**, 094516 (2018).
- [108] P. R. Muppalla, O. Gargiulo, S. I. Mirzaei, B. P. Venkatesh, M. L. Juan, L. Grünhaupt, I. M. Pop, and G. Kirchmair, “Bistability in a mesoscopic Josephson junction array resonator”, *Physical Review B* **97**, 024518 (2018).
- [109] J. Gao, “The physics of superconducting microwave resonators”, Ph.D. thesis, California Institute of Technology (2008).
- [110] R. G. Chambers and O. R. Frisch, “The anomalous skin effect”, *Proceedings of the Royal Society of London. Series A. Mathematical and Physical Sciences* **215**, 481 (1952).
- [111] C. Wang, C. Axline, Y. Y. Gao, T. Brecht, Y. Chu, L. Frunzio, M. H. Devoret, and R. J. Schoelkopf, “Surface participation and dielectric loss in superconducting qubits”, *Applied Physics Letters* **107**, 162601 (2015).
- [112] J. Wenner, R. Barends, R. C. Bialczak, Y. Chen, J. Kelly, E. Lucero, M. Mariantoni, A. Megrant, P. J. J. O’Malley, D. Sank, A. Vainsencher, H. Wang, T. C. White, Y. Yin, J. Zhao, A. N. Cleland, and J. M. Martinis, “Surface loss simulations of superconducting coplanar waveguide resonators”, *Applied Physics Letters* **99**, 113513 (2011).
- [113] A. Bruno, G. de Lange, S. Asaad, K. L. van der Enden, N. K. Langford, and L. DiCarlo, “Reducing intrinsic loss in superconducting resonators by surface treatment and deep etching of silicon substrates”, *Applied Physics Letters* **106**, 182601 (2015).
- [114] J. Goetz, F. Deppe, M. Haeberlein, F. Wulschner, C. W. Zollitsch, S. Meier, M. Fischer, P. Eder, E. Xie, K. G. Fedorov, E. P. Menzel, A. Marx, and R. Gross, “Loss mechanisms in superconducting thin film microwave resonators”, *Journal of Applied Physics* **119**, 015304 (2016).
- [115] J. M. Sage, V. Bolkhovsky, W. D. Oliver, B. Turek, and P. B. Welander, “Study of loss in superconducting coplanar waveguide resonators”, *Journal of Applied Physics* **109**, 063915 (2011).

- [116] H. Wang, M. Hofheinz, J. Wenner, M. Ansmann, R. C. Bialczak, M. Lenander, E. Lucero, M. Neeley, A. D. O’Connell, D. Sank, M. Weides, A. N. Cleland, and J. M. Martinis, “Improving the coherence time of superconducting coplanar resonators”, *Applied Physics Letters* **95**, 233508 (2009).
- [117] C. Müller, J. H. Cole, and J. Lisenfeld, “Towards understanding two-level-systems in amorphous solids: Insights from quantum circuits”, *Reports on Progress in Physics* **82**, 124501 (2019).
- [118] A. Bilmes, A. Megrant, P. Klimov, G. Weiss, J. M. Martinis, A. V. Ustinov, and J. Lisenfeld, “Resolving the positions of defects in superconducting quantum bits”, *Scientific Reports* **10**, 3090 (2020).
- [119] J. M. Martinis, K. B. Cooper, R. McDermott, M. Steffen, M. Ansmann, K. D. Osborn, K. Cicak, S. Oh, D. P. Pappas, R. W. Simmonds, and C. C. Yu, “Decoherence in Josephson Qubits from Dielectric Loss”, *Physical Review Letters* **95**, 210503 (2005).
- [120] W. A. Phillips, “Two-level states in glasses”, *Reports on Progress in Physics* **50**, 1657 (1987).
- [121] C. Kaiser, S. T. Skacel, S. Wünsch, R. Dolata, B. Mackrodt, A. Zorin, and M. Siegel, “Measurement of dielectric losses in amorphous thin films at gigahertz frequencies using superconducting resonators”, *Superconductor Science and Technology* **23**, 075008 (2010).
- [122] D. Leibfried, R. Blatt, C. Monroe, and D. Wineland, “Quantum dynamics of single trapped ions”, *Reviews of Modern Physics* **75**, 281 (2003).
- [123] D. Carney, P. C. E. Stamp, and J. M. Taylor, “Tabletop experiments for quantum gravity: A user’s manual”, *Classical and Quantum Gravity* **36**, 034001 (2019).
- [124] K. C. Schwab and M. L. Roukes, “Putting mechanics into Quantum mechanics”, *Physics Today* **58**, 36 (2005).
- [125] A. N. Cleland, “Foundations of nanomechanics: From solid-state theory to device applications”, *Advanced Texts in Physics* (Berlin ua: Springer, 2003).
- [126] J. S. Wu and T. L. Lin, “Free vibration analysis of a uniform cantilever beam with point masses by an analytical-and-numerical-combined method”, *Journal of Sound and Vibration* **136**, 201 (1990).
- [127] A. H. Ghadimi, S. A. Fedorov, N. J. Engelsen, M. J. Beryhi, R. Schilling, D. J. Wilson, and T. J. Kippenberg, “Elastic strain engineering for ultralow mechanical dissipation”, *Science* **360**, 764 (2018).
- [128] Y. Tsaturyan, A. Barg, A. Simonsen, L. G. Villanueva, S. Schmid, A. Schliesser, and E. S. Polzik, “Demonstration of suppressed phonon tunneling losses in phononic

- bandgap shielded membrane resonators for high-Q optomechanics”, *Optics Express* **22**, 6810 (2014).
- [129] A. Vinante, R. Mezzena, P. Falferi, M. Carlesso, and A. Bassi, “Improved Noninterferometric Test of Collapse Models Using Ultracold Cantilevers”, *Physical Review Letters* **119**, 110401 (2017).
- [130] A. D. Fefferman, R. O. Pohl, A. T. Zehnder, and J. M. Parpia, “Acoustic Properties of Amorphous Silica between 1 and 500 mK”, *Physical Review Letters* **100**, 195501 (2008).
- [131] R. Nawrodt, A. Zimmer, T. Koettig, C. Schwarz, D. Heinert, M. Hudl, R. Neubert, M. Thürk, S. Nietzsche, W. Vodel, P. Seidel, and A. Tünnermann, “High mechanical Q-factor measurements on silicon bulk samples”, *Journal of Physics: Conference Series* **122**, 012008 (2008).
- [132] K. Y. Fong, W. H. P. Pernice, and H. X. Tang, “Frequency and phase noise of ultrahigh Q silicon nitride nanomechanical resonators”, *Physical Review B* **85**, 161410 (2012).
- [133] A. Einstein, “Über die von der molekularkinetischen Theorie der Wärme geforderte Bewegung von in ruhenden Flüssigkeiten suspendierten Teilchen”, *Annalen der Physik* **322**, 549 (1905).
- [134] H. Nyquist, “Thermal Agitation of Electric Charge in Conductors”, *Physical Review* **32**, 110 (1928).
- [135] H. B. Callen and T. A. Welton, “Irreversibility and Generalized Noise”, *Physical Review* **83**, 34 (1951).
- [136] M. L. Gorodetsky, A. Schliesser, G. Anetsberger, S. Deleglise, and T. J. Kippenberg, “Determination of the vacuum optomechanical coupling rate using frequency noise calibration”, *Optics Express* **18**, 23236 (2010).
- [137] C. Cohen-Tannoudji, B. Diu, and F. Laloë, “Quantenmechanik”, 3rd ed., Vol. 1 (de Gruyter, Berlin, 2007).
- [138] D. J. Griffiths, “Introduction to quantum mechanics” (Prentice Hall, Inc., Upper Saddle River, New Jersey 07458, 1995).
- [139] D. A. Steck, “Quantum and atom optics” (2007).
- [140] C. Gardiner and P. Zoller, “Quantum Noise: A Handbook of Markovian and Non-Markovian Quantum Stochastic Methods with Applications to Quantum Optics”, 3rd ed., Springer Series in Synergetics (Springer-Verlag, Berlin Heidelberg, 2004).
- [141] H.-P. Breuer and F. Petruccione, “The Theory of Open Quantum Systems” (Oxford University Press, 2007).

- [142] A. D. O’Connell, M. Hofheinz, M. Ansmann, R. C. Bialczak, M. Lenander, E. Lucero, M. Neeley, D. Sank, H. Wang, M. Weides, J. Wenner, J. M. Martinis, and a. N. Cleland, “Quantum ground state and single-phonon control of a mechanical resonator.”, *Nature* **464**, 697 (2010).
- [143] Y. Chu, P. Kharel, W. H. Renninger, L. D. Burkhardt, L. Frunzio, P. T. Rakich, and R. J. Schoelkopf, “Quantum acoustics with superconducting qubits”, *Science* **358**, 199 (2017).
- [144] J. J. Viennot, X. Ma, and K. W. Lehnert, “Phonon-Number-Sensitive Electromechanics”, *Physical Review Letters* **121**, 183601 (2018).
- [145] L. R. Sletten, B. A. Moores, J. J. Viennot, and K. W. Lehnert, “Resolving Phonon Fock States in a Multimode Cavity with a Double-Slit Qubit”, *Physical Review X* **9**, 021056 (2019).
- [146] P. Arrangoiz-Arriola, E. A. Wollack, Z. Wang, M. Pechal, W. Jiang, T. P. McKenna, J. D. Witmer, R. V. Laer, and A. H. Safavi-Naeini, “Resolving the energy levels of a nanomechanical oscillator”, *Nature* **571**, 537 (2019).
- [147] J. Eschner, G. Morigi, F. Schmidt-Kaler, and R. Blatt, “Laser cooling of trapped ions”, *JOSA B* **20**, 1003 (2003).
- [148] D. J. Wineland and W. M. Itano, “Laser Cooling”, *Physics Today* **40**, 34 (1987).
- [149] C. Monroe, D. M. Meekhof, B. E. King, S. R. Jefferts, W. M. Itano, D. J. Wineland, and P. Gould, “Resolved-Sideband Raman Cooling of a Bound Atom to the 3D Zero-Point Energy”, *Physical Review Letters* **75**, 4011 (1995).
- [150] A. Vinante, M. Bahrani, A. Bassi, O. Usenko, G. Wijts, and T. H. Oosterkamp, “Upper Bounds on Spontaneous Wave-Function Collapse Models Using Millikelvin-Cooled Nanocantilevers”, *Physical Review Letters* **116**, 090402 (2016).
- [151] M. P. Blencowe and E. Buks, “Quantum analysis of a linear dc SQUID mechanical displacement detector”, *Physical Review B* **76**, 014511 (2007).
- [152] P. D. Nation, M. P. Blencowe, and E. Buks, “Quantum analysis of a nonlinear microwave cavity-embedded dc SQUID displacement detector”, *Physical Review B* **78**, 104516 (2008).
- [153] M. Poot, S. Etaki, I. Mahboob, K. Onomitsu, H. Yamaguchi, Y. M. Blanter, and H. S. J. van der Zant, “Tunable Backaction of a DC SQUID on an Integrated Micromechanical Resonator”, *Physical Review Letters* **105**, 207203 (2010).
- [154] M. Schmid, “DC SQUID based detection of a micromechanical oscillator”, *Master’s Thesis*, University of Innsbruck, Innsbruck (2018).

- [155] C. Song, “Microwave Properties of Vortices in Superconducting Resonators”, PhD Thesis, Syracuse University, Syracuse (2011).
- [156] C. Song, T. W. Heitmann, M. P. DeFeo, K. Yu, R. McDermott, M. Neeley, J. M. Martinis, and B. L. T. Plourde, “Microwave response of vortices in superconducting thin films of Re and Al”, *Physical Review B* **79**, 174512 (2009).
- [157] C. Song, M. P. DeFeo, K. Yu, and B. L. T. Plourde, “Reducing microwave loss in superconducting resonators due to trapped vortices”, *Applied Physics Letters* **95**, 232501 (2009).
- [158] S. Kwon, A. Fadavi Roudsari, O. W. B. Benningshof, Y.-C. Tang, H. R. Mohebbi, I. A. J. Taminiou, D. Langenberg, S. Lee, G. Nichols, D. G. Cory, and G.-X. Miao, “Magnetic field dependent microwave losses in superconducting niobium microstrip resonators”, *Journal of Applied Physics* **124**, 033903 (2018).
- [159] J. Kroll, F. Borsoi, K. van der Enden, W. Uilhoorn, D. de Jong, M. Quintero-Pérez, D. van Woerkom, A. Bruno, S. Plissard, D. Car, E. Bakkers, M. Cassidy, and L. Kouwenhoven, “Magnetic-Field-Resilient Superconducting Coplanar-Waveguide Resonators for Hybrid Circuit Quantum Electrodynamics Experiments”, *Physical Review Applied* **11**, 064053 (2019).
- [160] D. Bothner, D. Wiedmaier, B. Ferdinand, R. Kleiner, and D. Koelle, “Improving Superconducting Resonators in Magnetic Fields by Reduced Field Focussing and Engineered Flux Screening”, *Physical Review Applied* **8**, 034025 (2017).
- [161] J. D. Jackson, K. Muller, C. Witte, and M. Diestelhorst, “Klassische Elektrodynamik”, De Gruyter Studium (De Gruyter, 2014).
- [162] H. H. Zappe and B. S. Landman, “Analysis of resonance phenomena in Josephson interferometer devices”, *Journal of Applied Physics* **49**, 344 (1978).
- [163] P. Guéret, “A simple theory of resonance amplitudes in Josephson interferometers”, *Applied Physics Letters* **35**, 889 (1979).
- [164] D. B. Tuckerman and J. H. Magerlein, “Resonances in symmetric Josephson interferometers”, *Applied Physics Letters* **37**, 241 (1980).
- [165] G. Paternò, A. M. Cucolo, and G. Modestino, “Resonant modes in Nb baselayer interferometers with two Josephson junctions”, *Journal of Applied Physics* **57**, 1680 (1985).
- [166] J. Prat-Camps, “Shaping magnetic fields with superconductor-metamaterial hybrids”, PhD Thesis, Unversitat Autònoma de Barcelona, Barcelona (2015).
- [167] J. W. Ekin, “Experimental techniques for low-temperature measurements: Cryostat design, material properties, and superconductor critical-current testing” (Oxford University Press, Oxford ; New York, 2006).

- [168] E. Hazen, “Cryostat Instrumentation Cabling Grounding and Shielding” (2008).
- [169] J. Jaroszynski, “(unwanted) Noise suppression at the NHMFL” (2019).
- [170] D. Gandolfi, M. Niedermayr, M. Kumph, M. Brownutt, and R. Blatt, “Compact radio-frequency resonator for cryogenic ion traps”, *Review of Scientific Instruments* **83**, 084705 (2012).
- [171] F. Mueller, R. N. Schouten, M. Brauns, T. Gang, W. H. Lim, N. S. Lai, A. S. Dzurak, W. G. van der Wiel, and F. A. Zwanenburg, “Printed circuit board metal powder filters for low electron temperatures”, *Review of Scientific Instruments* **84**, 044706 (2013).
- [172] K. K. Likharev and V. K. Semenov, “Fluctuation Spectrum in Superconducting Point Junctions”, *Soviet Journal of Experimental and Theoretical Physics Letters* **15**, 442 (1972).
- [173] R. H. Koch, D. J. Van Harlingen, and J. Clarke, “Quantum-Noise Theory for the Resistively Shunted Josephson Junction”, *Physical Review Letters* **45**, 2132 (1980).
- [174] N. Antler, “Superconducting Nanobridge SQUID Magnetometers for Spin Sensing”, *Ph.D. thesis*, University of California, Berkeley, Berkeley (2014).
- [175] K. Hasselbach, D. Maily, and J. R. Kirtley, “Micro-superconducting quantum interference device characteristics”, *Journal of Applied Physics* **91**, 4432 (2002).
- [176] A. G. P. Troeman, H. Derking, B. Borger, J. Pleikies, D. Veldhuis, and H. Hilgenkamp, “NanoSQUIDs Based on Niobium Constrictions”, *Nano Letters* **7**, 2152 (2007).
- [177] R. Vijay, J. D. Sau, M. L. Cohen, and I. Siddiqi, “Optimizing Anharmonicity in Nanoscale Weak Link Josephson Junction Oscillators”, *Physical Review Letters* **103**, 087003 (2009).
- [178] M. J. Martínez-Pérez and D. Koelle, “NanoSQUIDs: Basics & recent advances”, *Physical Sciences Reviews* **2**, 10.1515/psr-2017-5001 (2017).
- [179] R. W. Cohen and B. Abeles, “Superconductivity in Granular Aluminum Films”, *Physical Review* **168**, 444 (1968).
- [180] G. Deutscher and S. A. Dodds, “Critical-field anisotropy and fluctuation conductivity in granular aluminum films”, *Physical Review B* **16**, 3936 (1977).
- [181] G. Deutscher, H. Fenichel, M. Gershenson, E. Grünbaum, and Z. Ovadyahu, “Transition to zero dimensionality in granular aluminum superconducting films”, *Journal of Low Temperature Physics* **10**, 231 (1973).

- [182] L. Grünhaupt, N. Maleeva, S. T. Skacel, M. Calvo, F. Levy-Bertrand, A. V. Ustinov, H. Rotzinger, A. Monfardini, G. Catelani, and I. M. Pop, “Loss Mechanisms and Quasiparticle Dynamics in Superconducting Microwave Resonators Made of Thin-Film Granular Aluminum”, *Physical Review Letters* **121**, 117001 (2018).
- [183] L. Grünhaupt, M. Spiecker, D. Gusenkova, N. Maleeva, S. T. Skacel, I. Takmakov, F. Valenti, P. Winkel, H. Rotzinger, W. Wernsdorfer, A. V. Ustinov, and I. M. Pop, “Granular aluminium as a superconducting material for high-impedance quantum circuits”, *Nature Materials* **18**, 816 (2019).
- [184] P. Winkel, I. Takmakov, D. Rieger, L. Planat, W. Hasch-Guichard, L. Grünhaupt, N. Maleeva, F. Foroughi, F. Henriques, K. Borisov, J. Ferrero, A. V. Ustinov, W. Wernsdorfer, N. Roch, and I. M. Pop, “Nondegenerate Parametric Amplifiers Based on Dispersion-Engineered Josephson-Junction Arrays”, *Physical Review Applied* **13**, 024015 (2020).
- [185] P. Winkel, “Superconducting quantumcircuits for hybrid architectures”, PhD Thesis, KIT, Karlsruhe (2020).
- [186] P. Winkel, K. Borisov, L. Grünhaupt, D. Rieger, M. Spiecker, F. Valenti, A. V. Ustinov, W. Wernsdorfer, and I. M. Pop, “Implementation of a Transmon Qubit Using Superconducting Granular Aluminum”, *Physical Review X* **10**, 031032 (2020).
- [187] E. E. Mitchell and S. K. H. Lam, “Niobium dc SQUIDS with Nanobridge Junctions”, *Physics Procedia SUPERCONDUCTIVITY CENTENNIAL Conference 2011*, **36**, 382 (2012).
- [188] K. Geerlings, S. Shankar, E. Edwards, L. Frunzio, R. J. Schoelkopf, and M. H. Devoret, “Improving the quality factor of microwave compact resonators by optimizing their geometrical parameters”, *Applied Physics Letters* **100**, 192601 (2012).
- [189] M. S. Khalil, M. J. A. Stoutimore, F. C. Wellstood, and K. D. Osborn, “An analysis method for asymmetric resonator transmission applied to superconducting devices”, *Journal of Applied Physics* **111**, 054510 (2012).
- [190] S. Probst, F. B. Song, P. A. Bushev, A. V. Ustinov, and M. Weides, “Efficient and robust analysis of complex scattering data under noise in microwave resonators.”, *The Review of scientific instruments* **86**, 024706 (2015).
- [191] F. Yang, T. Gozliniski, T. Storbeck, L. Grünhaupt, I. M. Pop, and W. Wulfhekel, “Microscopic charging and in-gap states in superconducting granular aluminum”, *Physical Review B* **102**, 104502 (2020).
- [192] I. Pietka, “Microstrip Resonators made from Granular Aluminum for Microwave Circuit Quantum Electrodynamics”, *Master’s Thesis*, Ruhr Universität Bochum, Bochum (2019).

- [193] K. Geerlings, *Measurement of High Q Weakly Coupled Microwave Resonators*, Tech. Rep. (2011).
- [194] R. Barends, “Photon-detecting superconducting resonators”, PhD Thesis, TU Delft, Delft (2009).
- [195] W. D. Oliver and P. B. Welander, “Materials in superconducting quantum bits”, *MRS Bulletin* **38**, 816 (2013).
- [196] A. Romanenko and D. I. Schuster, “Understanding Quality Factor Degradation in Superconducting Niobium Cavities at Low Microwave Field Amplitudes”, *Physical Review Letters* **119**, 264801 (2017).
- [197] R. B. Laibowitz, A. N. Broers, J. T. C. Yeh, and J. M. Viggiano, “Josephson effect in Nb nanobridges”, *Applied Physics Letters* **35**, 891 (1979).
- [198] I. Siddiqi, A. Verevkin, D. E. Prober, A. Skalare, W. R. McGrath, P. M. Echternach, and H. G. LeDuc, “Heterodyne mixing in diffusion-cooled superconducting aluminum hot-electron bolometers”, *Journal of Applied Physics* **91**, 4646 (2002).
- [199] M. Faucher, T. Fournier, B. Pannetier, C. Thirion, W. Wernsdorfer, J. C. Villegier, and V. Bouchiat, “Niobium and niobium nitride SQUIDS based on anodized nanobridges made with an Atomic Force Microscope”, *Physica C: Superconductivity* **368**, 211 (2002).
- [200] C. Granata, A. Vettoliere, P. Walke, E. Esposito, C. Nappi, P. Silvestrini, B. Ruggiero, and M. Russo, “NANO-SQUIDS based on niobium Dayem bridges for nanoscale applications”, *Journal of Physics: Conference Series* **234**, 042010 (2010).
- [201] D. C. Cox, J. C. Gallop, and L. Hao, “Focused Ion Beam Processing of Superconducting Junctions and SQUID Based Devices”, *Nanofabrication* **1**, 10.2478/nanofab-2014-0005 (2014).
- [202] N. D. Earnest, “Engineering Light-Matter Interactions with Metastable States in a Heavy Fluxonium”, Ph.D. thesis, University of Chicago, Chicago (2019).
- [203] D. Bothner, I. C. Rodrigues, and G. A. Steele, “Four-wave-cooling to the single phonon level in Kerr optomechanics”, arXiv:2104.02511 [cond-mat, physics:quant-ph] (2021).
- [204] M. F. Gely and G. A. Steele, “Superconducting electro-mechanics to explore the effect of general relativity in massive superpositions”, arXiv:2103.12729 [cond-mat, physics:quant-ph] (2021).
- [205] J. Hofer and M. Aspelmeyer, “Analytic solutions to the Maxwell–London equations and levitation force for a superconducting sphere in a quadrupole field”, *Physica Scripta* **94**, 125508 (2019).

-
- [206] M. G. Latorre, J. Hofer, M. Rudolph, and W. Wiczorek, “Chip-based superconducting traps for levitation of micrometer-sized particles in the Meissner state”, *Superconductor Science and Technology* **33**, 105002 (2020).

Publication list

- [1] D. Zoepfl, P. R. Muppalla, C. M. F. Schneider, S. Kasemann, S. Partel, and G. Kirchmair, “Characterization of low loss microstrip resonators as a building block for circuit QED in a 3D waveguide”, *AIP Advances* **7**, 085118 (2017).
- [2] D. Zoepfl, M. L. Juan, C. M. F. Schneider, and G. Kirchmair, “Single-Photon Cooling in Microwave Magnetomechanics”, *Physical Review Letters* **125**, 023601 (2020).
- [3] E. I. Rosenthal, C. M. F. Schneider, M. Malnou, Z. Zhao, F. Leditzky, B. J. Chapman, W. Wustmann, X. Ma, D. A. Palken, M. F. Zanner, L. R. Vale, G. C. Hilton, J. Gao, G. Smith, G. Kirchmair, and K. W. Lehnert, “Efficient and Low-Backaction Quantum Measurement Using a Chip-Scale Detector”, *Physical Review Letters* **126**, 090503 (2021).
- [4] P. Heidler, C. M. F. Schneider, K. Kustura, C. Gonzalez-Ballester, O. Romero-Isart, and G. Kirchmair, “Observing Non-Markovian Effects of Two-Level Systems in a Niobium Coaxial Resonator with a Single-Photon Lifetime of 10 ms”, [arXiv:2102.10016](https://arxiv.org/abs/2102.10016) [cond-mat, physics:quant-ph] (2021).

Appendix

Fabrication recipes

Here, I present cleaning procedures and fabrication recipes for all in-house fabricated samples of this thesis.

A.1 Wafer cleaning

Cleaning recipe for new wafers. Typically we do not use acetone when we cleaned the wafers using Piranha.

Piranha cleaning (optional)	
Ratio	H ₂ SO ₄ : H ₂ O ₂ (3:1)
Protocol	All steps with proper acid equipment and in fume-hood Fill beaker with 3 parts H ₂ SO ₄ Put in wafers using the quartz/glass holder Add 1 part H ₂ O ₂ Solution gets hot and develops smoke Leave for 5 min
Ultrasonic cleaning in warm acetone bath (only when not Piranha cleaned)	
Duration	5 min
Frequency	30 kHz
Power	100%
Finishing	Put quickly in IPA when getting sample out of acetone. Rinse with IPA afterwards and blow dry with N ₂

A.2 grAl SQUID resonators

Since we only had 495PMMA-A4 resist at that point in our cleanroom, we decided to use two layers of resist to increase the thickness to 400 nm. This was to ensure that the angled evaporation is going to the resist wall and not reaching the substrate at the bottom.

495 PMMA A4 resist spinning	
Dynamic dispensing	500 rpm
Spinning speed	2000 rpm
Spinning time	60 s
Hot plate temperature	200°C
Baking time	5 min
2nd layer	Repeat all steps for second layer with same properties
Measured thickness	400 ± 20 nm
Gold sputtering (when using sapphire substrates)	
Table position	All the way down
Ar pressure	0.07 mbar
Current	40 mA
Remarks	Blueish layer of gold
Electron beam lithography	
Acc. voltage	30 kV
Base dose	80 $\mu\text{C}/\text{cm}^2$
Dosefactor (large)	5
Dosefactor (small)	7
Aperture (large)	120 μm
Aperture (small)	10 μm
Gold etching	
Solution	I ₂ /KI/H ₂ O (1:4:40)
Etch time	10 s
Protocol	Quickly hold wafer in Lugol solution for 10s while opening tweezers When pulling it out directly rinse with a lot of DI water Place in beaker filled with DI water for short time Rinse with DI water Blow dry using N ₂
Resist development	
Solution	IPA/H ₂ O (3:1)
Temperature	6°C (beaker in chiller)
Time	1 min 45 s
Finish	Rinse with DI water and blow dry using N ₂
Electron beam evaporation (Plassys)	
Descum	
Ar flow	10 sccm
O ₂ flow	5 sccm
V _{beam}	200 V
I _{beam}	10 mA
V _{acc}	50 V
Gettering	
Crucible	Ti
Time	2 min
Rate	0.2 nm/s

continued on next page

First layer	
Crucible	AlOx
O ₂ flow	4.5 sccm (equals 700 $\mu\Omega\text{cm}$ according to calibration)
Thickness	20 nm
Rate	1 nm/s
Angle	0°
Second layer	
Crucible	AlOx
O ₂ flow	3.2 sccm (equals 50 $\mu\Omega\text{cm}$ according to calibration)
Thickness	40 nm
Rate	1 nm/s
Angle	35°
Lift off	
Solution	Acetone on hotplate 60°C
Time	At least 2 hours
Comments	Small beaker, wafer flat on bottom Covered with Al foil to prevent evaporation
Finish	Rinse with IPA and put in new beaker with acetone Ultrasonicate gently (135 kHz, 15%) Rinse again with IPA and blow dry with N ₂

A.3 Nb constriction SQUID resonators

The recipe for the Nb constriction resonators is very similar to the one from the grAl resonators. The only differences are that we use evaporated Niobium, do not use an angle for evaporation and use a thinner layer of resist.

495 PMMA A4 resist spinning	
Dynamic dispensing	500 rpm
Spinning speed	2000 rpm
Spinning time	60 s
Hot plate temperature	200°C
Baking time	5 min
Gold sputtering (when using sapphire substrates)	
Table position	All the way down
Ar pressure	0.07 mbar
Current	40 mA
Remarks	Blueish layer of gold

continued on next page

Electron beam lithography

Acc. voltage	30 kV
Base dose	80 $\mu\text{C}/\text{cm}^2$
Dosefactor (large)	5
Dosefactor (small)	7
Aperture (large)	120 μm
Aperture (small)	10 μm

Gold etching

Solution	I ₂ /KI/H ₂ O (1:4:40)
Etch time	10 s
Protocol	Quickly hold wafer in Lugol solution for 10s while opening tweezers When pulling it out directly rinse with a lot of DI water Place in beaker filled with DI water for short time Rinse with DI water Blow dry using N ₂

Resist development

Solution	IPA/H ₂ O (3:1)
Temperature	6°C (beaker in chiller)
Time	1 min 45 s
Finish	Rinse with DI water and blow dry using N ₂

Electron beam evaporation (Plassys)

Descum	
Ar flow	10 sccm
O ₂ flow	5 sccm
V _{beam}	200 V
I _{beam}	10 mA
V _{acc}	50 V
Gettering	
Crucible	Ti
Time	2 min
Rate	0.2 nm/s
First layer	
Crucible	AlO _x
O ₂ flow	3.2 sccm (equals 50 $\mu\Omega\text{cm}$ according to calibration)
Thickness	15 nm
Rate	1 nm/s
Angle	0°
Second layer	
Crucible	Nb
Thickness	40 nm
Rate	1 nm/s
Angle	0°
Remarks	Ramp up beam currents very slowly. May require to go to beam currents up to 340 mA to achieve 1 nm/s. Nb gets very hot and bright, don't look at it directly

continued on next page

Lift off	
Solution	Acetone on hotplate 60°C
Time	At least 2 hours
Comments	Small beaker, wafer flat on bottom Covered with Al foil to prevent evaporation
Finish	Rinse with IPA and put in new beaker with acetone Ultrasonicate gently (135 kHz, 15%) Rinse again with IPA and blow dry with N ₂

A.4 Nb-grAl hybrid SQUID resonators

This process is the very same as the one for the purely grAl SQUID resonators, Appendix A.2. The only difference is that we evaporate Nb instead of the low resistivity grAl layer (with an angle).

A.5 Nb/Ta-Al hybrid SQUID resonators

This is a two-step process which requires two lithography steps. The first step for the Nb-Al hybrid resonators is the same as for the pure Nb resonators, Appendix A.3. I will therefore only discuss the recipe for Ta-Al hybrid resonators here, which requires a new reactive ion etching step. The recipe for the second lithography step is the same for Nb and Ta.

ma-N 2403 resist spinning	
Dynamic dispensing	500 rpm (15s)
Spinning speed	2000 rpm
Spinning time	45 s
Hot plate temperature	90°C
Baking time	60 s
Electron beam lithography	
Acc. voltage	30 kV
Base dose	80 $\mu\text{C}/\text{cm}^2$
Dosefactor (large, pads)	3 (This is overexposed and leads to inclined edges, where the Al can go up the Ta. Otherwise the 200 nm edge is very steep and the Al may loose connection.)
Dosefactor (small)	2.2
Aperture (large)	120 μm
Aperture (small)	10 μm
Remarks	Requires zoom factor corrections of $\times 1.02$ for writefield alignment. Without you will get stitching errors.

continued on next page

Resist development	
Solution	ma-D 525 (TMAH 1% – 2.5%)
Time	90,s
Finish	Dip in DI water and rinse with DI water. Blow dry using N_2
Ar + Cl₂ etching (Sentech)	
RF Power	50 W
ICP Power	100 W
Ar flowrate	50 sccm
Cl ₂ flowrate	4 sccm
Time	260 s
Remarks	Directly dip in water after getting out of Sentech. Leads to controlled corrosion due to residual Cl ₂
Piranha cleaning step	
Remarks	Piranha step to remove resist residuals and clean wafer
2nd lithography - Double Layer resist spinning	
MMA EL13	1. layer. 700 nm layer of more sensitive copolymer.
Dynamic dispensing	500 rpm
Spinning speed	3000 rpm
Spinning time	100 s
Hot plate temperature	200°C
Baking time	5 min
PMMA A4	2. layer. 200 nm layer of less sensitive polymer.
Dynamic dispensing	500 rpm
Spinning speed	2000 rpm
Spinning time	100 s
Hot plate temperature	200°C
Baking time	5 min
Remarks	Measure thickness after each added layer with the ellipsometer and log.
Gold sputtering (when using sapphire substrates)	
Table position	All the way down
Ar pressure	0.07 mbar
Current	40 mA
Remarks	Blueish layer of gold
Electron beam lithography	
Acc. voltage	30 kV
Base dose	80 $\mu\text{C}/\text{cm}^2$
Dosefactor (trench)	7
Dosefactor (JJ)	6.8
Dosefactor (small)	5
Dosefactor (undercut)	1.2
Dosefactor (proximity)	1.7
Aperture (large)	120 μm
Aperture (small)	10 μm

continued on next page

Gold etching	
Solution	I ₂ /KI/H ₂ O (1:4:40)
Etch time	10 s
Protocol	Quickly hold wafer in Lugol solution for 10s while opening tweezer When pulling it out directly rinse with a lot of DI water Place in beaker filled with DI water for short time Rinse with DI water Blow dry using N ₂
Electron beam evaporation (Plassys)	
Pump	at least 4 h, typically over night
Ar milling	Ar milling step to remove oxide from Ta/Nb
Ar flow	4 sccm
Ar pressure	6.5×10^{-4} mbar
V_{beam}	400 V
I_{beam}	20 mA
V_{acc}	120 V
Time	3 min
Gettering	
Crucible	Ti
Time	2 min
Rate	0.2 nm/s
First layer	
Crucible	Al
Thickness	25 nm
Rate	1 nm/s
Angle	+25°
Oxidation	
Pressure	5 mbar
Time	1 min
Second layer	
Crucible	Al
Thickness	-25 nm
Rate	1 nm/s
Angle	-25°
Lift off	
Solution	Acetone on hotplate 60°C
Time	At least 2 hours
Comments	Small beaker, wafer flat on bottom Covered with Al foil to prevent evaporation
Finish	Rinse again with IPA and blow dry with N ₂

Programming

We developed a full-python architecture for measurements, data-analysis and logging in our lab. The following is a brief overview, which should help to understand the big picture and could be used as a starting point for debugging. The sources can be found in our gitlab python-repo, and a link to a automated created documentation (sphinx¹) using the code docstrings can be found on our web. All our devices are either directly connected using Ethernet, or running on a server pc which translates the USB device to a local network device.

B.1 Instruments class

The Instruments class is a wrapper class for our python drivers. The idea is that each device should be addressed the same and the class takes care to translate this to device specific driver commands. For example a VNA should always have the method *myVNA.meas_complex_avg(...)* that is a basic complex measurement with averages. However, depending on which VNA is used (for example Keysight old, Keysight new, Rohde+Schwarz,...), this requires different drivers. The task of the class is to identify the used device (by simply using an IP table) and load the correct drivers. Furthermore, this class allows a high-level integration to a database. Each time a parameter of a device is changed or a measurement is started, this class queries the current state of the device and pushes its parameters/state to a database.

Drivers The drivers are the actual core of the instrument class. Here the SCPI commands are translated to python functions using pyvisa². When a new device is added to the lab, one of the first tasks is to write an exhaustive driver to support the full functionality of the device. This is a very monotonous task, a documentation to code transfer, which unfortunately has to be done once.

¹<https://www.sphinx-doc.org>

²<https://pyvisa.readthedocs.io/en/latest/>

B.2 Experiments class

Here we add classes for typical experiments routines that are very similar for each iteration of the experiment. For example a DC-SQUID characteristic routine, or the quick frequency domain characterization of resonators/qubits (fluxmaps, powersweeps, etc...). It requires to specify the used instruments and offers methods like acquiring IV characteristics or measuring a fluxmap.

B.3 Datamodule

This is our main class for data storage and analysis. It offers quick methods for plotting (interactively: bokeh, holoviews, static: matplotlib), fitting (e.g. T1, T2, circlefits), selecting data (limit data to a specific range), further analysis (e.g. smoothing, interpolation, IQ analysis for qubits), and storing metadata about used cryostat state, used devices, etc... The data is saved in the HDF5 or netCDF4 (which builds on HDF5) format. We differentiate between four main data structures

data_table is 2D data in tabular structure. It is in principle just a wrapper class around pandas³ DataFrame class.

data_grid is a N-dimensional data format (typically 3D in our case, e.g. for fluxmaps). This is a wrapper class around xarray⁴, which supports interactive plotting and easy data extraction.

data_complex is again 2D data based on data_table. However this class only has two columns (frequency and complex scattering parameters) and offers useful functionalities for analyzing complex VNA data, like the circlefit routine.

data_IQ is a custom class which is used to analyze single-shot IQ measurements of qubits and offers methods to analyze qubit states and properties.

CircleFit This is our implementation of the circlefit routine [70, 103, 188–190], supporting notch/hanger, reflection, and reflection with impedance mismatch (circulator, directional coupler) models. It is included by default as a sub module in the data_complex class.

B.4 Monitoring

Our instruments class allows the integration of a monitoring database and webapp. We use a MariaDB database on a Raspberry Pi 4B in the lab, to store the current state of

³<https://pandas.pydata.org/>

⁴<http://xarray.pydata.org>

each instrument, which gets updated by the instrument class. We use this database further to store the current state of our cryostats, and further lab logging sensors (e.g. humidity, temperature, runtimes,...). The database can be maintained by phpmyadmin⁵, which is accessible via the url <http://logpi/phpmyadmin/>, while being in the internal lab network (e.g. on LM1).

B.4.1 Webapp backend: flask

We present the stored data in form of a webapp. For the back-end we use the python web-framework flask⁶, to provide an web api for the database. The server is running on the Raspberry Pi 4B in Lab3. We use nginx for a reverse proxy, and gunicorn as a http server. The flask main.py file can be found at `/home/pi/python_repo/Monitor/main.py`. After making changes to the server you have to restart the websocket by running the command `sudo systemctl kirchmairlab restart`.

B.4.2 Webapp frontend: Vue.js

For the front-end we use the JavaScript framework Vue.js⁷. The source can be found on gitlab (LogPi branch) or on the Raspberry Pi 4B in the lab in the folder `/home/pi/python_repo/Monitor/fronted/dashboard/src/`. After modifying the source, one has to rebuild the javascript file by running `yarn build` and restarting the kirchmairlab service (see Appendix B.4.1. Figure B.1 shows the current interface of the webapp that supports measurement device parameters, cryostat logging, lab logging, a webapp for often used snippets, and useful links to our jupyterhubs, code documentation, group wiki, gitlab server, mattermost team and clean room booking page.

⁵<https://www.phpmyadmin.net/>

⁶<https://flask.palletsprojects.com>

⁷<https://vuejs.org/>

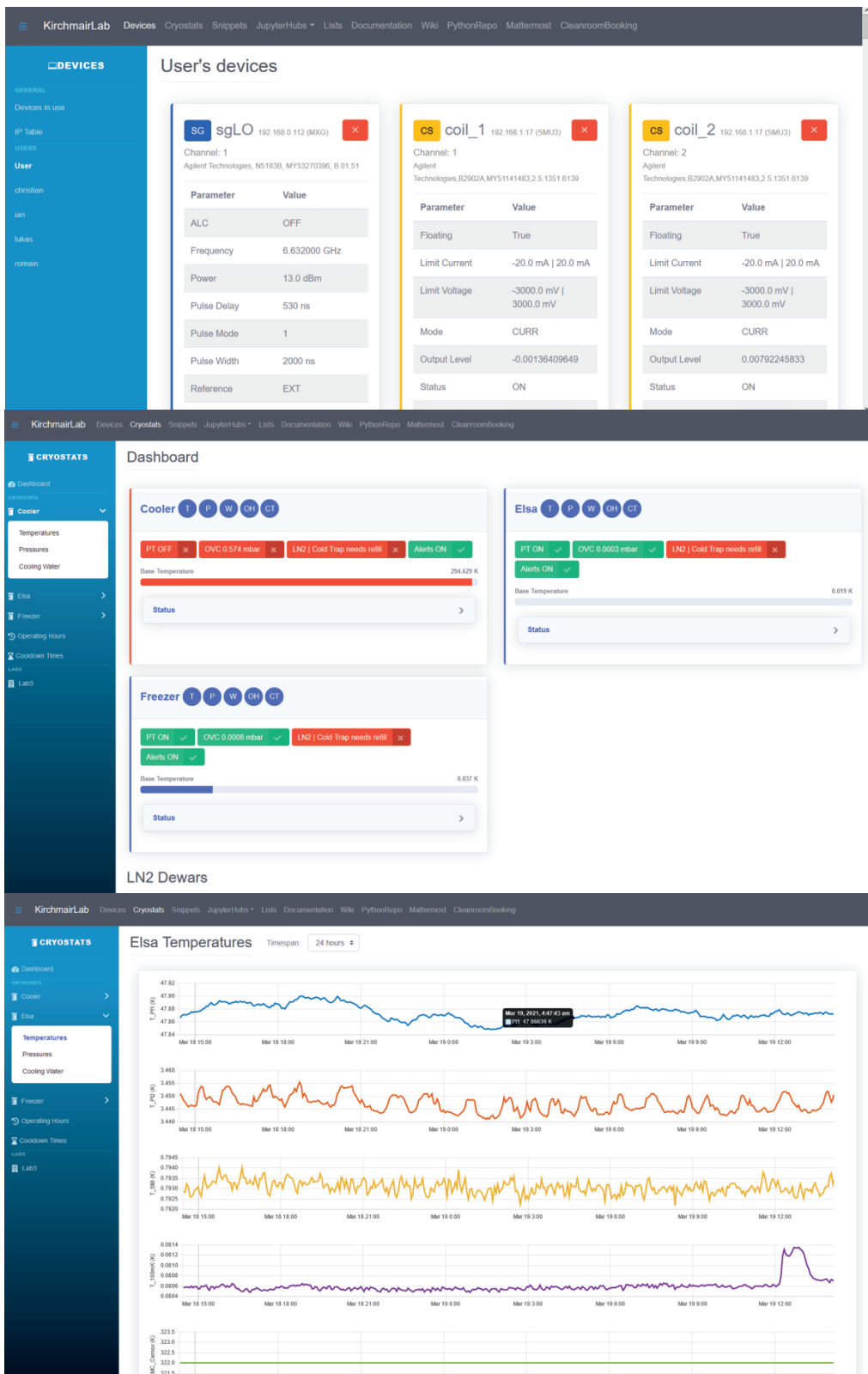


Figure B.1: Webapp interface.

Acknowledgements

Alright sonny, that's enough.
Just pack that in.

*(Monty Python
and the Holy Grail)*

That's it - a big part of my knowledge gathered in several years as a PhD candidate condensed in one thesis. This would have been impossible without the help and support of many excellent scientists, friends, and family, whom I want to express my sincere gratitude at this point.

First of all, I want to thank my supervisor Prof. Gerhard Kirchmair who made all this possible. I joined your young group in exciting times and was being part of expanding from a big lab with only a single cryostat (but an enormous optical table) to a small lab with two fridges, a second brand new lab with another cryostat, and a new running cleanroom with in-house nanofabrication. Thank you for giving me the support to explore superconducting circuits in such depth, for the many fruitful discussions, for the numerous shared insights, for proof-reading this thesis, and for your continuous efforts of being a great group leader, who cares about feedback and the well-being of his group, while still giving us the freedom to explore.

I want to thank Prof. Rudolf Grimm, Prof. Oriol Romero-Isart, and Prof. Markus Aspelmeyer for the co-supervision of my thesis. Even though there were not that many meetings, I enjoyed every discussion and learned something every time we talked.

Without the great help from Prof. Mathieu Juan, we probably still would not have detected a mechanical signal. Thank you Mathieu for being that exceptionally fast learning PostDoc with great and steady hands-on ideas that made the whole project a success. You contributed in so many ways that it is impossible to list it up here. Thank you very much, and I am very happy that you got a professorship. I wish you all the best with your new own group in Sherbrooke, and hope that you continue to collaborate.

Moreover, I want to thank David Zöpfl for the excellent work on the microwave setup, for many fruitful discussions, for implementing the circle fit routine together, for valuable design ideas, for all the setup improvements, and for creating the great output of the project.

I want to thank Max Zanner for his great efforts and results in the cleanroom, especially developing our qubit/junction process, for the stimulating discussions that always lead to a deeper comprehension of superconducting circuits, for all the energy he put into increasing the well-being and interaction of the group, for his questions that always create a fruitful follow-up discussion and motivate others, and for always being there for a Feierabendbier after very long cleanroom days.

For the many helpful discussions about DC-SQUIDS I want to thank Dr. Aleksei Sharafiev. Your deep knowledge about this topic is intriguing, and your calculations, PSCAN simulations, and whiteboard discussions helped a lot in my comprehension of SQUIDS. I will always remember the book by К.К. Лихарев, which you quickly pulled up once a more complicated question about SQUIDS came up.

I want to thank Michael Schmid for fighting through the beginning of the project as a Master Student and laying the foundation for all future work. Thank you for all the many hours of setting up the DC-wiring, soldering break-out boxes and filters, building measurement setups, characterizing the first DC-SQUIDS, and for understanding/discussing/calculating what is happening. One of the best acquisitions of our group was the manual coil winding machine, you ordered via ebay.

Moreover, I want to thank Dr. Markus Weiß for taking excellent care of the cleanroom, and his introductions to electron beam lithography and reactive ion etching. Thank you that you are always there once problems arise with the complex machines.

I want to thank Lukas Deeg for proof-reading this thesis and for being such a motivated PhD student. I look forward to working with you and following your progress.

In terms of granular Aluminum, I want to thank Isabel Pietka for setting up the granular Aluminum process in our cleanroom. Thank you for all the knowledge, simulations, calibrations and characterizations.

Moreover, I want to thank Dr. Ioan Pop and his research group, especially Dr. Lukas Grünhaupt and Dr. Patrik Winkel for enthusiastically sharing their knowledge about granular Aluminum and the helpful and fruitful discussions. I will always remember the HIQuing workshop about high impedance quantum circuits in Varzo with the eminently nice and open scientific atmosphere that led to many new insights and a better comprehension of high inductance materials for me. Thank you Francesco Valenti for the organization of this great event.

I want to thank Michele Calvese for setting up and characterizing the Nb constriction DC-SQUID. It is intriguing how you absorb knowledge, and I hope you will join the group as a Master Student soon.

I want to thank Prof. Reinhold Kleiner and Prof. Dieter Koelle for sharing their extraordinary knowledge about SQUIDS and letting me join their labs for two weeks. Dieter, I still remember the inspiring stories about your stay in Berkeley while we played a nice match of beach volleyball after work. And Reinhold, I will never forget the great discussion about science at the legendary summer fest at your home. Thank you for this great time and experiences!

Moreover, I want to thank Kevin Uhl and Dr. Matthias Rudolph for the collaboration with the DC-SQUIDS. Thank you for all your efforts, designs, fruitful discussions, and help in SQUID designs. Especially thank you Kevin for welcoming and integrating me that nicely in your groups when I went to Tübingen. Also I want to thank Julian Linek for letting me join his SQUID characterizations and sharing his knowledge.

For the cantilever fabrication and discussions about designs and properties I want to thank Dr. Michael Trupke and Stefan Minniberger. The final samples looked really great!

Furthermore, I want to thank Ian Yang for the many hours we spent in the cleanroom together, for our efforts in optimizing the laser cutting, ellipsometry, the Tantalum recipe, and for helpful discussions. I want to thank Oscar Gargiulo for his programming, helpful discussions, and creating the coffee club, where I got spoiled and probably never be able to drink bad coffee again. Moreover, I want to thank Phani for working together and giving me the experience of an authentic Indian engagement in his hometown, and Stefan, Romain, Desi, Teresa, Vasilisa, Raffi, Paul, Markus, Alvise, Desi, and Steffi for all the helpful discussions and working together in the lab and fab.

I want to thank Prof. Konrad Lehnert who adopted me for half a year. During this stay I learned a lot, had many inspiring discussions, and the stay further led to a nice publication. Konrad, you are an excellent and organized group leader with great humor, and I really appreciate how much time you take for all your group members in small meetings. I still remember discussions about leak checking and how a leak detector works, or hour long in-depth discussions about circuits. Thank you for this great time and experience, which really shaped me, and for sharing your superb knowledge about superconducting circuits. I also want to thank Eric, Lukas, Brad, Rob, Dan, Maxime, Max, Sarang, and Ben for integrating me that nicely into the group, for all the discussions, and sharing your knowledge with me.

Especially, I want to thank Dr. Eric Rosenthal for integrating me into his project. Your goal oriented way of working, your exceptional skills in designing and explaining complex microwave circuits, and your great intuition of how the complex systems have to behave are intriguing. I really enjoyed working with you and I am very happy and proud about the SIMBA. I wish you all the best with your new PostDoc position in Stanford and I hope that we keep in touch. Thank you for everything!

I want to thank Paul Heidler, Katja Kustura, Dr. Carlos Gonzalez-Ballester and Prof. Oriol Romero-Isart for the exciting and interesting project about Two Level Systems in a record coaxial cavity. I have learned a lot about loss mechanisms in microwave resonators and how quantum mechanics can again lead to very strange dynamics. Thank you for the nice collaboration.

Moreover, I want to express my gratitude to Dr. Heide Streicher, Dr. Alexander Kaiser, Dr. Eric Endres, Prof. Roland Wester, and the whole DK-ALM team for the great time within the Doktoratskolleg. It is an amazing experience being part of this great community. I have learned so much about AMO physics, and scientific and nonscientific skills. The stay abroad was one of the highlights of my PhD and also the summer schools and further gatherings were always a great opportunity to socialize and connect to excellent scientists. Thank you for enabling and organizing this wonderful graduate school and I hope that future generations of PhD will also be able to get this experience. I want to thank FWF for the funding of it (W1259-N27).

I want to thank Andreas Strasser, Gerhard Hendl, Bernhard Öttl, and Stefan Haslwanter for their great work in the IQOQI mechanic and electric workshop. Andreas, you have

always the most clever ideas for difficult designs and tasks, and the resulting pieces are always masterpieces. Thank you for making all our experiments possible.

Furthermore, I want to thank Nikolaus Falschlunger, Elisabeth Huck, Claudia Mevenkamp, Carina Theresa Sassermann, Elke Wölfmaier, and Markus Knabl for their great administrative support. Thank you for realizing the numerous orders over the last years, and for the support when problems came up.

I want to thank David Jordan, and Valentin Staubmann for the excellent IT support and debugging.

Vielen herzlichen Dank to my parents and my brother, who supported me throughout all my studies. Thank you for always being there and that I can count on you!

Thank you to all my friends, who balanced my life so that I would not become crazy in this spooky world of quantum physics.

And finally: Thank you Isi, for sharing the experience of writing up, for the many discussions (for example about quasiparticles), for all your opinions about figures and paragraphs, for all your support, for your genuine interest, for always being there, for not letting me starve to death, for making me always happy, and for being this wonderful person you are. Thank you for conquering life together with me! =)